

FEBEX Project
Final report

Post-mortem
bentonite analysis



FEBEX Project
Final report

Postmortem bentonite analysis



ENRESA
Dirección de Ingeniería de Residuos y Combustible
Emilio Vargas nº 7
28043 Madrid - España
Tfno.: 915 668 100
Fax: 915 668 169
www.enresa.es

Diseño y producción: TransEdit
Imprime: GRAFISTAFF, S.L.
ISSN: 1134-380X
D.L.: M-
XXX de 2006

This report has been drawn up on behalf of ENRESA.

This report has been drawn up within the context of the FEBEX project. Its contents represent only the opinions of the authors, which do not necessarily coincide with those of the other participants in the said project.

Edited by

M.V. Villar (CIEMAT)

from contributions of:

CIEMAT: M.V. Villar, A.M. Fernández, P. Rivas

CIMNE: A. Lloret, D. Daucausse

INPL: E. Montarges-Pelletier, K. Devineau, Villieras, F.

CEG-CTU: E. Hynková, Z. Cechova

UDC: L. Montenegro, J. Samper, L. Zheng

Euro-Géomat: J.-C. Robinet

VTT: A. Muurinen

NAGRA: H.P. Weber

Clay Technology AB: L. Börgesson, T. Sandén

EIG EURIDICE: J. Verstricht

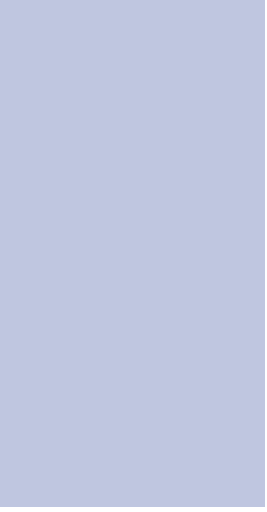


Table of Contents

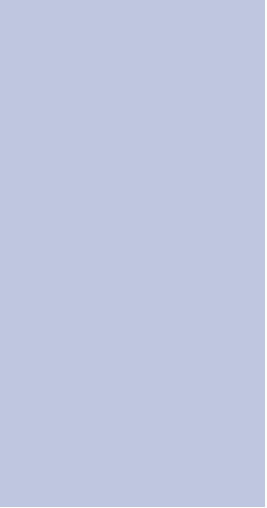


Table of Contents

| | |
|---|----|
| RESUMEN | 1 |
| ABSTRACT | 5 |
| 1. INTRODUCTION | 9 |
| 2. THE FEBEX BENTONITE | 15 |
| 3. DISMANTLING OF THE BARRIER AND BENTONITE SAMPLING | 23 |
| 4. BENTONITE ANALYSIS | 31 |
| 4.1. <i>Water content and dry density of the barrier</i> | 33 |
| 4.1.1. <i>CIMNE: In situ determinations</i> | 33 |
| 4.1.1.1. <i>Water content and dry density distributions in vertical cross sections</i> | 33 |
| 4.1.1.2. <i>Water content and dry density distribution in the vertical longitudinal section</i> | 33 |
| 4.1.1.3. <i>Comparison of measured water contents with the measurements of the in situ instrumentation</i> | 37 |
| 4.1.2. <i>CIEMAT: Laboratory determinations</i> | 39 |
| 4.1.3. <i>NAGRA: In situ and laboratory determinations</i> | 41 |
| 4.1.4. <i>Clay Technology AB: Laboratory determinations</i> | 44 |
| 4.2. <i>Analysis of tracers distribution</i> | 46 |
| 4.2.1. <i>UDC-CIEMAT: Deuterium</i> | 46 |
| 4.2.1.1. <i>Preliminary scoping calculations</i> | 50 |
| 4.2.1.2. <i>Deuterium laboratory sampling</i> | 50 |
| 4.2.1.3. <i>Deuterium isotopic analyses of aqueous extract samples</i> | 50 |
| 4.2.1.4. <i>Conversion of deuterium aqueous extract concentration to bentonite pore water concentration</i> | 54 |
| 4.2.1.5. <i>Discussion</i> | 54 |

| | |
|--|-----|
| 4.2.2. EIG EURIDICE: Iodide | 57 |
| 4.2.3. EIG EURIDICE: Boron | 58 |
| 4.3. Thermo-hydro-geochemical tests | 61 |
| 4.3.1. CIEMAT: Mineralogical, chemical and textural analysis | 62 |
| 4.3.1.1. Subsampling at the laboratory | 62 |
| 4.3.1.2. X-ray diffraction | 63 |
| 4.3.1.3. Chemical analysis | 67 |
| 4.3.1.4. Aqueous extracts | 69 |
| 4.3.1.5. Exchangeable cations | 76 |
| 4.3.1.6. Squeezing tests | 79 |
| 4.3.1.7. Textural analysis: nitrogen adsorption/desorption isotherms | 89 |
| 4.3.2. CIEMAT: Analysis of the water obtained in situ from the gas pipes | 90 |
| 4.3.3. INPL/LEM: Mineralogical, chemical and textural analysis | 93 |
| 4.3.3.1. Preparation of the samples | 93 |
| 4.3.3.2. X-ray diffraction | 93 |
| 4.3.3.3. Infrared spectroscopy | 98 |
| 4.3.3.4. Exchangeable cations and CEC | 99 |
| 4.3.3.5. Chemical analyses | 101 |
| 4.3.3.6. Microscopic analyses * | 102 |
| 4.3.3.7. Textural analysis | 105 |
| 4.3.4. VTT: Chemical changes caused by the concrete seal into bentonite | 112 |
| 4.4. Thermo-hydro-mechanical tests | 115 |
| 4.4.1. CIEMAT: Basic characterisation and THM properties | 117 |
| 4.4.1.1. Sampling at the laboratory | 117 |
| 4.4.1.2. Retention curves | 117 |
| 4.4.1.3. Porosimetry | 124 |
| 4.4.1.4. Hydraulic conductivity | 127 |
| 4.4.1.5. Swelling deformation tests | 127 |
| 4.4.1.6. Determination of preconsolidation pressure | 130 |
| 4.4.1.7. Thermal conductivity | 132 |
| 4.4.2. CTU: Basic characterisation and THM properties | 135 |
| 4.4.2.1. Basic properties | 135 |
| 4.4.2.2. Swelling properties | 141 |
| 4.4.2.3. Uniaxial strength | 142 |
| 4.4.2.4. Thermal properties | 145 |
| 4.4.3. EIG-EURIDICE: Hydraulic conductivity | 145 |
| 4.4.4. Euro-Géomat: Tests in joints | 148 |
| 4.4.4.1. Preparation of samples | 149 |

| | |
|---|-----|
| 4.4.4.2. Experimental methodology | 151 |
| 4.4.4.3. Microstructure | 153 |
| 4.4.4.4. Permeability and swelling pressure | 153 |
| 4.4.4.5. Moisture diffusion coefficient | 156 |
| 4.4.4.6. Infiltration tests in columns | 156 |
| 5. DISCUSSION | 161 |
| 5.1. Physical state of the barrier | 163 |
| 5.2. THG properties | 167 |
| 5.3. THM properties | 169 |
| 6. SUMMARY AND CONCLUSIONS | 173 |
| 7. REFERENCES | 179 |



Resumen



Resumen

El trabajo experimental del Proyecto FEBEX ha consistido en un ensayo *in situ*, realizado en condiciones naturales y a escala real, un ensayo en "maqueta", a escala casi real, y una gran serie de ensayos de laboratorio.

La mayor parte de los ensayos de laboratorio se han hecho previamente o en paralelo a los dos ensayos a gran escala. Es decir, sobre muestras del mismo material de las barreras del ensayo *in situ* y de la "maqueta", pero no de las propias barreras. Sin embargo, una parte de los ensayos de laboratorio (los incluidos en este documento) se ha hecho sobre muestras de bentonita obtenidas en el desmantelamiento parcial del ensayo *in situ*, realizado el año 2002, después de cinco años de calentamiento e hidratación.

Se han realizado dos tipos de ensayos: 1) de caracterización de la bentonita, con el objeto de conocer el estado de la barrera y para comparación con los resultados de predicción de los modelos THM y THG; y 2) ensayos para determinar los cambios en propiedades THM y THG ocurridos durante la operación como consecuencia de la acción combinada de la temperatura, el agua, las juntas y los solutos.

A continuación se presenta un resumen de las conclusiones obtenidas de los resultados de los ensayos de laboratorio incluidos en este documento.

La distribución de humedad y densidad seca de la bentonita en secciones verticales presenta simetría axial. No hay grandes variaciones entre la humedad media de secciones situadas alrededor del calentador y aquéllas alejadas de su influencia. Tampoco hay diferencias entre secciones situadas en zonas de diferente conductividad hidráulica del granito. Esta homogeneidad, así como la distribución radial de humedad en secciones verticales, es consecuencia del control de la bentonita sobre la cinética de hidratación, debido a la gran diferencia entre las permeabilidades de ésta y el granito. El grado de saturación medio de toda la bentonita extraída es del 85 por ciento.

La bentonita experimentó durante la operación un aumento generalizado de volumen que se ha traducido en una disminución desde la densidad seca de los bloques compactados ($1,70 \text{ g/cm}^3$) a la densidad seca media de la barrera calculada a partir de las medidas realizadas en las muestras extraídas ($1,58 \text{ g/cm}^3$). Esto es debido a la expansión de la bentonita para rellenar los huecos de construcción y

a la ligera descompresión que ha sufrido la barrera durante el desmantelamiento y muestreo.

La caracterización mineralógica y geoquímica realizada parece indicar que no se han producido grandes modificaciones en la bentonita durante la operación.

La capacidad de cambio catiónico ha aumentado respecto a la inicial, debido fundamentalmente al aumento generalizado de potasio y calcio intercambiables. Se ha observado un aumento de sodio intercambiable hacia el granito, tanto en las secciones sometidas a gradiente térmico como en las isoterms.

La hidratación de la bentonita en los bloques en contacto con el granito produce la disolución de los minerales más solubles (sulfatos, carbonatos y cloruros), que son transportados hacia la parte interna de la barrera. Con ello se han generado, a la fecha del desmantelamiento, diferentes frentes salinos según la movilidad de los iones disueltos: el comportamiento del Na, Ca y Mg es similar al del cloruro, mientras que la movilidad del sulfato es considerablemente menor. El movimiento de solutos es más rápido en las zonas afectadas por la temperatura.

La composición química y mineralógica de la bentonita en contacto con el tapón de hormigón es similar a la de la bentonita no tratada. Sólo se registra un aumento del contenido de aluminio y la aparición puntual de cantidades mayores de calcita y yeso. También se ha observado un aumento de Ca, Na y K intercambiables y un aumento de la salinidad del agua intersticial.

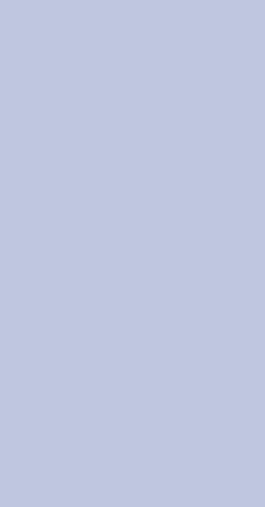
Se han determinado varias propiedades térmicas, hidráulicas y mecánicas de la bentonita extraída de la barrera para comprobar el posible cambio de comportamiento THM ocasionado durante el experimento.

La capacidad de retención de agua de las muestras obtenidas de la barrera desmontada es similar a la de muestras de bentonita no sometida al experimento. La conductividad hidráulica de las muestras del desmantelamiento depende fundamentalmente de su densidad seca (como ocurre con la bentonita no usada en la barrera), por lo que está relacionada con su posición en la barrera.

La capacidad de hinchamiento de la bentonita no ha cambiado irreversiblemente tras cinco años de operación en las condiciones del almacenamiento.

La presión de preconsolidación de las muestras de la barrera desmontada se ha reducido desde un valor inicial de 40 MPa a valores inferiores a 10 MPa (más bajos en el anillo externo de la barrera), lo que es debido a los cambios microestructurales asociados al aumento de volumen experimentado durante la hidratación.

Los ensayos realizados en muestras remoldeadas de bentonita del desmantelamiento, con juntas paralelas y perpendiculares al flujo, muestran que, una vez saturado, el medio se hace homogéneo y las juntas se sellan completamente, con lo que las propiedades hidro-mecánicas del material dependen sólo de su densidad seca.



Abstract



Abstract

The experimental work performed within the FEBEX Project has consisted of an *in situ* test, carried out under natural conditions and at full scale, a “mock-up” test performed at almost full scale and a large number of laboratory tests.

Most of the laboratory tests have been carried out prior to or in parallel with the two large-scale tests; in other words, on samples of the same barrier material as in the *in situ* and “mock-up” tests but not on the barriers themselves. However, part of the laboratory tests (those included in this document) have been performed on samples of bentonite obtained during the partial dismantling of the *in situ* test, performed in 2002 after five years of heating and hydration.

Two types of tests have been performed: 1) characterisation of the bentonite, with a view to gaining insight into the state of the barrier and for comparison with the results of THM and THG model predictions, and 2) tests to determine the changes in THM and THG properties occurring during operation as a result of the combined action of temperature, water, joints and solutes.

Presented below is a summary of the conclusions drawn from the results of the laboratory tests included in this document.

The distribution of the humidity and dry density of the bentonite in vertical sections shows axial symmetry. There are no major variations between the average humidity of sections located around the heater and those others that are outside its area of influence. Neither are there differences between sections located in areas of different hydraulic conductivity of the granite. This homogeneity, along with the radial distribution of humidity in vertical sections, is a result of the control exercised by the bentonite over hydration kinetics, due to the major difference between the permeabilities of the bentonite and the granite. The average degree of saturation of all the bentonite extracted is 85 percent.

During operation the bentonite underwent a generalised increase in volume that has led to a reduction from the dry density of the compacted blocks (1.70 g/cm^3) to the average dry density of the barrier calculated from the measurements performed on the samples extracted (1.58 g/cm^3). This is due to the expansion of the bentonite to fill the construction voids and to the slight decompression experienced by the barrier during dismantling and sampling.

The mineralogical and geochemical characterisation performed would appear to indicate that there

have not been major modifications in the bentonite during operation.

The cation exchange capacity has increased with respect to the initial value, fundamentally due to the generalised increase in exchangeable potassium and calcium. An increase in exchangeable sodium has been observed towards the granite in both the sections subjected to a thermal gradient and in the isotherm sections.

The hydration of the bentonite in the blocks in contact with the granite causes the dissolution of the most soluble minerals (sulphates, carbonates and chlorides), which are transported towards the inner part of the barrier. As of the date of dismantling, this has generated different saline fronts depending on the mobility of the dissolved ions: the behaviour of Na, Ca and Mg is similar to that of the chloride, while the mobility of the sulphate is considerably lower. The movement of solutes is quicker in areas affected by temperature.

The chemical and mineralogical composition of the bentonite in contact with the concrete plug is similar to that of the untreated bentonite. Only an increase in aluminium content and the occasional appearance of larger quantities of calcite and gypsum are recorded. An increase has been observed also in exchangeable Ca, Na and K, along with an increase in the salinity of the interstitial water.

Various thermal, hydraulic and mechanical properties of the bentonite extracted from the barrier have been determined, in order to check for possible changes in THM behaviour caused during the experiment.

The water retention capacity of the samples obtained from the dismantled barrier is similar to that of the samples of bentonite not subjected to the experiment. The hydraulic conductivity of the samples from dismantling depends fundamentally on dry density (as occurred with the bentonite not used in the barrier), as a result of which it is related to their position in the barrier.

The swelling capacity of the bentonite has not changed irreversibly after five years of operation under repository conditions. The pre-consolidation pressure of the samples from the dismantled barrier has decreased from the initial value of 40 MPa to values of less than 10 MPa (lower in the outer ring of the barrier), this being due to microstructural changes associated with the increase in volume experienced during hydration.

The tests performed on remoulded samples of bentonite from dismantling, with joints parallel and perpendicular to flow, show that once saturated the medium

becomes homogeneous and the joints seal completely, as a result of which the hydro-mechanical properties of the material depend only on its dry density.

1. Introduction

1. Introduction

The aim of FEBEX (Full-scale Engineered Barriers Experiment) is to study the behaviour of components in the near field for a high-level radioactive waste (HLW) repository in crystalline rock. The experimental work consists of three main parts:

- an “*in situ*” test, under natural conditions and at full scale, performed at the Grimsel Test Site (GTS, Switzerland);
- a “mock-up” test, at almost full scale, performed at CIEMAT facilities (Madrid); and
- a series of laboratory tests to complement the information from the two large-scale tests.

The project is based on the Spanish reference concept for disposal of radioactive waste in crystalline rock (AGP Granito): the waste canisters are placed horizontally in drifts and surrounded by a clay barrier constructed from highly compacted bentonite blocks (ENRESA 1995). In the two large-scale tests, the thermal effect of the wastes is simulated by means of heaters, while hydration is natural in the *in situ* test and controlled in the one performed on the mock-up. Both tests are monitored, this allowing the evolution of the temperature, total pressure, water content, water pressure, displacements and other parameters to be obtained continuously in different parts of the

barrier and the host rock, this information being used as a contrast to the predictions of the thermo-hydro-mechanical (THM) and thermo-hydro-geochemical (THG) models.

The *in situ* test is performed in a gallery excavated in the underground laboratory managed by NAGRA at Grimsel (Switzerland). The basic components of the test (Figure 1) are: the gallery, measuring 70 m in length and 2.3 m in diameter; the heating system, made up of two heaters placed inside a liner installed concentrically with the gallery and separated one from the other by a distance of 1.0 m, with dimensions and weights analogous to those of the real canisters; the clay barrier, formed by blocks of compacted bentonite; the instrumentation and the monitoring and control system for data acquisition and supervision and control of the test both autonomously and remotely, from Madrid. The gallery is closed by a concrete plug. The gallery was excavated through the Aare granite (Keusen *et al.* 1989) and it crosses a lamprophyre dike in the zone where the first heater was placed (ENRESA 1998b).

To build the clay barrier, various types of blocks were manufactured from the bentonite in the shape of 12-cm thick circular crown sectors. The blocks were arranged in vertical slices giving place to the

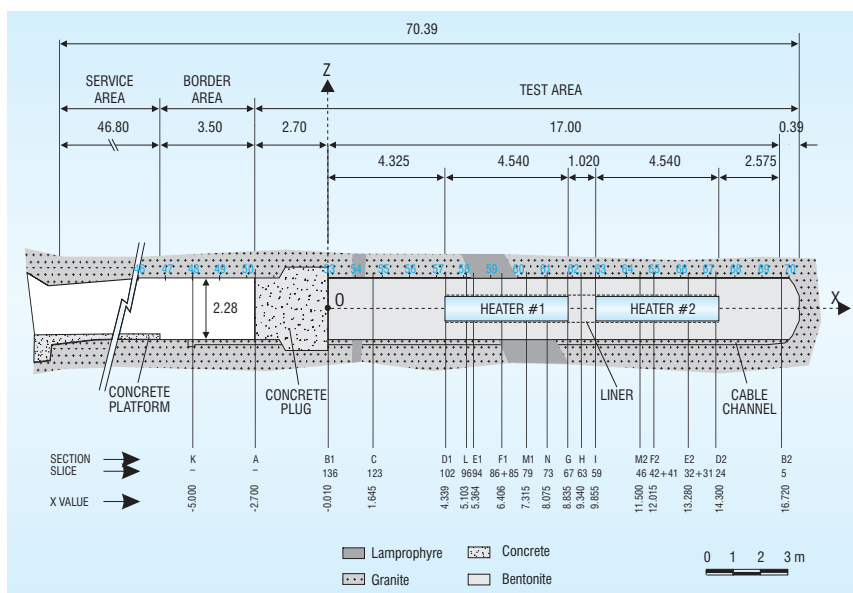


Figure 1: General disposition of principal elements in the test zone before dismantling (ENRESA 2000).

geometry of the barrier shown in Figure 2 for the heater and non-heater areas. In both areas, the three exterior rings are equal; in the heater area the interior ring is in contact with the steel liner. The blocks were obtained through uniaxial compaction of the FEBEX clay with its hygroscopic water content at pressures of between 40 and 45 MPa, what gave place to dry densities of 1.69-1.70 g/cm³ and block weights of between 18 and 23 kg. The initial dry density of the blocks was selected by taking into account the probable volume of the construction gaps and the need to have a barrier with an average dry density of 1.60 g/cm³ (ENRESA 2000).

The heating stage of the *in situ* test, known as operational stage, began on February 27th 1997. After five years of operation, the heater closer to the gallery entrance was switched off (February 2002). In the following months (spring and summer 2002) the heater and all the bentonite and instruments preceding and surrounding it were extracted (Bárcena *et al.* 2003).

The engineered barriers (waste, canister, and clay barrier) are key elements in the final disposal concept for HLW. The clay barrier has the multiple purpose of providing mechanical stability for the canister, by absorbing stresses and deformations, of sealing discontinuities in the adjacent rock and retarding the arrival of groundwater at the canister and of re-

taining/retarding the migration of the radionuclides released, once failure of the canister and lixiviation of the spent fuel have occurred.

The behaviour of a HLW repository is determined, to a large extent, by the characteristics of the design and construction of the engineered barriers and especially by the changes that may occur in the mechanical, hydraulic, and geochemical properties as a result of the combined effects of heat generated by the radioactive decay and of the water and solutes contributed by the surrounding rock. Therefore, in FEBEX I and II, it was considered of fundamental importance that the processes taking place in the near field be understood and quantified, for the evaluation of long-term behaviour. As a consequence, a program of laboratory tests was designed to study and comprehend the processes that take place in the clay barrier under simple and controlled conditions and to develop the governing equations. Moreover, the dismantling of section 1 of the *in situ* test provided the opportunity to check the predictions of the models and the modifications experienced by the bentonite in a direct and representative way.

Hence, an exhaustive postmortem bentonite sampling and analysis program was designed (AITEMIN 2000, 2002; Villar *et al.* 2002a). Basically, it has consisted on taking clay samples to characterise the solid and liquid phases, in order to confirm predic-

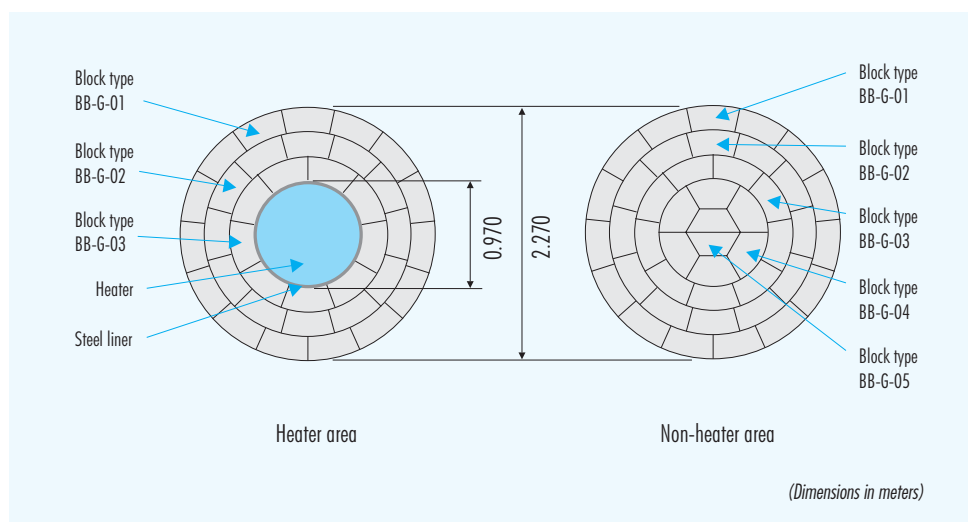


Figure 2: Geometry of the clay barrier in the FEBEX *in situ* test at GTS (ENRESA 2000).

tions and validate existing models of THM and THG processes. Samples have been taken from different parts of the clay buffer in order to:

- Analyse the physical, mechanical and chemical changes occurred in the clay by effect of heat and hydration, taking also into account the effect of joints.
- Analyse the chemical evolution of the bentonite pore water as a function of the hydration and temperature profiles.
- Study the flow paths of the different types of chemical tracers that were placed in the clay and the clay/rock contact during the installation phase.
- Calibrate some of the sensors installed in the barrier (TDR), according to the measurements made on the bentonite during the dismantling (water content).

Therefore, the main objectives of the bentonite sampling and analyses program are:

- The characterisation of the actual state of the barrier.
- The identification of physico-chemical alterations in the clay.

Several laboratories have participated in this Task, since there was a wide variety of tests proposed, which besides are experimentally difficult and time-consuming.

This document collects the results obtained by each organisation on the bentonite analyses performed after dismantling. Some of the groups have prepared detailed internal reports of their work that have been summarised in this document. A list of these reports –in which comprehensive descriptions of the results can be found– is shown below:

- Daucausse, D. & Lloret, A. (2003) Results of “in situ” measurements of water content and dry density. FEBEX report 70-UPC-L-5-012. 85 pp. Barcelona.
- Fernández, A.M. & Rivas, P. (2004): Task 141: Postmortem bentonite analyses. Geochemical

behaviour. FEBEX report 70-IMA-L-0-109. 71 pp. Madrid.

- Montarges-Pelletier, E.; Devineau, K.; Villieras, F.; Bouquet, E.; Pelletier, M.; Razafitianamaharavo, A.; Barres, O.; Lambert, P.; Charpentier, D.; Mosser-Ruck, R. & Cathelineau, M. (2003) Postmortem FEBEX bentonite samples. Mineralogical and textural analysis. Final report INPL/LEM. 34 pp. Vandoeuvre-lès-Nancy.
- Muurinen, A. (2003): Analysis of the samples from the cement-bentonite interface of the FEBEX *in situ* experiment. VTT processes. FEBEX Study 70-VTT-l-6-02. 14 pp. Helsinki.
- Montenegro, L.; Samper, J.; Zheng, L. ; Fernández, A.M. & Rivas, P. (2004): Sampling, laboratory analyses and numerical modelling of deuterium in the in situ Febex experiment. FEBEX report 70-ULC-L-6-03. 65 pp. La Coruña.
- Villar, M.V. (2003): Task 141: Postmortem bentonite analysis. Contribution of CIEMAT (THM) to Deliverable D11. Internal report CIEMAT/DIAE/54520/12/03. FEBEX report 70-IMA-L-6-107v0. 49 pp. Madrid.
- CTU-CEG (2003) FEBEX Project II. Report from September 1, 2002 to August 31, 2003. 42 pp. Prague.
- Robinet, J.C. (2003): Study of the effects of the joints on the hydraulic and hydro-mechanical properties of the FEBEX in situ test. Internal Report Euro-Géomat Consulting. FEBEX report. 43 pp. Orléans.
- Albert, W.; Weber, H.P.; Meier, E. & Dubois, D. (2003): Grimsel Test Site: FEBEX II. Excavation of TDR probes, section M1; Laboratory analyses of bentonite samples; New calibration + calculation of water content from TDR data. Interner Bericht 03-03. NAGRA. 61 pp. Wetingen.
- Verstricht, J. (2004): Work Package 1. Task 1.4 Post-mortem analysis. Bentonite. Technical Report 70-EIG-L-6-02. ESV EURIDICE GIE. 24 pp. Mol.

2. The FEBEX bentonite

2.The febex bentonite

The FEBEX bentonite used to manufacture the blocks for the *in situ* test comes from the Cortijo de Archidona deposit (Almería, Spain) and has been selected by ENRESA as suitable material for the backfilling and sealing of HLW repositories. It is the same clay material used for the FEBEX Project in the mock-up (Madrid, Spain) and other THM and THG tests. The processing at the factory consisted in disaggregation and gently grinding, drying at 60 °C and sieving by 5 mm.

The physico-chemical properties of the FEBEX bentonite, as well as its most relevant thermo-hydro-mechanical and geochemical characteristics obtained during FEBEX I are summarised in the final report of the project (ENRESA 2000) and are shown in detail in ENRESA (1998a), CIEMAT (1999), UPC (1999), Villar (2000, 2002), Lloret *et al.* (2002, 2004) and Fernández (2003). Several laboratories participated in these characterisation tasks. A summary of the results obtained is gathered below.

The mineralogical composition of the FEBEX bentonite has been analysed by X-ray diffraction (XRD). The montmorillonite content is higher than 90 percent (92 ± 3 %). The smectitic phases are actually made up of a smectite-illite mixed layer, with 10-15 percent of illite layers. Besides, the bentonite contains variable quantities of quartz (2 ± 1 %), plagioclase (2 ± 1 %), K-felspar, calcite and opal-CT (cristobalite-trydimite, 2 ± 1 %). By weight from dense concentrates and SEM observation, the following minerals have been identified: mica (biotite, sericite, muscovite), chlorite, non-differentiated silicates (Al, K, Fe, Mg, Mn), augite-diopside, hypersthene, hornblende, oxides (ilmenite, rutile, magnetite, Fe-oxides), phosphates (apatite, xenotime, monazite) and other non-differentiated minerals of titanium and rare earth.

Their contribution to bentonite composition is around 0.8 percent. Other accessory and trace minerals determined and identified are shown in [Table I](#) and [Table II](#).

The structural formula of the smectite, calculated from the chemical analysis of the less than 2 μm fraction, Ca-homoionised, is shown in [Table III](#).

The mineralogical composition has been also observed and quantified by optical microscopy study of thin sections. The textural heterogeneity itself is the main feature that can be described in the sample. The FEBEX bentonite is mainly composed of clay aggregates whose aspect ranges between dark isotropic low crystalline size ones to those presenting preferred orientation and relatively large (sub-micrometric) crystals. The remaining elements of the texture are glassy materials, volcanic rock fragments and individual accessory minerals (quartz and feldspars). Calcite is usually present as espartitic crystals replacing feldspars, but it has been observed also as isolated micritic cements.

With respect to the chemical composition, [Table IV](#) shows the average content values of the major elements and [Table V](#) shows the average values of the minor and trace elements of the FEBEX bentonite. The content of chlorides and sulphates is worthy of mention.

[Table VI](#) shows the average content values of the exchangeable cations along with the cation exchange capacity (CEC), as determined by different methods and laboratories.

The chemical composition of an aqueous extract of bentonite:water ratio of 1:4 is presented in [Table VII](#).

Table I
Accessory minerals of the FEBEX bentonite determined by a normative calculation and SEM identification.

| Mineral | Content (%) |
|--|-------------|
| Organic matter (expressed as CO ₂) | 0.35 ± 0.05 |
| Carbonates (calcite, dolomite) | 0.60 ± 0.13 |
| Soluble sulphates (gypsum) | 0.14 ± 0.01 |
| Low soluble sulphates (barite, celestite) | 0.12 ± 0.05 |
| Sulphurs (pyrite) | 0.02 ± 0.01 |
| Chlorides (halite) | 0.13 ± 0.02 |

Table II
Poorly ordered minerals of the FEBEX bentonite determined by selective chemical methods by two laboratories.

| Amorphous Phases (%) | CSIC-Zaidín | CIEMAT |
|--------------------------------|---------------|---------------|
| SiO ₂ | 1.48 ± 0.11 | 0.038 ± 0.005 |
| Al ₂ O ₃ | 0.035 ± 0.005 | 0.035 ± 0.005 |
| Fe ₂ O ₃ | 0.105 ± 0.009 | 0.105 ± 0.009 |

Table III
Structural formula of the Ca-homoionised smectite.

| IV Charge | VI Charge | Interl. Charge | Structural formula |
|-----------|-----------|----------------|--|
| -0.22 | -0.97 | 1.19 | $(\text{Si}_{7.78}\text{Al}_{0.22})^{\text{IV}}(\text{Al}_{2.77}\text{Fe}_{0.33}^{3+}\text{Fe}_{0.02}^{2+}\text{Mg}_{0.81}\text{Ti}_{0.02})^{\text{VI}}\text{O}_{20}(\text{OH})_4$ (Ca _{0.50} Na _{0.08} K _{0.11}) |

Table IV
Chemical composition of FEBEX bentonite as determined by two laboratories (%).

| | CSIC-Zaidín | CIEMAT |
|--------------------------------------|--------------|--------------|
| SiO ₂ | 58.92 ± 1.74 | 57.89 ± 1.55 |
| Al ₂ O ₃ | 19.48 ± 1.05 | 17.95 ± 0.71 |
| FeO | – | 0.25 ± 0.10 |
| Fe ₂ O ₃ total | 3.48 ± 0.63 | 2.84 ± 0.12 |
| MgO | 4.83 ± 0.27 | 4.21 ± 0.21 |
| MnO | 0.06 ± 0.02 | 0.04 ± 0.00 |
| CaO | 2.51 ± 0.09 | 1.83 ± 0.10 |
| Na ₂ O | 2.28 ± 0.11 | 1.31 ± 0.09 |
| K ₂ O | 1.21 ± 0.08 | 1.04 ± 0.05 |
| TiO ₂ | 0.27 ± 0.06 | 0.23 ± 0.01 |
| P ₂ O ₅ | 0.06 ± 0.02 | 0.03 ± 0.01 |
| H ₂ O ⁽¹⁾ | 5.07 ± 0.76 | 8.66 ± 2.88 |
| H ₂ O ⁺⁽²⁾ | – | 4.31 ± 0.41 |
| CO ₂ org | 0.19 ± 0.04 | 0.35 ± 0.05 |
| CO ₂ inorg | 0.52 ± 0.07 | 0.26 ± 0.06 |
| SO ₂ total | – | 0.21 ± 0.10 |
| F ⁻ | 0.21 ± 0.03 | 0.18 ± 0.01 |

¹Determined at 220°C; ²Structural water.

Table V
Minor and trace elements of the FEBEX bentonite (ppm).

| Ni | Zn | Ba | Sr | Zr | Co | Cu | Cr | Rb |
|-----------------|-------------------------------|--------|--------|------|------|---------|------|------|
| 20±3 | 65±4 | 164±25 | 220±23 | 43 | 9±3 | 25±9 | 8±2 | 41±2 |
| Cl ⁻ | SO ₄ ²⁻ | Ce | La | V | Y | U | Th | Li |
| 774±144 | 984±65 | 74±6 | 40±3 | 16±2 | 25±3 | 2.0±0.5 | 19±1 | 54±3 |

Table VI
Average values of exchangeable cations and cation exchange capacity (CEC) as determined by different methods (meq/100g).

| | CSIC-Zaidin ¹ | CIEMAT ¹ | CIEMAT ² |
|-----------------------------|--------------------------|---------------------|---------------------|
| Ca ²⁺ | 43 ± 5 | 42 ± 3 | 35 ± 2 |
| Mg ²⁺ | 32 ± 3 | 32 ± 2 | 31 ± 3 |
| Na ⁺ | 24 ± 4 | 25 ± 2 | 27 ± 0 |
| K ⁺ | 2.1 ± 0.2 | 2.5 ± 0.3 | 2.6 ± 0.4 |
| Sum of exchangeable cations | 101 ± 4 | | 96 ± 0 |
| CEC ³ | | 102 ± 4 | |

¹Determined by displacement by 1M NH₄AcO at pH 7 after washing of soluble salts (ENRESA 2000), the values were recalculated to give a sum of cations equal to CEC; ²Determined by displacement by 0.5M CsNO₃ at pH 7 (Fernández 2003); ³Determined by NaAcO/NH₄AcO pH=8.2 (ENRESA 2000).

Table VII
Solubilised elements in the 1:4 bentonite:water aqueous extract as determined by two laboratories. Concentrations are related to the dry mass of clay (mmol/100 g, dried at 110°C).

| | pH | Cl ⁻ | SO ₄ ²⁻ | HCO ₃ ⁻ | Na ⁺ | K ⁺ | Mg ²⁺ | Ca ²⁺ | SiO ₂ |
|---------------------|------|-----------------|-------------------------------|-------------------------------|-----------------|----------------|------------------|------------------|------------------|
| CIEMAT ¹ | 8.73 | 1.979 | 0.979 | 1.184 | 5.017 | 0.073 | 0.055 | 0.050 | 0.145 |
| UAM ² | 7.93 | 2.03 | 1.84 | 1.56 | 6.04 | 0.062 | 0.146 | 0.067 | |

¹Fernández 2003. Sr²⁺ and Fe³⁺ were found in concentrations lower than 10⁻³ mmol/100g.

²ENRESA 2000. As, V, Br, Sr, Ti, Mn, Fe, Ni, Cu, Zn and Y in concentrations lower than 10⁻³ mmol/100g.

The liquid limit of the bentonite is 102±4 percent, the specific gravity 2.70±0.04, and 67±3 percent of particles are smaller than 2 μm. The hygroscopic water content in equilibrium with the laboratory atmosphere (relative humidity 50±10 %, temperature 21±3 °C, total suction about 100 MPa) is 13.7±1.3 percent. The value obtained for the external specific surface using nitrogen adsorption technique (BET method) is 32±3 m²/g and the total specific surface

obtained using the Keeling hygroscopicity method is about 725 m²/g. The analysis of the mercury intrusion data reveals that the intra-aggregate pores (smaller than 0.006 μm) represent the 73-78 percent of total pore volume when the bentonite is compacted at a dry density of 1.7 g/cm³.

The saturated permeability to distilled water ($k_{w,r}$, m/s) of samples of untreated FEBEX bentonite com-

packed at different dry densities is exponentially related to dry density (ρ_d , g/cm³). A distinction may be made between two different empirical fittings depending on the density interval:

for dry densities of less than 1.47 g/cm³:

$$\log k_w = -6.00 \rho_d - 4.09 \quad [1]$$

($r^2=0.97$, 8 points)

for dry densities in excess of 1.47 g/cm³:

$$\log k_w = -2.96 \rho_d - 8.57 \quad [2]$$

($r^2=0.70$, 26 points)

The determinations were done at room temperature. The variation in the experimental values with respect to these fittings is smaller for low densities than it is for higher values, with an average –in absolute values– of 30 percent.

The swelling pressure (P_s , MPa) of FEBEX samples compacted with their hygroscopic water content and flooded with deionised water up to saturation at room temperature can be related to dry density (ρ_d , g/cm³) through the following equation:

$$\ln P_s = 6.77 \rho_d - 9.07 \quad [3]$$

($r^2=0.88$, 52 measurements)

In this case, the difference between experimental values and this fitting is, on average, 25 percent. This dispersion, which is wider for higher dry densities, is due both to the natural variability of bentonite and to the measurement method used, which does not allow high degrees of accuracy.

Retention curves (or soil water characteristic curves, SWCC) were determined under free volume conditions for samples compacted at different initial dry densities following various paths (wetting, drying, wetting after drying). Taking into account the results obtained in wetting paths from 148 to 0.1 MPa, an empirical relation between suction (s , MPa) and water content (w , %) dependent on initial dry density (ρ_{d0} , g/cm³) has been established, this matching the following expression:

$$w = (-3.79 \rho_{d0} + 1.42) \ln s + (25.36 \rho_{d0} - 5.48) \quad [4]$$

The retention curve of the bentonite has been also determined in samples compacted to different dry

densities under different temperatures (Lloret *et al.* 2004, Villar & Lloret, 2004). In this case, the volume of the samples remained constant during the determinations, since they were confined in constant volume cells. To impose the different relative humidities the cells were placed in desiccators with sulphuric acid solutions of various concentrations. The data from these laboratory determinations are shown in [Figure 3](#).

From measurements performed at laboratory temperature on small blocks of bentonite compacted at different densities and water contents, it was found that thermal conductivity (λ , W/m·K) may be related exponentially to water content (w , %) in the interval studied. This empirical relation, which also includes the contribution made by dry density (ρ_d , g/cm³), is expressed as follows:

$$\ln \lambda = \ln (0.8826 \rho_d - 0.8909) + 0.003 w \quad [5]$$

On the other hand, the thermal conductivity (λ , W/m·K) of the compacted bentonite is related to the degree of saturation (S_r) through the following expression:

$$\lambda = A_2 + \frac{A_1 - A_2}{1 + e^{(S_r - x_0)/dx}} \quad [6]$$

where A_1 represents the value of λ for $S_r=0$, A_2 the value of λ for $S_r=1$, x_0 the degree of saturation for which thermal conductivity is the average of the two extreme values and dx is a parameter. This equation was chosen because it accurately represents the behaviour of conductivity versus water content (degree of saturation), which are directly related but not in a linear fashion (Villar 2000, 2002). The fitting obtained, with an r^2 of 0.923, gives the following values for each parameter:

$$\begin{aligned} A_1 &= 0.57 \pm 0.02 \\ A_2 &= 1.28 \pm 0.03 \\ x_0 &= 0.65 \pm 0.01 \\ dx &= 0.100 \pm 0.016 \end{aligned}$$

Some isothermal infiltration tests and heat flow tests at constant overall water content were performed during the FEBEX I project and they were back-analysed using CODEBRIGHT. It is possible to fit the experimental data using a cubic law for the relative permeability ($k_r = S_r^3$) and a value of 0.8 for the tortuosity factor (τ).

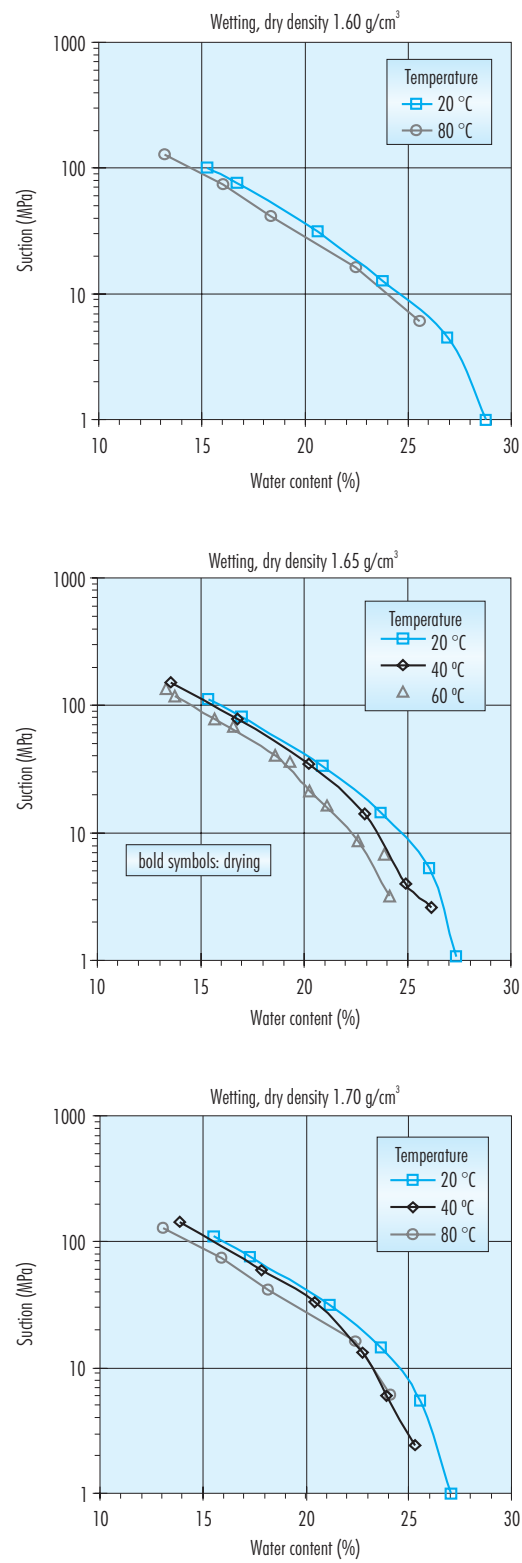


Figure 3: Water retention curves at different temperatures and for different bentonite densities (Lloret et al. 2004).



3. Dismantling of the barrier and bentonite sampling



3. Dismantling of the barrier and bentonite sampling

The partial dismantling of the FEBEX *in situ* test was carried out during the summer of 2002, after five years of continuous heating during which the temperature at the heater/bentonite contact was maintained at 100 °C. Heater number 1 was switched off four months before starting the dismantling operations, since the temperature in the area affected by the dismantling should be reduced to a level compatible with manual works (25-30 °C). The dismantling operations included the demolition of the concrete plug and the removal of all the bentonite in front of and surrounding the heater. A large number of samples from all types of materials were taken for analysis. The dismantling was carried out causing a minimum disturbance in the section of the test corresponding to the second heater that was kept in operation at all times and remains in place fully operative. A detailed description of the dismantling and sampling operations is given in Bárcena *et al.* (2003).

Also the process of data acquisition was maintained during the dismantling. This allowed to follow the evolution of temperature and relative humidity (among other parameters) during cooling, and to know exactly which were the conditions of the barrier at the mo-

ment of dismantling. Thus, in the instrumented section C (see Figure 1 for location), far away from the heater, the temperatures decreased from values between 21 and 23 °C to values around 18 °C. The tendency of the relative humidity evolution recorded by the sensors placed in this section did not change as a consequence of the switching off, but the relative humidity slightly decreased when the adjacent sections started to be dismantled, probably as a consequence of the higher ventilation (Figure 4). In the sections around the heater, the switching off provoked an overall drop of temperature to values around 25 °C (Figure 5), which implied a modification of the relative humidity registered by the sensors. Hence, the relative humidity near the heater increased from values of 20-24 % before switching off to values of 32-52 % just before dismantling, while in the outermost part of the barrier the relative humidity slightly increased as a consequence of cooling (Figure 6).

Upon exposure, the bentonite sections presented a consistent appearance; although the joints between blocks were clearly visible all the construction gaps were sealed, even the big apertures hewn in the bentonite for the passing of the cable bunches (Figure 7). Differences in coloration of the bentonite re-

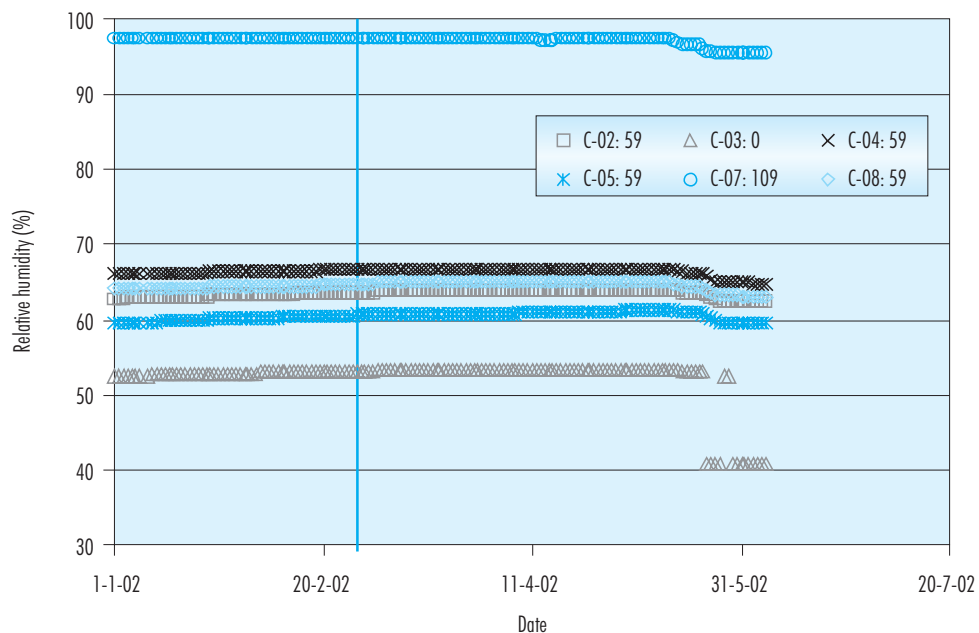


Figure 4: Evolution of the relative humidity registered before dismantling by the capacitive sensors (70-AND-WC) in the instrumented section C (S11). The location of the sensors with respect to the gallery axis is indicated in cm.

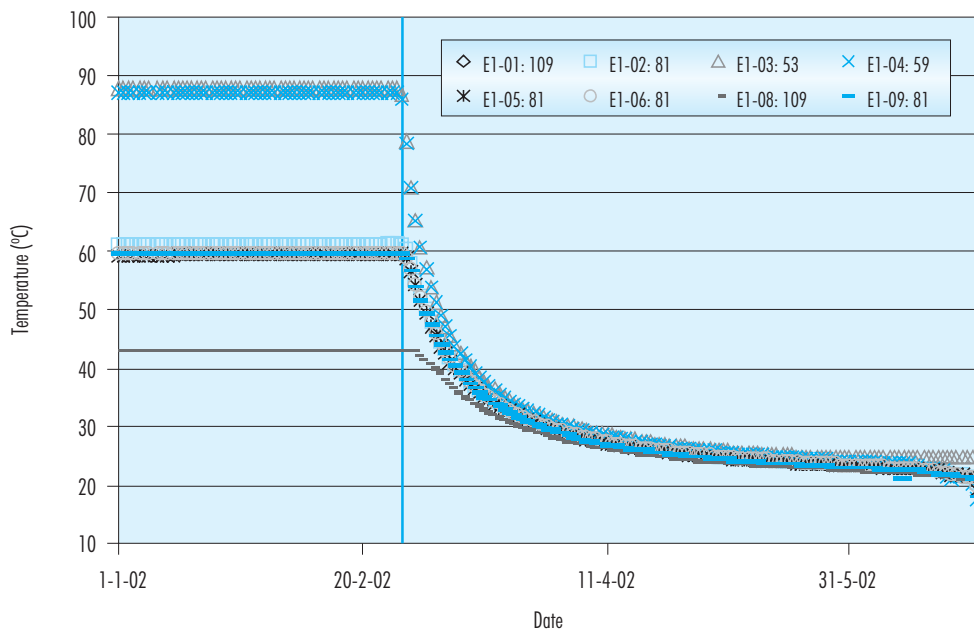


Figure 5: Evolution of the temperature registered before dismantling by the capacitive sensors (70-AND-WC) in the instrumented section E1 (S21). The location of the sensors with respect to the gallery axis is indicated in cm.

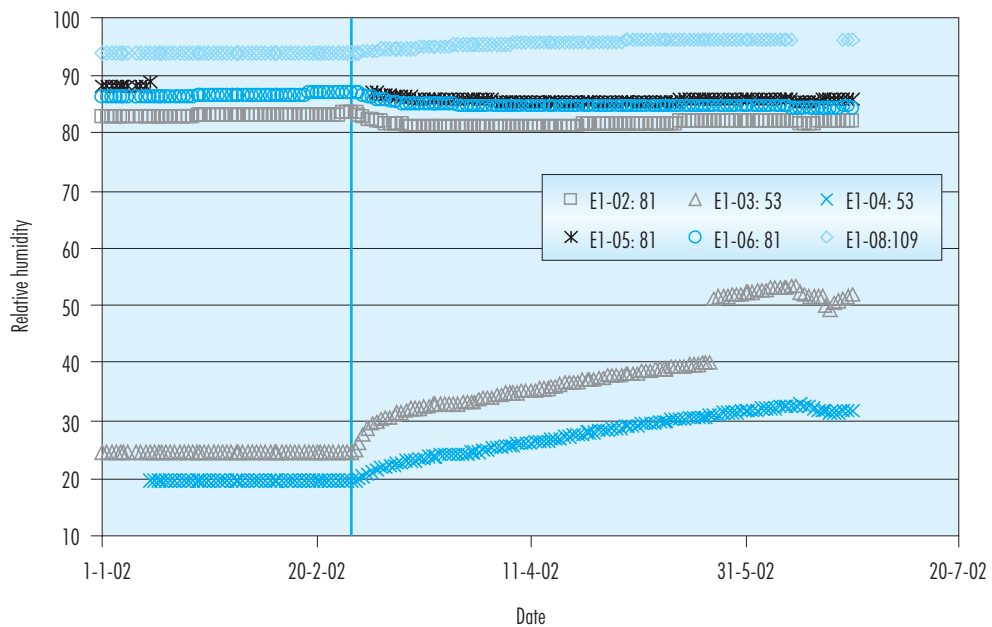


Figure 6: Evolution of the relative humidity registered before dismantling by the capacitive sensors (70-AND-WC) in the instrumented section E1 (S21). The location of the sensors with respect to the gallery axis is indicated in cm.

lated to the variations of its water content were observed, the outer rings of the barrier showing darker colours.

During the dismantling, the radial dimension of some blocks of different slices was measured. The average values obtained in each barrier ring (external, intermediate and internal) of different sections are plotted in Figure 8, together with the initial dimensions of the same kind of blocks. It is clear that the higher expansion has taken place in the outer ring, and that the ring closest to the heater has slightly shrunk, due probably to the effect of heating, since this shrinking has not been observed in the sections without heater. In those sections even the central block (not included in the figure) has swollen. In fact, in the sections with heater, the radial dimension of the blocks of the external ring has increased a 4 percent, while the radial dimension of the blocks of the inner ring has decreased a 1 percent.

On the other hand, the location of the bentonite sampling points was fixed to allow a good representation of physico-chemical alterations and hydration distribution. The sampling took place in vertical sections normal to the axis of the tunnel –correspond-

ing to original block slices–, and in each section several samples were taken along different radii. According to the Sampling Book (AITEMIN 2002), bentonite samples were taken from different vertical sections in order to perform the following analyses (Figure 9):

- Water content and dry density have been determined in samples from sections S8, S9, S10, S11, S13, S14, S15 and S16 –located in the region between the concrete seal and the heater–, and from sections S18, S20, S22, S27, S29 and S31, located in the region where the heater was placed. The determinations were performed mostly *in situ* by CIMNE, but also in the laboratory by CIEMAT, NAGRA and Clay Technology.
- Thermo-hydro-mechanical tests have been performed in samples from sections S19, S23, S28 and S31 by CIEMAT, and in samples from section S7, S12, S19 and S28 by CTU. Samples were taken from sections S12 and S19 to perform permeability tests by EURIDICE GIE. Tests on joints have been performed by Euro-Géomat on samples taken from sections S11 and S29.

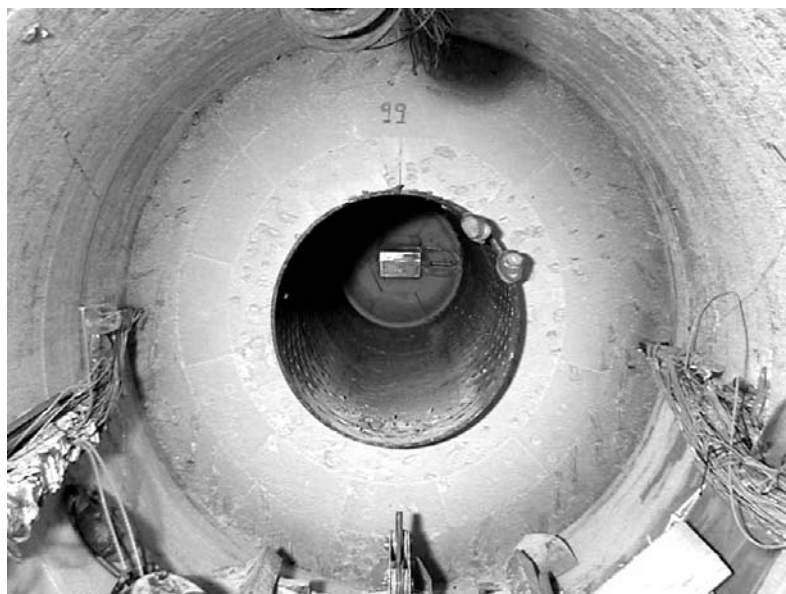


Figure 7: Appearance of the bentonite barrier after dismantling of the first sections and extraction of the heater.

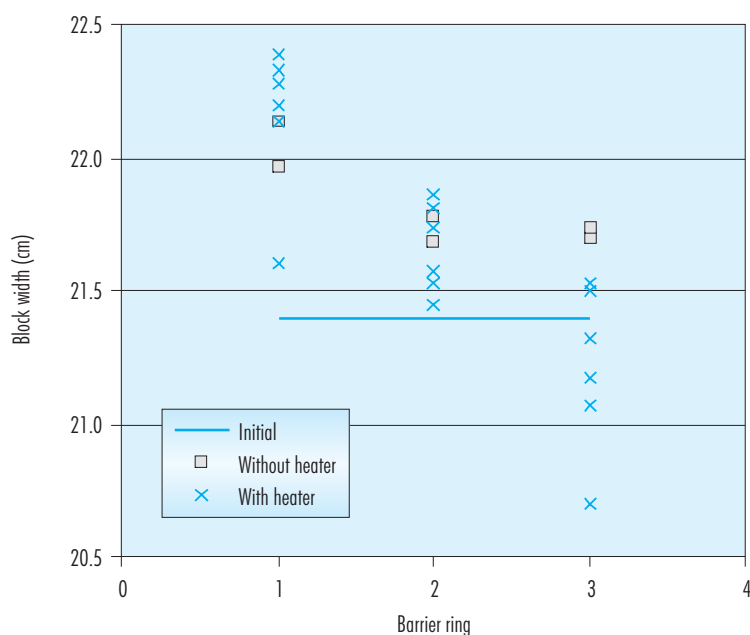


Figure 8: Radial dimension of the blocks in three different rings measured in situ during dismantling of several sections (1: external; 2: intermediate; 3: inner).

- ❑ Mineralogical and geochemical characterisation has been carried out by CIEMAT in samples from sections S12, S19, S28 and S31, and by INPL-LEM in samples from section S29.
- ❑ In samples from the section in contact with the concrete seal (S7) the modification of the clay and the pore water in contact with alkaline solutions has been studied by VTT and CIEMAT.
- ❑ Samples from section S15 and S20 were taken in order to compare the water obtained in the gas pipes and the pore water obtained in laboratory (the results are not reported herein.)
- ❑ Samples of the bentonite adhered to the back lid of the heater, to the coupons and to the liner have been used for geochemical and mineralogical analyses and to evaluate the formation of possible corrosion products (the results are not reported herein.)
- ❑ Samples from section S29 –where glass ampoules containing deuterium were placed– have been analysed jointly by UDC and CIEMAT.
- ❑ Three sections in the zones where filter papers with tracers were placed were sampled (S26, S28 and S30) and the blocks in which tracers were placed were taken from sections S20, S25, S26 and S29. The tracer analyses have been performed by EURIDICE GIE and CIEMAT.

The samples were taken either in the form of cores or of whole blocks that have been further sampled in the laboratory. The blocks were preserved immediately after extraction in plastic film, two layers of vacuum-sealed aluminised PET-sheets and plastic bags. The first PET-sheet was vacuum-sealed after flushing nitrogen in it. Protection against mechanical actions was used to ensure the integrity of the material. The samples were referred to according to the key given in the procedure 070-PC-TA-0002 and the Sampling Book (AITEMIN 2002).

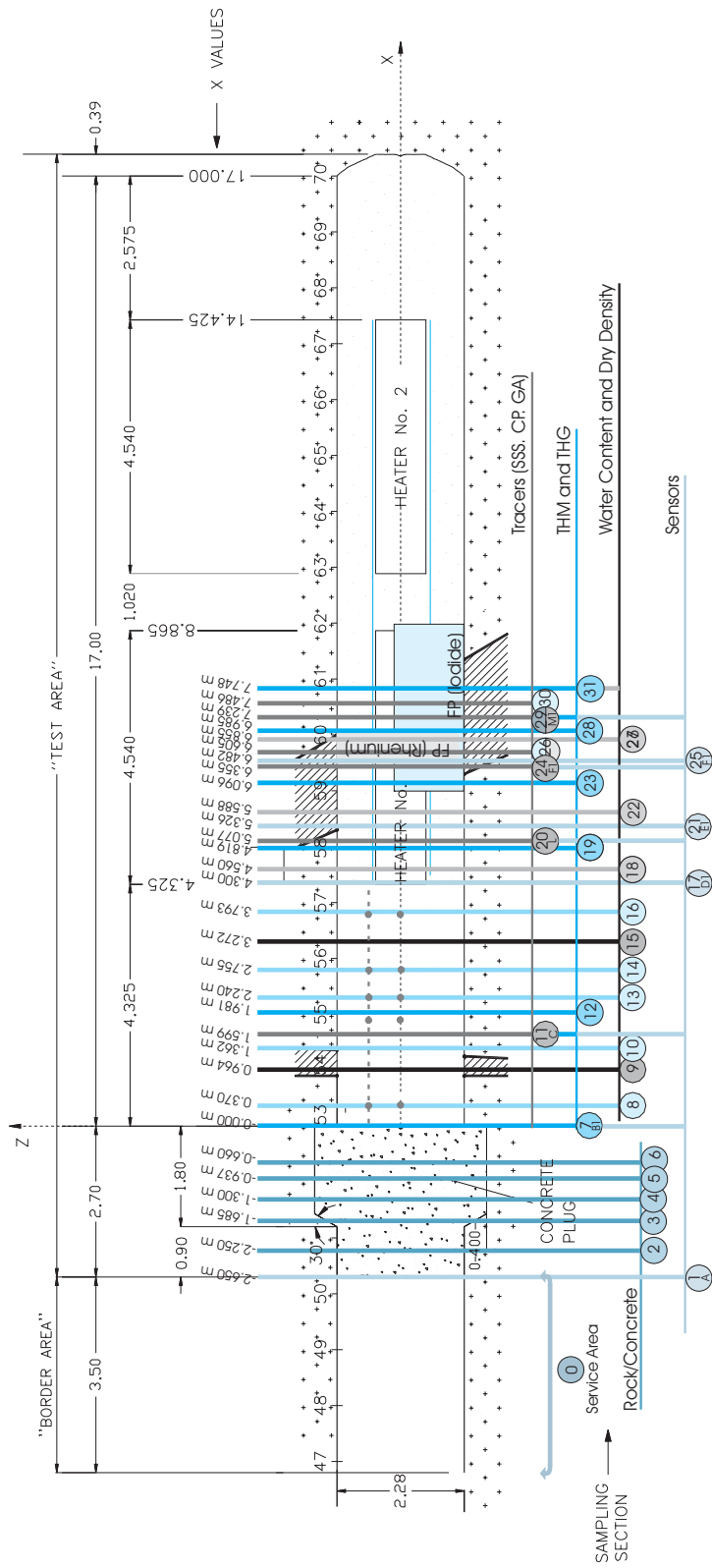


Figure 9: Location of sampling sections (Bárceña et al. 2003).

4. Bentonite analysis

4. Bentonite analysis

The work program of the different organisations for the postmortem bentonite analysis is described in Villar *et al.* 2002a. The tests done on the samples taken are grouped in three categories: thermo-hydro-geochemical tests, tests for the analysis of tracers distribution and thermo-hydro-mechanical tests. Besides, the actual state of the barrier was checked by determining *in situ* and in laboratory the water content and dry density of the bentonite in different positions.

Most of the results obtained are reported as a function of the distance to the gallery axis of the bentonite sample, since sampling has been accomplished along radii of different sections (Figure 9). The length of the bentonite radius is 114 cm in the sections without heater and 65 cm in the sections with heater.

4.1. Water content and dry density of the barrier

Water content (w) is defined as the ratio between the weight of water and the weight of dry solid expressed as a percentage. Dry density (ρ_d) is defined as the ratio between the weight of the dry sample and the volume occupied by it prior to drying. The participant laboratories have used different methods to determine dry density, what has been undertaken sometimes through the determination of bulk density.

4.1.1. CIMNE: *In situ* determinations

Water content and density of the bentonite were measured by CIMNE at the Grimsel Test Site during the partial dismantling operation carried out in the spring of 2002 in Grimsel (Daucausse & Lloret 2003).

The sampling tool used was a drilling machine with a 40 mm inner diameter barrel. All core samples were taken along radii in vertical sections. More than 320 samples were taken, 11-12 per radius in the sections without heater and 6-7 per radius in the sections with heater. The samples were taken following a direction that was parallel to the tunnel axis and usually, the length of the samples was 12 cm. Samples were divided in four subsamples with a length of 3 cm. Gravimetric water content was obtained by drying one of the subsamples during 24 hours using a ventilated oven maintained at 110 °C. Bulk density was calculated in the other three subsamples, measuring their volumes by dipping the

subsample coated with wax in water. The average value of these three bulk densities and the water content measured in the fourth subsample were used to evaluate the dry density of the sample. More than 320 water content determinations and 480 density determinations were made.

4.1.1.1. Water content and dry density distributions in vertical cross sections

The distribution of the values of water content and dry density presents an axial symmetry. As an example, Figure 10 shows the measured values for water content and dry density along six radial lines and a block in section S15. Only small changes in water content are observed among samples taken from different radii near the gallery wall, probably due to preferential flow of water in the contact of the gallery with the transducer wires conductions. A strong reduction in dry density can be observed in the 20 cm nearest to the rock, indicating an important heaving of the clay in this area associated to the increase in water content. This observation agrees well with the increase in the radial dimension measured in the blocks of the external ring (Figure 8). On the other hand, it can be observed that the maximum dry density was measured 30 cm from the centre of the drift. Similar tendencies can be observed in the other sections where water contents and dry densities were measured (Figure 11 and Figure 12).

Some of the blocks taken were thoroughly sampled to determine the water content and dry density distribution inside them (72 determinations per block). No effect of a preferential flow of water through the joint between blocks was detected (Figure 13). The water content and density distribution inside the blocks follow the pattern imposed by the radial flow that was observed in all the sections.

4.1.1.2. Water content and dry density distribution in the vertical longitudinal section

The variation of water content, dry density and the resulting degree of saturation in a longitudinal section is shown in Figure 14. The degrees of saturation have been computed from measurements of water content and dry density, considering that the density of water in bentonite is the same than that of free water (1 g/cm³). Despite the lack of data in some parts of the gallery, it can be observed how the highest water contents (about 18 percent in the axis of the

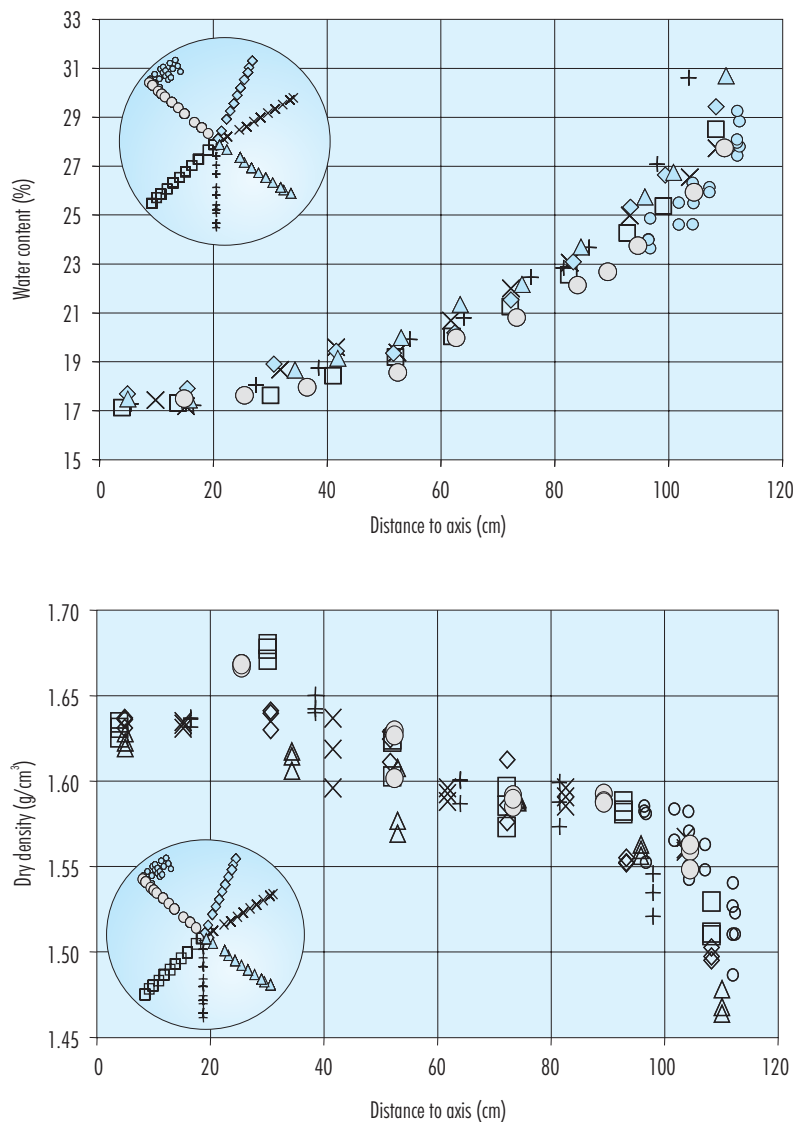


Figure 10: Water content and dry density along six radial lines and a block in section S15.

drift) are found near the concrete plug and towards the beginning of the heater ($x \approx 400$ cm).

Taking into account the axial symmetry of the water content and the density distributions, it is possible to fit polynomial functions to represent their variations with the distance to the gallery axis (Daucausse & Lloret 2003). From the polynomial functions fitted it is possible to obtain the average value in axial vertical sections. The average values for water content,

dry density and degree of saturation thus obtained are shown in Table VIII. The average value of dry density found, 1.58 g/cm^3 , is slightly lower than that given by AITEMIN upon construction of the barrier, 1.60 g/cm^3 (ENRESA 2000, p. 210). This could be a consequence of the slight decompression suffered by the barrier on dismantling and sampling. On the other hand, the data provided show that there are no major variations between the sections around the heater and those out of it. There are neither differ-

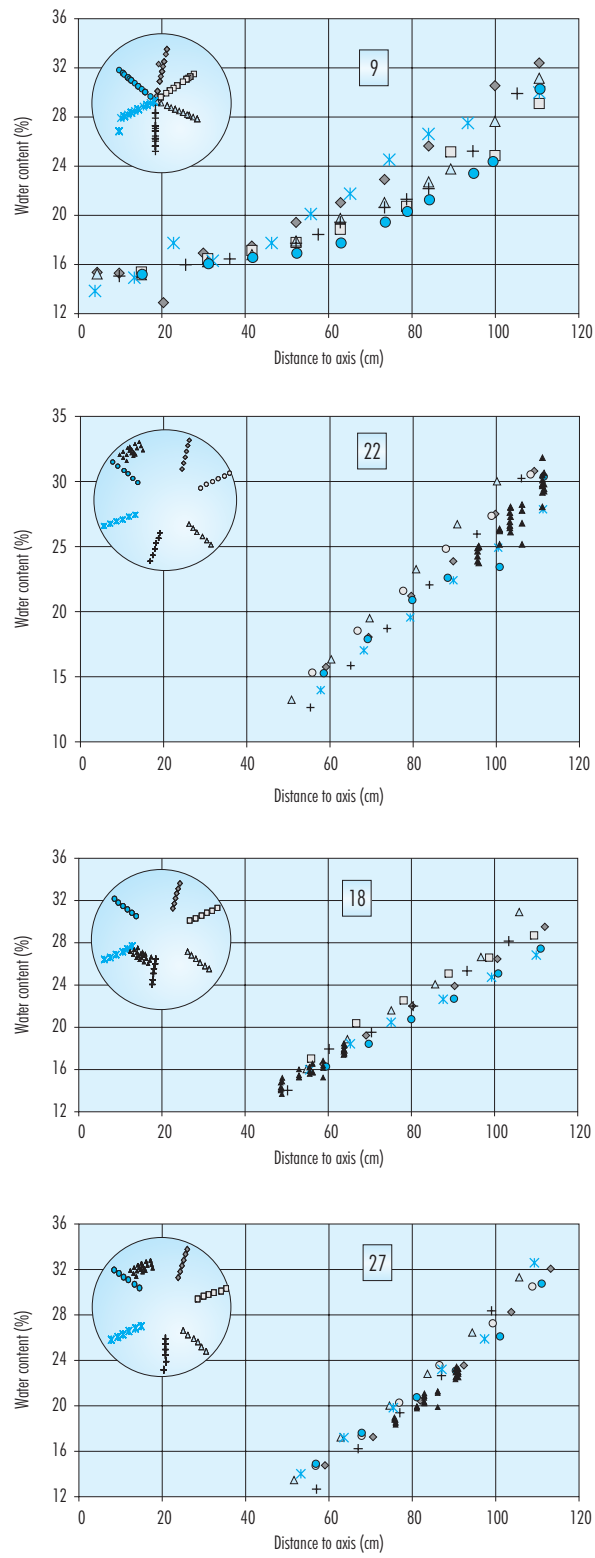


Figure 11: Water content measurements in sections S9, S18, S22 and S27.

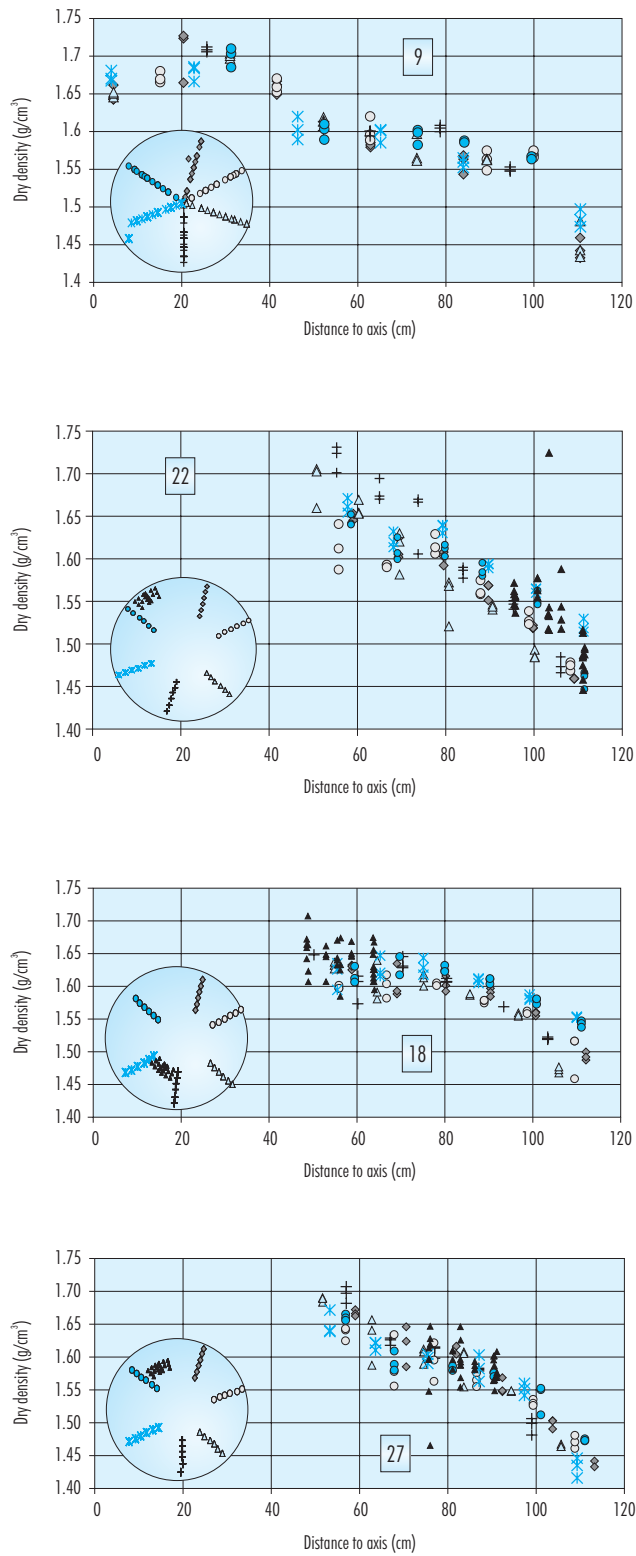


Figure 12: Dry density measurements in sections S9, S18, S22 and S27.

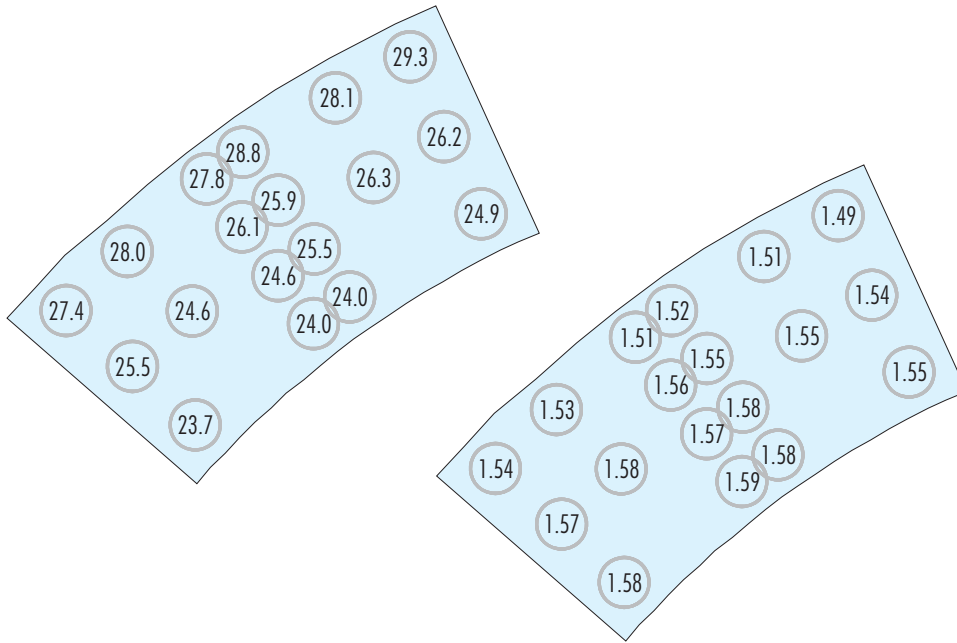


Figure 13: Values of water content (%) and dry density (g/cm^3) measured in the block BB15-1.

ences in average water content among the different sections placed around the heater, despite the fact that the geological characteristics of the gallery, especially with respect to water conductivity, were not homogeneous around the first heater, due to the presence of a lamprophyre dike. This fact and the radial distribution of water content measured in vertical sections are a consequence of the predominant control of the bentonite upon the hydration kinetics, as a result of the big difference between the bentonite and granite permeabilities, which are in the order of 10^{-14} and 10^{-11} m/s (ENRESA 20000, p. 180), respectively.

4.1.1.3. Comparison of measured water contents with the measurements of the *in situ* instrumentation

In order to infer water content from the measurements of air relative humidity recorded by the hygrometers and psychrometers placed in the bentonite during the experiment, it is necessary to relate relative humidity to suction and suction to water content in clay. To relate air relative humidity (RH , %) to suction (s , MPa), the psychrometric law is used:

$$s = -10^{-6} \frac{R \times T}{V_w} \ln \left(\frac{RH}{100} \right) \quad [7]$$

where T is the absolute temperature, R the universal constant of gases ($8.3143 \text{ J}/\text{mol}\cdot\text{K}$) and V_w the molar volume of water ($1.80 \cdot 10^{-5} \text{ m}^3/\text{mol}$).

In order to calculate the water content (w , %) from suction measurements (s , MPa) the following empirical relationship has been used to fit the water retention curve:

$$w = (\alpha + bn) \left[1 + \left(\frac{s}{P_0 e^{-\eta(n-n_0)} e^{-\alpha(T-T_0)}} \right)^{\frac{1}{1-\lambda}} \right]^{-\lambda} \quad [8]$$

where w is the water content in percentage, n the porosity, s the suction in MPa, and T the temperature in $^{\circ}\text{C}$. The values of parameters α , b , P_0 , η , n_0 , α , T_0 and λ are indicated in Table IX. The parameters were obtained by fitting the data from laboratory determinations of the water retention curve at different dry densities and temperatures (Figure 3). The differences between measured values and the estimated values using Equation 8 are smaller than 2 percent in terms of water content.

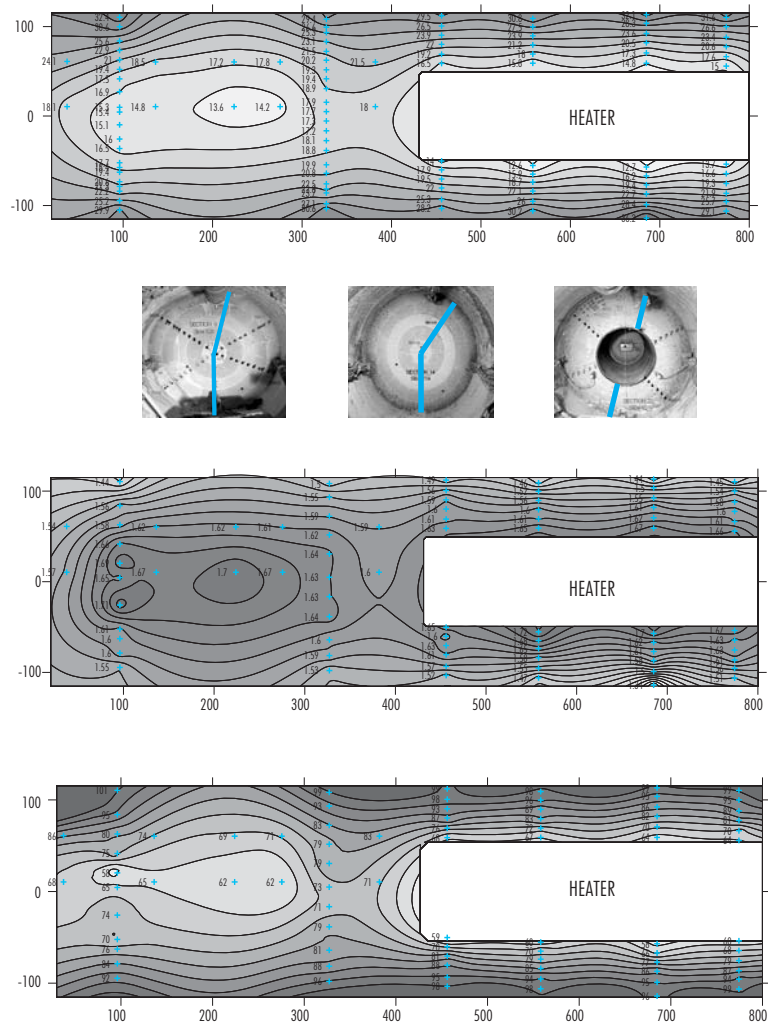


Figure 14: Longitudinal distribution of water content (%), dry density (g/cm^3) and degree of saturation (%) along the gallery.

Table VIII

Average values of water content, dry density and degree of saturation in different vertical sections along the gallery.

| Section | x^1 (cm) | w (%) | ρ_d (g/cm^3) | S_r (%) |
|---------|------------|-------|-------------------------------------|-----------|
| 9 | 96 | 22.9 | 1.58 | 85 |
| 15 | 327 | 22.8 | 1.58 | 86 |
| 18 | 456 | 23.1 | 1.58 | 87 |
| 22 | 558 | 22.6 | 1.57 | 85 |
| 27 | 685 | 22.6 | 1.56 | 84 |
| 31 | 774 | 22.8 | 1.58 | 85 |

¹distance from the concrete plug.

Table IX
Values of parameters in Equation 8.

| a | b | P_0 (MPa) | λ | η | n_0 | α (1/°C) | T_0 (°C) |
|-------|-------|-------------|-----------|--------|-------|-----------------|------------|
| 10.96 | 41.89 | 12.68 | 0.211 | 7.97 | 0.4 | 0.00647 | 20 |

The comparison between the water content measured in the samples retrieved and the values of water content obtained from the instrumentation (hygrometers and psychrometers) is shown in Figure 15. The values for air relative humidity considered in the comparisons correspond to the last readings registered before the removal of the bentonite blocks where the sensors were installed. It can be seen that the agreement between the values obtained with the instrumentation and the values of water content measured directly is very good. In any case, the differences are of the same order than the errors due to the empirical law used to fit the laboratory water retention curves. The bigger discrepancies are obtained near the gallery wall, where the measured water content is higher than the estimated from relative humidity measurements. Probably, this discrepancy is due

to the errors in the estimation of water content from suction when the dry density is very low.

4.1.2.CIEMAT: Laboratory determinations

Blocks bound to THM, THG and tracers determinations have been also sampled for water content and dry density, which have been determined in two different positions of each block along a radius. In the sections without heater, only the three external rings of the sections have been sampled. Consequently, at least six determinations have been made along a given radius of the barrier, whose length is about 114 cm in the sections without heater and 65 cm in the sections with heater. The gravimetric water content (w) has been determined by oven drying at 110

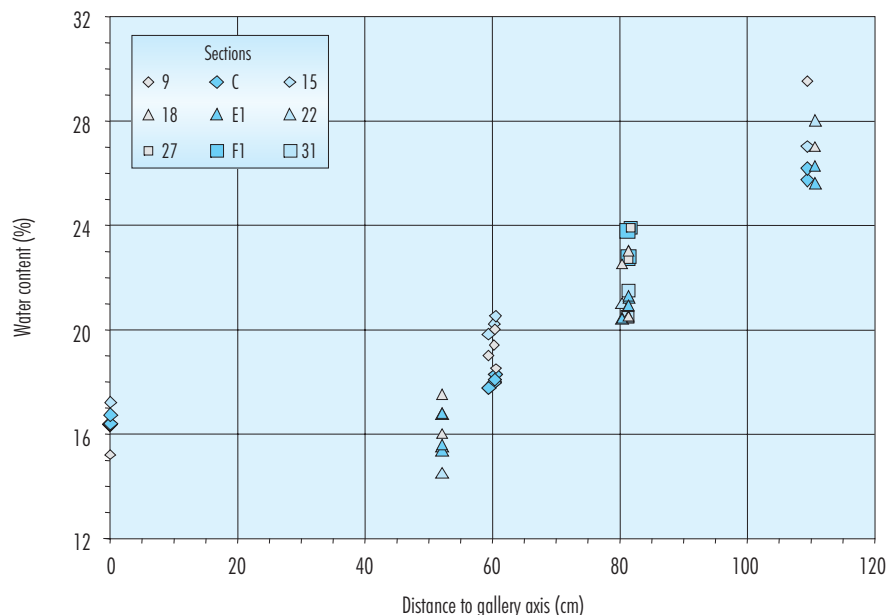


Figure 15: Comparison between the water content measured in samples extracted from sections S9, S15, S18, S22, S27 and S31 (bold symbols), and the water content inferred from the measurements of the instrumentation located in sections C, E1 and F1 (open symbols).

°C during 24 hours. The volume of the specimens needed to calculate their dry density has been determined by immersing them in a recipient containing mercury and by weighing the mercury displaced, as established in UNE Standard 7045 "Determination of soil porosity."

The results obtained for the different sections sampled are plotted in Figure 16. No differences in water content are noticed between the sections with heater and the sections without heater. The water content decreases from the external blocks to the blocks closer to the heater in an approximately exponential way. The higher values are around 30 percent and the lower around 15 percent, being the mean value 22 percent. The water contents higher than 30 percent found in some external blocks of section 29 are justified by their proximity to the cable bunch, which is a preferential water pathway.

The dry densities measured are plotted in Figure 17 as a function of the distance to the gallery axis. The arithmetic mean of all the values measured is 1.58 g/cm³, well below the initial dry density of the blocks (which was 1.70 g/cm³), due to the filling of the construction gaps as a result of the expansion caused by saturation. The initial dry density of the blocks was selected by taking into account the prob-

able volume of the construction gaps and the need to have a barrier with an average dry density of 1.60 g/cm³ (ENRESA 2000). The dry density drop with respect to the initial one is higher from the heater towards the gallery wall, especially in the blocks closer to the granite. In these blocks, the dry density decreases even below the average dry density of the barrier to values around 1.50 g/cm³. On the contrary, near the heater the dry density remains around 1.70 g/cm³, due to the shrinkage caused by the initial desiccation and the compression exerted by the adjacent expanding blocks. Again, the exceptionally low values of dry density (around 1.40 g/cm³) found in some external samples of section 29 are related to their proximity to the cable bunch.

The degrees of saturation have been calculated for each sample taken into account its dry density and water content and considering the density of water as 1.00 g/cm³. The degrees of saturation are higher than 60 percent all through the barrier, and have a mean value of 83 percent. The highest values –found in the proximity to the granite– are close to 100 percent, although full saturation is not even reached in the proximity of the gallery wall. This is probably due to the decrease of dry density that goes with hydration and to the continuous demand of water by the inner drier bentonite.

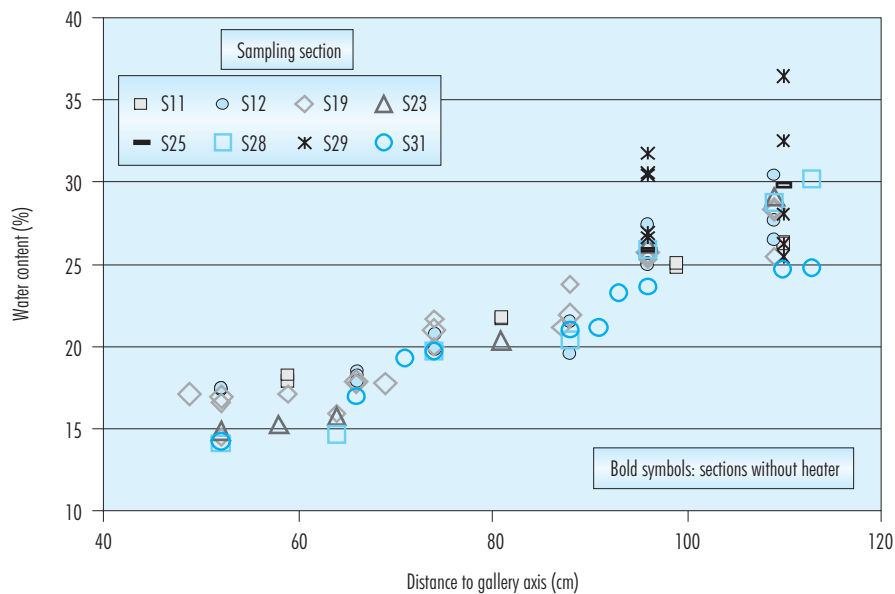


Figure 16: Water contents measured along radius of different sections.

Table X summarises the results presented above as a function of the position of the blocks with respect to the gallery axis.

These parameters have been also determined in samples from section S7, the one in contact with the concrete plug (Fernández & Rivas 2004). The distribution of dry density and water content throughout the section follows a quite different pattern than in the rest of the sections. For this reason the results are presented separately (Figure 18). The average water content measured is 28.2 percent, and the average dry density 1.48 g/cm^3 , much higher and lower, respectively, than the values measured in the rest of the sections (Table X). The fact that the concrete were pumped with a high water content (ENRESA 2000, p. 209) would cause a sudden increase of the water content of the clay and its swelling. Afterwards, the concrete plug surface may have behaved as a preferential water passageway during the operational phase of the experiment.

4.1.3. NAGRA: *In situ* and laboratory determinations

NAGRA has determined the gravimetric water content and dry density of several samples taken in the

proximity to the TDR probes placed in Grimsel in order to determine the volumetric water content of the bentonite and be able to calibrate the measurements of the TDR probes (Albert *et al.* 2003). The samples were taken in cores drilled from sampling sections S29 and S30. The cores were drilled close to the TDR probes and parallel to them, *i.e.* parallel to the gallery axis. The position of the TDR probes in the instrumented section M1 (sampling section S29) is indicated in Figure 19. The core diameter was 4 cm and the length about 25 cm, as each core crossed two layers of bentonite blocks (Figure 20).

NAGRA performed water content measurements at the GTS (the measurements were performed directly after sampling within about 5 to 10 minutes) and on backup samples at the Clay Laboratory of the ETH-Zurich. The samples for ETH were vacuum-packed and sealed in a plastic tube and measured within a few days after sampling.

The gravimetric water content of samples has been determined in accordance with SN 670 3406 (Swiss Code) by drying of the samples at 105 to 110 °C. The time required to dry the bentonite samples strongly depends on the sample weight.

At the GTS a scale for weighing samples with an accuracy of one hundredth of a gram has been taken.

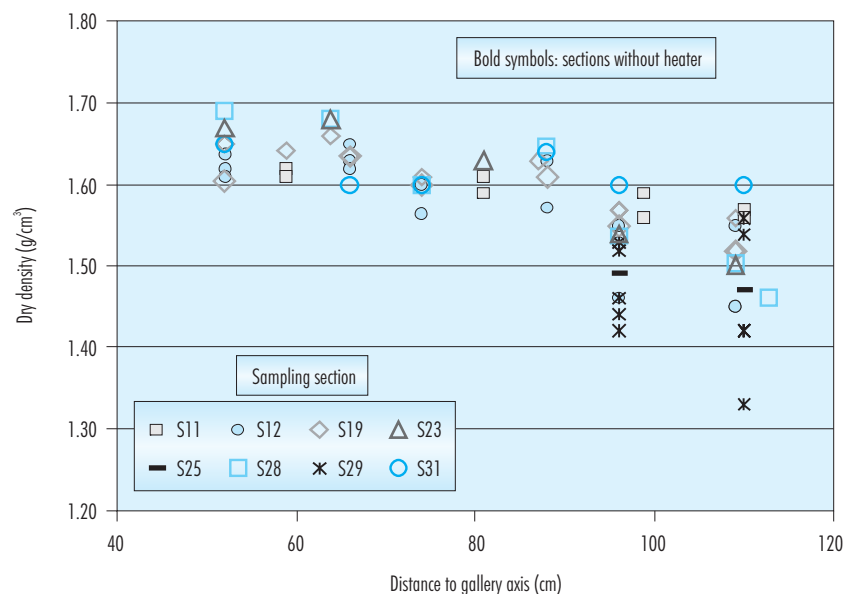


Figure 17: Dry densities measured along radius of different sections.

Table X
Mean values along the barrier of physical characteristics determined at CIEMAT laboratories.

| Position | Dry density (g/cm ³) | Water content (%) | Degree of saturation (%) |
|--|----------------------------------|-------------------|--------------------------|
| External ring of sections without heater | 1.53 | 26.5 | 93 |
| Medium ring of sections without heater | 1.59 | 20.8 | 81 |
| Internal ring of sections without heater | 1.62 | 17.9 | 73 |
| External ring of sections with heater | 1.51 | 27.6 | 95 |
| Medium ring of sections with heater | 1.59 | 21.8 | 85 |
| Internal ring of sections with heater | 1.65 | 16.1 | 67 |
| Average | 1.58 | 22.2 | 83 |

To get reliable water content data, samples with a weight of 50 to 100 grams and two samples at the same location were measured. To determine the required drying time of the bentonite samples, the water content was measured after 1, 2, 3, 4, 5 and 6 days of drying in subsamples of 50 to 80 grams. It was concluded that with this type and weight of

samples, 24 hours of drying is not long enough. There is quite a big difference in measured water content between 1 day and 3 days drying and a small change between 3 and 5 days drying. After 5 days no significant change was observed. Therefore it was decided to dry all samples during 5 days at 105 –110°C.

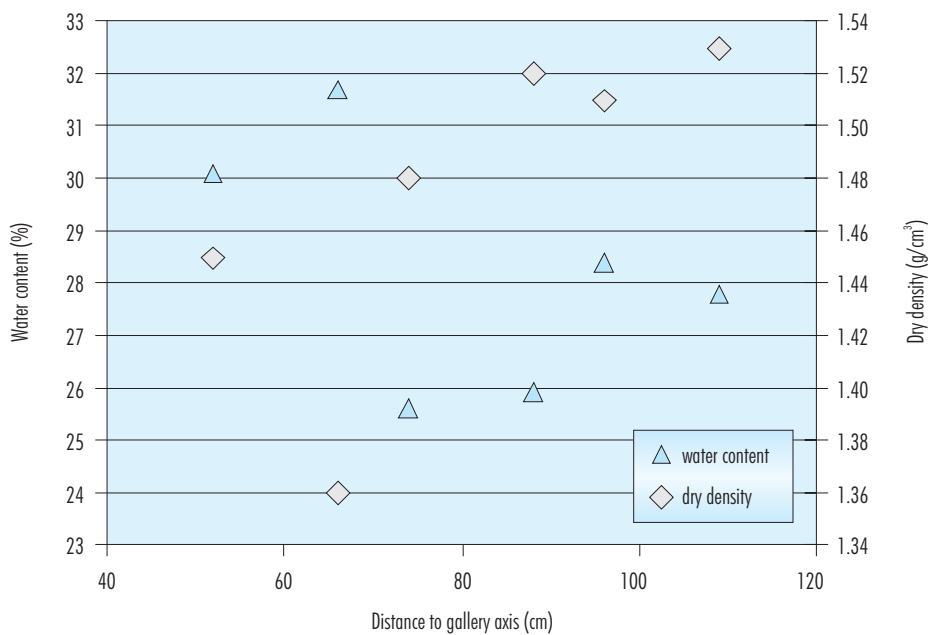


Figure 18: : Water contents and dry densities measured along a radius of section S7.

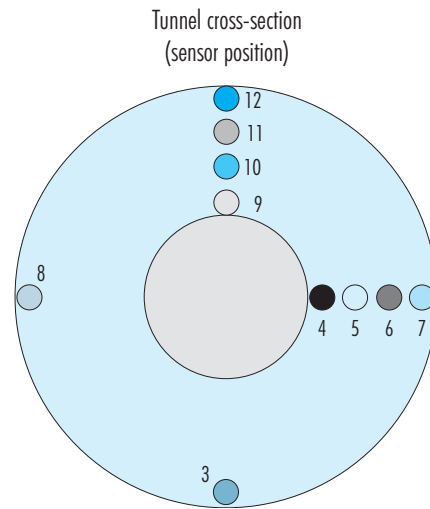


Figure 19: Position of TDR probes in instrumented section M1 (sampling sections S29 to S31).

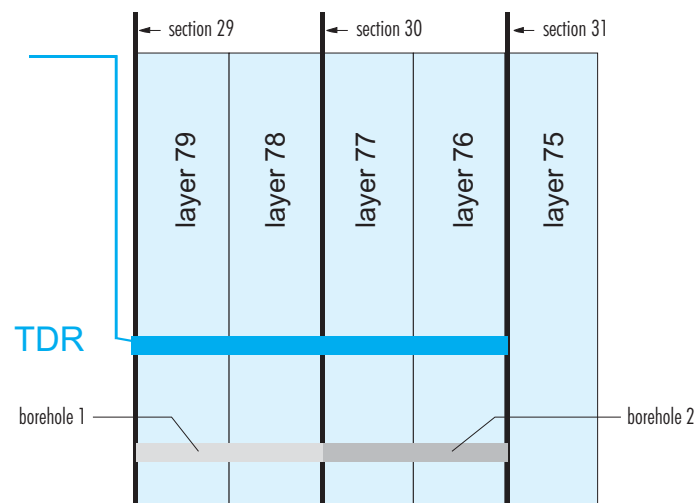


Figure 20: Sketch of the position of TDRs and sampling boreholes related to installation layers and sampling sections.

At the ETH-Zurich few grams of bentonite samples were dried during 2 days for the water content determinations. The accuracy of the scale used was 0.002 g. Considering the smaller sample size and the higher precision of the scale for the ETH measurements the accuracy of the calculated water content with both methods is comparable ($\pm 0.2\%$)

The results of the gravimetric water content measurements near the TDR position determined at GTS and ETH-Zurich are plotted in Figure 21. On average, the gravimetric water content determined at the GTS is 1 to 4 percent higher than the water content measured at the ETH which can be explained by water lost during transport from the GTS

to ETH and the longer storage time before measurement.

The bulk density of the samples was measured in the laboratory of ETH-Zurich with the mercury immersion method. The dry density is later calculated by taking into account the water content of the sample. The estimated absolute error of this method is about $\pm 0.02 \text{ g/cm}^3$. Gravimetric water content as well as the dry and bulk density of a horizontal and a vertical profile through the bentonite buffer are illustrated in Figure 22 and Figure 23.

The volumetric water content has been calculated as the gravimetric water content times the dry density. The values obtained in the different positions sampled at a depth of 24 cm from section S29 are plotted in Figure 24.

4.1.4. Clay Technology AB: Laboratory determinations

The following two series of sampling were performed on the bentonite buffer by Clay Technology during the dismantling of FEBEX:

1. Altogether 30 samples were taken between the canister and the rock in a radial direction at 60° clockwise from the vertical axis in section S22. These samples were directly taken to Clay Technology where their water content was determined.
2. Three full blocks located in section S20 (BB20-6, BB20-7 and BB20-8) were extracted, packed and sent to Clay Technology. Water content and density were determined on 33 samples taken in the blocks with the individual distance of 2 cm. In addition 24 double samples were taken and investigated, which means that altogether 57 values of density and water content were achieved.

The water content was determined by weighing $\sim 30 \text{ g}$ sample before and after drying at 105°C for 24 hours. The density was determined by weighing $\sim 50 \text{ g}$ sample at first in air and then immersed in paraffin oil for 15 seconds. From these values the dry density, void ratio and degree of water saturation were determined, using for the density of the water (ρ_w) the value of 1.0 g/cm^3 and for the density of the particles (ρ_s) the value of 2.70 g/cm^3 .

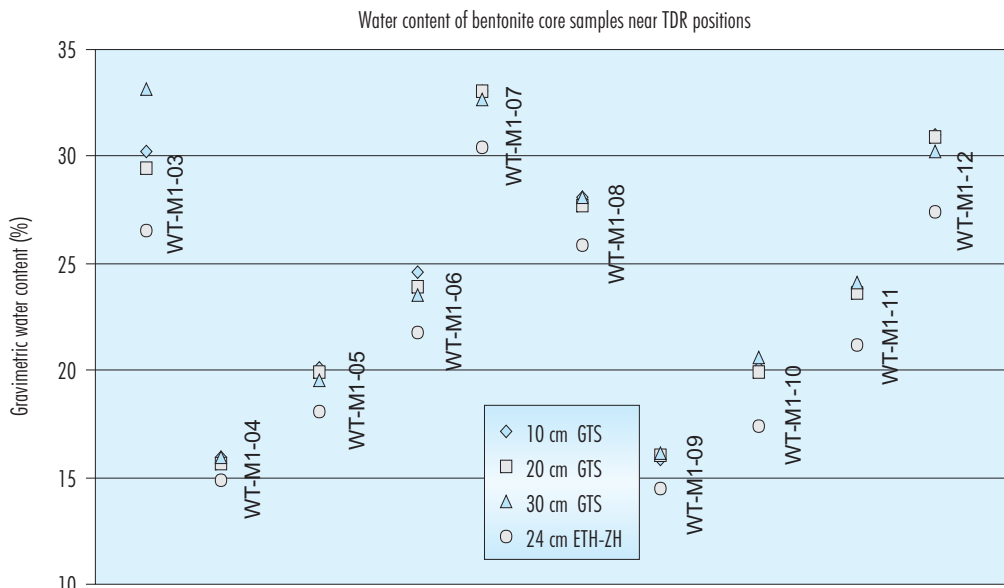


Figure 21: Gravimetric water content of core samples near TDR positions (indicated in Figure 19) determined at GTS and ETH-Zurich (the distances indicated are measured from the surface of section S29 towards the bottom of the gallery).

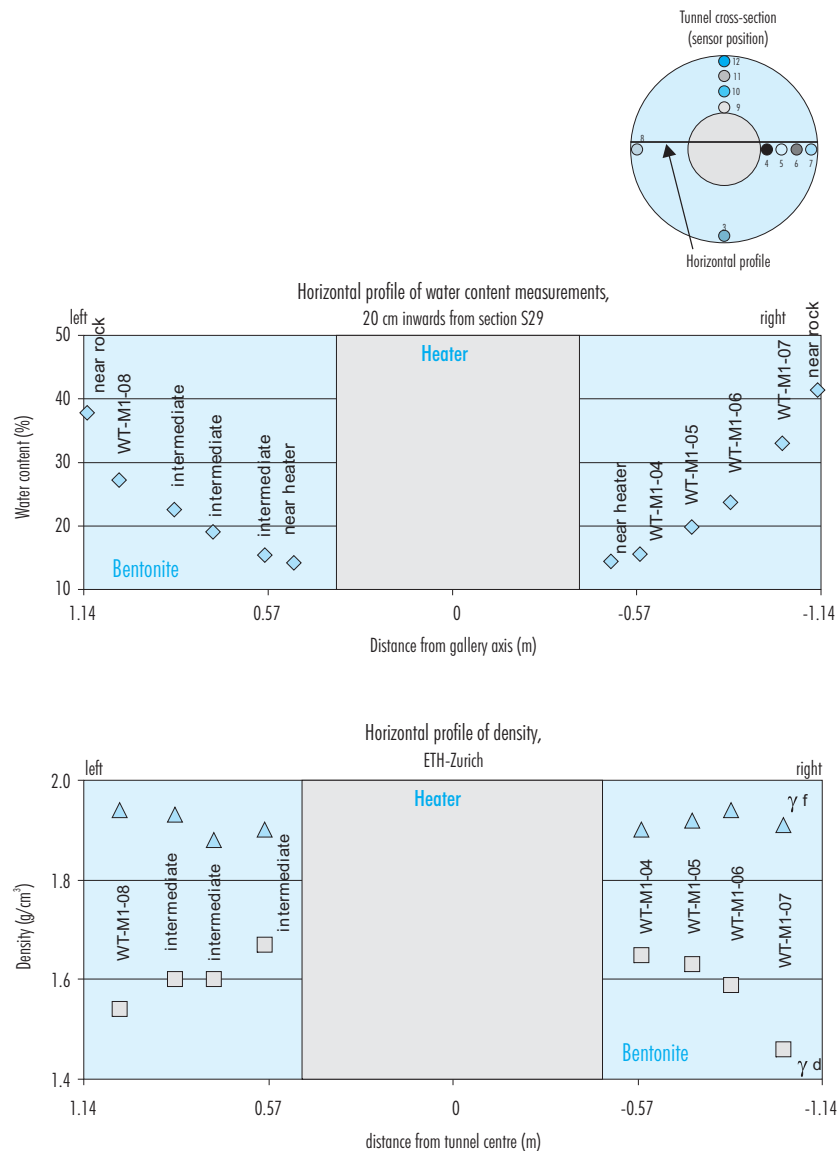


Figure 22: Horizontal profile of in situ water content measurements on core samples (upper figure) and laboratory density measurements (lower figure). Bulk density is indicated by triangles and dry density by squares.

The results are compiled in Figure 25 to Figure 28. Figure 25 shows that the bulk density is approximately constant along the radius but the other results show that there is a strong gradient in water content, which means that there is also a strong gradient in dry density and void ratio. The dry density close to the heater is about the same as the initial dry density of the blocks, which means that the gradient mainly is caused by different amount of swelling of the buffer. Figure 26 shows that the water content is the same for the two series of analyses

at the inner block but also that there is an increasing difference with increasing radius for the outer two blocks up to as much as 5 percent.

4.2. Analysis of tracers distribution

4.2.1. UDC-CIEMAT: Deuterium

Deuterated water ($^2\text{H}_2\text{O}$) was proposed as a conservative tracer for the *in situ* test (Febex Technical Re-

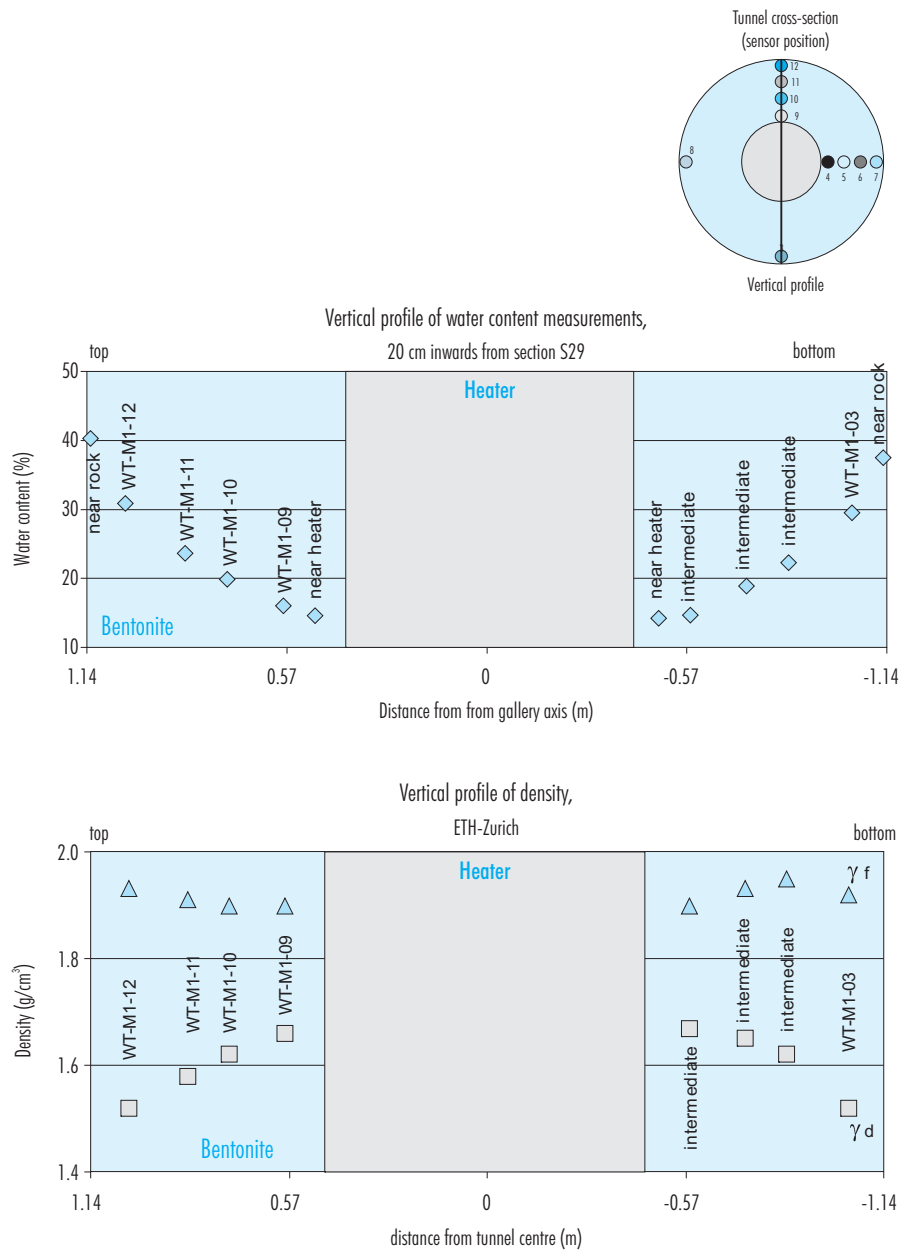


Figure 23: Vertical profile of in situ water content measurements on core samples (upper figure) and laboratory density measurements (lower figure). Bulk density is indicated by triangles and dry density by squares.

port 70-ULC-L-2-004). Deuterium is a stable isotope that has the unique property of forming part of the water molecule. Therefore, it will move with water like a conservative tracer. However, it potentially will participate in processes that could induce its isotopic fractionation. These processes may include: (1) fractionation due to the water uptake during bentonite hydration; and (2) fractionation due to evapora-

tion/condensation processes in areas close to the heaters.

Five sources containing deuterium in glass ampoules were placed in five bentonite blocks in section S29 (Figure 29). To fill the ampoules placed in the five blocks of the *in situ* test, deuterated water was provided by CIEMAT with a deuterium content

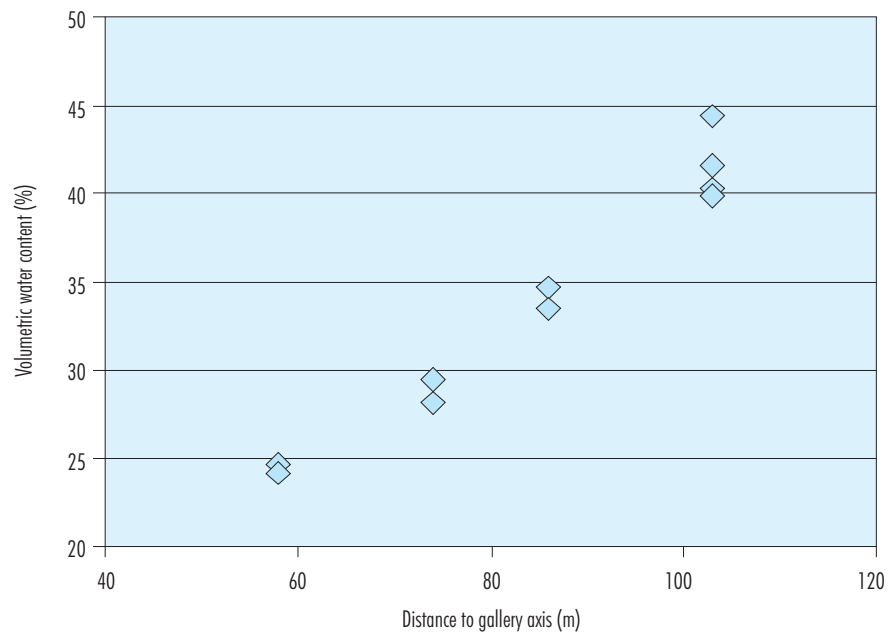


Figure 24: Volumetric water content at TDR positions measured at the ETH-Zürich (samples taken at 24 cm from the surface of section S29).

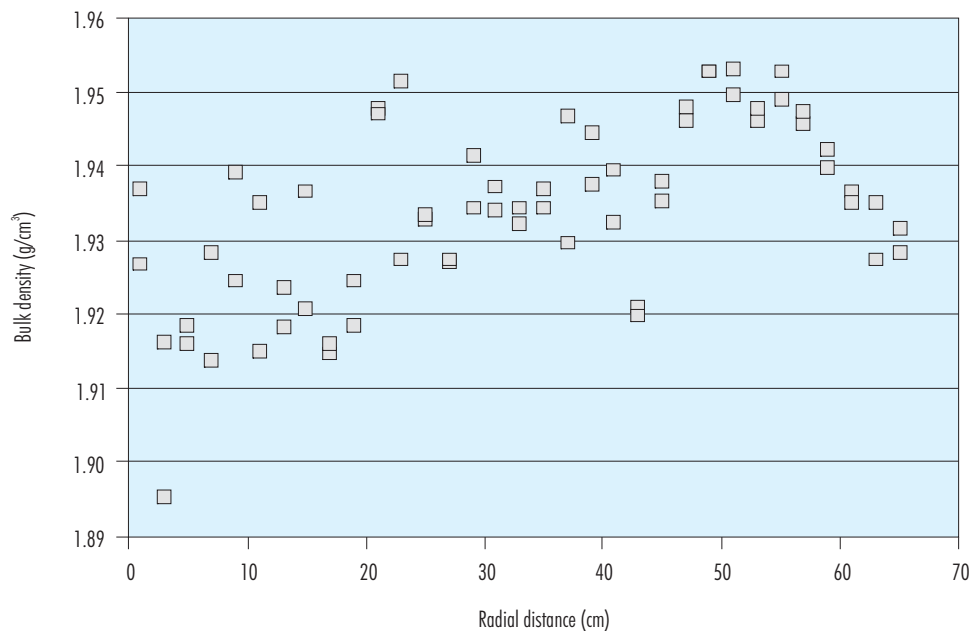


Figure 25: Bulk density as function of the radial distance from the liner determined on blocks from section S20 (BB20-6, BB20-7 AND BB20-8) taken following a radial direction at 60° counterclockwise from the vertical axis

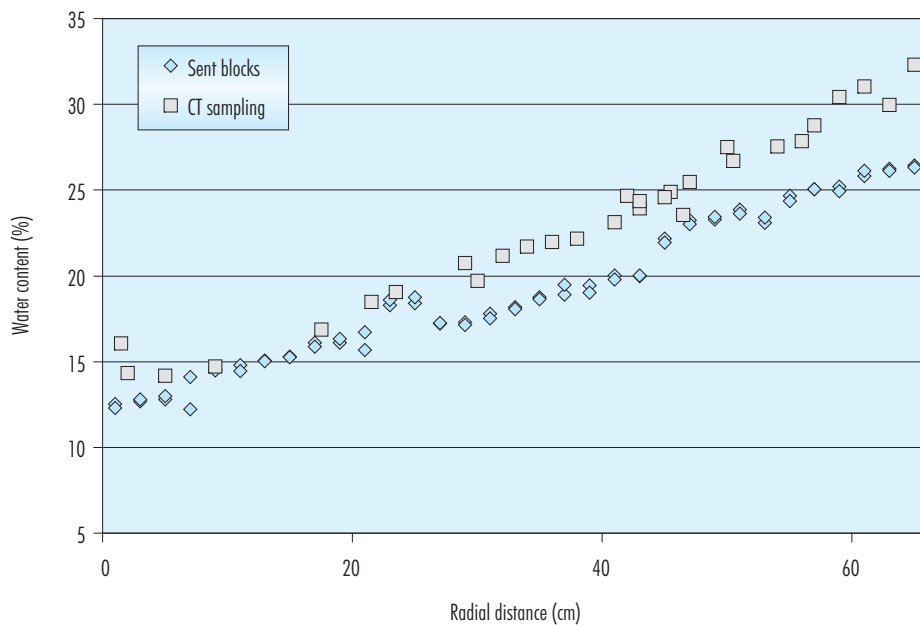


Figure 26: Water content as function of the radial distance from the liner determined on blocks from section S20 (Sent blocks) and from section S22 (CT sampling).

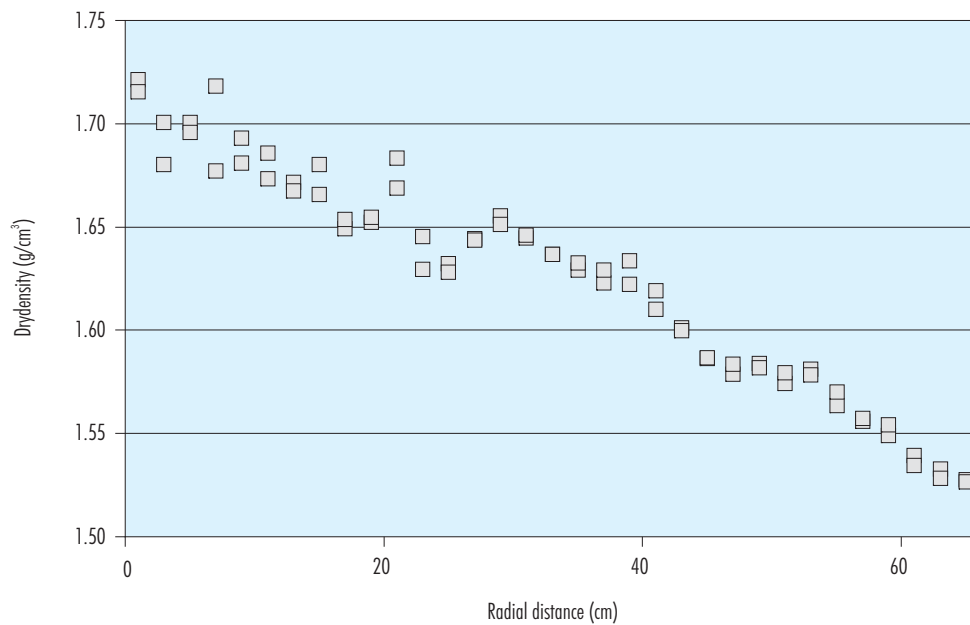


Figure 27: Dry density as function of the radial distance from the liner determined on blocks of section S20 (BB20-6, BB20-7 AND BB20-8) taken at a radial direction at 60° counterclockwise from the vertical axis.

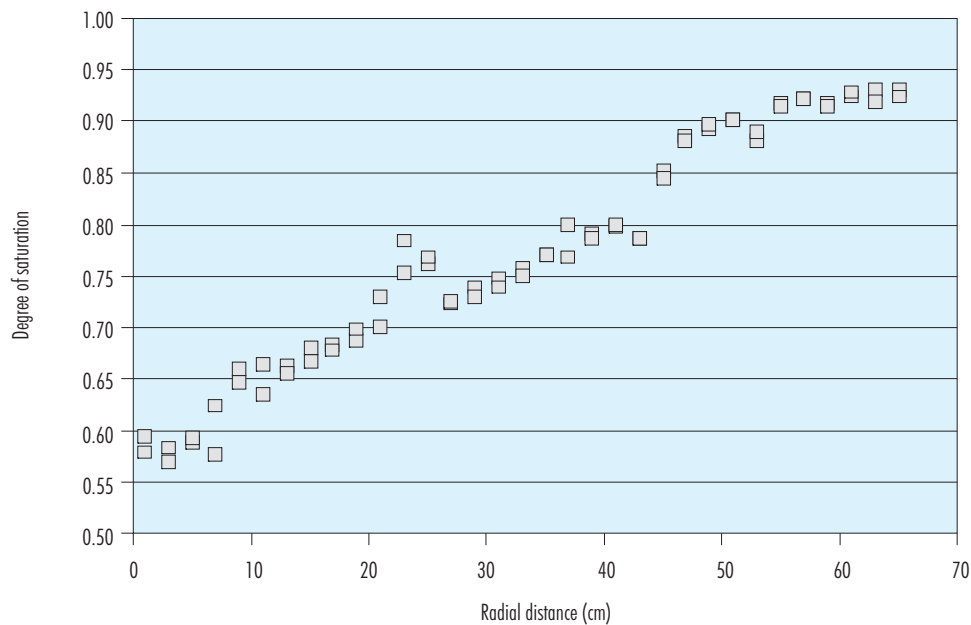


Figure 28: Degree of saturation as function of the radial distance from the liner determined on blocks from section S20 (BB20-6, BB20-7 AND BB20-8) taken at a radial direction at 60° counterclockwise from the vertical axis.

of 99.95 %. A new dissolution of deuterated water was prepared by UDC by diluting 200 μL of D_2O at 99.95 % of ^2H in a volumetric flask with 500 mL of bidistilled water of known δD to reach the desired composition ($\delta\text{D}=500$ ‰) and concentration (0.04% of ^2H). Pyrex glass ampoules (13 mm OD, 100 mm length, 0.5 mm thickness) were filled with 10 mL of this deuterated water (0.04%), and then vacuum-sealed with the aid of a gas torch (FEBEX Especificación 70-ULC-H-3-001, FEBEX Especificación 70-IMA-H-3-05). Finally, at the GTS, the glass ampoules were placed inside a hole drilled at the centre of the bentonite block and capped with 45-mm long compacted clay plugs.

The blocks taken during dismantling were (Figure 29): the five bentonite blocks containing the glass ampoules (BB29-5 to BB29-9) and four blocks above them completing the two central radii (BB29-10 to BB29-13).

The UDC methodology for deuterium determination followed 3 stages (Febex Internal Note 70-ULC-D-6-03, Febex Specification 70-IMA-H-6-16):

1. Scoping calculations were performed to study the expected behaviour of deuterium in the bentonite blocks.
2. Acquisition of a general description of deuterium ratios (δD). The main activities within this stage were:
 - Checking the status of glass ampoules to find out whether they were broken or not. This was done in the five blocks.
 - Collecting samples to derive the distribution of δD values.
 - Samples were also taken at a section without deuterium (section 19) in order to have reference δD values of the bentonite.
 - Deuterium isotopic analyses. They were carried out in the Laboratorio de Isótopos Estables (Stable Isotopes Laboratory) of the Servicio Interdepartamental de Investigación of Universidad Autónoma de Madrid (UAM).
3. Based on the results of the previous stage, further sampling and analyses were performed.

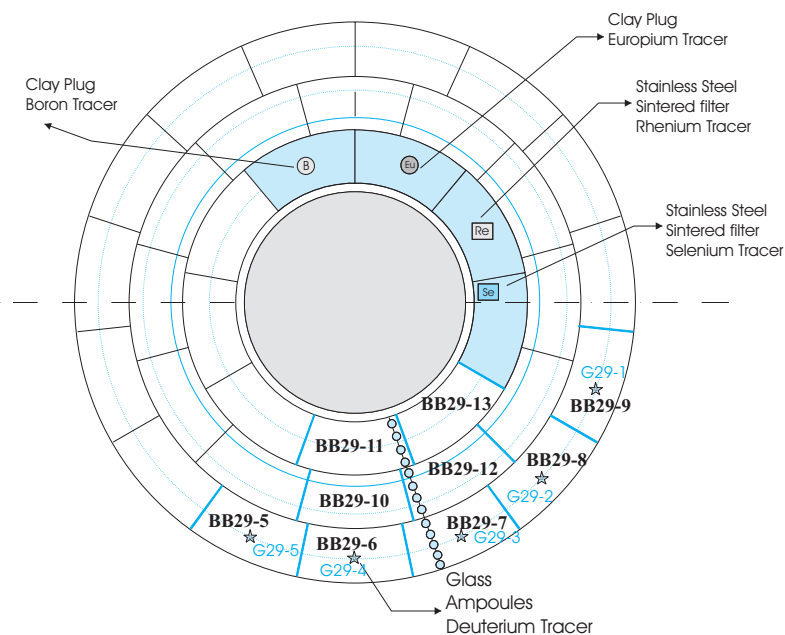


Figure 29: Location of deuterium ampoules (stars), of bentonite blocks taken for deuterium analyses and of sampling points (circles).

4.2.1.1. Preliminary scoping calculations

Scoping calculations were performed to study the expected behaviour of deuterium in the bentonite blocks. 1D scoping calculations are shown in Figure 30. These predictions assume that this tracer is conservative and does not suffer isotopic fractionation.

4.2.1.2. Deuterium laboratory sampling

Sampling of the selected bentonite blocks (BB29-5 to BB29-13) was carried out in CIEMAT in October 2002. It should be pointed out that glass ampoules were found only in three of the five bentonite blocks: BB29-7, BB29-8 and BB29-9. Most of the selected bentonite blocks were very damaged, probably during extraction. The sampling in the bentonite block BB29-13 (Figure 31) was impossible due to this circumstance. The glass ampoules in bentonite blocks BB29-7, BB29-8 and BB29-9 were found broken (Figure 32 and Figure 33). Only for block BB29-7 all the pieces of the glass ampoule were found. At the moment it is not possible to distinguish if the breaking was produced during the dismantling or during the operation phase of the *in situ* test.

A total of 124 samples were collected from bentonite blocks BB29-7 to BB29-13 (except block BB29-10). Most of the samples correspond to blocks BB29-7, BB29-12 and BB29-11. The final location of deuterium sampling points is shown in Figure 29.

Bentonite pore water for deuterium isotopic determination was obtained by CIEMAT from 18 of these samples using the aqueous extract method with low solid to liquid ratio. 10 g of bentonite were dispersed into 40 mL of water (1:4 ratio). After centrifugation, the supernatant solutions were sent for isotopic and chemical analysis. Besides, deuterium isotopic determinations were performed on a bentonite sample from block BB19-14 (without deuterium) and in the water used to prepare the aqueous extracts.

4.2.1.3. Deuterium isotopic analyses of aqueous extract samples

A total of 20 liquid samples were sent for isotopic analyses. Deuterium isotopic analyses (δD) were performed with Isotope Ratio Mass Spectrometry (IRMS). Figure 34 shows the isotopic results of the

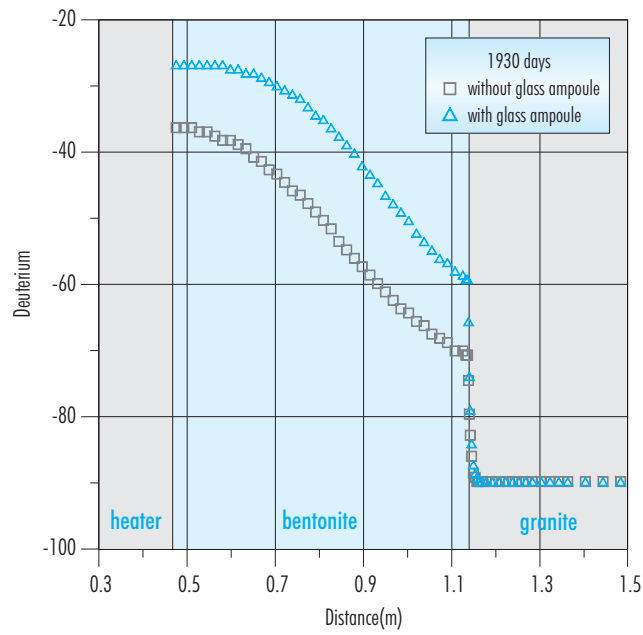


Figure 30: Predictions of deuterium relative concentrations with and without considering glass ampoule assuming a pore water diffusion coefficient of $1.59 \cdot 10^{-10} \text{ m}^2/\text{s}$.



Figure 31: Bentonite block BB29-13.

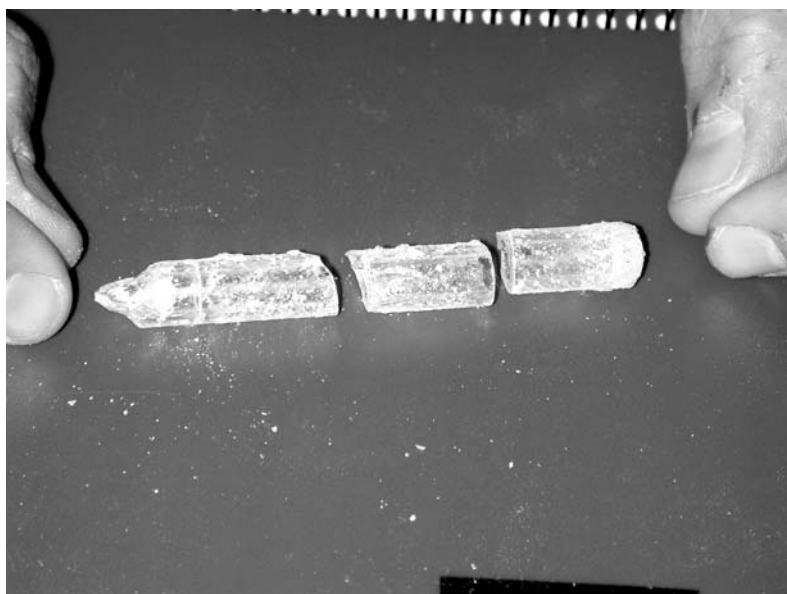


Figure 32: Deuterium glass ampoule found in bentonite block BB29-7.



Figure 33: View of the top part of deuterium glass ampoule found in bentonite block BB29-7.

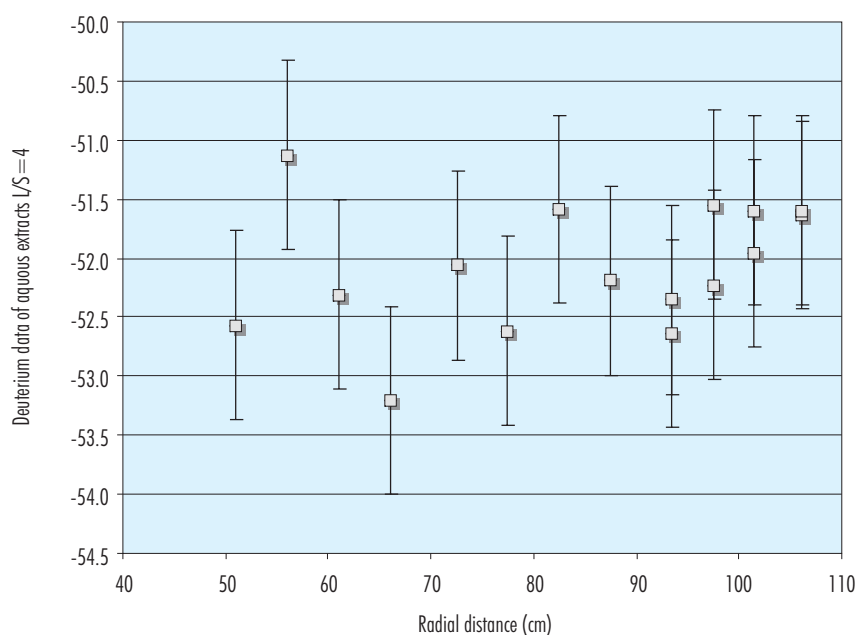


Figure 34: Deuterium data δD_{VSMOW} (‰) of aqueous extracts samples (s:l ratio 1:4) versus radial distance from gallery axis in bentonite blocks BB29-7, BB29-11 and BB29-12.

aqueous extract samples (solid:liquid ratio of 1:4) as a function of the radial distance from the heater. The data error for each sample (0.8 ‰) is also shown. All samples have values between -51.1 and -53.2. Two of the selected samples were analysed twice to check the data reproducibility, and it was found to be good.

Plans for stage 3 of the work included: (1) to select additional samples along a radius of section 19 at the same locations as those used by CIEMAT for geochemical analyses, (2) to obtain the value of δD for intact FEBEX bentonite and for Grimsel granitic

water; and (3) to analyse the oxygen-18 content of the 20 samples from section S29 (FEBEX Specification 70-IMA-H-6-16).

Based on the results of deuterium isotopic data, further confirmatory deuterium sampling and analyses were performed in section S29. Three additional samples were prepared using lower solid:liquid ratio, 1:1, in order to check the accuracy of the previous measurements. 10 g of bentonite were dispersed in 10 mL of water (1:1 ratio). After centrifugation, the supernatant solutions were sent for deuterium analysis. Table XI shows the results for these 3 samples.

Table XI
Additional deuterium data of aqueous extract samples (s:l ratio 1:1). Precision of data is 0.8 ‰.

| Identification | δD_{VSMOW} (‰) |
|-----------------------|------------------------|
| BB29-7/2-5 | -52.3 |
| Pieces near the glass | -51.4 |
| Intact bentonite | -49.7 |

Given the large scatter of measured δD values, further sampling along a radius of section S29 and oxygen-18 analyses of the previous 20 samples from section 29 were discarded.

4.2.1.4. Conversion of deuterium aqueous extract concentration to bentonite pore water concentration

The isotopic results of aqueous extract samples correspond to solid:liquid ratios of 1:4 and 1:1. Therefore, it is necessary to convert deuterium aqueous extract concentration to bentonite pore water concentration. Let R be the ratio of the mass of added water to the mass of the clay sample ($R = 4$ and 1). Mass balance before and after mixing the bentonite sample with ultrapure water ensures that:

$$c_b \cdot w + c_{bd} \cdot R(1+w) = (R(1+w) + w)c_{ae} \quad [9]$$

where c_b is bentonite pore water concentration, w is initial water content, c_{bd} is bidistilled water concentration, R is liquid:solid ratio and c_{ae} is aqueous extract concentration.

Deuterium samples were prepared for a ratio $R = 4$. Therefore, Equation 9 becomes:

$$c_b \cdot w + c_{bd} \cdot 4(1+w) = (4(1+w) + w)c_{ae} \quad [10]$$

The concentration of the aqueous extract can be written as:

$$c_{ae} = \frac{c_b w + c_{bd} 4(1+w)}{5w+4} = c_b \frac{w}{5w+4} + c_{bd} \frac{4+4w}{5w+4} \quad [11]$$

After performing the measurements in the aqueous extract water sample, the concentration in the bentonite sample is derived from:

$$c_b = c_{ae} \frac{5w+4}{w} - c_{bd} \frac{4+4w}{w} \quad [12]$$

The aqueous extract sample is highly diluted compared to the bentonite concentration. In fact, the concentration of the aqueous extract is the result of a mixing of c_{bd} and c_b :

$$c_{ae} = c_b \cdot f + (1-f)c_{bd} \quad [13]$$

where the mixing fraction f is given by:

$$f = \frac{w}{5w+4} \quad [14]$$

which in general has the following expression:

$$f = \frac{w}{(R+1)w+R} \quad [15]$$

Figure 35 shows a plot of the mixing fraction, f , for a water content of 0.25. It can be seen that f is about 0.05 for $R = 4$. The reciprocal of f can be considered as a "dilution factor". Such dilution factor is equal to 21 for $R = 4$ while it decreases to 6 for $R = 1$.

Such large dilution factors may be a significant drawback because the analytical errors in measuring c_{ae} translate into large errors when c_b is computed according to Equation 12. Let ε_{ae} be the analytical error for the determination of a given parameter. This error is equal to 0.8 ‰ for $\delta D_{SMOW}(‰)$. A simple error analysis of Equation 12 indicates that the analytical error for c_b , ε_b , is given by:

$$\varepsilon_b = \varepsilon_{ae} \sqrt{\frac{1}{f^2} + \frac{1}{(1-f)^2}} \quad [16]$$

The term within the square root is a multiplicative factor that propagates the errors in the aqueous extract to the errors in the "inferred" composition. Figure 36 illustrates this factor. For $R = 4$, this factor is equal to 21. It means an error of 0.8 ‰ for δD will translate into an error in the inferred composition of 16.8 ‰. Such an error is not admissible for deuterium. Therefore, a smaller ratio is required. For $R = 1$, the error factor is equal to 6 and the error in the inferred composition is of 4.8 ‰.

Deuterium data of aqueous extract samples with a ratio $R=4$ (solid:liquid ratio 1:4) and $R=1$ (solid:liquid ratio 1:1) have been transformed into bentonite pore water δD values by using Equation 12. These values are plotted together in Figure 37 with error bands considering Equation 16. One can see that the error bands for $R = 4$ are too large. In fact, the error bands would be smaller if the samples had been prepared with a ratio of $R = 1$. Figure 38 shows the upper and lower limits for the error bands of deuterium data of bentonite pore water.

4.2.1.5. Discussion

Available deuterium data do not allow drawing clear conclusions due to:

- Data precision. Although precision of deuterium data of aqueous extract samples, c_{ae} , at $R = 4$ is 0.8 ‰ (Figure 34), this analytical error in measuring c_{ae} translates into large errors when bentonite pore water values, c_b , are computed ac-

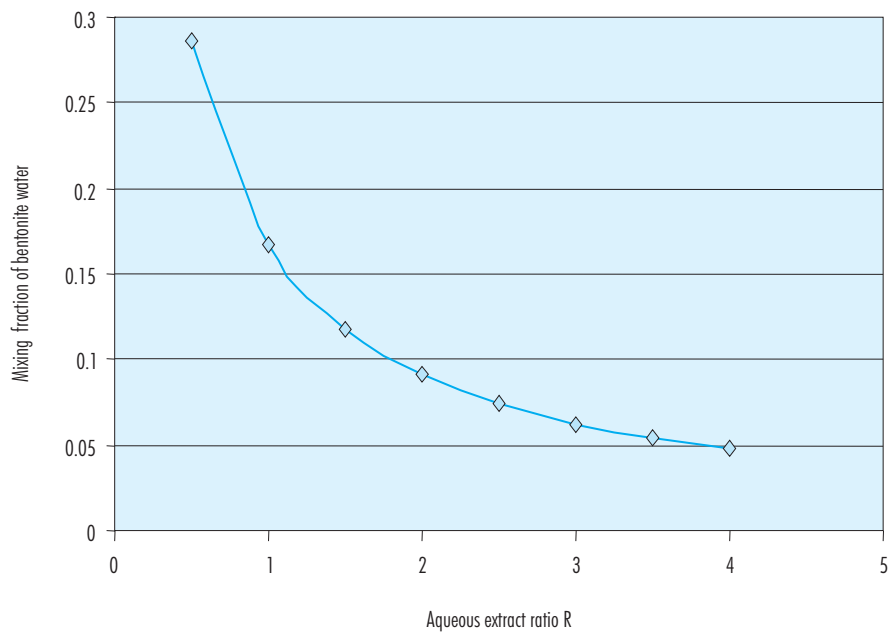


Figure 35: Mixing fraction as a function of R (liquid:solid ratio).

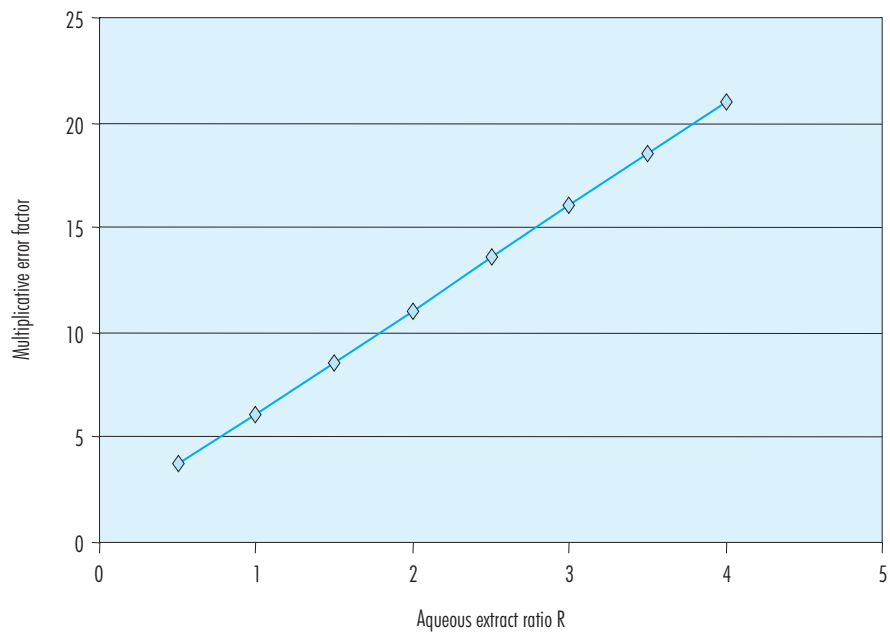


Figure 36: Multiplicative error factor for aqueous extract data in function of R (liquid:solid ratio).

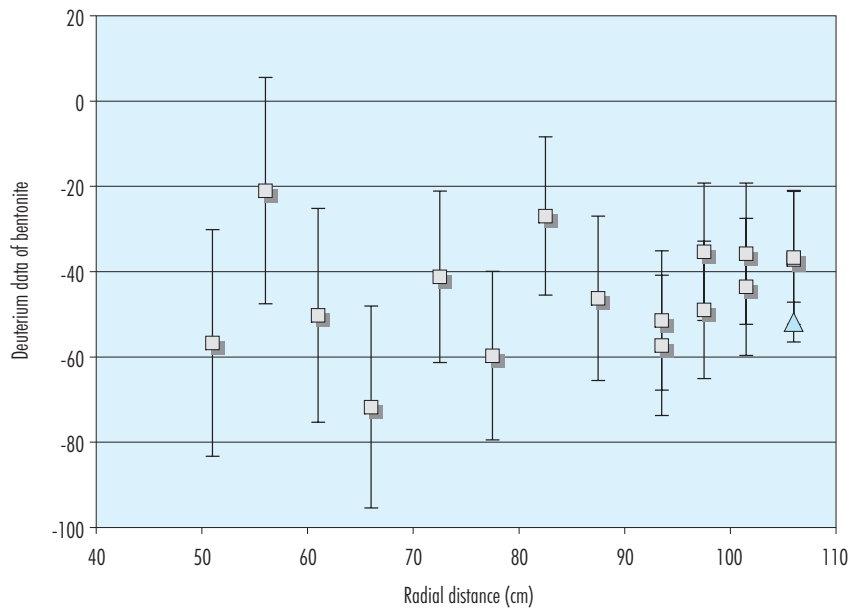


Figure 37: δD values of bentonite pore waters versus radial distance ($r=0$ corresponds to heater axis). Error bands have been computed by multiplying the lab precision of 0.8 ‰ by the multiplicative error factor considering Equation 16. The error band is much smaller for $R = 1$ (triangle at a distance of 106 cm).

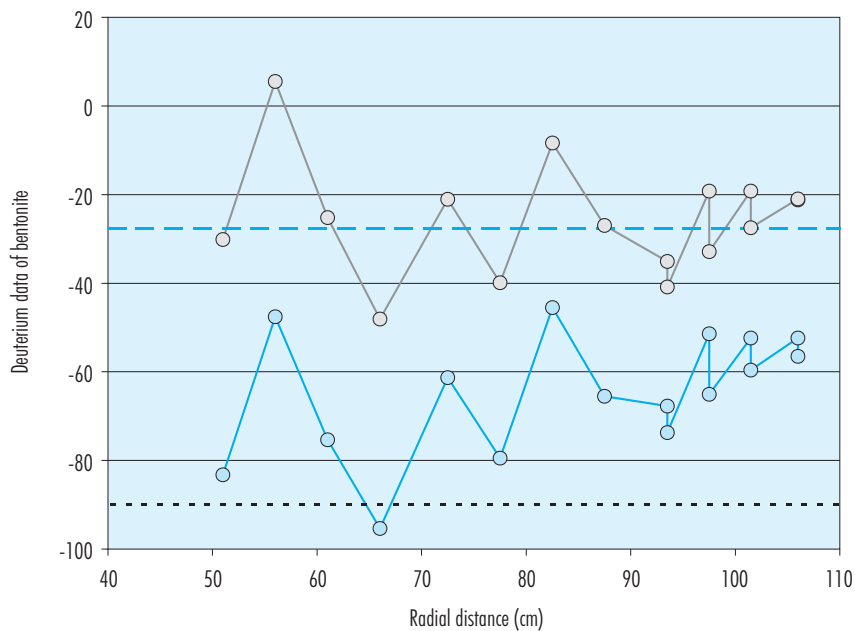


Figure 38: Upper and lower limits of error bands for delta values of bentonite pore waters versus radial distance ($r=0$ corresponds to heater axis). Deuterium data for intact bentonite pore water (-27.71 ‰) and granite (-90 ‰) are also shown.

according to Equation 12 (Figure 37). Error bands for c_b are too large. With a ratio of $R = 1$ error bands would have been much smaller.

- Uncertainties on glass ampoules breaking. Only 3 were found broken. Most likely glass ampoules broke during the operation phase, because if they had broken during dismantling clay samples near the glass should still show high deuterium ratios. However, since the amount of deuterated water added was not large enough there is not clear evidence of deuterium migration.

There are uncertainties in deuterium data and interpretation due to:

- Preliminary scoping calculations were not fully realistic because they did not account for isotopic fractionation.
- Deuterium mass added into bentonite blocks was probably not large enough for serving as a tracer for the *in situ* test.
- Bentonite pore water deuterium concentration has been derived from aqueous extract samples. There are uncertainties on the isotopic transfer (fractionation) between internal (inter-

layer) and external water (double layer water and free water).

- Deuterium analyses were performed in liquid phase but it should be explored the possibility to measure deuterium directly in bentonite samples.

4.2.2. EIG EURIDICE: Iodide

The blocks BB30-1, BB30-2 and BB30-3 were retrieved by EIG EURIDICE during the dismantling operations for the determination of the tracer distribution (Verstricht 2004). The location of the blocks in the section is shown in Figure 39. The blocks were packaged immediately after removal, and transported to EIG EURIDICE, where they were kept in a storage room at a temperature of 4 °C.

Once in the laboratory, samples were taken from the different blocks through different hand tools (pushing tube, cutting knife), as shown in Figure 40. During the sampling, we took the necessary measures to avoid any cross contamination.

To determine the sampling positions, we considered both contact surfaces, to account for the (initial) wa-

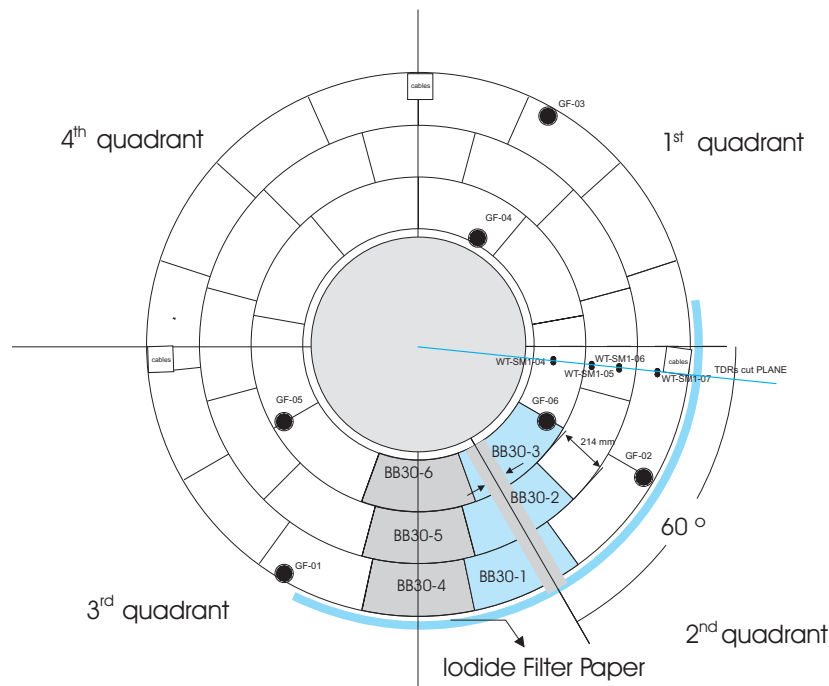


Figure 39: Location of blocks taken in section S30.



Figure 40: Sampling of a I-doped block by pushing tube.

ter flow along the block joints, and the inside of the blocks. The clay samples were dried at 105 °C. An aqueous extraction was carried out and the solutions were analysed with ICP-MS. The estimated uncertainty (2σ) is 15 percent.

The sample positions for block BB30-1 (in contact with the filter paper) are shown in Figure 41. All dimensions are given in mm, and the block is shown with the side facing the gallery entrance downwards. The analysis results (in $\mu\text{g/g}$ dry clay) are also shown in the same figure. From this block we analysed 26 samples. In addition to samples at the surface, also samples inside the block were taken. We took two radial profiles (E1 to E6 at the surface, and E1' to E6' at some 40 mm depth). Samples E5 to E10 constitute an in-depth profile.

For block BB30-2 (the middle block), the sample positions and the analysis results are shown in Figure 42. From this block, eight samples have been analysed. The results for block BB30-3 (in contact with the heater liner) are shown in Figure 43. Here, five samples have been analysed.

The iodide concentration measured in each sample is plotted in Figure 44 as a function of the distance

to the gallery axis, i.e. following a radius of the barrier. The outer block (in contact with the I-doped sheet) shows a I-concentration that increases in the direction of the heater, while the highest concentrations are found in the middle block (BB30-2). This is the expected behaviour for a conservative tracer that has moved with the water front, being leached from the filter paper and having concentrated in the further zones reached by the water front.

The reliability of the results is confirmed by the repeatability of adjacent samples, as can be seen in the block BB30-1 and at the interfaces of block BB30-2 (samples B2-JI and B3-JE).

4.2.3. EIG EURIDICE: Boron

The block BB-25-2 –located in the contact with the gallery wall– was doped with boron (isotopically enriched in ^{10}B) contained in a sintered stainless steel plug placed in the middle of the block. After retrieval during dismantling, CIEMAT prepared the sampling by cutting the block in slices: 10 slices towards the heater (D-0 to D-9) and 4 slices towards the gallery wall. One slice contained the source. It

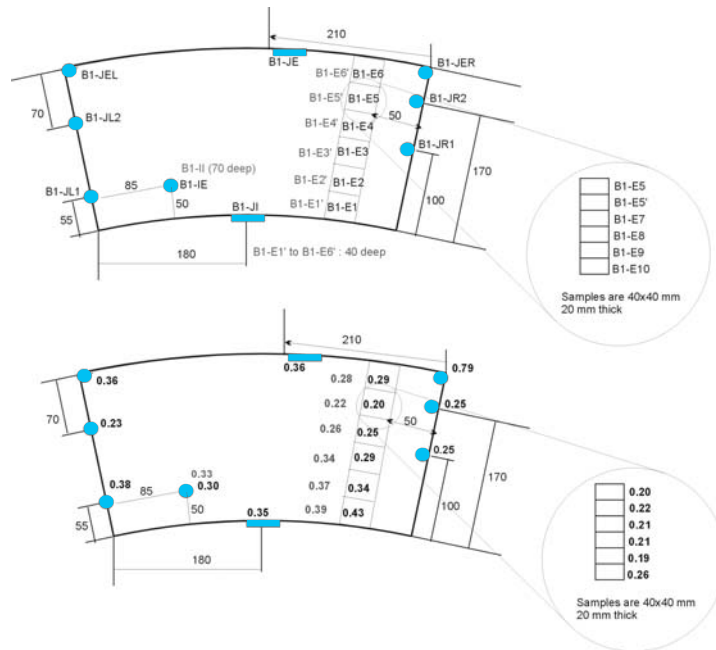


Figure 41: Sampling positions (above) and analysis results (below, in $\mu\text{g/g}$ dry clay) for block BB30-1.

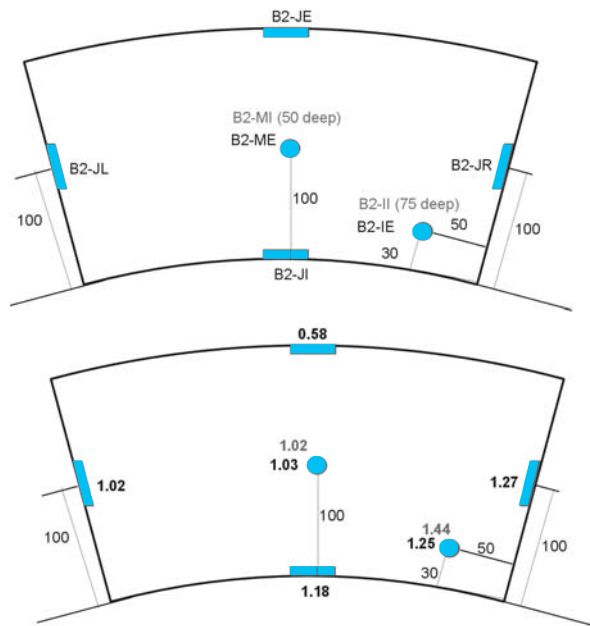


Figure 42: Sampling positions (above, in mm) and analysis results (below, in $\mu\text{g/g}$ dry clay) for block BB30-2.

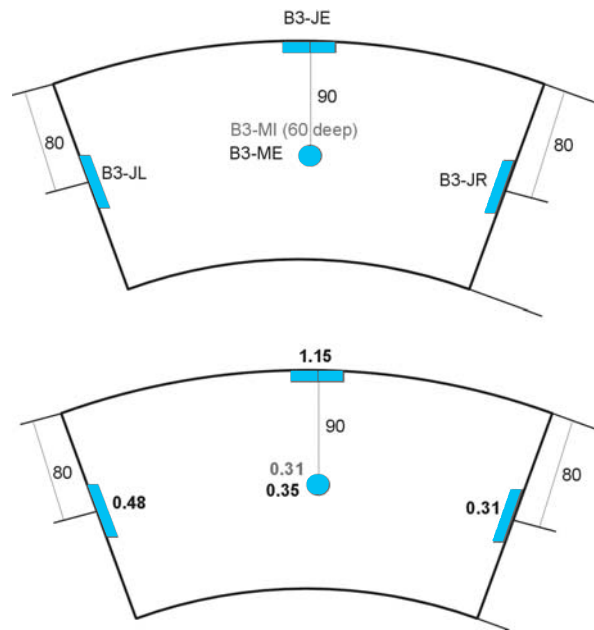


Figure 43: Sampling positions (above, in mm) and analysis results (below, in $\mu\text{g/g}$ dry clay) for block BB30-3.

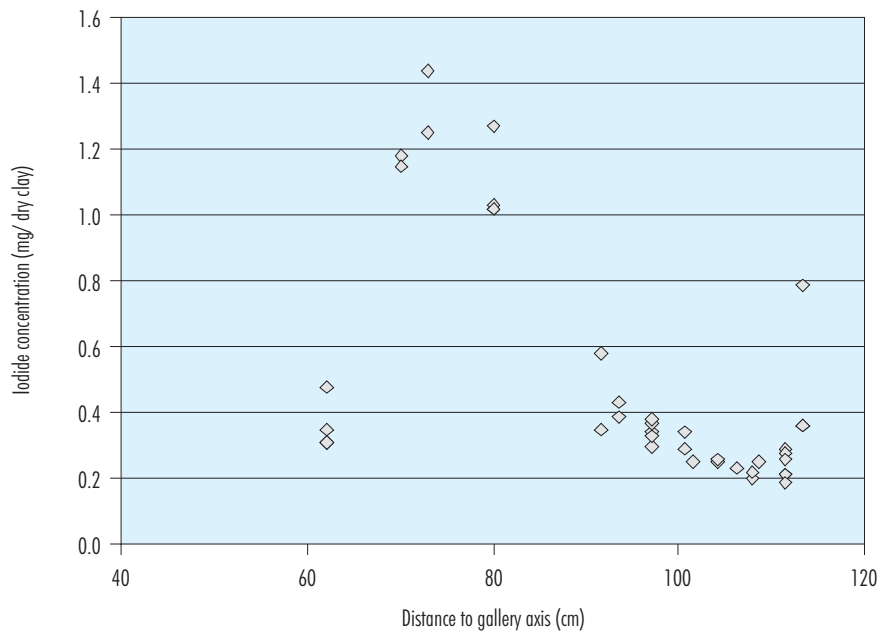


Figure 44: Iodide concentration as a function of the distance to the gallery axis in the samples analysed by EIG EURIDICE (section S30).

was expected that the preferential migration of the boron would be towards the heater (hydration). The individually packaged slices were sent to EIG EURIDICE for analysis.

The following analysis procedure has been applied (Verstricht 2004):

- drying of the samples, grinding and homogenising; only one side of each slice was taken for analysis, as discussed with CIEMAT;
- 200 mg of clay is mixed with 25 mL of a 5% HNO₃ solution;
- shaking during 2 hours;
- further dilution of this mixture;
- measurement through ICP-MS.

From four samples, five extractions have each time been carried out to obtain an idea of the statistical distribution of the results due to measurement uncertainty and sample preparation. The estimated uncertainty on the measurement results (2σ) is 10 per cent.

Preliminary analyses indicated an isotope ratio $^{10}\text{B}/^{11}\text{B}$ of 35/65 (the natural abundance being

20/80). The individual results, plotted in Figure 45, give the total B concentration in each slice (no isotopic concentrations) in $\mu\text{g/g}$ dry clay. No clear pattern can be seen. The boron concentration seems quite regular over the whole sampling region. At both ends, the concentration seems to decrease, but this would require a larger sampling range.

4.3. Thermo-hydro-geochemical tests

The geochemical analyses performed on solid samples have two main objectives: (1) to analyse the physical, chemical and mineralogical alterations occurred in the clay by effect of heat and hydration, and (2) to support the interpretation of the pore water extraction results in order to analyse the chemical evolution of the bentonite pore water as a function of the hydration and temperature profiles.

The THG studies have been focussed in four sections in the heater zone –S19, S23, S28, S29– and another one in the zone between the concrete and the heater –S12–. Besides, samples taken from section S7 (in contact with the concrete seal) have been analysed by CIEMAT and VTT.

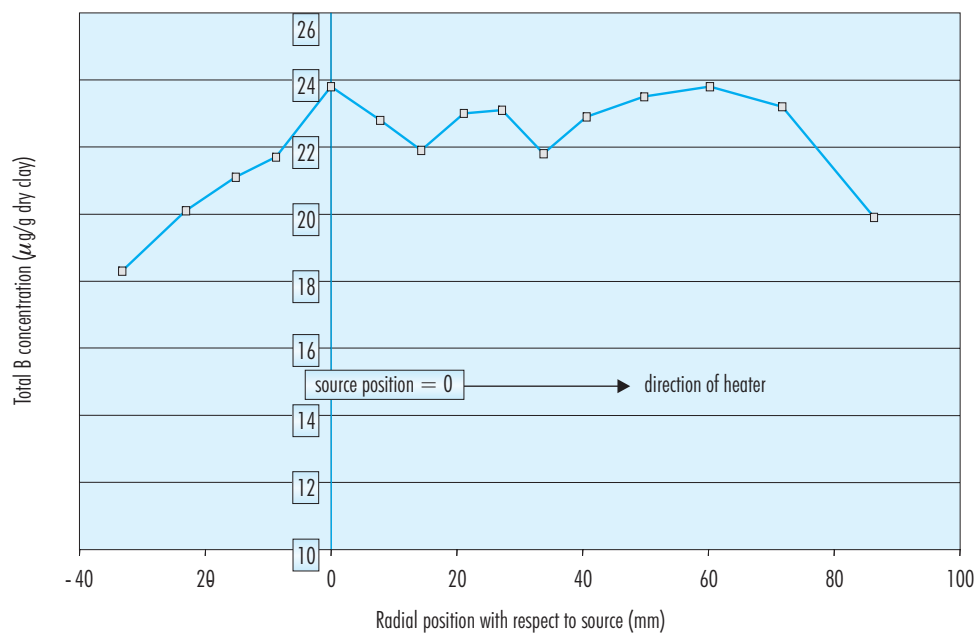


Figure 45: Distribution of boron along a radial line.

4.3.1. CIEMAT: Mineralogical, chemical and textural analysis

CIEMAT has performed analyses in bentonite from different sections to know the chemical, mineralogical and microstructural alterations occurred in the clay by effect of heat and hydration: section S7 (interface bentonite-concrete), section S12 (without heater), sections S19 and S28 (around the heater) and section 31 (bentonite / heater back lid contact).

A general analysis of the solid phase was performed to characterise its chemical, mineralogical (clay phases, main and accessory minerals) and microstructural transformations. The main analyses carried out have been: X-ray diffraction (XRD), chemical composition and thermal analyses (differential thermal analysis, DTA, and thermo-gravimetry, TG).

In addition to the mineralogical studies, the exchangeable cations (EC) and soluble salts (SS) were also determined. The possible exchange and saline gradients indicate the direction of the ionic diffusion processes through the bentonite. The variation of these parameters during the test may not necessarily involve mineralogical transformations of the smecti-

te, but just a precipitation of accessory minerals around clay particles or changes in the initial cation exchange complex, although this variation could be a precursor of such transformations.

Besides, in order to analyse the chemical evolution of the bentonite pore water as a function of the hydration and temperature profiles, three sections were analysed: S7, S12 and S19. The pore water extraction was performed by squeezing. The same blocks in which the solid characterisation was performed were selected for pore water extraction.

4.3.1.1. Subsampling at the laboratory

Once at CIEMAT laboratories, the blocks were half-sectioned along the radius, in order to obtain material for the THG and THM tests (Figure 46). The THG half was sliced in three parts (Figure 47): an internal part for analysing the soluble salts and exchangeable cations, an intermediate part for squeezing and solid phase characterisation, and an external part considered as a spare sample. The part committed to the analyses of the soluble salts distribution and exchangeable cations was further sliced in six



Figure 46. Sampling of blocks for THG analyses at CIEMAT.

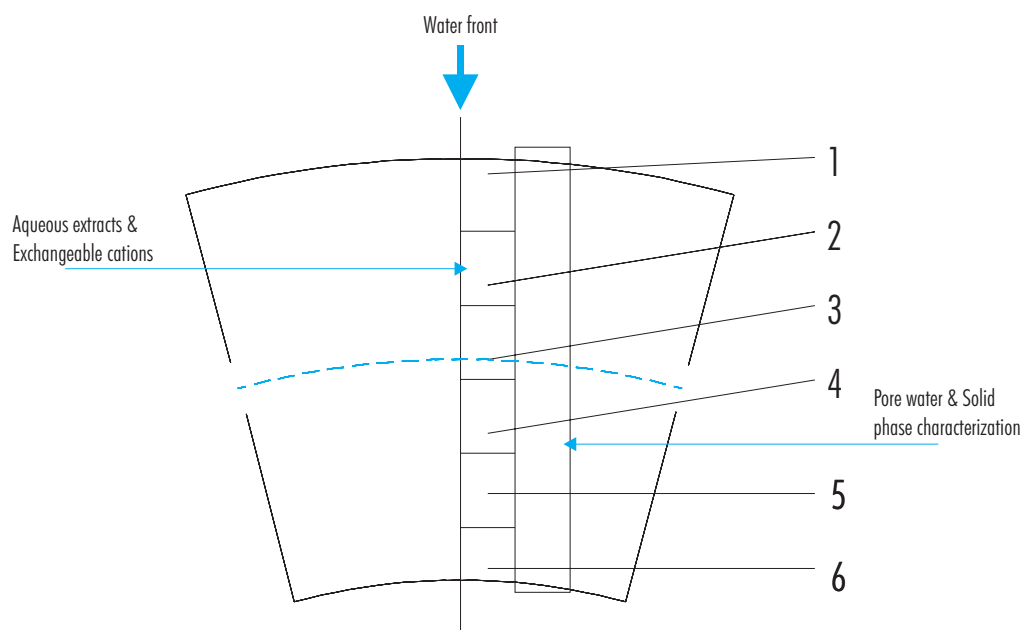


Figure 47. Subsampling of bentonite blocks for THG analyses.

pieces, referenced from 1 to 6 in the direction from the external to the internal part of the barrier.

Table XII shows all the samples selected by CIEMAT for THG analyses, their position in the sampling section, and the kind and number of determinations performed in them. All the samples have been taken from whole blocks sent to CIEMAT, except those belonging to section S31, that were obtained by drilling (BS31-22) and carving (BS31-26) *in situ* in the bentonite in contact with the back lid of the heater (Figure 48).

The dry density and water content of these samples are those indicated in section 4.1.2. However, for the THG analyses, the water content has been also determined by heating the sample to a temperature of 150 °C, instead of the standard 110 °C, since it has been proven that the total interlayer water of smectites is lost at 150-220 °C. The water contents obtained by heating at 150 °C are a 10 ± 5 percent higher than those obtained at 110 °C.

4.3.1.2 . X-ray diffraction

The mineralogical analysis was performed by X-ray diffraction techniques. Diffraction patterns from sam-

ples dried at 60 °C and powdered to a particle size below $60 \mu\text{m}$ were analysed. From the $< 2 \mu\text{m}$ particle size fraction, obtained by sedimentation, the oriented aggregate diffraction patterns were obtained on a suspension allowed to air-dry over a glass plate (OA), solvated with ethylene glycol (OA + EG) and heated at 500 °C. A Philips PW 1730 diffractometer has been used, with an anticatode of Cu ($\text{CuK}\alpha$), using an acceleration voltage of 35 kV and a current intensity in the filament of 40 mA. The apertures of divergence and reception were 1 and 0.2°, respectively, using a Ni filter. The exploration velocity was of 2°/min for the random powder sample (total analysis of the sample) and 1°/min for the oriented preparations with the $< 2 \mu\text{m}$ fraction. On the powder diffraction pattern a semiquantitative analysis of the minerals present in the sample was carried out. The mineral percentage content of the sample was corrected by their corresponding reflectance powder (Schultz 1964).

The XRD patterns obtained for powder samples of section S7, S12, S19 and S31 are shown in Figure 49, Figure 50, Figure 51 and Figure 52, respectively. In all these figures the XRD pattern of the untreated FEBEX bentonite is shown for comparison (indicated

Table XII
Samples taken for THG analyses by CIEMAT.

| Block reference | Section | Distance to gallery axis (cm) | Clockwise angle with vertical axis (°) | Type and number of analyses ¹ | |
|-----------------|---------|-------------------------------|--|---|---|
| BB7-4 | S7 | 103 | 220 | SS (6), EC (6), squeezing (1), XRD (1), CA, SSA | |
| BB7-5 | | 81 | 250 | SS (6), EC (6) | |
| BS7-6 | | 59 | 270 | SS (6), EC (6) | |
| BB12-1 | S12 | 103 | 60 | SS (6), EC (6) | |
| BB12-2 | | 81 | 60 | SS (6), EC (6) | |
| BB12-3 | | 59 | 60 | SS (6), EC (6) | |
| BB12-4 | | 103 | 180 | SS (6), EC (6) | |
| BB12-5 | | 81 | 180 | SS (6), EC (6) | |
| BB12-6 | | 59 | 180 | SS (6), EC (6) | |
| BB12-10 | | 103 | 300 | SS (6), EC (6), squeezing (1), XRD (1), CA, SSA | |
| BB12-11 | | 81 | 300 | SS (6), EC (6), squeezing (1), XRD (1), CA, SSA | |
| BB12-12 | | 59 | 300 | SS (6), EC (6), squeezing (1), XRD (1), CA, SSA | |
| BB19-1 | | S19 | 103 | 60 | SS (6), EC (6), squeezing (1), XRD (1), CA, SSA |
| BB19-2 | | | 81 | 60 | SS (6), EC (6), squeezing (1), XRD (1), CA, SSA |
| BB19-3 | | | 59 | 60 | SS (6), EC (6), squeezing (1), XRD (1), CA, SSA |
| BB19-10 | 103 | | 300 | SS (6), EC (6) | |
| BB19-11 | 81 | | 300 | SS (6), EC (6) | |
| BB19-12 | 59 | | 300 | SS (6), EC (6) | |
| BB19-13 | 103 | | 230 | SS (6), EC (6) | |
| BB19-14 | 81 | | 255 | SS (6), EC (6) | |
| BB19-15 | 59 | | 220 | SS (6), EC (6) | |
| BB28-1 | S28 | | 103 | 60 | SS (6), EC (6) |
| BB28-2 | | | 81 | 60 | SS (6), EC (6) |
| BB28-3 | | | 59 | 60 | SS (6), EC (6) |
| BS31-22 | S31 | | 35 | 160 | SS (6), EC (6), XRD (1), SSA |
| BS31-26 | | | 20 | 0 | SS (6), EC (6), XRD (1), SSA |

¹SS: soluble salts; EC: exchangeable cations; XRD: X-ray diffraction; CA: chemical analysis; SSA: specific surface area

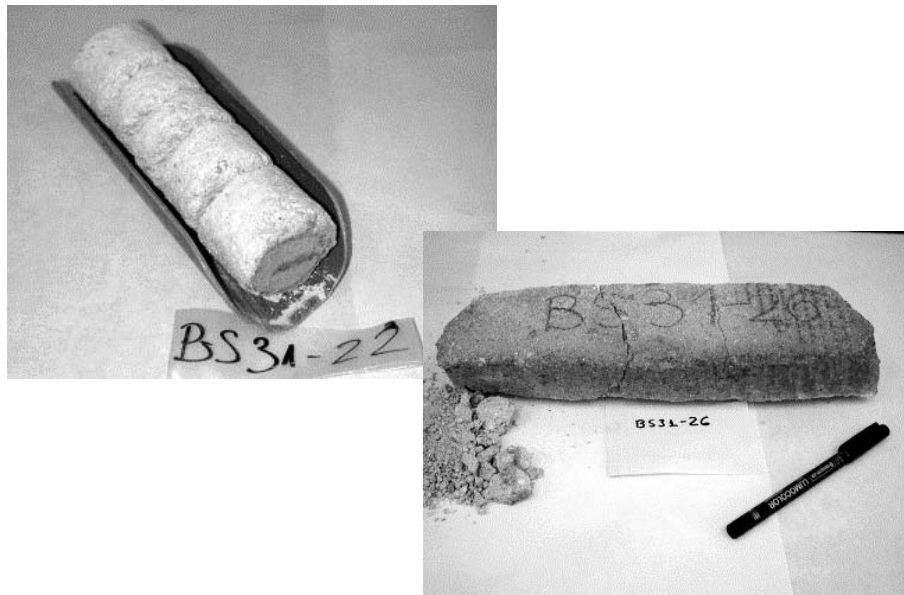


Figure 48: Borehole sample obtained in the back lid of the heater (BS31-22) and a piece of bentonite block obtained at the heater contact (BS31-26).

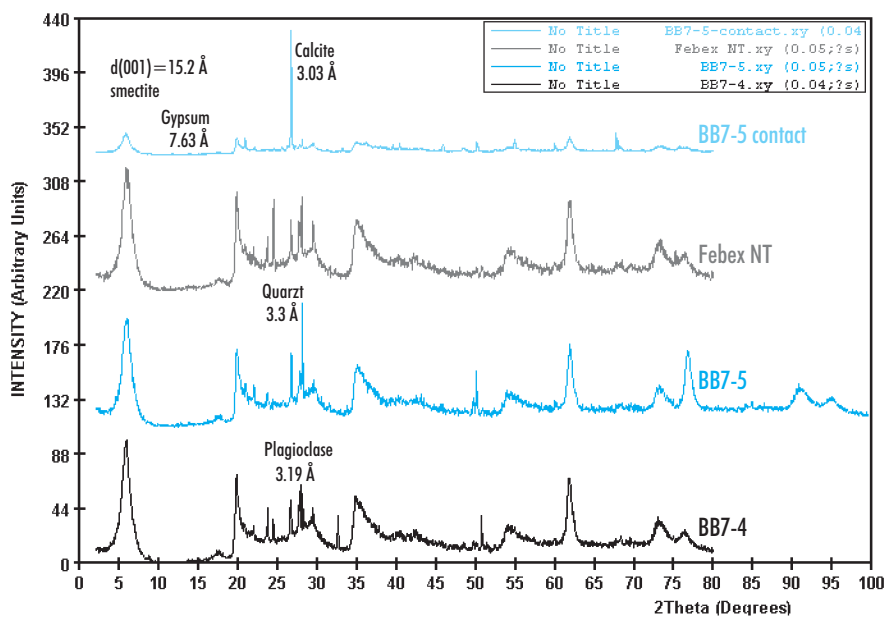


Figure 49: XRD pattern of random powder of samples from section S7 (total sample).

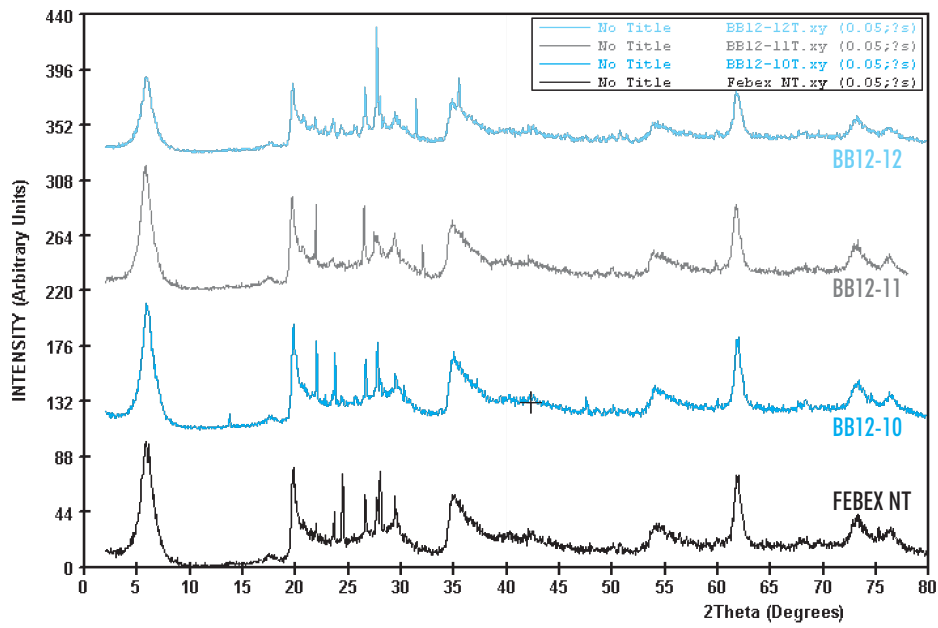


Figure 50: XRD pattern of random powder of samples from section S12 (total sample).

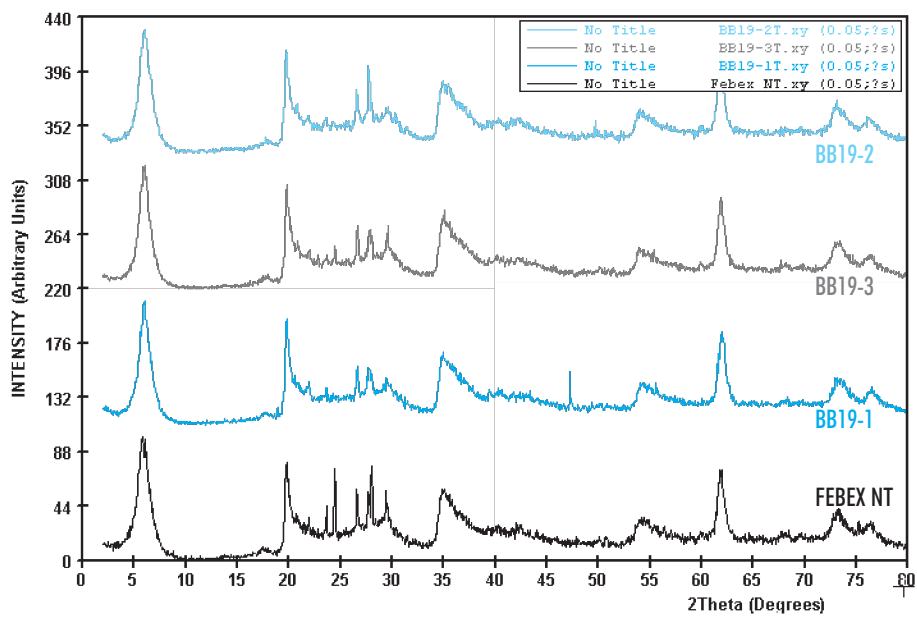


Figure 51: XRD pattern of random powder of samples from section S19 (total sample).

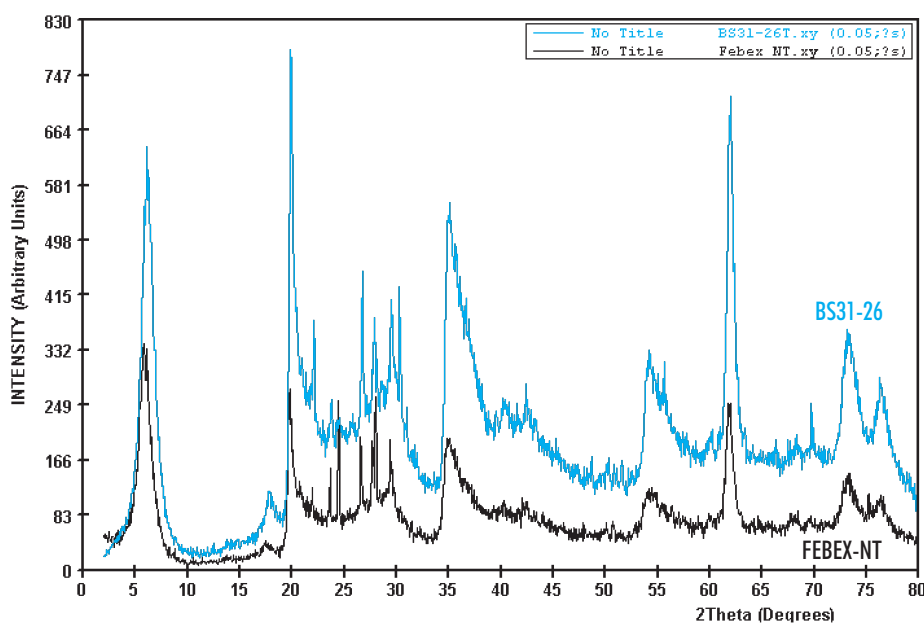


Figure 52: XRD pattern of random powder of sample BS31-26 (total sample).

as FEBEX NT). No significant differences have been found between the treated samples and the untreated one: the predominant mineral is a smectite with basal spacings $d(001)$ at around 15 Å (which indicates a predominance of bivalent cations in exchange positions), and there are also minor quantities of quartz, plagioclase, K-feldspars, calcite and cristobalite. Only an increase of calcite and gypsum was found in a bentonite sample that was directly in contact with the concrete plug (BB7-5-contact sample, Figure 49). Also, the sample BS31-26, that was in contact with the heater back lid and consequently subjected to the highest temperatures, presents higher peak intensities (Figure 52).

The basal spacings $d(001)$ of the smectite for the different treatments are shown in Table XIII. No significant differences are found among them, except for the sample subjected to the highest temperature (BS31-26) for which the basal spacings in the oriented aggregates are slightly higher. Some samples of section S19 were analysed right after sampling without further treatment, *i.e.* in their compacted state and with their original water content. These samples showed, with respect to the results obtained in the dried powder, an increment of water in interlayer po-

sitions to two and three layers (Table XIV), especially in the sample closer to the gallery wall (BB19-1).

4.3.1.3. Chemical analysis

For chemical analysis of the major and trace elements of the solid phase, the sample has been previously dissolved using a HF – aqua regia mixture. 500 mg of sample were transferred to a PTFE closed vessel and 4 mL of concentrated HF and 2 mL of aqua regia were added. The vessel was kept overnight at 90° C and, after cooling, the content was transferred to a PTFE evaporating dish, 2 mL of concentrated HClO_4 were added, and the content was allowed to evaporate until white fume appeared under infrared lamp. Finally, the residue was dissolved using diluted HNO_3 .

Afterwards, the *total alkalinity* of the samples was determined by potentiometric titration using a Metrohm 682 titrator. The *major cations* were analysed by Inductively Coupled Plasma-Atomic Emission Spectrometry (ICP-AES) in a Perkin-Elmer Elan 5000 spectrometer. *Sodium* and *potassium* were determined by flame atomic emission spectrometry (AAS-Flame) in a Perkin Elmer 2280 spectrometer,

Table XIII
Basal spacing $d(001)$ of the smectite (Å) measured in the XRD patterns.

| Sample | Position ¹ (cm) | Random powder | OA ² | OA + EG ³ | OA + 550°C ⁴ |
|---------|----------------------------|---------------|-----------------|----------------------|-------------------------|
| FEBEX | — | 15.30 | 14.25/12.53 | 16.90 | 9.60 |
| BB7-4 | 103 | 15.38 | 14.12/12.46 | 16.66 | 9.62 |
| BB7-5 | 81 | 15.56 | 14.41/12.70 | 16.66 | 9.52 |
| BB12-10 | 103 | 15.03 | 14.12/12.46 | 16.66 | 9.62 |
| BB12-11 | 81 | 15.56 | 14.41/12.70 | 16.66 | 9.52 |
| BB12-12 | 59 | 15.29 | 14.12/12.14 | 16.68 | 9.42 |
| BB19-1 | 103 | 14.65 | 14.38/12.59 | 16.53 | 9.56 |
| BB19-2 | 81 | 14.90 | 14.54/12.60 | 16.57 | 9.62 |
| BB19-3 | 59 | 15.03 | 14.38/12.29 | 16.51 | 9.62 |
| BS31-26 | 20 | 15.03 | 14.90 | 16.90 | 9.68 |

¹Distance to gallery axis; ²Oriented aggregate; ³Oriented aggregate solvated; ⁴Oriented aggregate heated at 550°C.

Table XIV
Basal spacing $d(001)$ of the smectite in non-dried BB19 samples (Å).

| Sample | Position ¹ | Powder | Compacted |
|--------|-----------------------|--------|-----------|
| BB19-1 | 102 | 14.65 | 16.86 |
| BB19-2 | 81 | 14.90 | 15.02 |
| BB19-3 | 59 | 15.03 | 15.37 |

¹Distance to gallery axis.

and trace elements were determined by ICP-MS (Finningan Mat SOLA). Anions were analysed by ion chromatography (Dionex DX-4500i). The silica was determined using a UV-Vis spectrophotometer by means of the silico-molybdic colourimetric method. It was estimated that the maximum analytical errors were $\pm 10\%$ for the major ions.

On the other hand, thermal analysis (TG/DTA) of the bulk sample has been performed using a Perkin-Elmer 1700 DTA (differential thermal analysis) apparatus at a scan rate of 10 °C/min and under a dynamic air atmosphere (40 cm³/min) at temperatures between 25°C and 980 °C.

The chemical composition of the solid phase of some samples from section S7, S12, S19 and S31 is shown in [Table XV](#), [Table XVI](#), [Table XVII](#) and [Table XVIII](#), respectively. The chemical composition of the untreated FEBEX sample is also indicated in the tables under the reference "FEBEX". The most significant changes observed in all the sections are the losses of reduced species with respect to the original FEBEX sample. There is a decrease of FeO, and total SO₂, and an increase of Fe₂O₃. A decrease of divalent cations (Ca, Mg, Sr, Ba) with respect to the original FEBEX sample has been observed in all the samples analysed. In section S7 there is also a con-

siderable increase of Al_2O_3 . To illustrate these issues the chemical composition (major elements) of samples from another radius of section S19 and from S31 are plotted in Figure 53 together with the results for the untreated sample. In the samples from external positions (BB19-13, BB19-1) there is an increase of Fe_2O_3 and MgO with respect to samples taken from hotter areas.

The structural formulae of the smectitic phase of samples from section S7 has been calculated from the chemical analysis of the less than $2\ \mu\text{m}$ fraction, and is shown in Table XIX. The structural formula of the untreated FEBEX is also shown. A decrease of exchangeable K is observed in the samples from Grimsel.

4.3.1.4. Aqueous extracts

The soluble salts have been analysed in aqueous extract solutions. Crushed bentonite samples were placed in contact with deionised and degassed water at a solid to liquid ratio of 1:4, shaken end-over-end and allowed to react for 2 days under atmospheric conditions. After phase separation by

centrifugation (30 minutes at 12500 rpm) and filtering, the supernatant solutions were analysed.

It must be pointed out that smectite particles with a size lower than $0.45\ \mu\text{m}$ (colloids) were detected and analysed in the aqueous extract solutions of the samples more hydrated, *i.e.* the samples in contact with the granite. For this reason, an increase of Al, Fe, Ca and K has been measured in the more hydrated samples. Since this increase is an artefact caused by insufficient filtering of the solution, these values have not been plotted in the figures. This effect is not detected in samples with a lower water content.

In Figure 54 the distribution of the soluble salts in section S7 is shown. The concentration of these ions in the untreated FEBEX bentonite is indicated for comparison. The chloride concentration has the original values at a distance between 70 and 90 cm from the gallery axis (25-35 cm from the heater); in the other distances the values are lower than the original chloride inventory. The sulphate increases at a distance between 10-25 cm from the heater and remains constant in the rest of positions. In the mentioned centimetres, there is also an increase of sodium, potassium and calcium. The bicarbonate in-

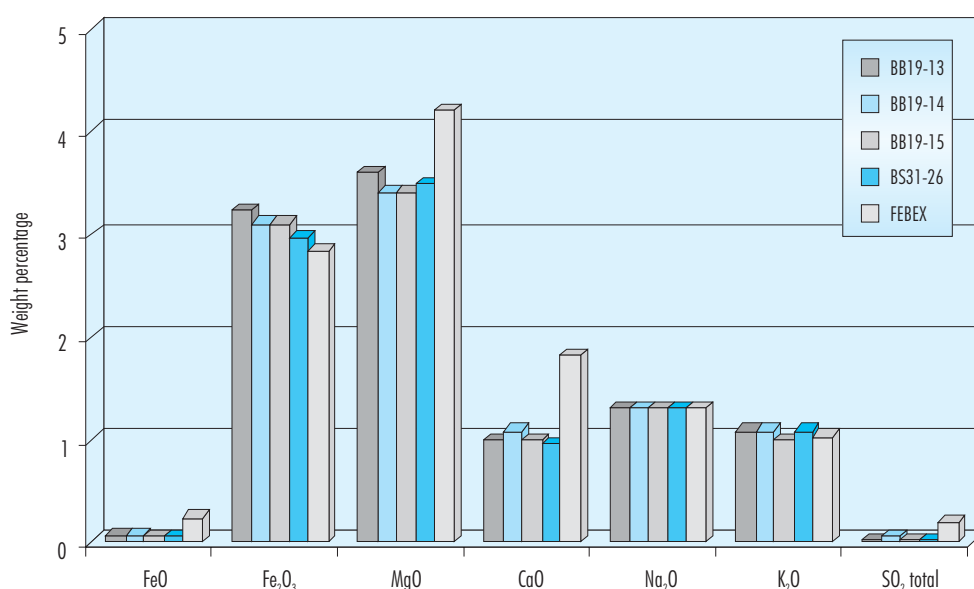


Figure 53: Chemical composition of samples from section S19 and S31 and of the untreated sample.

Table XV
Chemical composition of the solid phase for different samples of section S7.

| | BB7/4-1 | BB7/5 | FEBEX |
|---|---------|--------|--------------|
| Position ¹ (cm) | 103 | 81 | – |
| SiO ₂ (%) | 60.87* | 59.74* | 58.71 ± 1.89 |
| Al ₂ O ₃ (%) | 22.85 | 23.39 | 17.99 ± 0.71 |
| FeO (%) | 0.12 | 0.14 | 0.25 ± 0.09 |
| Fe ₂ O ₃ (%) | 3.01 | 2.84 | 2.85 ± 0.12 |
| MgO (%) | 3.7 | 3.8 | 4.21 ± 0.21 |
| MnO (%) | n.d. | n.d. | 0.03 ± 0.00 |
| CaO (%) | 1.5 | 1.5 | 1.83 ± 0.10 |
| Na ₂ O (%) | 1.4 | 1.4 | 1.31 ± 0.09 |
| K ₂ O (%) | 1.2 | 1.0 | 1.04 ± 0.05 |
| TiO ₂ (%) | 0.16 | 0.14 | 0.23 ± 0.01 |
| P ₂ O ₅ (%) | 0.06 | 0.06 | 0.02 ± 0.01 |
| H ₂ O (130°C) (%) | 13.4 | 13.0 | n.d. |
| H ₂ O (220°C) (%) | 14.6 | 13.8 | 14.1 ± 0.7 |
| Loss at 950°C (%) | 19.7 | 19.8 | 19.5 ± 1.8 |
| CO ₂ total (%) | 0.48 | 0.70 | 0.61 ± 0.05 |
| CO ₂ organic (%) | 0.26 | 0.51 | 0.35 ± 0.05 |
| CO ₂ inorganic (%) | 0.22 | 0.18 | 0.26 ± 0.06 |
| SO ₂ total (%) | 0.12 | 0.16 | 0.21 ± 0.10 |
| H ₂ O ⁺ (220-950°C) (%) | 4.5 | 5.1 | 4.31 ± 0.41 |
| Ba (ppm) | 116 | 78 | 164 ± 25 |
| Sr (ppm) | 145 | 138 | 220 ± 23 |

¹Distance to gallery axis; *:Calculated to obtain a sum of oxides of 100%.

creases with respect to the content in the original FEBEX in the most internal block.

The distribution of the soluble salts in section S12 is shown in [Figure 55](#). There is a lixiviation of chloride and sodium in the bentonite block closer to the gallery wall, increasing the concentrations of these ions in the second and third blocks of the same radius, above their initial inventories. The maximum values

are located in the middle part of the bentonite barrier radius. With respect to sulphates, there is also a leaching in the most hydrated zones but sulphate moves slower than chloride and the maximum value is located at ~14 cm from the rock. There is an increase of bicarbonate in the external part of the radius, probably due to the dissolution of calcite in the more hydrated zones. In the inner samples the bicarbonate concentration is more or less constant.

Table XVI
Chemical composition of the solid phase of samples from section S12.

| | Oxides (%) | | | | Element (ppm) | | | | |
|--|------------|---------|---------|------------|---------------|---------|---------|-------|--------|
| | BB12-10 | BB12-11 | BB12-12 | FEBEX | BB12-10 | BB12-11 | BB12-12 | FEBEX | |
| Position ¹ | 103 | 81 | 59 | | 103 | 81 | 59 | | |
| SiO ₂ | 66.37* | 66.19* | 65.23* | 58.71±1.89 | Ba | 86 | 95 | 115 | 164±25 |
| Al ₂ O ₃ | 17.38 | 17.38 | 18.31 | 17.99±0.71 | Sr | 165 | 155 | 123 | 220±23 |
| FeO | 0.08 | 0.10 | 0.08 | 0.25±0.09 | Ce | 43 | 48 | 50 | 74±5 |
| Fe ₂ O ₃ | 3.30 | 3.32 | 3.29 | 2.85±0.12 | Co | 9.2 | 9.7 | 9.4 | 9±3 |
| MgO | 3.5 | 3.6 | 3.4 | 4.21±0.21 | Cr | 9.2 | 8.7 | 14 | 8±2 |
| MnO | 0.04 | 0.04 | 0.05 | 0.03±0.00 | Cu | 12 | 13 | 11 | 25±9 |
| CaO | 0.90 | 0.92 | 1.10 | 1.83±0.10 | La | 19 | 22 | 23 | 40±3 |
| Na ₂ O | 1.2 | 1.2 | 1.4 | 1.31±0.09 | Mo | <5 | <5 | <5 | n.d. |
| K ₂ O | 1.0 | 1.0 | 1.1 | 1.04±0.05 | Ni | 16 | 17 | 15 | 20±3 |
| TiO ₂ | 0.22 | 0.24 | 0.24 | 0.23±0.01 | Sn | <10 | <10 | <10 | n.d. |
| P ₂ O ₅ | 0.06 | 0.07 | 0.06 | 0.02±0.01 | V | 9.9 | 11 | 10 | 16±2 |
| H ₂ O (130°C) | 11.70 | 11.70 | 11.30 | n.d. | W | <25 | <25 | <25 | |
| H ₂ O (220°C) | 13.08 | 12.69 | 12.69 | 14.1±0.7 | Y | 13 | 13 | 14 | 25±3 |
| Loss at 950°C | 19.00 | 18.60 | 18.40 | 19.5±1.8 | Zn | 50 | 49 | 45 | 65±4 |
| CO ₂ total | 0.51 | 0.51 | 0.59 | 0.61±0.05 | Cs | 5.9 | 6.0 | 6.9 | n.d. |
| CO ₂ organic | 0.22 | 0.22 | 0.37 | 0.35±0.05 | Se | <0.1 | <0.1 | <0.1 | n.d. |
| CO ₂ inorganic | 0.29 | 0.29 | 0.22 | 0.26±0.06 | Li | 51.0 | 50.0 | 47.0 | n.d. |
| SO ₂ total | 0.08 | 0.08 | 0.08 | 0.21±0.10 | | | | | |
| H ₂ O ⁺ (220-950°C) | 5.33 | 5.32 | 5.04 | 4.31±0.41 | | | | | |

¹Distance to gallery axis; *:Calculated to obtain a sum of oxides of 100%.

In [Figure 56](#) the distribution of the soluble salts in section S19 is shown. The concentration of these ions in the FEBEX bentonite without treatment is indicated for comparison. Clearly, there is an increase of chloride content towards the heater, with a maximum value located at 18-19 cm of the heater contact. The sodium is the counterion following the chloride movement. The sulphate movement seems not to be so well defined, although a decrease of concentra-

tion is observed in the most external zones. The bicarbonate concentration increases in the most hydrated zones.

The distribution of the soluble salts in section S28 is shown [Figure 57](#). There is an increase of chloride content towards the heater as well as of sulphate. However, the chloride ions move faster than sulphate. The counterion associated to chloride is so-

Table XVII
Chemical composition of the solid phase of samples from section S19.

| | Oxides (%) | | | | Element (ppm) | | | | |
|--|------------|--------|--------|------------|---------------|--------|--------|-------|----------|
| | BB19-1 | BB19-2 | BB19-3 | FEBEX | BB19-1 | BB19-2 | BB19-3 | FEBEX | |
| Position ¹ | 103 | 81 | 59 | | 103 | 81 | 59 | | |
| SiO ₂ | 58.69 | 59.16 | 58.89 | 58.71±1.89 | Ba | 138 | 177 | 221 | 164 ± 25 |
| Al ₂ O ₃ | 17.47 | 16.68 | 16.52 | 17.99±0.71 | Sr | 154 | 163 | 160 | 220 ± 23 |
| FeO | 0.08 | 0.08 | 0.06 | 0.25±0.09 | Ce | 58 | 55 | 50 | 74 ± 5 |
| Fe ₂ O ₃ | 3.08 | 2.95 | 2.98 | 2.85±0.12 | Co | 11 | 11 | 10 | 9 ± 3 |
| MgO | 3.6 | 3.4 | 3.4 | 4.21±0.21 | Cr | 6.9 | 7.2 | 5.6 | 8 ± 2 |
| MnO | 0.03 | 0.03 | 0.03 | 0.03±0.00 | Cu | 12 | 12 | 12 | 25 ± 9 |
| CaO | 1.0 | 1.1 | 1.0 | 1.83±0.10 | La | 21 | 17 | 16 | 40 ± 3 |
| Na ₂ O | 1.3 | 1.3 | 1.3 | 1.31±0.09 | Mo | <5 | <5 | <5 | |
| K ₂ O | 1.10 | 1.10 | 0.99 | 1.04±0.05 | Ni | 16 | 16 | 9 | 20 ± 3 |
| TiO ₂ | 0.24 | 0.24 | 0.23 | 0.23±0.01 | Sn | <10 | <10 | <10 | |
| P ₂ O ₅ | 0.06 | 0.06 | 0.06 | 0.02±0.01 | V | 10 | 11 | 9 | 16 ± 2 |
| H ₂ O (130°C) | 8.2 | 10.6 | 11.7 | n.d. | W | <25 | <25 | <25 | |
| H ₂ O (220°C) | 9.2 | 11.92 | 13.08 | 14.1±0.7 | Y | 13 | 11 | 10 | 25 ± 3 |
| Loss at 950°C | 14.4 | 16.8 | 18.0 | 19.5±1.8 | Zn | 49 | 49 | 47 | 65 ± 4 |
| CO ₂ total | 0.48 | 0.55 | 0.48 | 0.61±0.05 | Cs | 6.0 | 6.1 | 5.5 | |
| CO ₂ organic | 0.22 | 0.26 | 0.26 | 0.35±0.05 | Eu | 2.0 | 2.2 | 1.7 | |
| CO ₂ inorganic | 0.26 | 0.29 | 0.22 | 0.26±0.06 | Se | <0.1 | <0.1 | <0.1 | |
| SO ₂ total | 0.04 | 0.06 | 0.04 | 0.21±0.10 | Li | <2 | <2 | <2 | |
| H ₂ O ⁺ (220-950°C) | 4.7 | 4.3 | 4.4 | 4.31±0.41 | | | | | |

¹Distance to gallery axis.

dium. In the most hydrated zone, *i.e.* bentonite in contact with granite, there is a strong dissolution of calcite-dolomite, evidenced by the high content of bicarbonate.

The content of soluble salts in a sample from section S31 taken at the contact with the back lid of the heater is shown [Figure 58](#). There is an increase of chloride content towards the heater, with a maxi-

mum at the heater contact zone. Also, there is a maximum in the sulphate concentration very close to the heater, but not at the contact zone.

The distribution of soluble salts along one radius of each section analysed is shown in [Figure 59](#). The hydration of bentonite at the external blocks in contact with the granite produces the dissolution and dilution of the more soluble trace minerals in the ben-

Table XVIII
Chemical composition of the solid phase of sample BS31-26.

| Oxides (%) | BB31-26 | FEBEX | Element (ppm) | BB31-26 | FEBEX |
|---|---------|--------------|---------------|---------|----------|
| SiO ₂ | 59.97 | 58.71 ± 1.89 | Ba | 253 | 164 ± 25 |
| Al ₂ O ₃ | 16.74 | 17.99 ± 0.71 | Sr | 164 | 220 ± 23 |
| FeO | 0.07 | 0.25 ± 0.09 | Ce | 58 | 74 ± 5 |
| Fe ₂ O ₃ | 2.97 | 2.85 ± 0.12 | Co | 10 | 9 ± 3 |
| MgO | 3.5 | 4.21 ± 0.21 | Cr | 5.5 | 8 ± 2 |
| MnO | <0.03 | 0.03 ± 0.00 | Cu | 12 | 25 ± 9 |
| CaO | 0.96 | 1.83 ± 0.10 | La | 27 | 40 ± 3 |
| Na ₂ O | 1.3 | 1.31 ± 0.09 | Mo | <5 | |
| K ₂ O | 1.1 | 1.04 ± 0.05 | Ni | 15 | 20 ± 3 |
| TiO ₂ | 0.22 | 0.23 ± 0.01 | Sn | <10 | |
| P ₂ O ₅ | 0.06 | 0.02 ± 0.01 | V | 10 | 16 ± 2 |
| H ₂ O (130°C) | 9.1 | n.d. | W | <25 | |
| H ₂ O (220°C) | 10.5 | 14.1 ± 0.7 | Y | 15 | 25 ± 3 |
| Loss at 950°C | 15.5 | 19.5 ± 1.8 | Zn | 50 | 65 ± 4 |
| CO ₂ Total | 0.44 | 0.61 ± 0.05 | Cs | 6.3 | |
| CO ₂ organic | 0.22 | 0.35 ± 0.05 | Eu | 2.1 | |
| CO ₂ inorganic | 0.22 | 0.26 ± 0.06 | Se | <0.1 | |
| SO ₂ Total | 0.04 | 0.21 ± 0.10 | Li | <2 | |
| H ₂ O ⁺ (220-950°C) | 4.50 | 4.31 ± 0.41 | | | |

tonite (sulphates, carbonates and chlorides). As a result, saline fronts are generated due to the different mobility of the dissolved ions. Chloride moves as a conservative anion. The movement of sulphates and bicarbonates must be basically regulated by gypsum and calcite equilibrium, respectively (Fernández *et al.* 2001, Fernández 2003).

The main counterion that follows chloride movement is sodium. Sodium moves with the same tendency than chloride. However, the implication of sodium in exchange reactions modifies the relative concentration of both ions, and there is an excess of sodium content with respect to chloride. As the hydration front progresses, the dissolution of car-

Table XIX
Structural formula of the smectite (<2 μm fraction) for different samples of section S7.

| Sample | IV Charge | VI Charge | Interl. Charge | Structural formula |
|---------|-----------|-----------|----------------|--|
| FEBEX | -0.34 | 0.67 | 1.00 | $(\text{Si}_{7.66} \text{Al}_{0.34})^{\text{IV}} (\text{Al}_{2.76} \text{Fe}^{3+}_{0.33} \text{Mg}_{1.03})^{\text{VI}} \text{O}_{20}(\text{OH})_4 (\text{Ca}_{0.12} \text{Mg}_{0.13} \text{Na}_{0.25} \text{K}_{0.25})$ |
| BB7/4-1 | -0.18 | -0.76 | 0.93 | $(\text{Si}_{7.82} \text{Al}_{0.18})^{\text{IV}} (\text{Al}_{2.93} \text{Fe}^{3+}_{0.29} \text{Fe}^{2+}_{0.01} \text{Mg}_{0.76} \text{Ti}_{0.01})^{\text{VI}} \text{O}_{20}(\text{OH})_4 (\text{Ca}_{0.14} \text{Mg}_{0.14} \text{Na}_{0.23} \text{K}_{0.13})$ |
| BB7/5 | -0.08 | -0.77 | 0.85 | $(\text{Si}_{7.92} \text{Al}_{0.08})^{\text{IV}} (\text{Al}_{2.93} \text{Fe}^{3+}_{0.28} \text{Fe}^{2+}_{0.01} \text{Mg}_{0.78} \text{Ti}_{0.01})^{\text{VI}} \text{O}_{20}(\text{OH})_4 (\text{Ca}_{0.12} \text{Mg}_{0.12} \text{Na}_{0.23} \text{K}_{0.13})$ |

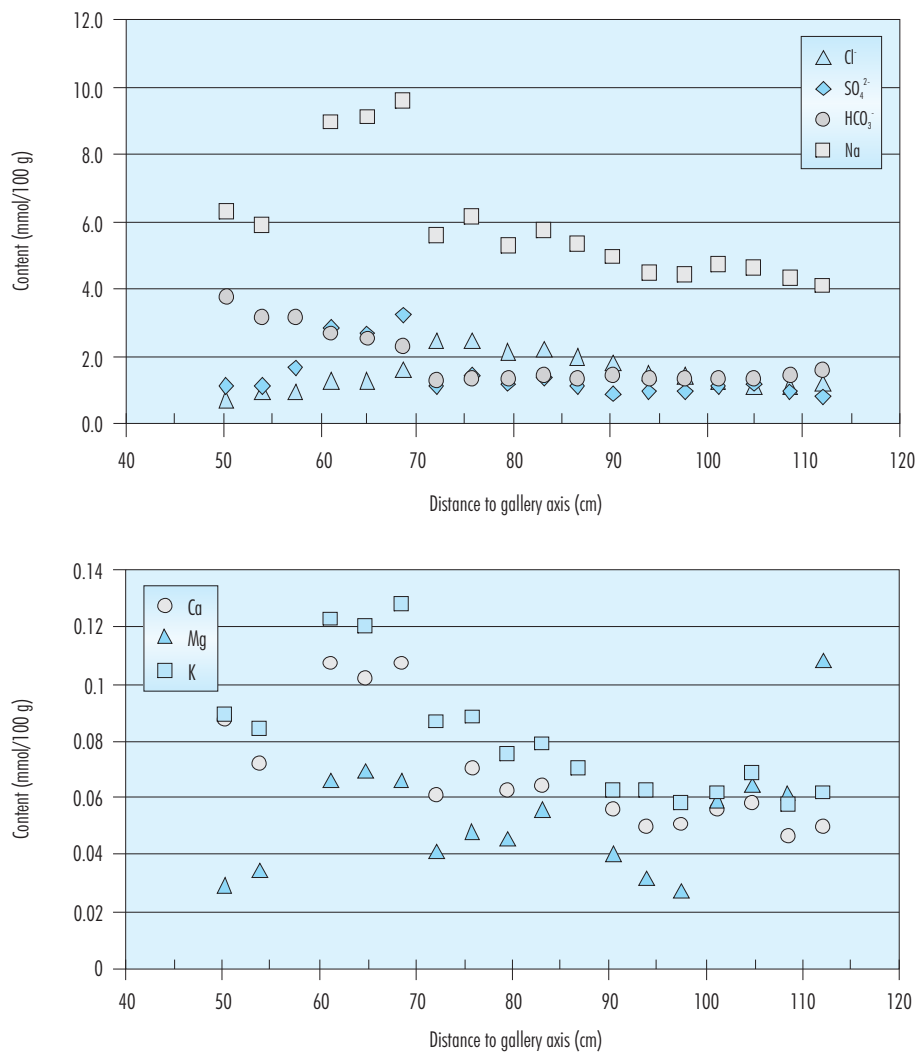


Figure 54: Distribution of soluble salts in section S7 (Ion content at 1:4 solid to liquid ratio in FEBEX sample (mmol/100g): Cl: 2.185 ±0.396, SO₄²⁻: 1.026 ±0.068, Na: 5.017, Ca: 0.050, Mg: 0.055, K: 0.073, HCO₃⁻: 1.184).

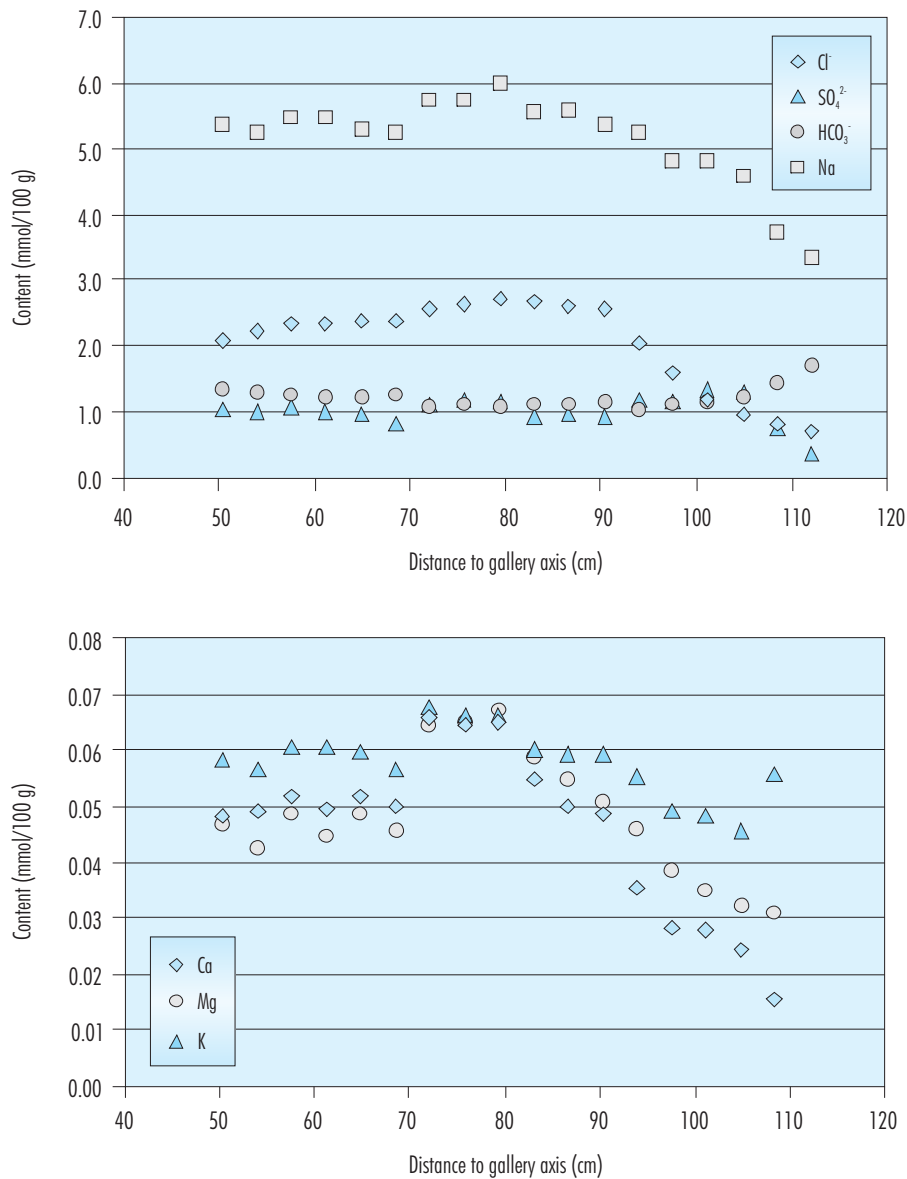


Figure 55: Distribution of soluble salts in section S12 (Ion content at 1:4 solid to liquid ratio in FEBEX sample (mmol/100g): Cl: 2.185 ± 0.396 , SO_4^{2-} : 1.026 ± 0.068 , Na: 5.017, Ca: 0.050, Mg: 0.055, K: 0.073, HCO_3^- : 1.184).

bonates and sulphates produces the liberation of calcium. Consequently, the exchange of sodium by calcium in the exchange positions must be induced, changing the relative concentration of the sodium, bicarbonate and pH in the aqueous extracts solution. The other major cations, calcium and magnesium, show a parallel increase, but their concentrations are at least 5-10 times lower than sodium.

These results are similar to those obtained in tests at intermediate scale (Cuevas *et al.* 1997, ENRESA 2000).

On the other hand, the salt movement seems to be faster in the heater sections (S19 and S28) than in the zone without heater (S12 and S7). The highest salt contents have been found in section S28, then

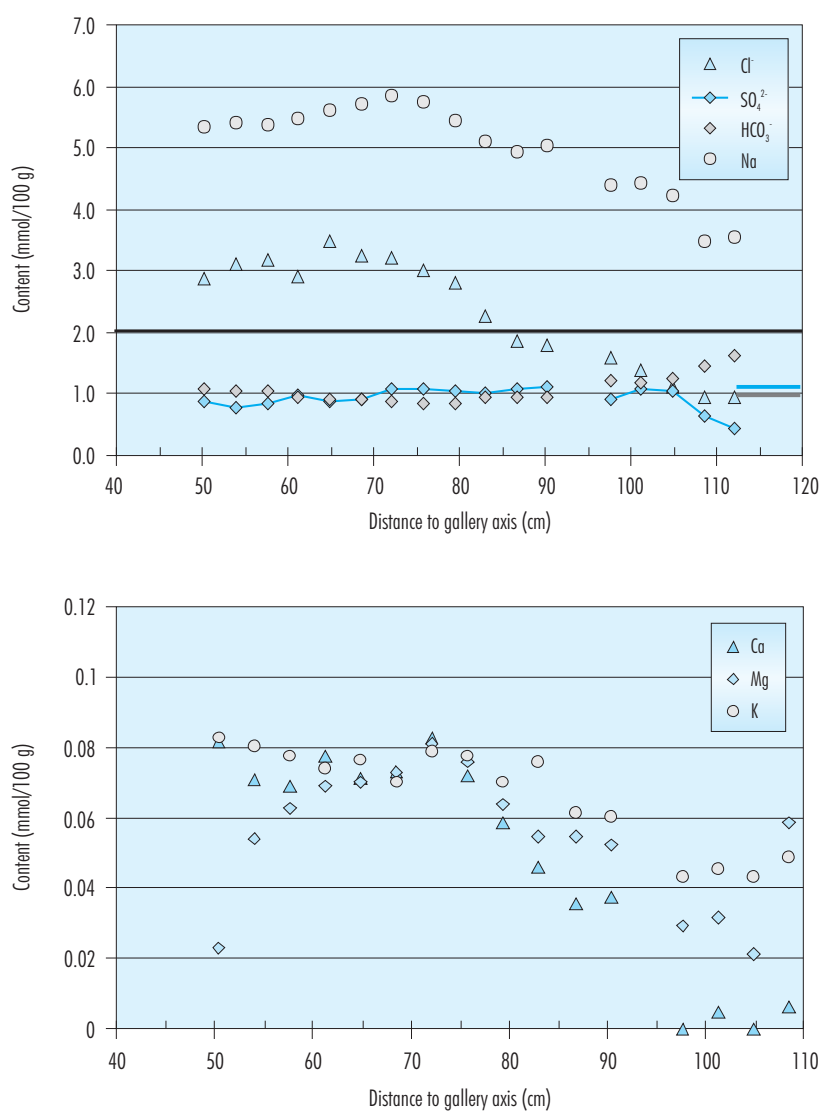


Figure 56: Distribution of soluble salts in section S19 (Ion content at 1:4 solid to liquid ratio in FEBEX sample (mmol/100g): Cl: 2.185 \pm 0.396, SO₄²⁻: 1.026 \pm 0.068, Na: 5.017, Ca: 0.050, Mg: 0.055, K: 0.073, HCO₃⁻: 1.184).

in section S19 and finally in section S12 (without heater). The section 28 has the influence of the two heaters.

4.3.1.5. Exchangeable cations

In order to determine the exchangeable cations, a CsNO₃ solution was used (Sawhney 1970). Caesium acts as a high selective cation to displace all exchangeable cations from the montmorillonite if its concentration is sufficiently high. Bentonite samples

were equilibrated with CsNO₃ 0.5M at a solid to liquid ratio of 0.25 kg/L in a glove box. Samples were shaken end-over-end for 2 days. After phase separation by centrifugation, the supernatant solutions were filtered by 0.45 μ m and analysed.

The concentration of cations in exchange positions along a radius of section S7 is shown in Figure 60. There is a noticeable increase of Ca, Na and K and a decrease of Mg in exchange positions in all the samples analysed. The increase is particularly im-

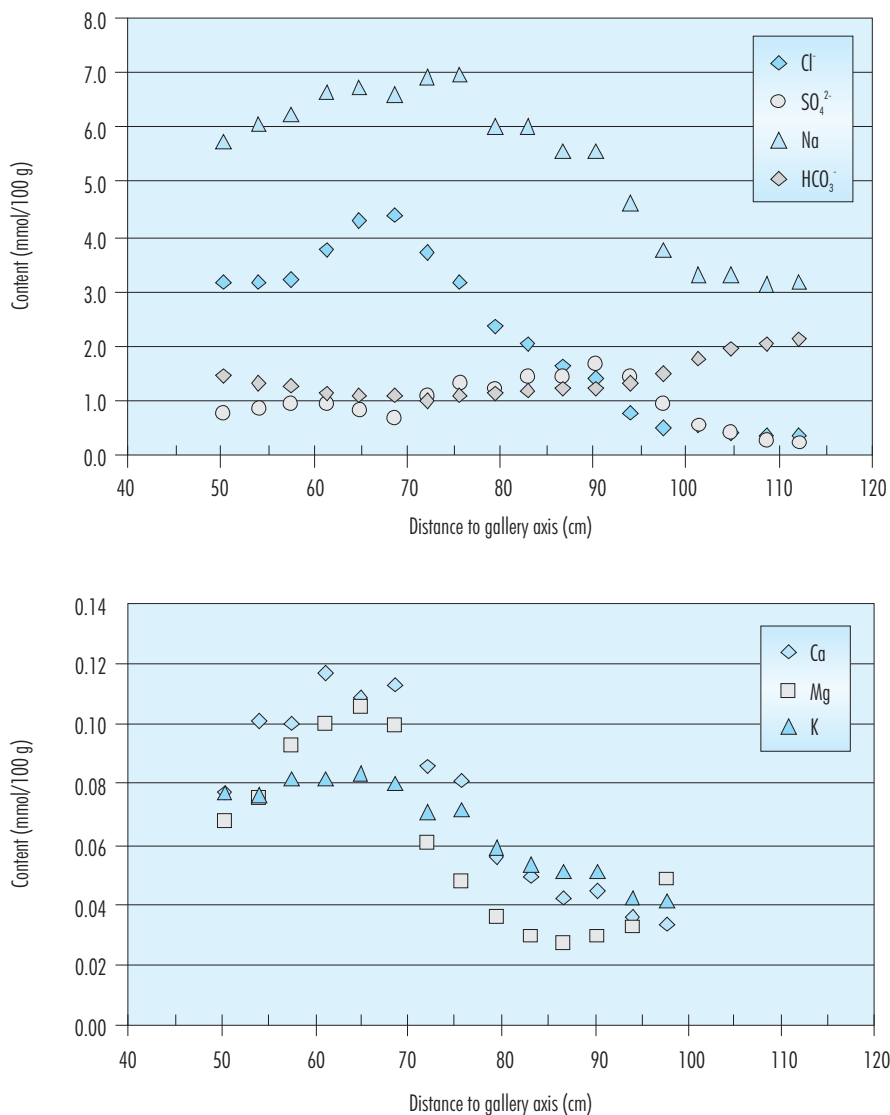


Figure 57: Distribution of soluble salts in section S28 (Ion content at 1:4 solid to liquid ratio in FEBEX sample (mmol/100g): Cl: 2.185 ± 0.396 , SO_4^{2-} : 1.026 ± 0.068 , Na: 5.017, Ca: 0.050, Mg: 0.055, K: 0.073, HCO_3^- : 1.184).

portant towards the central part of the barrier, where it is accompanied by a significant decrease in Mg occupation. The sum of exchangeable cations remains approximately constant in all the samples from section S7 and in the order of 102 meq/100g, i.e. higher than that for untreated FEBEX bentonite (96 meq/100g, Table VI).

The concentration of cations in exchange positions along different radii of section S12 is shown in Fig-

ure 61. There is a clear increase with respect to the untreated clay of potassium and calcium in all the samples, this increase being sharper towards the granite in the case of potassium. The other cations display different distribution patterns depending on the radius considered. It is particularly noticeable the high content of magnesium (over 40 meq/100g) in the external blocks BB12-10 and 11, that has not been found in analogous positions in the other radii. Since there are no differences among these radii

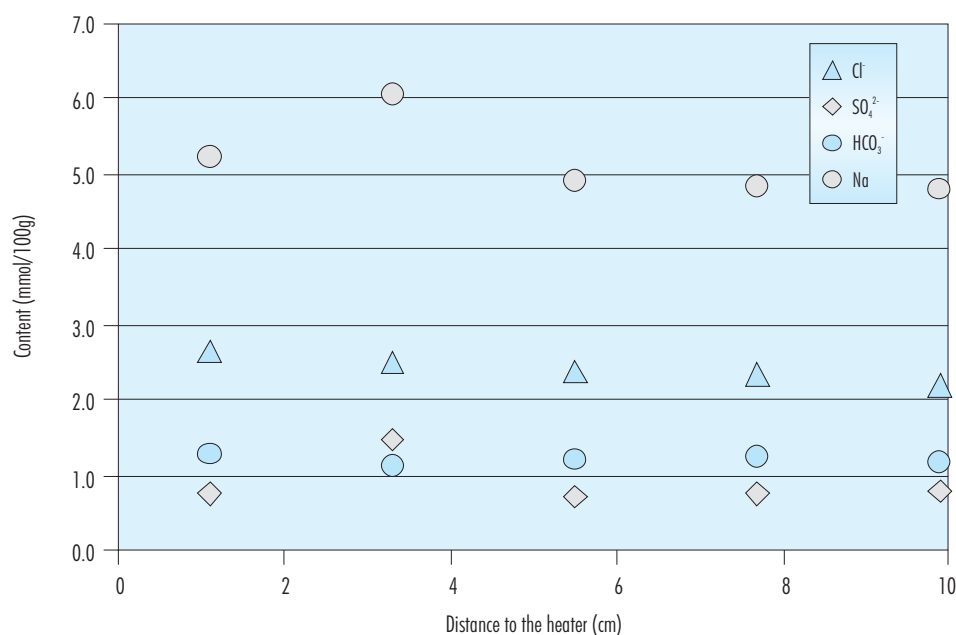


Figure 58: Distribution of soluble salts in sample BS31-22 (the distances indicated refer to the back lid of the heater) (Ion content at 1:4 solid to liquid ratio in FEBEX sample (mmol/100g): Cl: 2.185 ± 0.396 , SO_4^{2-} : 26 ± 0.068 , Na: 5.017, Ca: 0.050, Mg: 0.055, K: 0.073, HCO_3^- : 1.184).

in the temperature experienced during operation or in the water content reached at the end of the experiment, it is considered that most of the variations observed in the exchange complex are due to analytical uncertainties and to the natural heterogeneity of the bentonite. The sum of exchangeable cations remains approximately constant in all the samples and in the order of 105 meq/100g, i.e. higher than that of the untreated FEBEX bentonite (96 meq/100g).

The concentration of cations in exchange positions along a radius of section S19 (blocks BB19-13, BB19-14 and BB19-15) is shown in Figure 62. There is an increase of calcium and potassium with respect to the reference bentonite in all the samples, more important in the external block, where the sodium content is also higher. As well, the occupation of magnesium seems to increase towards the gallery wall. Accordingly, the sum of exchangeable cations is higher than 115 meq/100g in the block in contact with the granite.

The concentration of cations in exchange positions along a radius of section S28 (blocks BB28-1,

BB28-2 and BB28-3) is shown in Figure 63. There is an overall increase with respect to the untreated bentonite of exchangeable calcium and potassium, sharper in the external and internal blocks. The occupation of sodium increases towards the gallery wall while that of magnesium decreases towards the internal part of the barrier, especially in its middle part. The highest concentration of calcium is found in the closeness to the heater. The sum of exchangeable cations along a radius is shown in Figure 64.

The concentration of cations in exchange positions along the sample BS31-22 is shown in Figure 65. The results are plotted as a function of the distance to the back lid of the heater. Overall, there is an increase of calcium and potassium in these samples with respect to the original sample.

In Figure 66 the exchangeable cations results obtained for the different sections are compared (except section S7). There is an important increment of potassium in exchange position with respect to the initial value, more stressed in the external and internal blocks. An increase of sodium and magnesium is observed in the samples closer to the gallery wall.

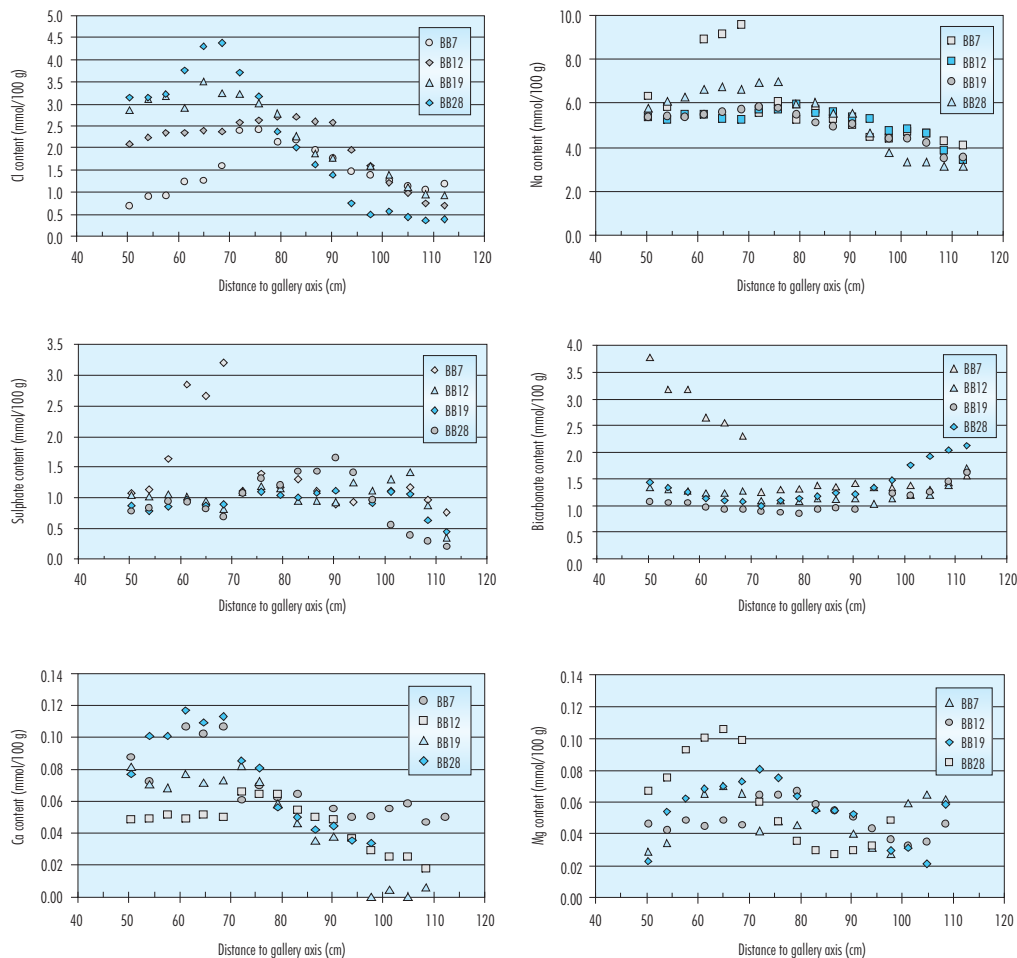


Figure 59: Distribution of soluble salts in the different sections (Ion content at 1:4 solid to liquid ratio in FEBEX sample (mmol/100g): Cl: 2.185 ± 0.396 , SO_4^{2-} : 1.026 ± 0.068 , Na: 5.017, Ca: 0.050, Mg: 0.055, K: 0.073, HCO_3^- : 1.184).

In the case of calcium, there is also an overall increase in its content, especially at the heater contact and at the bentonite-granite contact. Therefore, different processes –linked to hydration and to the high temperature– could be responsible of this increment. An increase of the sum of exchangeable cations has been detected in most of the samples analysed.

4.3.1.6. Squeezing tests

Several blocks taken from different sampling sections have been squeezed to obtain the pore water. The squeezing process involves the expulsion of interstitial fluid from the saturated argillaceous mate-

rial being compressed (Entwisle & Reeder 1993, Pearson *et al.* 2003).

In squeezing experiments, the volume of water extracted depends basically on the water content of the rock sample, the rock properties (e.g. dry density, the relative contents of easily-squeezed clays and of stiffer materials like quartz and calcite), the squeezing pressure applied, the squeezing time and the size of the squeezing apparatus (volume and diameter).

The squeezing rig at CIEMAT is similar to that developed by Peters *et al.* (1992) and Entwisle and Reeder (1993). The squeezer has been designed to allow a one-dimensional compression of the sample (Cuevas

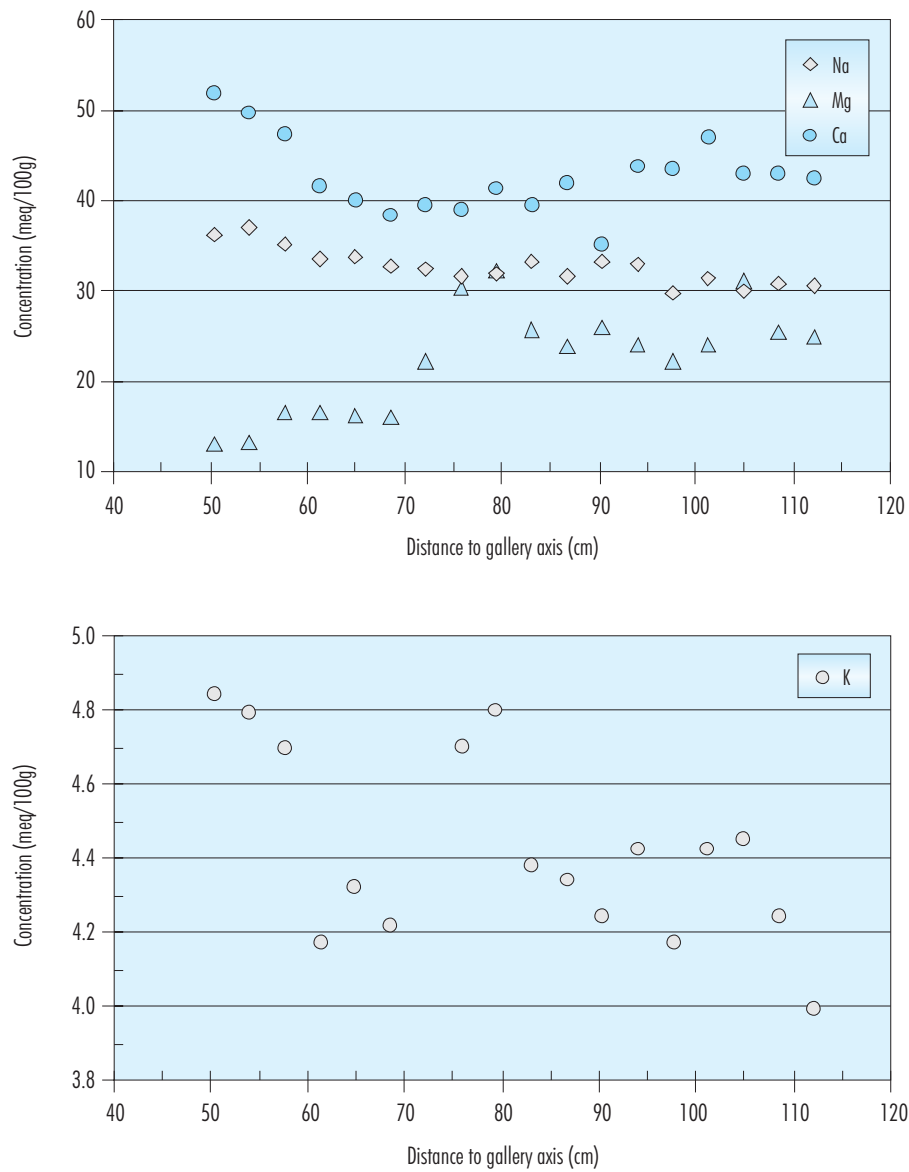


Figure 60: Distribution of exchangeable cations in samples taken along a radius of section S7 (Original sample (meq/100g): Na: 27, Ca: 35, Mg: 31, K: 2.6).

et al. 1997, Fernández et al. 2001, 2003) by means of an automatic hydraulic ram operating downwards with squeezed water expelled into polypropylene syringes at both top and bottom of the cell (Figure 67). The compaction chamber is made of AISI 329 stainless steel (for its high tensile strength and resistance to corrosion) with an internal diameter of 70 mm. The whole system is under ambient conditions (lab

temperature of about 25°C) and not under anoxic atmosphere, although at the beginning of the test the system is flushed with nitrogen gas.

The samples for squeezing were fragmented to lumps fitted to the squeezing cell size or small pieces of about 25-200 grams. The applied stress was increased progressively up to the selected pres-

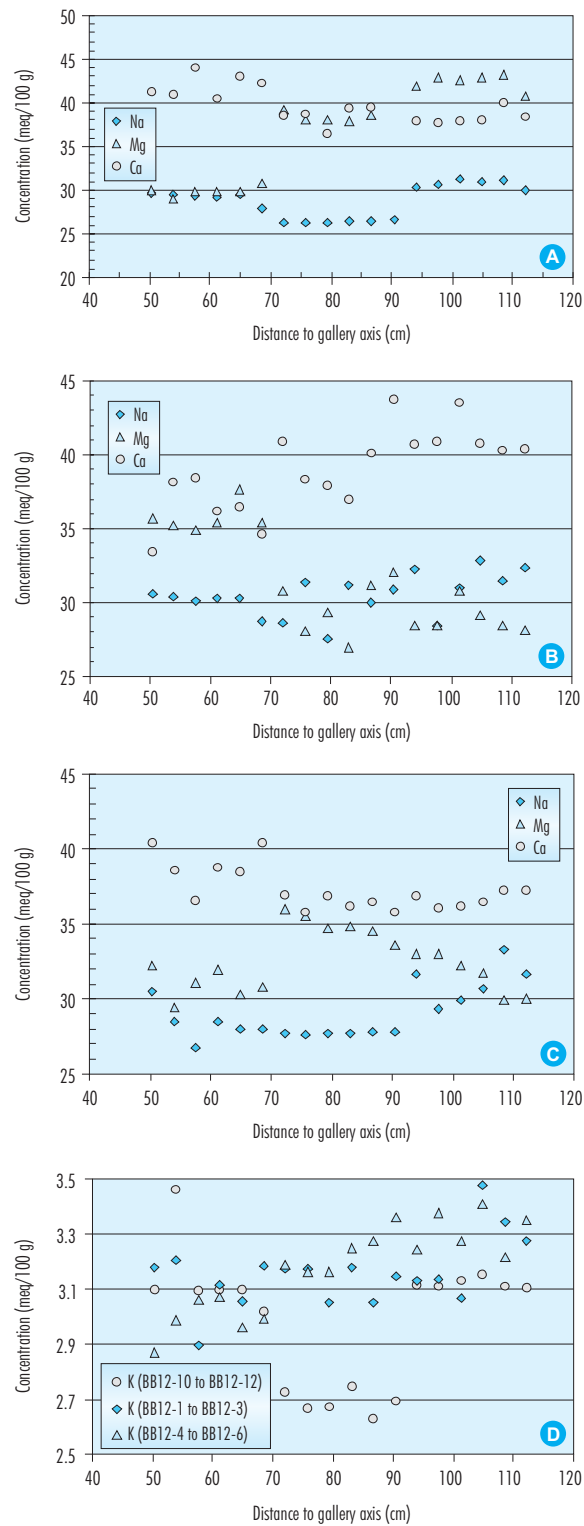


Figure 61: Distribution of exchangeable cations in samples taken along different radii of section S12 (A: BB12-10 to 12, B: BB12-1 to 3, C: BB12-4 to 6, D: potassium) (Original sample (meq/100g): Na: 27, Ca: 35, Mg: 31, K: 2.6).

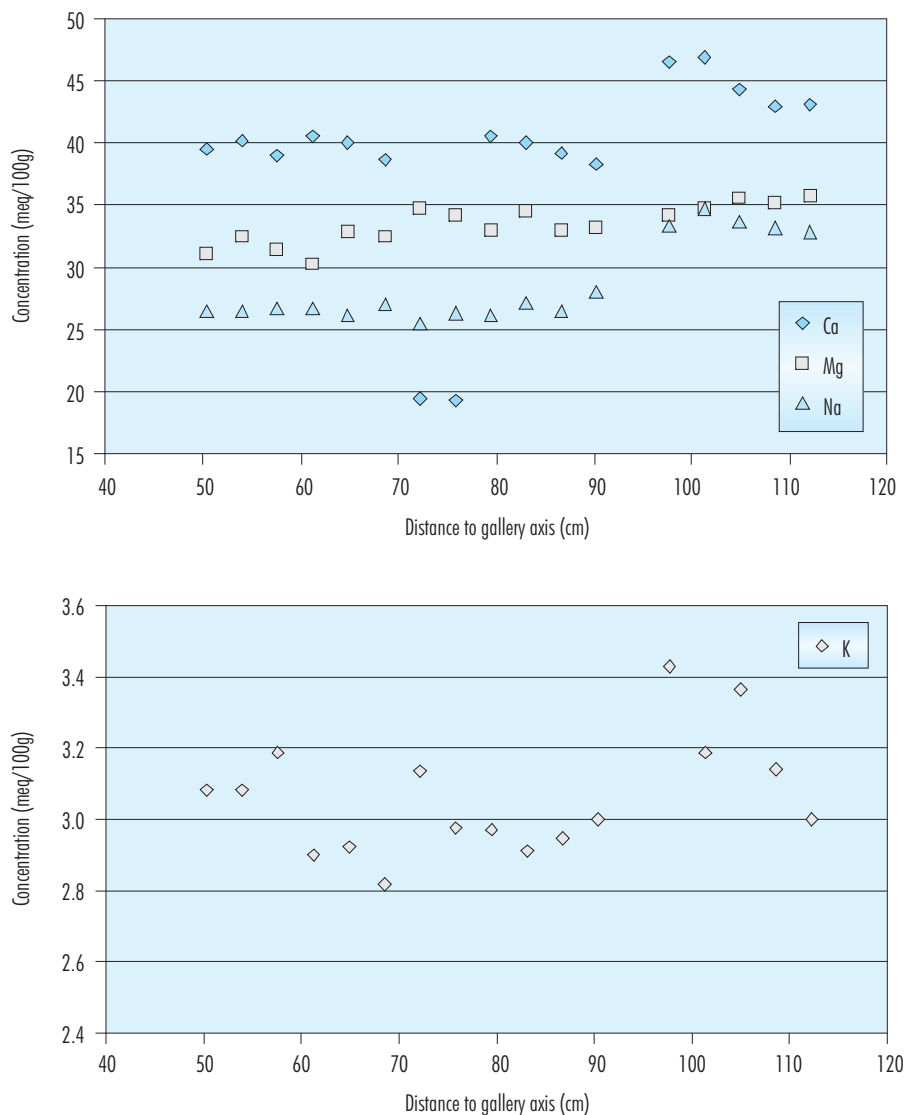


Figure 62: Distribution of exchangeable cations in samples taken along a radius of section S19 (Original sample (meq/100g): Na: 27, Ca: 35, Mg: 31, K: 2.6).

sure. As low as possible squeezing pressures have been used to avoid ultrafiltration and ionic fractionation phenomena. When the maximum of squeezed water has been obtained, the syringe is removed, avoiding any sample contact with the atmosphere. The sample collected (5-10 mL) is weighed, filtered and stored in a refrigerator at 4°C until it is analysed, in order to prevent any possible alterations.

The squeezing technique can be applied to obtain pore water in samples with a water content greater

than 18 percent with squeezing pressures below 60 MPa.

The details and characteristics of every squeezing tests performed with samples from Grimsel can be found in Fernández & Rivas (2004). The chemical composition of the water obtained from samples of sections S7, S12 and S19 is shown in Table XX, Table XXI and Table XXII, respectively.

The pressure applied to obtain the pore water varies as a function of the water content. A pressure of 25

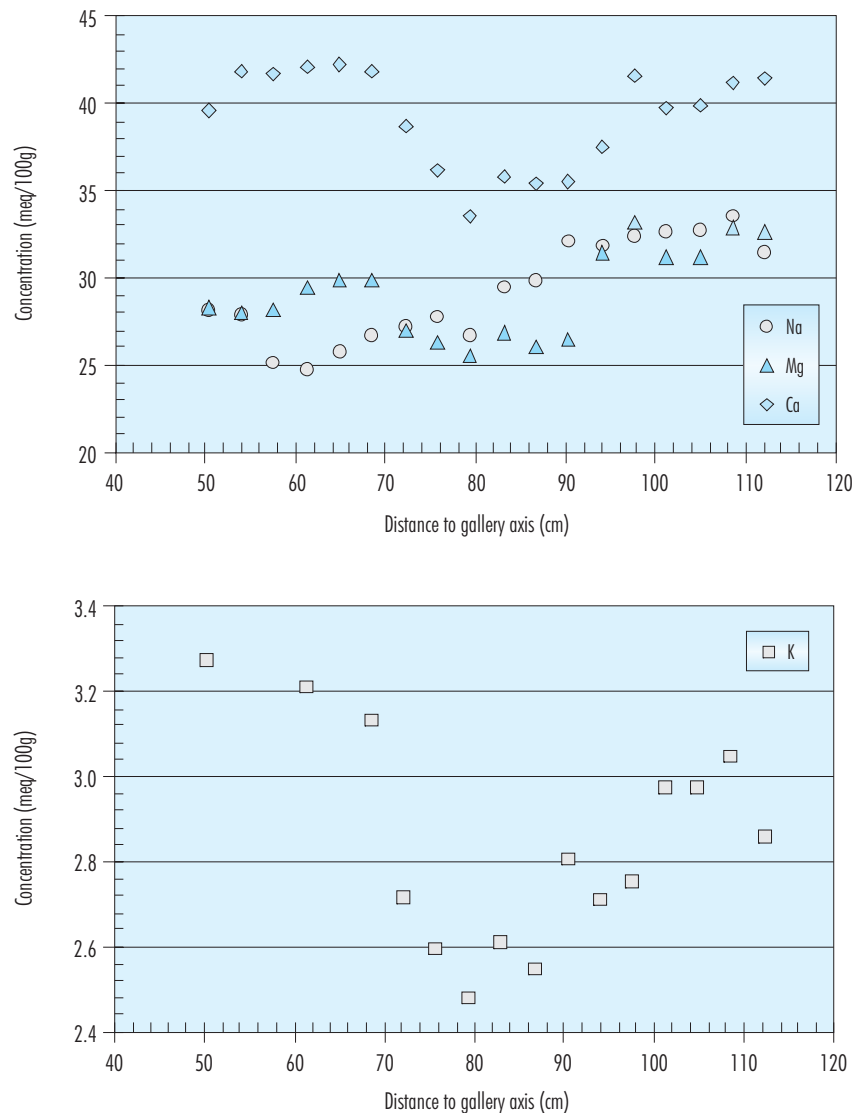


Figure 63: Distribution of exchangeable cations in samples taken along a radius of section S28 (Original sample (meq/100g): Na: 27, Ca: 35, Mg: 31, K: 2.6).

MPa is enough for samples with an initial water content higher than 22-23 percent. However, if the water content is lower than these values, a pressure of 70 MPa must be applied. The water content of the block in contact with the heater in section S19 (BB19-3) was not enough to perform the squeezing test.

Regarding the chemical composition of the pore water extracted by squeezing, the distribution of solutes follows the same tendency observed in the

aqueous extracts (Figure 68 and Figure 69), i.e. the saline front detected in the soluble salt distribution is also observed in the squeezing experiments. There is an increase of the soluble ions concentration towards the inner part of the bentonite barrier, related to the evolution of the hydration front. There is an intense mobilisation of ions towards the most internal part of the bentonite barrier in sections S7 and S12. However, it is expected that the content of ions in the *true* pore water be higher, since this extraction

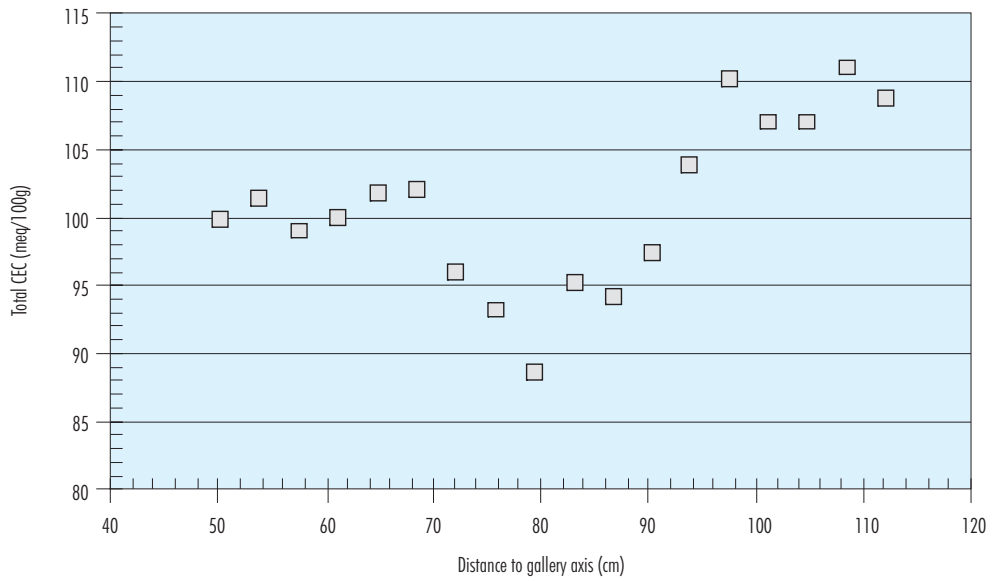


Figure 64: Sum of exchangeable cations in samples taken along a radius of section S28.

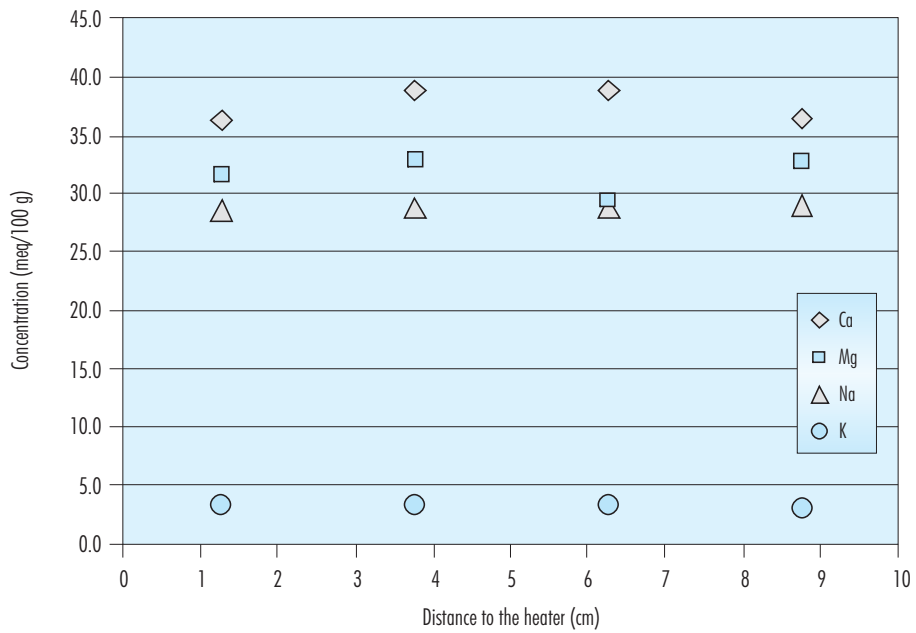


Figure 65. Distribution of exchangeable cations in sample BS31-22 (Original sample (meq/100g): Na: 27, Ca: 35, Mg: 31, K: 2.6).

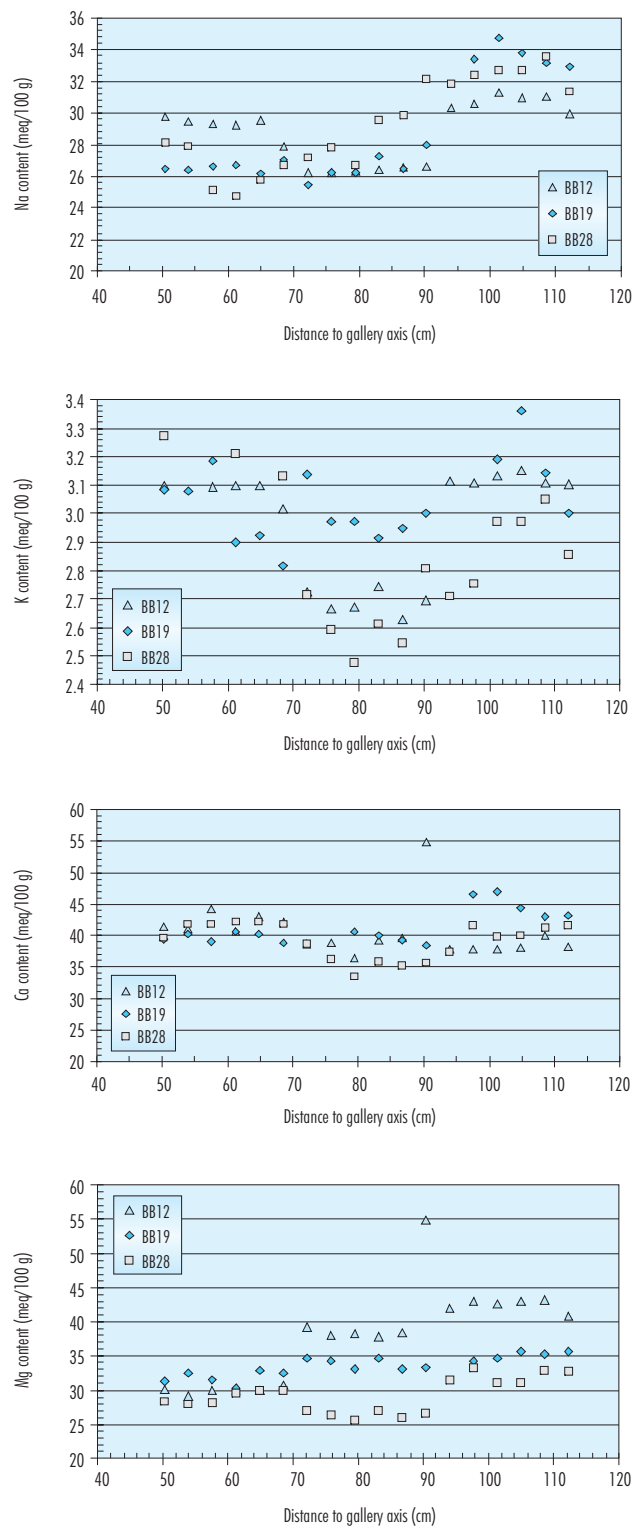


Figure 66: Distribution of exchangeable cations along a radius in different sections of the bentonite barrier (Original sample (meq/100g): Na: 27, Ca: 35, Mg: 31, K: 2.6).

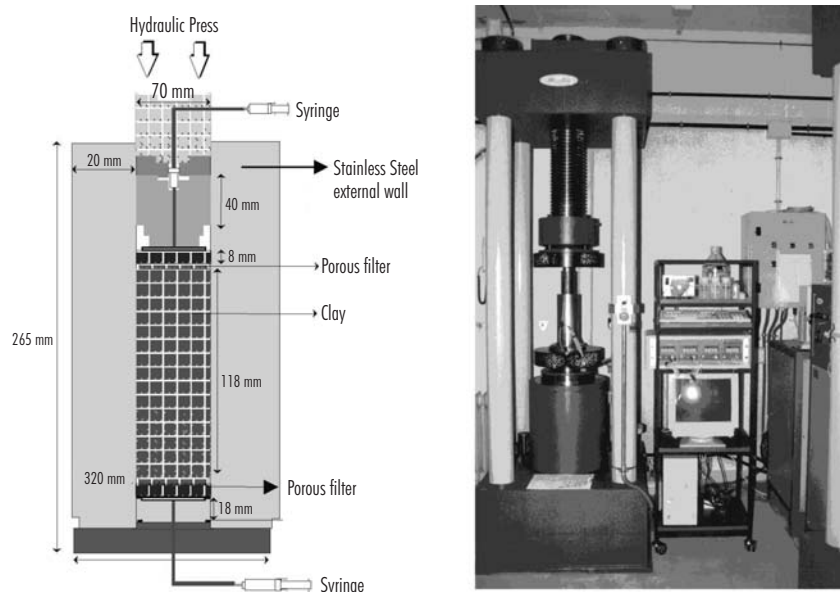


Figure 67. Squeezed water extraction apparatus used at CIEMAT.

Table XX
Chemical composition of the pore water obtained by squeezing in samples from section S7.

| | BB7-4 | BB7-5 |
|---------------------------------------|-------|-------|
| pH | 7.8 | 7.9 |
| Electrical neutrality (%) | 2.62 | 1.04 |
| Ionic strength (M) | 0.10 | 0.26 |
| Na ⁺ (meq/L) | 87.0 | 187.0 |
| K ⁺ (meq/L) | 0.79 | 0.16 |
| Mg ²⁺ (meq/L) | 14.2 | 65.8 |
| Ca ²⁺ (meq/L) | 17.5 | 54.9 |
| Sr ²⁺ (meq/L) | 0.098 | 0.320 |
| Al ³⁺ (meq/L) | | 0.08 |
| Mn ²⁺ (meq/L) | 0.005 | 0.010 |
| Cl ⁻ (meq/L) | 67.7 | 236.9 |
| SO ₄ ²⁻ (meq/L) | 43.7 | 60.4 |
| Br ⁻ (meq/L) | 0.36 | 0.08 |
| NO ₃ ⁻ (meq/L) | 0.07 | 1.31 |
| HCO ₃ ⁻ (meq/L) | 1.98 | 3.31 |

Table XXI
Chemical composition of the pore water obtained by squeezing in samples from section S12.

| | BB12-10 |
|---------------------------------------|---------|
| pH | 7.6 |
| Electrical neutrality (%) | 5.4 |
| Ionic strength (M) | 0.03 |
| Na ⁺ (meq/L) | 33.2 |
| K ⁺ (meq/L) | 0.31 |
| Mg ²⁺ (meq/L) | 4.28 |
| Ca ²⁺ (meq/L) | 4.44 |
| Sr ²⁺ (meq/L) | 0.032 |
| Al ³⁺ (meq/L) | |
| Mn ²⁺ (meq/L) | 0.005 |
| Cl ⁻ (meq/L) | 24.6 |
| SO ₄ ²⁻ (meq/L) | 11.8 |
| Br ⁻ (meq/L) | 0.02 |
| NO ₃ ⁻ (meq/L) | 0.12 |
| HCO ₃ ⁻ (meq/L) | 1.43 |
| SiO ₂ (meq/L) | 0.44 |

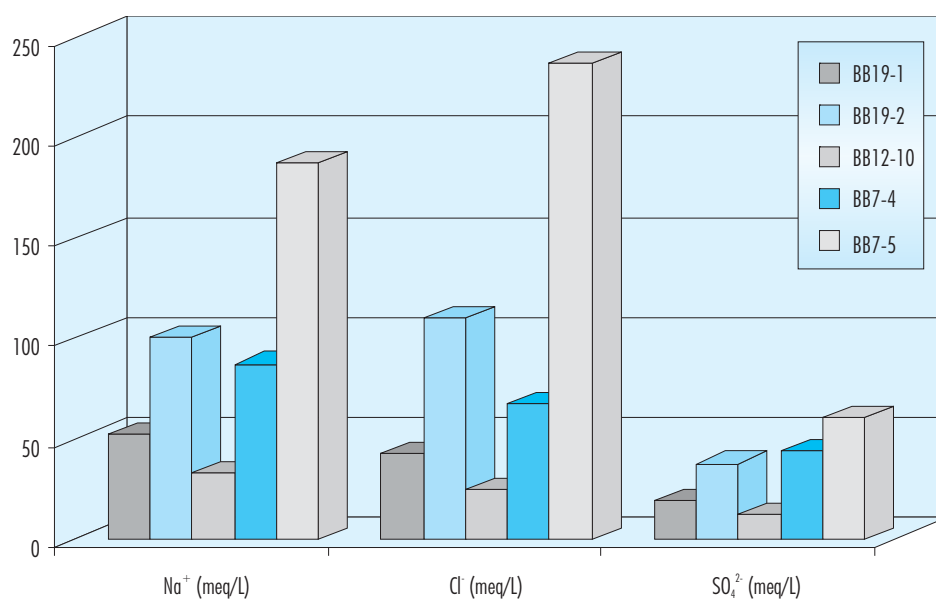


Figure 68. Distribution of chloride, sodium and sulphate in the pore water obtained by squeezing.

Table XXII
Chemical composition of the pore water obtained by squeezing in samples from section S19.

| | BB19-1 | BB19-2 |
|---------------------------------------|--------|--------|
| pH | 7.5 | 7.7 |
| Electrical neutrality (%) | 0.12 | 0.50 |
| Ionic strength (M) | 0.06 | 0.13 |
| Na ⁺ (meq/L) | 52.2 | 100.0 |
| K ⁺ (meq/L) | 0.33 | 0.33 |
| Mg ²⁺ (meq/L) | 5.51 | 29.0 |
| Ca ²⁺ (meq/L) | 5.29 | 22.6 |
| Sr ²⁺ (meq/L) | 0.039 | 0.162 |
| Al ³⁺ (meq/L) | 0.07 | 0.06 |
| Mn ²⁺ (meq/L) | 0.003 | 0.015 |
| Cl ⁻ (meq/L) | 42.3 | 110.0 |
| SO ₄ ²⁻ (meq/L) | 18.4 | 37.5 |
| Br ⁻ (meq/L) | 0.03 | 0.09 |
| NO ₃ ⁻ (meq/L) | 0.02 | 0.61 |
| HCO ₃ ⁻ (meq/L) | 2.57 | 2.64 |

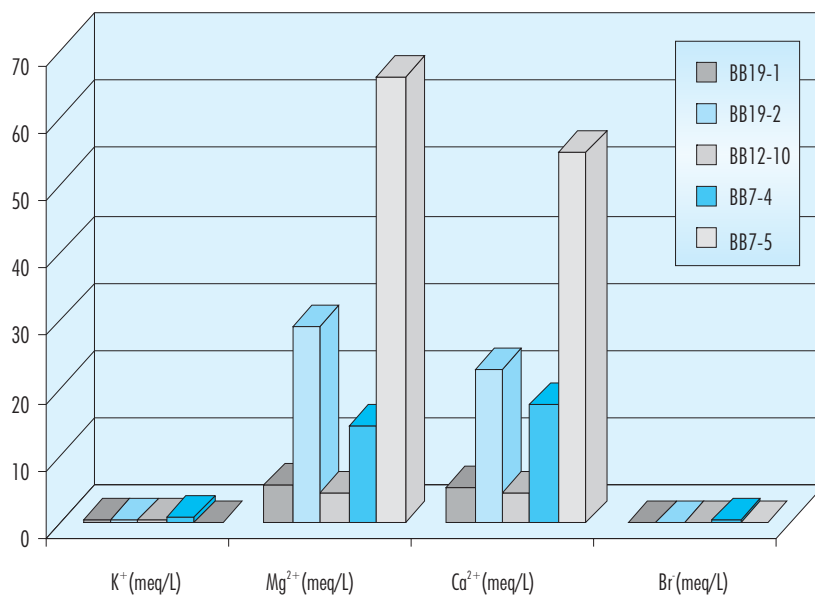


Figure 69. Distribution of cations in the pore water obtained by squeezing.

technique produces the expulsion of some amount of the interlayer water and, therefore, the dilution of the water samples (Fernández 2003). The salinities of the water obtained in the more leached zones are similar to those obtained in the gas pipelines (see section 4.3.2).

4.3.1.7. Textural analysis: nitrogen adsorption/desorption isotherms

The dry state of the bentonite can be further characterised by nitrogen adsorption-desorption isotherms. In the adsorption of non-polar molecules such as nitrogen, the layered structure remains closed, and the external surface area of the stacks of layers, corresponding to both the external faces and the edges of the montmorillonite particles, is obtained. Nitrogen adsorption/desorption isotherms have been obtained at 77 K (liquid nitrogen temperature) on a discontinuous volumetry sorptometer Micromeritics ASAP 2010. Before measurement, the samples were outgassed by heating at 90 °C under a residual vacuum of 0.01 Pa during 18 hours. Depending on the porosity, 0.05 to 0.25 grams of sample were used. Surface areas, a_s , were determined using the standard BET method (Brunauer *et al.* 1938). The presence of micropores in the samples has been assessed using the t -plot method (de Boer *et al.* 1965).

Figure 70 displays the nitrogen adsorption-desorption isotherms obtained for an untreated FEBEX bentonite sample and for samples from Grimsel expressed as gas volume. The Grimsel samples were taken from blocks of section S12 and S19, from the bentonite in contact with the back lid of the heater (BS31-26 and BS31-22N) and from a block in contact with a corroded instrument (SHSDI01A).

All the adsorption isotherms have the characteristic feature of the type IV isotherm with a very important hysteresis loop due to capillary condensation in mesopores formed between different montmorillonite particles or tactoids. The curves exhibit a H3 hysteresis loop in desorption, characterising the presence of slit-shaped pores (Greeg & Sing 1982). However, the volume of gas adsorbed by the samples in contact with the heater is lower than for the other samples.

Table XXIII shows the relevant parameters deduced from the BET and t -plot treatments. It is interesting to note that the BET surface area is lower in the bentonite near the heater contact (samples BS31-22N, BS31-26 and BB19-3). Also, it seems that there is an increase in the size of quasicrystals in the samples in contact with the heater, since the total external surface decreases, probably by the effect of heating.

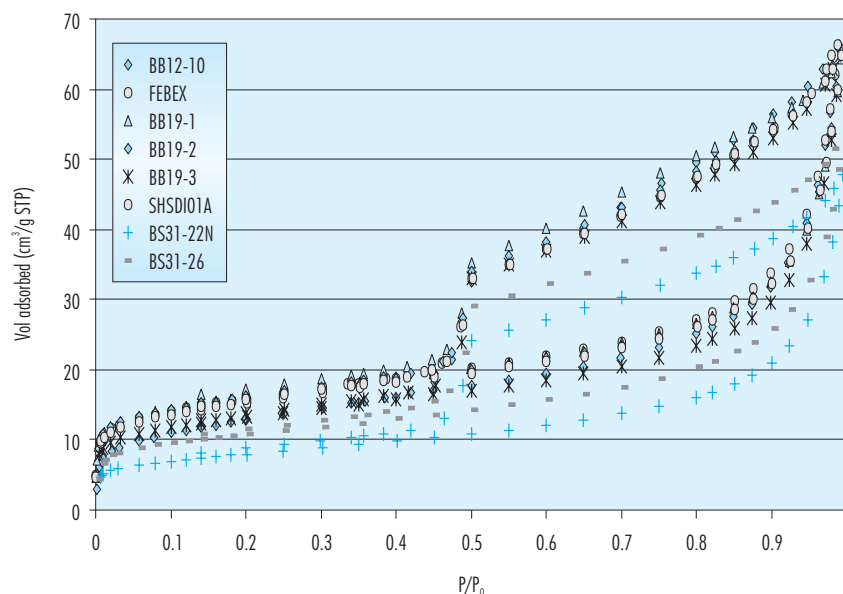


Figure 70: Adsorption-desorption isotherm of N_2 at 77 K for untreated FEBEX sample (FEBEX) and samples from Grimsel.

Table XXIII
Parameters deduced from the BET and t -plot treatment on the adsorption of N_2 at 77 K

| | C_{BET} | $V_{m, liq}$ (cm^3/g) | S_{BET} (m^2/g) | S_{tot} (m^2/g) | V_{tot} (cm^3/g) | S_{micro} (m^2/g) | $S_{ext micro}$ (m^2/g) | $S_{ext meso}$ (m^2/g) |
|----------|-----------|------------------------------|--------------------------|--------------------------|---------------------------|----------------------------|--------------------------------|-------------------------------|
| FEBEX | 388 | $1.99 \cdot 10^{-2}$ | 56.38 | 61.53 | $9.60 \cdot 10^{-2}$ | 20.73 | 35.65 | 29.35 |
| BB12-10 | 117 | $1.65 \cdot 10^{-2}$ | 46.53 | 45.60 | $9.56 \cdot 10^{-2}$ | 7.81 | 38.72 | 29.45 |
| BB19-1 | 765 | $2.02 \cdot 10^{-2}$ | 57.12 | 60.93 | $9.23 \cdot 10^{-2}$ | 18.23 | 38.89 | 25.73 |
| BB19-2 | 774 | $2.00 \cdot 10^{-2}$ | 46.53 | 64.02 | $9.32 \cdot 10^{-2}$ | 7.98 | 38.55 | 25.11 |
| BB19-3 | 464 | $1.67 \cdot 10^{-2}$ | 47.08 | 65.48 | $9.16 \cdot 10^{-2}$ | 15.46 | 31.62 | 26.16 |
| SHSDI | 402 | $1.92 \cdot 10^{-2}$ | 54.34 | 54.34 | $9.25 \cdot 10^{-2}$ | 17.40 | 36.94 | 26.26 |
| BS31-26 | 382 | $1.35 \cdot 10^{-2}$ | 38.16 | 38.16 | $7.49 \cdot 10^{-2}$ | 8.26 | 29.90 | 25.32 |
| BS31-22N | 310 | $9.97 \cdot 10^{-2}$ | 28.17 | 28.17 | $7.10 \cdot 10^{-2}$ | 5.88 | 22.29 | 23.39 |

C_{BET} : parameter related to the heat of adsorption; V_m : monolayer capacity derived from the BET treatment; S_{BET} : BET surface area; S_{tot} : total external surface area derived from the slope of the straight line passing through the origin of the t -plot; $S_{ext micro}$: surface area derived from the slope of the second straight line of the t -plot; V_{tot} : total pore volume, derived from the amount of nitrogen adsorbed at P/P_0 of 0.98; $S_{ext meso}$: surface area derived from the slope of the third straight line of the t -plot; S_{micro} : $S_{BET} - S_{ext micro}$ = surface area of the micropores.

The adsorption isotherms were replotted following the procedure of de Boer *et al.* (1965) in the form V_a vs. t , where t is the mean thickness of the adsorbed layer calculated according to the Harkins & Jura (1944) method. This method has been used for analysing the microporosity. The original slope of the t -plot (Figure 71) indicates a total specific surface area of $61.5 m^2/g$ for the FEBEX sample¹ and lower values for the treated samples, being the differences more substantial in the samples closer to the heater. The reduction of micropores is significant in this dry state.

The mesopores were analysed by the BJH method (Barrett *et al.* 1951). In the case of mesopores, no significant variations were found among the different samples, except for those closer to the heater (Table XXIV).

4.3.2. CIEMAT: Analysis of the water obtained *in situ* from the gas pipes

To study the gases that can be generated in the test area by the effects of corrosion or by the presence of

micro-organisms in the bentonite, a number of ceramic pipes were installed in the clay barrier for the measurement of the gas pressures generated and the sampling of those gases as well as the measurement of the gas permeability (ENRESA 1998). During the operational phase, some of these pipes –those closer to the bentonite/granite interface– were found filled with water. This water was sampled by GRS and sent to CIEMAT to perform its chemical analysis. The knowledge of the chemistry of this water may allow to determine the transient evolution of the pore water in the bentonite/granite interface and, on the other hand, allows the comparison with the pore water samples obtained by squeezing in laboratory from bentonite blocks taken during the dismantling.

Six pipes of 60 mm in diameter and 3 m in length with two connections at the one end to conduits that reach to the exterior of the concrete plug were installed in the clay barrier surrounding heater 1, parallel to the axis of the drift, between the instrumented sections L ($x=5.103 m$) and N ($x=8.075 m$) (Figure 1). Three units (GF-SL-01, GF-SL-02 and GF-SL-03) were fitted in the granite/bentonite contact

¹The value of the external specific surface is highly dependent on the conditions of its determination, for this reason the value reported here for untreated FEBEX differs from the value reported in section .

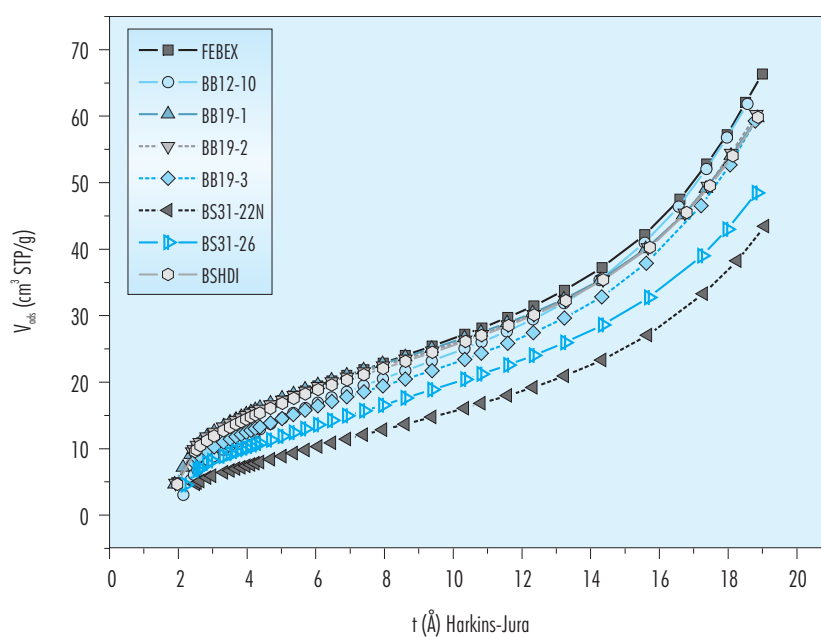


Figure 71: t-plot according to Harkins-Jura method.

Table XXIV
Main parameters calculated with the BJH method for mesopores.

| Sample | Desorption branch | | | Adsorption branch | | |
|----------|---|---------------------------------------|-------------------------|---|---------------------------------------|-------------------------|
| | Cumulative pore volume (cm ³ /g) | Pore surface area (m ² /g) | Average pore radius (Å) | Cumulative pore volume (cm ³ /g) | Pore surface area (m ² /g) | Average pore radius (Å) |
| FEBEX | 1.1·10 ⁻¹ | 69 | 30 | 9.5·10 ⁻² | 36 | 53 |
| BB12-10 | 1.0·10 ⁻¹ | 75 | 55 | 1.0·10 ⁻¹ | 39 | 103 |
| BB19-1 | 1.0·10 ⁻¹ | 74 | 56 | 9.0·10 ⁻² | 34 | 106 |
| BB19-2 | 1.0·10 ⁻¹ | 71 | 58 | 9.2·10 ⁻² | 33 | 110 |
| BB19-3 | 6.2·10 ⁻² | 44 | 57 | 5.7·10 ⁻² | 19 | 122 |
| SHSDI01A | 1.0·10 ⁻¹ | 69 | 59 | 9.2·10 ⁻² | 34 | 107 |
| BS31-26 | 8.4·10 ⁻² | 62 | 55 | 7.8·10 ⁻² | 28 | 114 |
| BS31-22N | 7.5·10 ⁻² | 54 | 56 | 7.2·10 ⁻² | 23 | 127 |

(Figure 72), one unit (GF-SL-05) in the surface of the liner, and two units (GF-SL-04 and GF-SL-06) in holes drilled in an intermediate zone of the clay barrier. The pipes are of sintered ceramic material with an average pore size of $65 \mu\text{m}$, composed of pieces of 1 m joined by Teflon couplers (ENRESA 1998).

The fragility shown by this ceramic material, especially after being wet, led to protecting the pipes installed in the drill holes of the barrier with a covering of perforated metal (GRS 1996, Jockwer & Wiczorek 1999). The filter pipes could easily be penetrated by both gases and liquids, which allowed gas and moisture sampling from the buffer as well as gas injection into the buffer.

Sampling and analysis of gases of the *in situ* test has been performed by GRS. This sampling started in December 1996, almost 3 months prior to switching on the electrical heaters. Sampling was continued from January 1997 until January 1999 and from August 2000 until February 2002 (when the dismantling starts) every three months. The water sent to CIEMAT belongs to the pipes GF-SL-01, GF-SL-02 and GF-SL-03, all of them located at the granite/bentonite contact (Figure 73). This water

was collected in three different gas sampling campaigns: February 1998, December 2001 and January 2002. The water was contained in gas tight sampling bags, always preserved of any contact with atmospheric air. As well, during dismantling a water sample trapped in one of the most external gas pipe tubing was collected and analysed. This water was obtained under atmospheric air conditions and preserved in a plastic vial.

The results of the chemical analyses of the water samples are shown in Table XXV. The waters show large variation in their chemical composition. The waters from pipes GF-SL-01 and GF-SL-02 are of Na-Cl type, while the water from pipe GF-SL-03 is of Na-Cl-SO₄ type. In all the samples the concentration of Ba, Ni, Zn, Be, Bi, Cd, Co, Cr, Cu, Mo, Pb and Ti are below the detection limits.

The salinities and ionic strength of these waters are far away from a GTS granite groundwater (see composition in Table XXVI, ENRESA 2000), showing the influence of the bentonite barrier. They show ion concentrations similar to those of a bentonite pore water, though slightly more diluted.

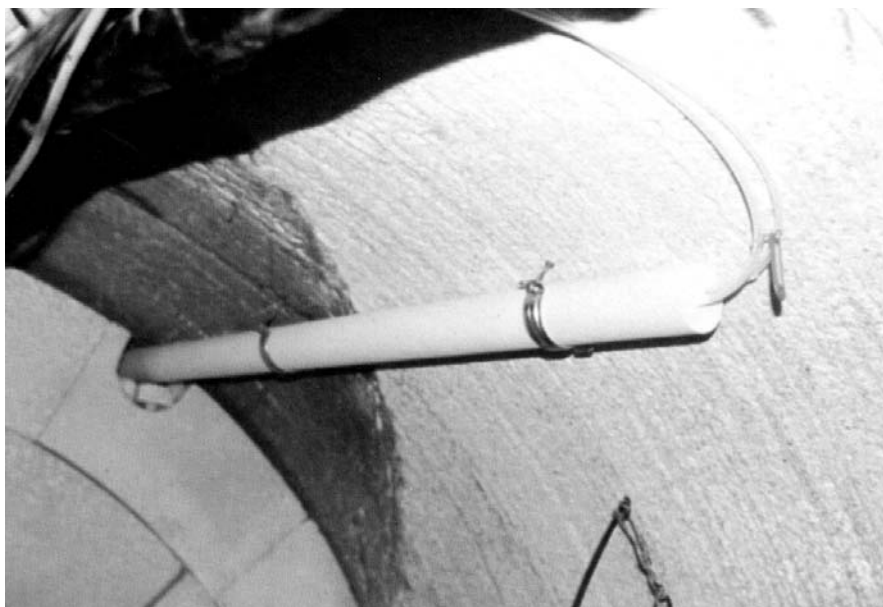


Figure 72: GRS ceramic tubes at the bentonite/granite interface for the sampling and measurement of gas flow (ENRESA 1998b).

4.3.3. INPL/LEM: Mineralogical, chemical and textural analysis

INPL/LEM has analysed six samples from section S29 with the main objective of detecting any sign of mineralogical change or modification of clay material properties such as cationic exchange capacity or swelling behaviour.

The samples were obtained by drilling in positions not equally spaced along the radius (Figure 74): three in the inner bentonite ring, taken from the same block (BS29-30, BS29-31 and BS29-32), two in a block of the middle bentonite ring (BS29-28 and BS29-29), and one in the outer bentonite ring (BS29-27). For the transportation of the samples, specific containers were built in order to avoid changes in pressure, temperature and water content conditions (Figure 75-I). Once at the laboratory, the external PVC layer was removed with a saw (Figure 75-II) and the opening of the container was finally carried out under neutral atmosphere (glove bag).

The different results have been compared to those obtained for the reference bentonite, FO, which could be identified as the initial state of the bentonite material. This reference material was taken from

a non-treated block analogous to those compacted for the *in situ* test sent by AITEMIN to INPL/LEM. The six treated samples have been compared to each other, to evidence any variation of their properties upon their respective distances from the central heater, or upon the saturation state they might have suffered in the tunnel.

4.3.3.1. Preparation of the samples

To the naked eye (Figure 75-IV) the six samples showed different hydration states, from higher (BS29-27) to lower (BS29-32), corresponding to the positions of the samples with respect to the central heating cylinder. As most of the scheduled analyses are generally carried out on powdered samples, one half of the samples was ground after drying overnight at 105 °C. The weight losses (equivalent to water losses) for the six bentonite cores went from 14 percent for the inner sample (BS29-32) to 22 percent for the outer sample (BS29-27).

4.3.3.2. X-ray diffraction

X-ray diffraction (XRD) data were obtained from a D8 Bruker diffractometer with Co K α 1 radiation

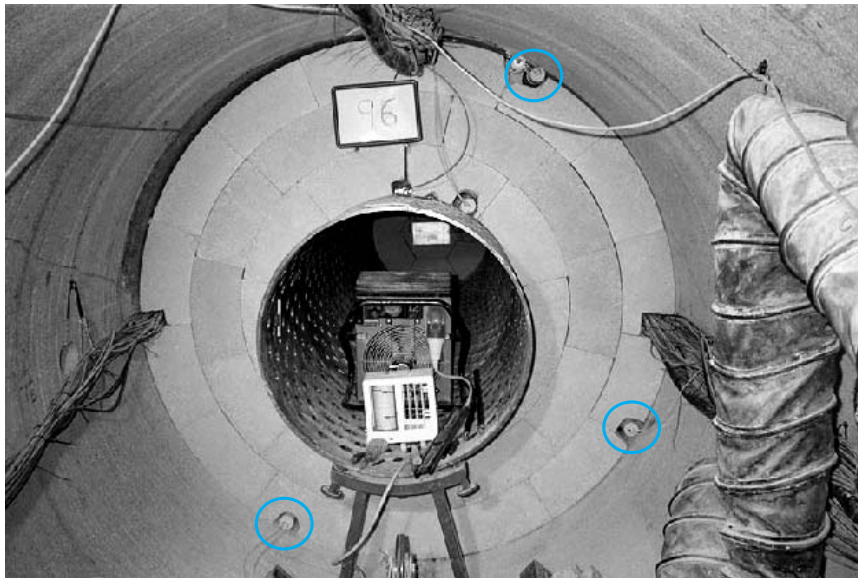


Figure 73: Position of gas pipes in installation slice 96 (sampling section S20) (ENRESA 1998b). Gas pipes GF-SL-01, GF-SL-02 and GF-SL-03 marked with a circle.

Table XXV
Chemical composition of the water taken from the gas pipes in different sampling campaigns

| | February 1998 | December 2001 | | | February 2002 | | | July 2002 |
|--------------------------------------|-------------------------------------|---------------|----------|-------------------------------------|---------------|----------|-------------------------------------|-----------|
| | GF-SL-02 | GF-SL-01 | GF-SL-02 | GF-SL-03 | GF-SL-01 | GF-SL-02 | GF-SL-03 | GF-SL-03 |
| Water type | Na-Cl-HCO ₃ ⁻ | Na-Cl | Na-Cl | Na-Cl-SO ₄ ²⁻ | Na-Cl | Na-Cl | Na-Cl-SO ₄ ²⁻ | Na-Cl |
| I.S. (M) | 0.02 | 0.07 | 0.06 | 0.09 | 0.05 | 0.03 | 0.06 | 0.07 |
| pH | 7.7 | 7.9 | 7.8 | 7.8 | 7.9 | 7.7 | 7.5 | 8.4 |
| Eh (mV) | | -103 | -182 | | | 184 | 213 | |
| Cl ⁻ (mg/L) | 356 | 1300 | 1100 | 1500 | 1500 | 876 | 1500 | 2100 |
| SO ₄ ²⁻ (mg/L) | 121 | 281 | 27 | 818 | 310 | 43 | 752 | 770 |
| HCO ₃ ⁻ (mg/L) | 241 | | | | 592 | 493 | 361 | 283 |
| Br ⁻ (mg/L) | 0.9 | 2.8 | 2.0 | 2.8 | 3.0 | 1.4 | 2.6 | 4.7 |
| NO ₃ ⁻ (mg/L) | < 0.1 | < 1 | < 1 | < 1 | < 1 | < 1 | < 1 | < 1 |
| F ⁻ (mg/L) | 3.7 | 1.6 | 2.3 | 1.8 | 1.3 | 2.9 | 1.7 | |
| I ⁻ (mg/L) | 1.4 | 1.0 | 2.5 | 0.75 | 1.1 | 1.8 | 0.7 | |
| SiO ₂ (mg/L) | 36.4 | 12.5 | 10.7 | 5.1 | | 67.3 | 65.8 | |
| Ca (mg/L) | 10 | 29 | 20 | 57 | 16 | 16 | 64 | 50 |
| Mg (mg/L) | 5.5 | 29 | 18 | 47 | 39 | 17 | 62 | < 4 |
| Na (mg/L) | 365 | 2400 | 1900 | 2800 | 1200 | 700 | 1300 | 1600 |
| K (mg/L) | 8.7 | 19 | 17 | 23 | 20 | 13 | 22 | 34 |
| Mn (mg/L) | | < 0.03 | < 0.03 | 0.06 | < 0.03 | < 0.03 | 0.05 | < 0.3 |
| Al (mg/L) | 0.06 | < 0.01 | < 0.01 | < 0.01 | 0.1 | < 0.05 | < 0.05 | < 0.5 |
| B (mg/L) | | 3.2 | 2.8 | 2.7 | 3.1 | 2.0 | 2.4 | 0.75 |
| Ba (mg/L) | | < 0.05 | < 0.05 | < 0.05 | < 0.05 | < 0.05 | < 0.05 | < 0.5 |
| Fe (mg/L) | 0.03 | 0.04 | 0.04 | 0.03 | < 0.05 | < 0.05 | < 0.05 | < 0.3 |
| Fe ²⁺ (μg/L) | | 44 | 47 | 25 | < 0.05 | < 0.05 | < 0.05 | |
| Sr (mg/L) | | 0.79 | 0.53 | 1.4 | 0.56 | 0.30 | 1.0 | < 0.5 |
| Cs (μg/L) | | 0.5 | 0.5 | 0.5 | 0.2 | 0.2 | 0.2 | |
| Se (μg/L) | | ≤ 10 | ≤ 10 | 20 | | | | |
| As (μg/L) | | 7.0 | 2.6 | 6.0 | 5.1 | 3.4 | 5.5 | |
| Re (μg/L) | | 6.2 | < 0.5 | 3.5 | 5.9 | 0.5 | 5.3 | |
| U (μg/L) | | 0.7 | | 0.9 | < 1 | < 0.5 | 0.9 | |
| Th (μg/L) | | < 0.5 | ≤ 0.5 | < 0.5 | < 1 | 0.5 | 0.5 | |

Table XXVI
Chemical characteristics (major components) of the groundwater taken from two boreholes at the GTS (Aare granite) (ENRESA 2000)

| Borehole | SF14-i3 | SF14-i3 |
|--------------------------------------|---------------------------|---------------------------|
| Date | 18/07/96 | 8/06/00 |
| Water type | Na-Ca-HCO ₃ -F | Na-Ca-HCO ₃ -F |
| pH | 8.9 | 9.4 |
| O ₂ (mg/L) | | 0.2 |
| Eh (mV) | 420 | -120 |
| Ionic Strength (mol/L) | 0.001 | |
| Alkalinity, CaCO ₃ (mg/L) | 20 | |
| Cl ⁻ (mg/L) | 2.8 | 0.52 |
| SO ₄ ²⁻ (mg/L) | 6.9 | 7.1 |
| HCO ₃ ⁻ (mg/L) | 23.3 | 29.6 |
| Br (mg/L) | 0.01 | < 0.1 |
| NO ₃ ⁻ (mg/L) | 0.11 | 0.1 |
| F (mg/L) | 4.3 | 5 |
| SiO ₂ (mg/L) | 9.1 | 9.4 |
| NH ₄ ⁺ (mg/L) | < 0.1 | 0.42 |
| Ca (mg/L) | 7.4 | 6.1 |
| Mg (mg/L) | 0.083 | < 0.4 |
| Na (mg/L) | 9.1 | 10 |
| K (mg/L) | 2.7 | 0.2 |
| TOC (mgC/L) | 4.9 | 1.4 |
| Sr (μg/L) | 240 | 175 |

($\lambda = 1.7902 \text{ \AA}$), using 0.036° step and 2 s collection time. The diffractometer is equipped with a (θ , 2θ) goniometer and a position sensitive detector (PSD).

Prior to the random powder determinations, the samples were dried at 105°C for 12 hours. For oriented slides, a preliminary separation step was done, to isolate the granulometric fraction inferior to 2 microns, following the method developed by

Rouiller *et al.* (1972). After separation, the resulting slurry was deposit on a glass slide. XRD collecting was carried out at room conditions, after saturation with ethylene glycol and finally after heating at 550°C .

Greene-Kelly tests (Greene-Kelly 1952) were performed on the reference sample and the six post-mortem samples in order to check the location of

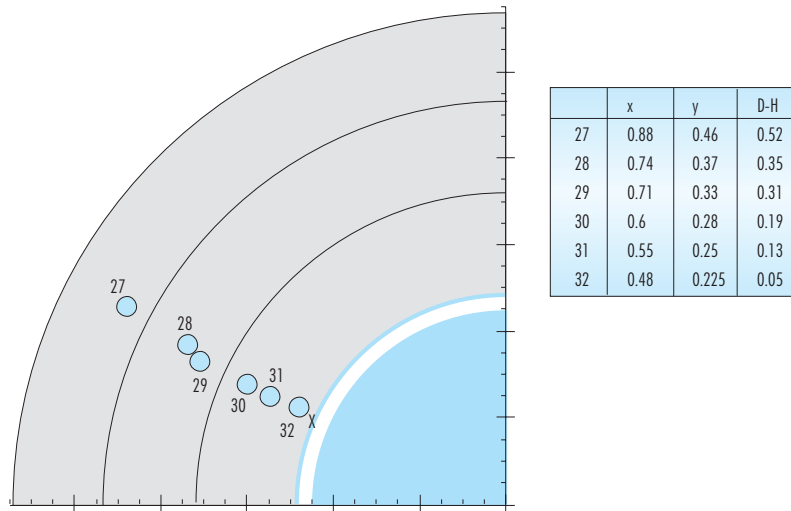


Figure 74: Location and coordinates (meters, D-H is the distance to the heater liner) of samples taken for LEM in sampling section S29.



Figure 75: Container (I), opening of the PVC cover (II), appearance of the cores (IV).

the layer charge. For that purpose, 100 mg of raw bentonite were suspended in 0.1M LiCl solutions, in order to substitute the interlayer cations of the clay material by Li^+ ions. After several washings to remove ions excess, the clay was separated from the suspension by centrifugation. Oriented slides were then prepared with the different slurries and heated at 400 °C overnight. This thermal treatment is supposed to favour Li migration into vacant octahedral sites in the case of dioctahedral smectites. For clays displaying a layer charge mainly located in the octahedral sheet, this migration is supposed to hinder swelling of the layers upon glycerol saturation (Lim & Jackson 1986).

Random powder

Scans of the bulk sample as random powder were carried out to evidence accessory minerals. The XRD pattern obtained for the untreated sample (FO) shows the diffraction bands corresponding to basal planes of the smectite with basal spacings $d(001)$ close to 15 Å. This interlayer distance reveals the predominance of calcium cations in the interlayer space of the clay mineral. Accessory phases such as quartz and feldspar could be detected.

A first analysis of XRD patterns of postmortem samples (Figure 76a) shows a drastic signal loss between reference sample (FO) and treated samples (BS's) in the low angles region. The diffraction line centred at 15 Å, due to (001) plane of smectite minerals, is not detected anymore. In the same 2θ region, there is instead a broad diffraction area that could mean a very strong decrease of order in the layer stacking of the swelling phyllosilicate, or different hydration states. However, the general shape of the patterns for treated bentonites looks similar to the FO curve, although they all show lower peak intensities.

Figure 76b shows an enlargement of the [35-30°] 2θ region, where typical diffraction bands of quartz and plagioclase occur. Felspars contribution strongly decreases for treated samples. The slight differences between the six treated samples are assigned to sample heterogeneity.

Oriented aggregates

The different steps included in the separation of the less than 2 µm fraction involve, among other modifications of the sample, a total re-saturation of the

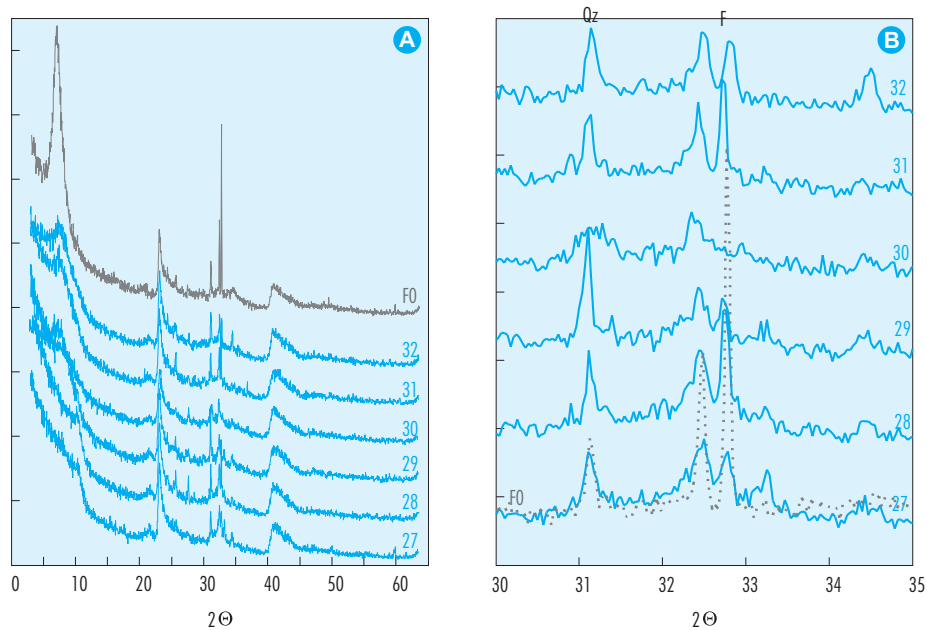


Figure 76: XRD patterns of unoriented powders of BS29 samples (dashed line in B plot: FO).

clay material. Thus, XRD patterns of resulting oriented slides show again the basal spacing line centred around 14.4 Å, and this for all the treated samples (Table XXVII and Figure 77). Calculation of FWHM (band width at half-height) for the (001) lines does not show any evolution in the thickness of clay particles, and then does not reveal any modification of layer stacking ordering. The crystallite thickness (calculated with Scherrer formulation) is close to 60 Å for all samples. With ethylene glycol saturation, swelling was observed for all the samples, with no modification of the basal spacings. Thus, no layer charge modification could be evidenced.

Greene-Kelly test was performed on Li-exchanged bentonites. Swelling capacity was checked after heating overnight at 400 °C, with glycerol saturation. None of the seven samples presented swelling upon glycerol saturation (Figure 78, sample BS29-32). This confirms that the initial bentonite FO is a montmorillonite, with a layer charge mainly located in the octahedral sheet. This also suggests that the charge location has not changed for the postmortem samples.

4.3.3.3. Infrared spectroscopy

Infrared (IR) spectra were collected in diffuse reflectance mode using a Bruker IFS 55 Fourier IR spectrometer at a resolution of 4 cm⁻¹ (200 scans, on powdered bentonite mixed with pure KBr) under room conditions of pressure and temperature. The assignation of IR absorption bands is shown in Table XXVIII.

The spectra obtained are shown in Figure 79. At first sight no difference could be evidenced between the six treated samples and the reference one (FO). However, it could be noticed a slight increase in carbonates contribution, centred at 1440 cm⁻¹. Figure 80 shows an enlargement of the bending vibrations region in which clay layer and accessory minerals vibrations occur. There is no modification in this region, the contributions that could be assigned to accessory minerals such as feldspars or quartz (bands or shoulders centred at 938, 791, 729, 688 or 622 cm⁻¹, Table XXVIII) do not show any shift in wave number and no band appears or disappears.

The fine granulometric fraction (< 2 μm) was extracted from these samples and IR spectra were col-

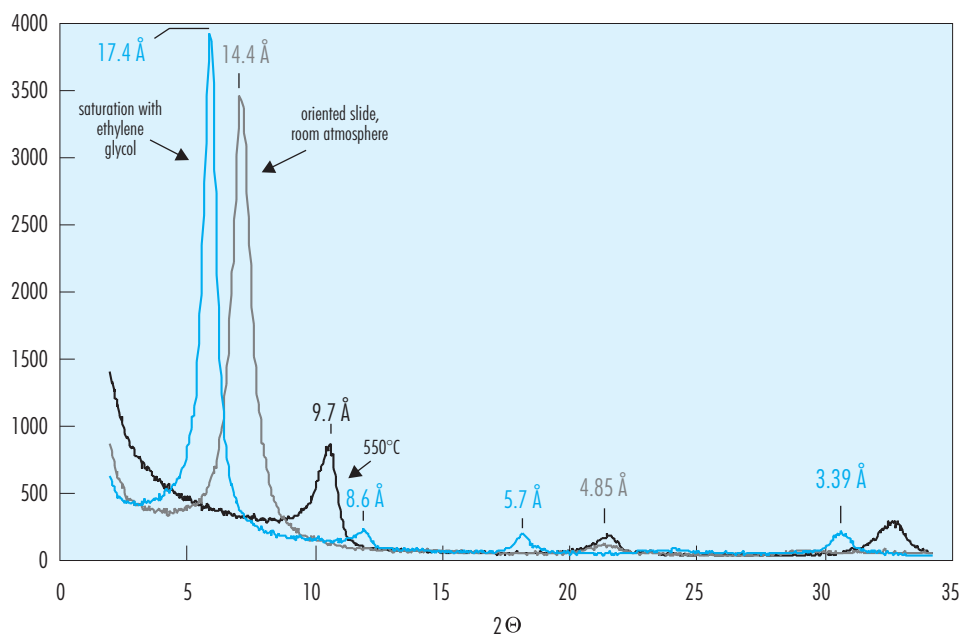


Figure 77: Diffractograms obtained on oriented slides of BS29-27 sample (< 2 μm fraction), at room temperature and humidity, after ethylene glycol saturation and after heating at 550 °C.

Table XXVII
Diffraction maxima $d(001)$ of smectite for reference (F0) and BS29 samples (in Å).

| Treatment | F0 | 27 | 28 | 29 | 30 | 31 | 32 |
|-----------|------|------|------|------|------|------|------|
| RT / RWP | 15.2 | 14.4 | 14.8 | 14.8 | 14.7 | 14.7 | 14.8 |
| EG | 17.6 | 17.4 | 16.8 | 16.9 | 17.1 | 17.2 | 17.1 |
| 550 °C | 10.0 | 9.7 | 9.7 | 9.6 | 9.8 | 9.7 | 9.6 |

RT / RWP: room temperature and water pressure; EG: saturated with ethylene-glycol.

Table XXVIII
Assignment of IR absorption bands.

| Wave number (cm ⁻¹) | Vibrating group |
|---------------------------------|--|
| 1017-1012 | montmorillonite δ SiO, δ Al ₂ OH |
| 936 | δ SiO from Ca-felspar, anorthite |
| 920 | montmorillonite δ AlAlOH |
| 882 | montmorillonite δ AlFeOH/ or carbonates |
| 845 | montmorillonite δ AlMgOH |
| 791 | δ FeMgOH from montmorillonite or δ SiO from quartz or cristobalite |
| 729 | felspar, anorthite |
| 688 | Montmorillonite or felspar |
| 622 | Montmorillonite/cristobalite/anorthite |

lected in the fine fraction of each sample. The separation method implies the carbonates dissolution, thus, their contribution in IR absorbance around 1450 cm⁻¹ disappears (vibration mode ν_3 from CO₃²⁻). The bending vibration region (Figure 81a) reveals accessory minerals removal. There is a sharpening of the vibration bands centred at 1028 cm⁻¹ and 918 cm⁻¹.

The weak vibration band centred at 882 cm⁻¹ was observed for both the treated bentonites and the reference sample F0. This band could be assigned to AlMgOH groups of the montmorillonite crystal structure as well as to the vibration mode ν_2 from CO₃²⁻ in carbonate-like minerals (Russel & Fraser 1992). The latter interpretation should be preferred as this

band was not observed for the bulk bentonite. Figure 81b shows that no modification of the clay fraction could be evidenced with this method. The six treated bentonites yielded similar spectra.

4.3.3.4. Exchangeable cations and CEC

As the nature of the interlayer cations affects not only the exchange properties but also the swelling capacity and the rheological behaviour, the different cations occupation has been determined. The exchangeable cations and the CEC were measured using cobalt-hexamine chloride (Cl₃Co(NH₃)₆) solutions. About 50 mg of bentonite were weighed and placed in polypropylene tubes. 30 mL of a cobalt-

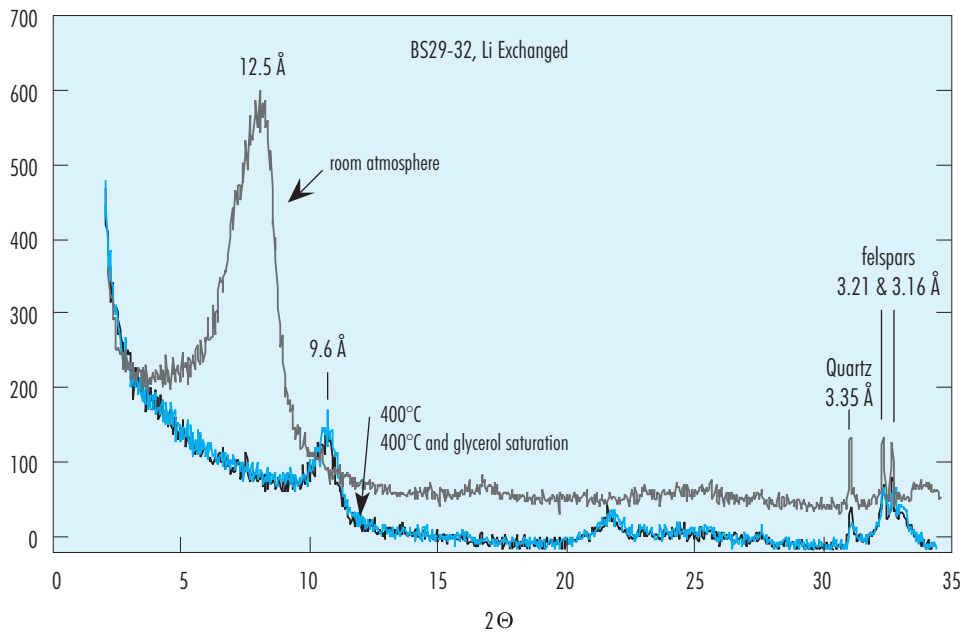


Figure 78: Diffractograms obtained on oriented slides of Li-exchanged BS29-32 sample at room temperature and humidity, after heating at 400°C and after saturation with glycerol.

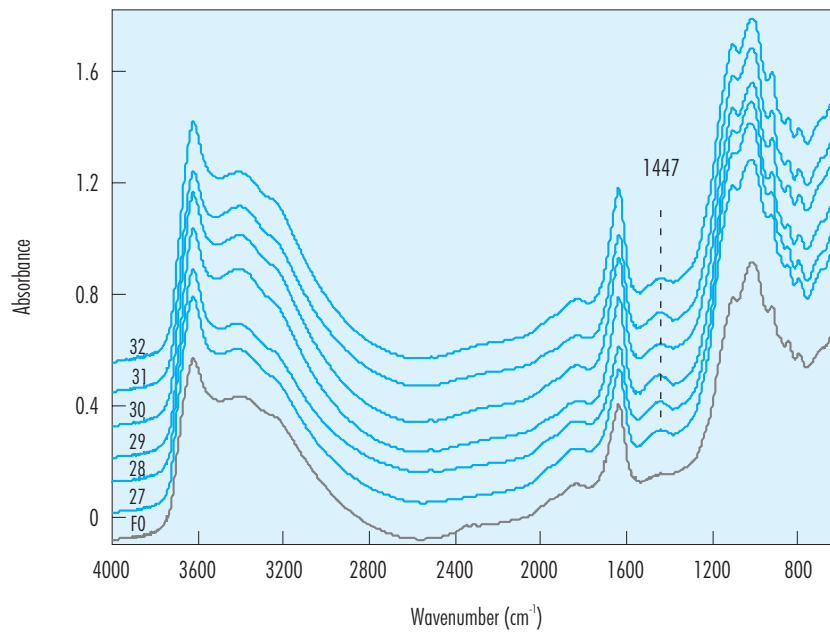


Figure 79: IR spectra for untreated (FO) and treated (BS29's) samples.

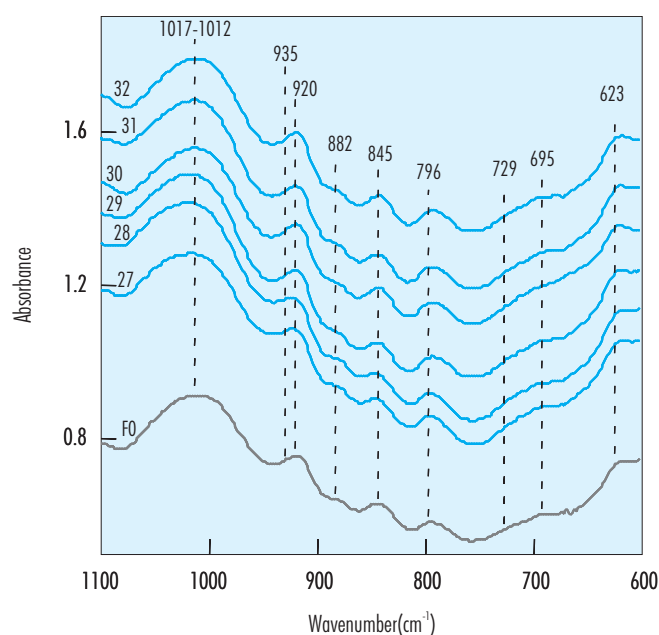


Figure 80: IR spectra for untreated (F0) and treated (BS29's) samples, bending vibration band region.

hexamine solution, with initial concentration equal to 0.5 mol/L was added to the powder. The tubes were left overnight under soft stirring at 25 °C. After centrifugation to separate liquid and solid fractions, the final concentrations were calculated employing UV spectrometer measurements, including a preliminary calibration with a series of cobalt-hexamine solutions. The CEC was evaluated from the rest method, based on the adsorbed amount. The supernatants were analysed to determine simultaneously the concentration of Ca, Na, Mg and K by atomic absorption. The CEC of the untreated FEBEX bentonite was also determined by INPL/LEM using the BaCl₂ salts method.

The two methods employed by INPL/LEM to determine the CEC have given similar results: 100 meq/100g in the case of the BaCl₂ method and 99 meq/100g for the Cl₃Co(NH₃)₆ method. The distribution of the interlayer cations, as determined by atomic absorption by INPL/LEM, was very similar to that reported by CSIC (Table XXIX). The differences observed are not really significant and can be a result of sample heterogeneity, due to variations of accessory minerals presence, such as carbonates or feldspars. Na and Mg contents are both modified

upon the distance from the central heater. Na content decreases from outer to inner samples whereas Mg content increases (Figure 82a). This modification induces a slight increase of divalent cations proportion towards the heater (Figure 82b).

As it was revealed by XRD results, the different bentonite blocks show little variations in their mineralogical composition and so the variations described here can be due to bentonite block heterogeneity. The evolution of the nature of interlayer cations should be correlated with the interstitial water composition and chemical analyses.

4.3.3.5. Chemical analyses

Chemical analyses were performed at the Centre of Petrographic and Geochemical Research (CRPG, Vandoeuvre, France). The samples were preliminary smelted with LiBO₂ and dissolved with HNO₃. Major elements were determined by ICP-AES, minor and trace elements were determined by ICP-MS.

Chemical analyses (Table XXX) give comparable results to those reported for the FEBEX bentonite (ENRESA 2000). Ferric iron is predominant as those analyses revealed very low FeO contents for all the

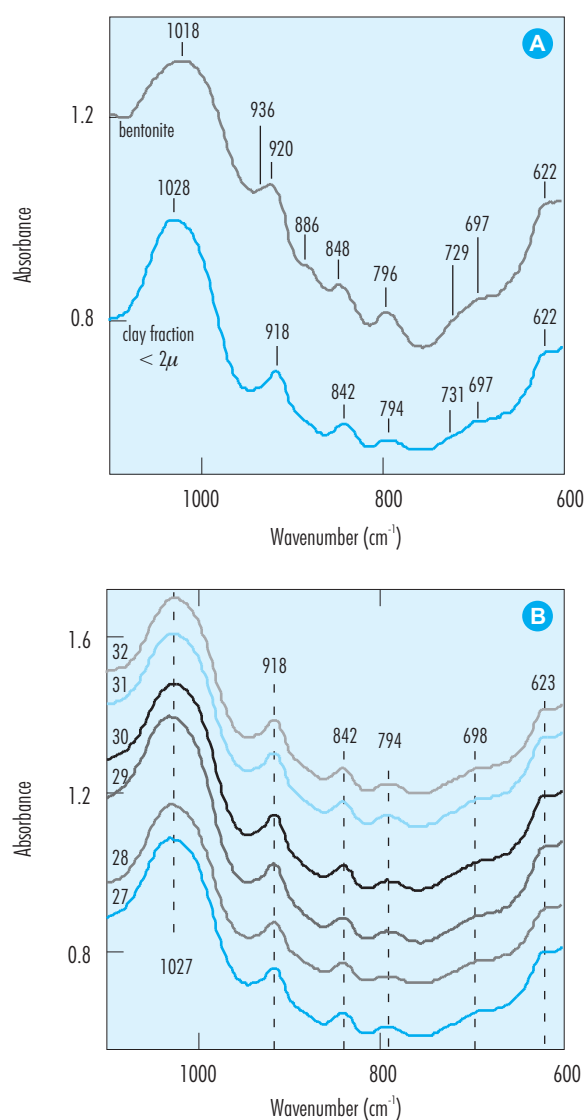


Figure 81: IR spectra for < 2 μm fraction of treated bentonites, bending vibration region: A) BS29-28 sample, bulk and clay fraction; B) BS29 samples clay fraction.

samples. Chemical analyses of F0 and BS29's samples do not evidence any variation in bentonite composition. However, whereas CEC measurement showed that magnesium cations were increasing from outer to inner samples, from chemical analyses, this element appears rather constant.

Concerning sodium, calcium and potassium cations, chemical analyses are in good correlation with CEC measurements. These three latter cations, unlike magnesium, are not involved in the unit cell for-

mula of clay material. Thus, a very beginning of octahedral sheet dissolution is one way to explain the increase of magnesium in the interlayer space.

4.3.3.6. Microscopic analyses

The reference bentonite and two of the six postmortem samples (BS29-27 and BS29-32) were studied with Scanning Electron Microprobe (SEM) in order to unravel any modification of clay layer morphology and to identify new mineral phases that could

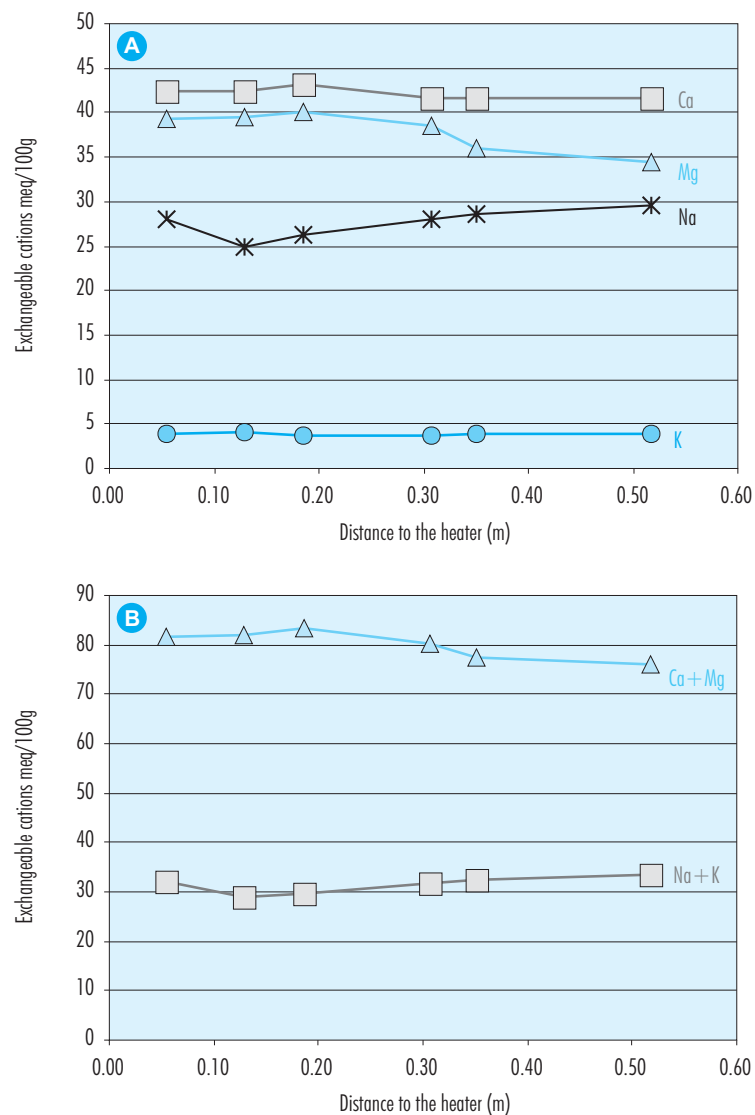


Figure 82: Interlayer cations in BS29's samples as determined by INPL/LEM.

have been formed during the operation of the *in situ* test. These first microscopic analyses were supplemented by Transmission Electron Microprobe (TEM) coupled to Energy Dispersive X-ray Spectroscopy (TEM-EDXS), in order to determine the composition of clay layer and accessory minerals.

Scanning Electron Microprobe

SEM observations were carried out at the University Henri Poincaré (Nancy, France). They were per-

formed on a microprobe HITACHI S2500 FEVEX, featuring a maximal resolution of 2.5 Å, which corresponds to 200000 magnification. Observations were complemented with EDS analyses for semi-quantitative determination of mineral composition.

SEM observations were performed on bulk samples, *i.e.* clay material and accessory minerals, and on secondary minerals after removal of the clay fraction. For that, the bentonite was suspended in ethanol, dispersed with ultrasound and left for sedimentation.

Table XXIX
Cation exchange capacity as determined by INPL/LEM in BS29 samples.

| Sample reference | CEC ¹ meq/100g | Ca ²⁺ meq/100g | Mg ²⁺ meq/100g | Na ⁺ meq/100g | K ⁺ meq/100g | CEC ² meq/100g |
|------------------------------|------------------------------|------------------------------|------------------------------|-----------------------------|----------------------------|------------------------------|
| Febex bentonite ³ | | 43 ± 5 | 32 ± 3 | 24 ± 4 | 2.1 ± 0.2 | 101 ± 4 |
| Febex bentonite | 99 | 39 | 36 | 26 | 2.9 | 104 |
| BS29-27 | 105 | 42 | 34 | 30 | 3.9 | 110 |
| BS29-28 | 103 | 42 | 36 | 29 | 3.9 | 111 |
| BS29-29 | 103 | 42 | 39 | 28 | 3.8 | 113 |
| BS29-30 | 105 | 43 | 40 | 26 | 3.6 | 113 |
| BS29-31 | 103 | 42 | 40 | 25 | 4.0 | 111 |
| BS29-32 | 105 | 42 | 39 | 28 | 3.9 | 113 |

¹Calculated from final $Cl_3Co(NH_3)_6$; ²Calculated as sum of exchangeable cations; ³CSIC, Table VI.

Table XXX
Chemical analysis of samples from section S29 performed by INPL/LEM.

| % | F0 | 27 | 28 | 29 | 30 | 31 | 32 |
|--|-------|-------|-------|-------|-------|-------|-------|
| Loss at 1000 °C | 18.57 | 8.65 | 9.55 | 12.04 | 11.63 | 11.23 | 13.11 |
| CO ₂ total | 0.35 | 0.46 | 0.51 | 0.49 | 0.37 | 0.41 | 0.40 |
| FeO | 0.12 | 0.14 | 0.15 | 0.14 | 0.12 | 0.12 | 0.11 |
| S total | 0.025 | 0.025 | 0.038 | 0.038 | 0.026 | 0.031 | 0.026 |
| Percentages normalised with respect to loss at 1000 °C | | | | | | | |
| SiO ₂ | 65.26 | 65.28 | 65.07 | 65.37 | 65.34 | 65.61 | 65.64 |
| Al ₂ O ₃ | 20.84 | 21.07 | 20.94 | 20.91 | 20.77 | 20.90 | 20.94 |
| Fe ₂ O ₃ | 3.57 | 3.65 | 3.68 | 3.63 | 3.64 | 3.49 | 3.53 |
| MnO | 0.04 | 0.03 | 0.03 | 0.03 | 0.03 | 0.05 | 0.03 |
| MgO | 5.01 | 4.90 | 5.00 | 4.88 | 5.17 | 4.92 | 5.02 |
| CaO | 2.16 | 2.23 | 2.35 | 2.36 | 2.29 | 2.27 | 2.14 |
| Na ₂ O | 1.60 | 1.37 | 1.39 | 1.29 | 1.25 | 1.26 | 1.19 |
| K ₂ O | 1.19 | 1.22 | 1.30 | 1.20 | 1.21 | 1.17 | 1.22 |
| TiO ₂ | 0.23 | 0.24 | 0.24 | 0.25 | 0.24 | 0.24 | 0.22 |
| P ₂ O ₅ | 0.09 | <d.l. | <d.l. | 0.07 | 0.07 | 0.09 | 0.07 |

Afterwards the supernatant was removed. This operation was repeated until a clear supernatant was obtained. Few drops of diluted n-butylamine were added in the first operation to favour the removal of the clay fraction. The final slurry was dried and dropped on a carbon-layered tape.

Reference bentonite FO is mainly composed of smectite phase (Figure 83). Fluffy clay minerals cover almost entirely the disseminated secondary minerals, which are: quartz, sodic and calcic plagioclases, potassic feldspars, biotites, carbonates (calcite and ankerite), iron oxides, titanium oxides, strontium sulphates (celestite) and calcium phosphates (apatite).

No differences could be noticed between sample FO and sample BS29-27, the closer to the gallery wall. Clay matrix displays similar flake morphology (Figure 84a) and identical composition. Moreover, identical accessory minerals were observed.

BS29-32 is the closest sample to the heater. As in the previous sample, clay matrix displays similar flake morphology. However, some variations could be noticed on accessory minerals. Potassic feldspars display dissolution crevices (Figure 84b). Nearby those corroded feldspars, neoformed crystals of potassic feldspars could be observed (Figure 84c). The spectra of the analyses reveal identical composition of the feldspars in the reference sample (FO) and in sample BS29-32. Furthermore, clay minerals in the vicinity of feldspars display a slightly different morphology, filamentous (Figure 84c). No analysis could be performed since the volumes concerned are too small. Biotites are still present, but reveal corrosion gulfs (Figure 84d). As these corrosion marks were observed for this sample only, they could be explained by the location of the sample close to the heater.

Transmission Electron Microprobe

For TEM observations, bentonite powder was suspended in ethanol and then subjected to ultrasound to increase the dispersion of particles. One drop of the resulting suspension is then laid down on a

nickel grid covered by a thin carbon layer. The analyses were performed on PHILIPS CM20 microprobe at 10 eV and 200 kV. EDX were collected during 40 s to avoid elements migration under electron beam. EDX spectra were treated in order to get atomic percentages.

Unit cell formulae were deduced from EDX using the calculation method of Harvey (1943), *i.e.* on the basis of 11 oxygen atoms per unit cell for particles of 2:1 type. In those calculations, iron was always considered as ferric (Fe^{3+}) and it has been taken into account the presence of Mg in the interlayer space (Table XXXI). The interlayer charge calculated from TEM observations is 1.18 for the reference bentonite (FO) and 1.16 for sample BS29-32.

TEM analysis of the clay minerals (<2 μm fraction) did not evidence any variation in the layer composition (Montarges-Pelletier *et al.* 2003). The global chemistry of the montmorillonite remained constant. From the analyses, the reference bentonite was placed in the diagram «Celadonite-Muscovite-Pyrophyllite» (Figure 85) (Hower & Mowatt 1966). As it could be deduced from the layer charge, this smectite belongs to the “High charge montmorillonite” group.

4.3.3.7. Textural analysis

Porosity has been measured by gas and water adsorption. In the first case, nitrogen reveals voids between clay aggregates (mesoporosity, 20-950 Å) and voids within aggregates (microporosity, 8-20 Å), but nitrogen molecules cannot access the interlayer space due to their size. Water molecules can sorb on the whole surface, including the interlayer surface. Consequently, for bentonite, it can be assumed that water molecules will be more sensitive to microporosity decrease than nitrogen molecules.

Nitrogen adsorption volumetry

Nitrogen adsorption experiments were conducted in compacted samples (centimetre size) (obtained by gently disaggregation of the blocks) and in powder

Table XXXI
Structural formula of the smectite determined from EDX analyses.

| Sample | Structural formula |
|------------|---|
| FEBEX (FO) | $(\text{Si}_{7.68} \text{Al}_{0.32}) (\text{Al}_{3.02} \text{Fe}_{0.44} \text{Mg}_{0.86}) \text{O}_{20} (\text{OH})_4 (\text{Mg}_{0.28} \text{K}_{0.10} \text{Na}_{0.16} \text{Ca}_{0.18})$ |
| BS29-32 | $(\text{Si}_{7.72} \text{Al}_{0.28}) (\text{Al}_{3.02} \text{Fe}_{0.36} \text{Mg}_{0.83}) \text{O}_{20} (\text{OH})_4 (\text{Mg}_{0.32} \text{K}_{0.04} \text{Na}_{0.16} \text{Ca}_{0.18})$ |

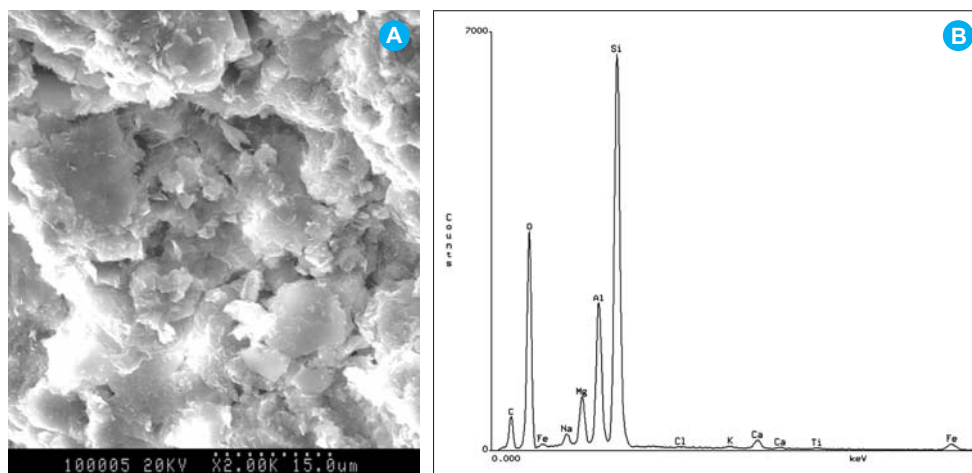


Figure 83: SEM micrographs for FO reference bentonite: A) clay matrix, B) clay composition.

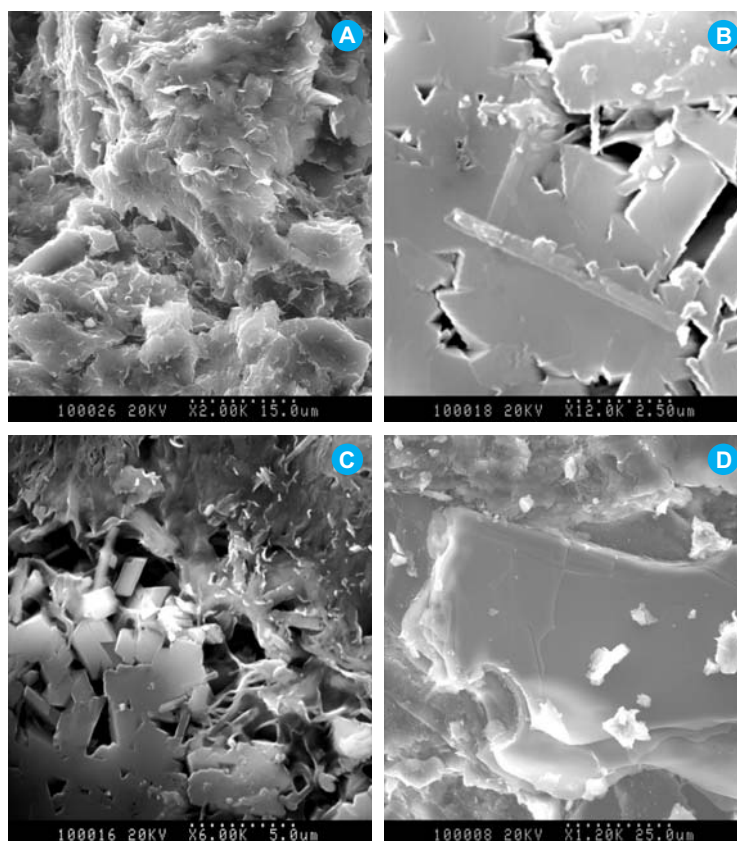


Figure 84: SEM micrographs: A) clay matrix, sample BS29-27; B) K-feldspars, sample BS29-32; C) K-feldspars and filamentous clays, sample BS29-32; D) biotite, sample BS29-32.

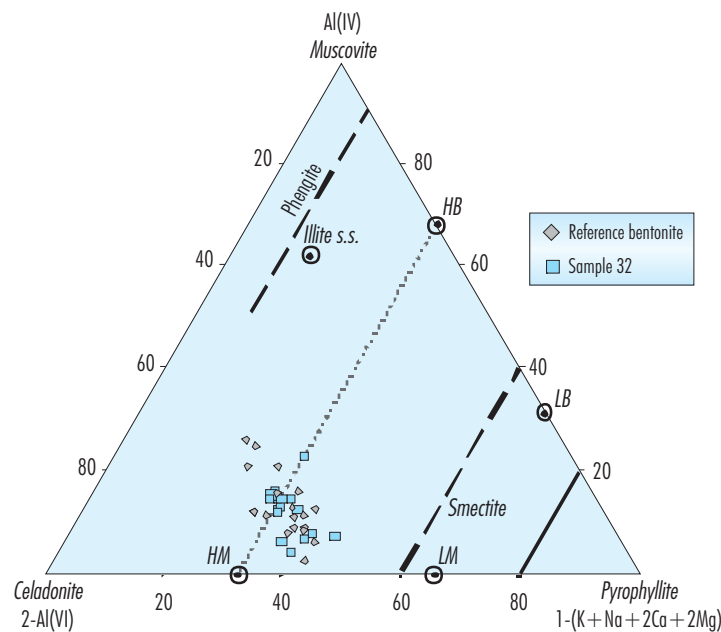


Figure 85: Diagram « Celadonite-Muscovite-Pyrophyllite » and reported TEM-EDXS analyses of clay particles of reference bentonite (FO) and postmortem sample BS29-32 (HB: high charge beidellite, LB: low charge beidellite, HM: high charge montmorillonite, LM: low charge montmorillonite).

bentonite (obtained after grinding, with no subsequent sieving).

Adsorption-desorption isotherms were obtained using a lab-built classical step-by-step volumetric setup, with successive introductions of nitrogen (purity of N_2 -gas >99.995 %). All samples were preliminary outgassed at 120 °C for 18 hours under a residual pressure of 10^{-9} bar. The measurements were conducted at liquid N_2 temperature (-196 °C) with the samples kept in a bath of liquid N_2 at constant level. Pressure measurements were carried out with two absolute gauges (Edwards) in the range 0-0.01 bar and 0-1 bar. The saturation pressure of nitrogen at -196 °C was recorded using a third gauge during the whole experiment. The adsorption isotherm was obtained from the measurement of equilibrium pressures before and after contact with the sample.

Specific surface areas, a_s , are calculated with the BET method (Brunauer *et al.* 1938; AFNOR NF X 11-621) and the De Boer method (*t*-plot, De Boer *et al.* 1965). The latter method was also used to estimate microporous and external surfaces. Micropore filling happens at low and very low relative

pressure values, and includes then the domain of the monolayer adsorption on external surface. To be able to distinguish adsorption onto external surface from adsorption into the micropores, the experimental isotherm is compared to a reference curve, obtained for a non-porous solid, with chemical features and energetic constant as close as possible to those of the studied sample.

The BJH method (Barret *et al.* 1951) was employed to obtain the mesopore size distribution (20-950 Å). For the calculations, pores were assumed to be slit-shaped.

Figure 86 presents nitrogen adsorption isotherms obtained for the different powder samples. For the six samples coming from Grimsel, the curves are closely superimposed, no modification of the pore size distribution is evidenced. However, differences could be noticed between the treated and the reference (FO) samples. The beginning of the curve looks similar, and calculation of BET surface area (Figure 87) shows that the volume needed to fill the monolayer is quite the same for all the samples, FO included. However, the end of the adsorption branch goes to higher adsorbed volumes for the treated samples and

the hysteresis is less marked, indicating a more continuous distribution in pore size.

Surface area of the powder samples stays in a small range of values, between 64 m²/g and 77 m²/g with no evident evolution for the samples 27 to 32 (Figure 87a). From *t*-plot analysis, the external surface area, which is equivalent to the non-microporous surface area (pore radius > 20 Å), could be determined (Figure 87b). The ratio “external surface area / surface area” reveals that there is an increase of the quantity of high size pores for all the samples BS29’s. This increase is associated with the decrease of micropores volume (Figure 87c) and the increase of mesopores volume deduced from BJH analysis (Figure 87d).

The adsorption analyses have been performed also on compacted samples. We have seen on the reference sample F0 that there was no strong difference between powder and compacted sample concerning nitrogen adsorption (Figure 88a and Table XXXII). This is not true for the treated samples, for which much lower BET surface areas α_s (between 32 and 40 m²/g) were obtained for compacted than for powder samples (Figure 88b and Table XXXII).

Concerning the powder samples, there is no progressive change of the surface area with the distance to the heater, and thus no link can be established between the temperature suffered by bentonite samples and their pore size distribution. However, since a general decrease of microporosity has been observed in all the treated samples, it must be related to the overall increase of water content that has taken place

during the operation phase all through the barrier. Actually, even in the inner part of the buffer the water content increased during the cooling phase preceding dismantling. This hydration could explain the closure of some pathways to the porosity and thus could explain the microporosity decrease. The decrease of microporosity associated with relatively constant surface areas suggests that inter-aggregate porosity is unchanged although intra-particle porosity is affected by the thermo-hydraulic conditions occurring in the gallery.

Water adsorption gravimetry

Water vapour gravimetric adsorption experiments were carried out using a lab-built quasi-equilibrium setup designed around a Setaram MTB 10-8 symmetrical microbalance. Water vapour was supplied to the sample (thermostated at 30 °C) from a source kept at 41 °C at a slow flow rate to ensure quasi-equilibrium conditions at all times (Poirier *et al.* 1987). The simultaneous recording of mass uptake and equilibrium pressure directly yields the water vapour adsorption isotherm. The initial sample weight was 110.7 mg and they were outgassed at 110 °C during 18 h under a residual pressure of 0.1 Pa.

Figure 89 presents the water adsorption curves obtained for the reference sample F0 and the treated samples BS29-27, BS29-29 and BS29-32. Because of the different water contents reached by each sample according to its position inside the barrier, the initial state of the four bentonites is not equiva-

Table XXXII
BET analysis results for the reference and BS29 samples.

| Sample reference | α_s , BET (m ² /g) | C_{BET} | Monolayer volume (cm ³ /g) |
|-------------------|--------------------------------------|-----------|---------------------------------------|
| F0 compacted | 69 | 414 | 15.86 |
| F0 powder | 77 | 505 | 17.71 |
| BS29-31 compacted | 43 | 277 | 9.8 |
| BS29-31 powder | 75 | 332 | 17.3 |
| BS29-32 compacted | 38 | 269 | 8.7 |
| BS29-32 compacted | 45 | 320 | 10.3 |
| BS29-32 powder | 70 | 395 | 15.9 |
| BS29-32 powder | 64 | 213 | 14.6 |

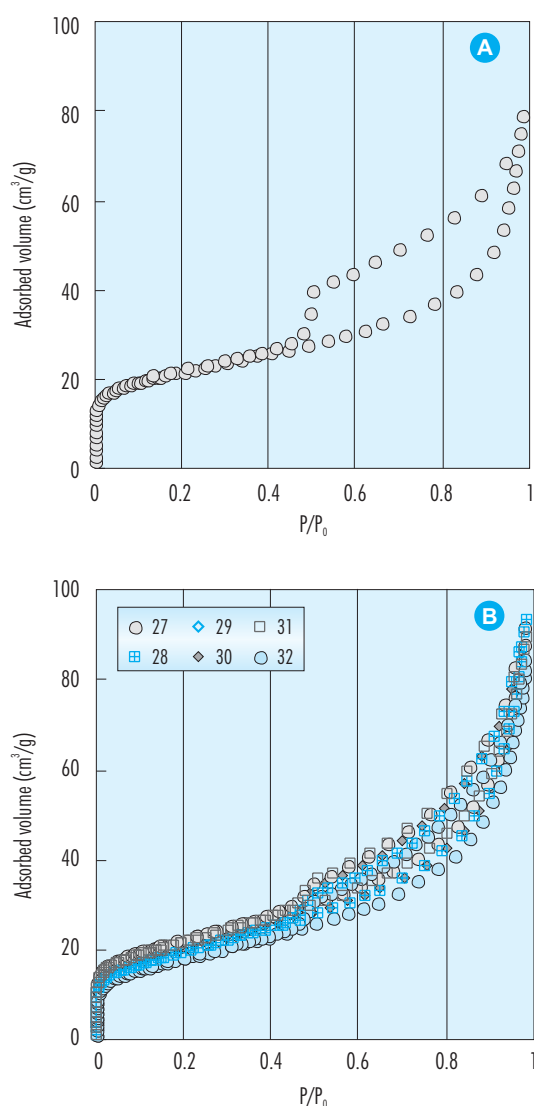


Figure 86: Nitrogen adsorption isotherms for powder samples: A) reference bentonite FO, B) BS29 samples 27 to 32.

lent, in spite of identical outgassing conditions before the water adsorption experiment. This different initial state explains why these samples display different shapes for the adsorption branch. In the case of water adsorption, the surface areas can be calculated using two different cross-sectional areas for adsorbed water molecules. Indeed, one has to consider the presence of water molecules interactions with the solid surface, which induce an increase of the occupied area on the surface. Thus, for water molecules in liquid state, the cross-sectional area A'

is taken as 10.6 \AA^2 (Gregg & Sing 1982), and for water molecules in interaction with solid surface, A' is taken as 14.8 \AA^2 (Harkins & Jura 1944). The calculated surface areas are shown in Table XXXIII. The three postmortem samples display lower surface areas than the reference sample, and this decrease of surface area is greater for BS29-27 than for the two other samples. The adsorption curves for BS29-32 (inner) and BS29-29 (middle) are almost superimposed, and therefore, calculated surface areas are similar for these two samples. Since BS29-27 is the

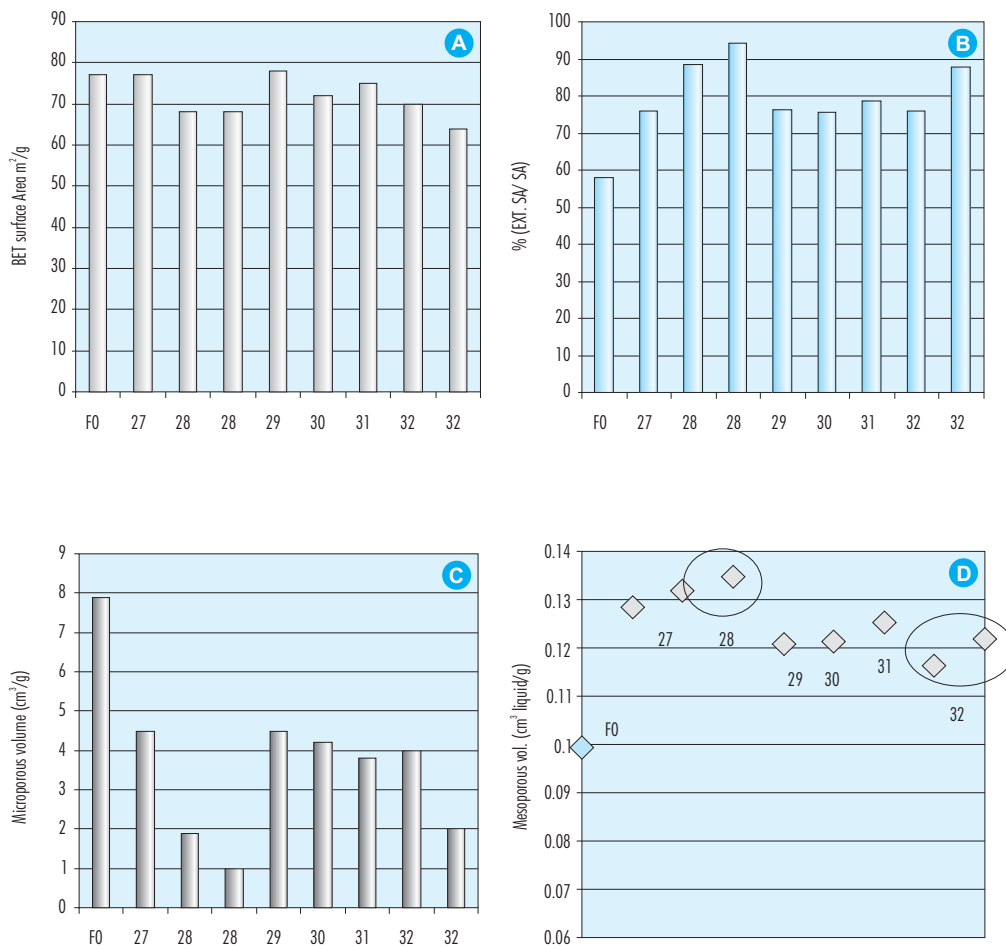


Figure 87: Nitrogen adsorption data analysis of powder samples: A) BET surface area, B) external surface area calculated from t-plot, C) micropore volume calculated from t-plot, D) mesoporous volume calculated with the BJH method on the adsorption branch with a slit-shaped pore model.

Table XXXIII
Surface areas (a_s) calculated from water adsorption in BS29 samples considering a monolayer with different cross-sectional areas of the water molecule.

| a_s (m ² /g) | 10.6 Å ² | 14.8 Å ² |
|---------------------------|---------------------|---------------------|
| F0 | 344 | 480 |
| BS29-27 | 192 | 269 |
| BS29-29 | 247 | 345 |
| BS29-32 | 263 | 367 |

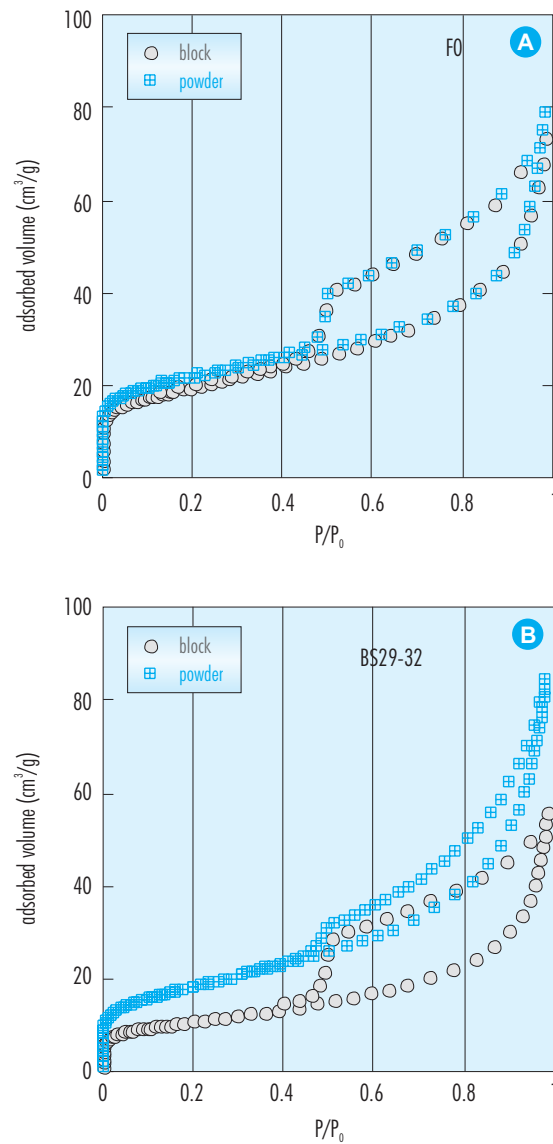


Figure 88: N₂ adsorption isotherms for compacted and powder samples: A) FO, B) BS29-32.

outer sample, its thermo-hydraulic story gives place to a high degree of saturation for the whole duration of the *in situ* test. This high degree of water saturation could have provoked a reordering of clay platelets, resulting in a decrease of intra-aggregate porosity. This surface area reduction should be more visible for water adsorption than for nitrogen adsorption since water molecules are supposed to reach the totality of pore volume and interlayer space.

The desorption branch is quite similar for the four samples. Usually, the reproducibility of water adsorption process for a same sample is checked on the desorption branch, assuming that the saturated state is equivalent for all the samples. Therefore, it can be assumed that BS29-29 and BS29-32 were not strongly modified, and not in an irreversible way: after saturation, the curves follow the same path of desorption as for FO. Although sample BS29-27 displayed a clearly different adsorption curve, the de-

sorption finally reached back the reference bentonite desorption curve ($P/P_0 < 0.3$), suggesting that the observed modifications are reversible.

4.3.4. VTT: Chemical changes caused by the concrete seal into bentonite

To study the extension of the chemical changes caused by the concrete seal into the bentonite, two concrete/bentonite core samples (C/BS7-15 and C/BS7-16) were taken at the middle and outer ring of section S7 by drilling through the concrete plug into the bentonite. Dry drilling was used in the bentonite in order to avoid its wetting. The samples were sealed in plastic bags, from which the air was evacuated, and the bags were then closed in metallic transportation vessels. The vessels were flushed with nitrogen in order to keep the samples in a low-oxygen condition. The sample vessels were then transported to Finland.

The sample vessels were opened in a nitrogen glove box where the oxygen content was 30-300 ppm. The diameters of both bentonite samples were about 70 mm. The length of the bentonite core of

the sample C/BS7-15 was 100 mm and that of C/BS7-16 about 140 mm.

The samples were sawn with a band saw into smaller pieces. Figure 90 shows the treatment procedure for the bentonite sample C/BS7-16, which was selected for detailed studies. The bentonite core was first split into smaller slices, 5 to 25-mm thick, in order to avoid diffusive transport of the components in the pore water. The slices were numbered from C/BS7-16/1 to C/BS7-16/10, starting from the concrete-bentonite interface. The slices were then closed in gas-tight plastic vessels and moved into a better glove box for further treatment. The oxygen content in this glove box was 2-4 ppm.

The surface of the sample cylinder had been in contact with the air during drilling. Drilling had also heated and possibly dried the sample surface somewhat. To decide the depth to which the surface of the core had to be taken away, the water content profile along the diameter of the bentonite core was determined for a 5-mm thick slice of C/BS7-16/6. Slightly lower water content could be seen in the 5-mm thick external surface of the core. In order to obtain representative samples for the analysis, the surface was removed from all slices to a depth of 5 mm.

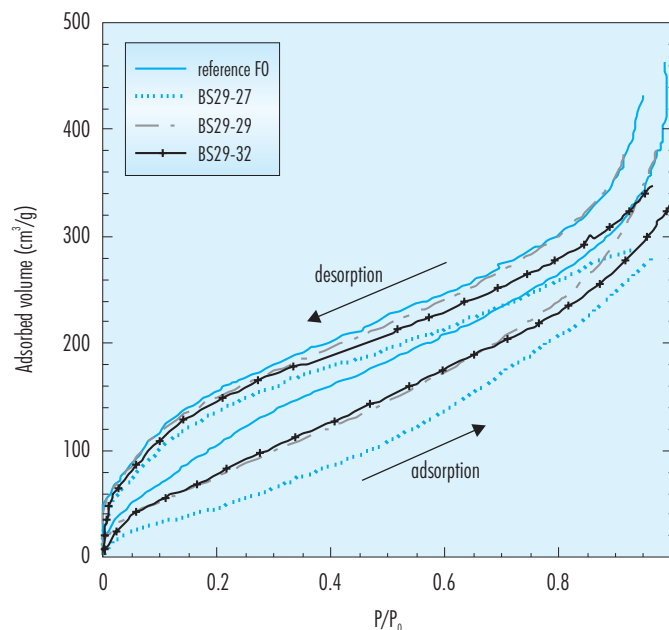


Figure 89: Water adsorption gravimetry for FO, BS29-27, BS29-29 and BS29-32 samples.

Cylindrical subsamples were cut from the slices of C/BS7-16 for squeezing of the pore water. From the same slices, subsamples were taken also for water content measurement and measurement of occupation of the exchangeable cations.

The extension of the chemical changes was studied by analysing the pore water chemistry and exchangeable cations vs. the distance from the concrete/bentonite interface. Squeezing of the pore waters was carried out in a nitrogen glove box in titanium cells, as shown in Figure 91. The pressure was increased stepwise to about 100 MPa and the pore water was collected in a syringe.

The analyses of the pore water were carried out by the methods described in Figure 92. More details of the methods are given in Muurinen (2001). The water content of the bentonite was determined by drying the sample at 105 °C. The dried samples were used for determination of the occupation of the exchangeable cations. The determination was carried out by the method given by Müller-Vonmoos & Kahr (1983), where the cations are released with NH_4SCN in ethanol.

The water content in the clay at different distances from the interface before and after the squeezing

was determined. No systematic change in the water content vs. the distance from the interface could be seen. An average water content of 26 percent was found in the proximity to the concrete plug. The volume of pore water squeezed in each subsample varied between 1.44 and 2.01 mL.

Table XXXIV presents the concentrations and other measured parameters in the squeezed pore waters. The pH values vary from 8.25 to 8.32. The measured concentrations of S(-II) and Fe^{2+} were below the determination limits (0.2 mg/L) of the methods. There is large scattering in the Eh values, but no systematic dependence on the distance from the interface can be seen.

Figure 93 presents the concentrations of major cations and anions and their total concentrations in the pore waters. The values are given in meq/L to make comparison of the charge balance possible. The charge balance is rather good, i.e. within a few percent. There is systematic change in the total dissolved solids vs. the distance from the surface. The chloride and magnesium concentrations increase clearly and sodium and sulphate decrease somewhat at longer distances from the interface.

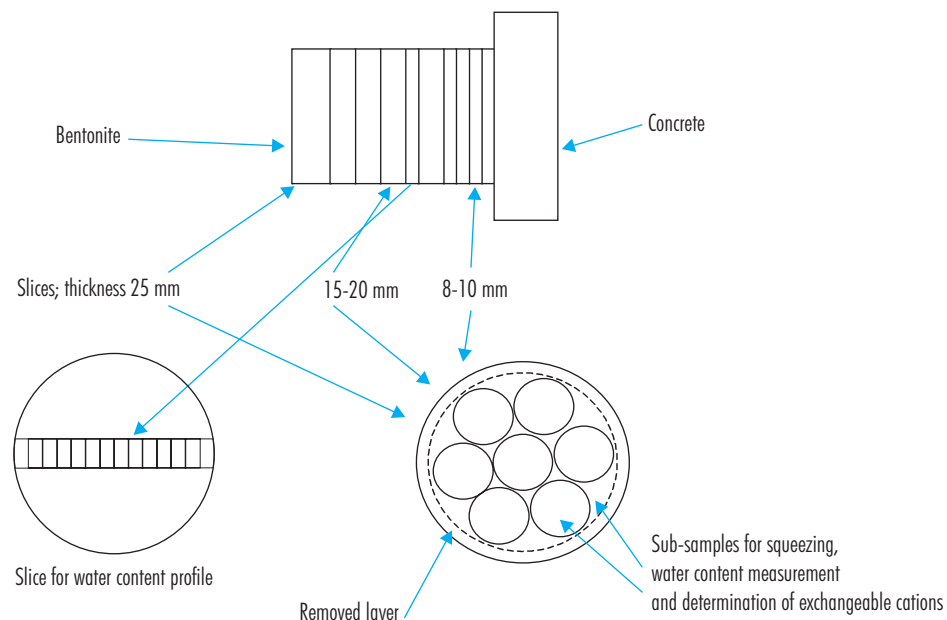


Figure 90: Schematic presentation of splitting of the bentonite sample C/BS7-16 for different studies.

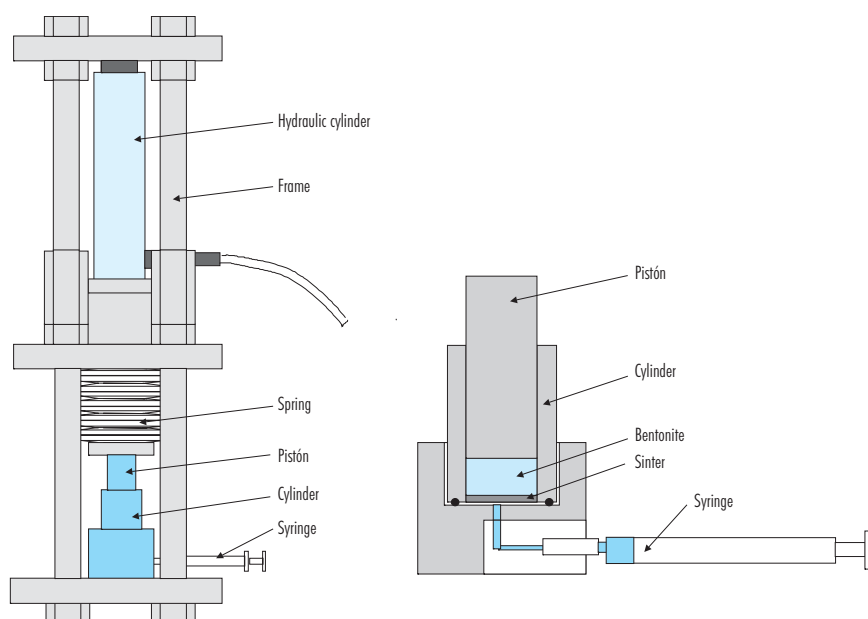


Figure 91: Apparatus for squeezing of pore waters.

Table XXXIV
Composition of the pore water squeezed in different slices of the sample C/BS7-16 (meq/L).

| Sample/slice | pH | Eh (mV) | Na ⁺ | Ca ²⁺ | Mg ²⁺ | HCO ₃ ⁻ | Cl ⁻ | SO ₄ ²⁻ |
|--------------|------|---------|-----------------|------------------|------------------|-------------------------------|-----------------|-------------------------------|
| 16/1 | 8.25 | -58 | 64.0 | 13.4 | 3.0 | 1.4 | 52.0 | 26.8 |
| 16/2 | 8.25 | -115 | 57.7 | 10.4 | 2.8 | 1.1 | 50.3 | 22.4 |
| 16/5 | 8.29 | -18 | 54.6 | 10.6 | 7.2 | 1.2 | 52.9 | 22.2 |
| 16/8 | 8.32 | -52 | 54.9 | 9.6 | 10.0 | 1.2 | 54.2 | 21.8 |
| 16/10 | 8.28 | -74 | 55.8 | 11.6 | 14.0 | 1.1 | 60.3 | 20.2 |
| Uncertainty | ±0.1 | ±50 | ±10 % | ±15 % | ±15 % | ±20 % | ±15 % | ±15 % |

The cation occupation in the bentonite is presented in Table XXXV. For comparison the values given by Fernández *et al.* (2004) (Table VI) for initial FEBEX bentonite have been included in the table. The dependence on the distance from the interface is clarified in Figure 94. It seems that the CEC has decreased from the initial value near the concrete-bentonite interface and the CEC value increases while

going deeper into the bentonite. At the depth of the sample length (140 mm) CEC has approximately reached the initial CEC of the FEBEX bentonite. The decreased CEC possibly indicates the change caused by the concrete in the bentonite. There are also systematic changes in the concentrations of the individual cations as a function of the distance to the concrete surface.

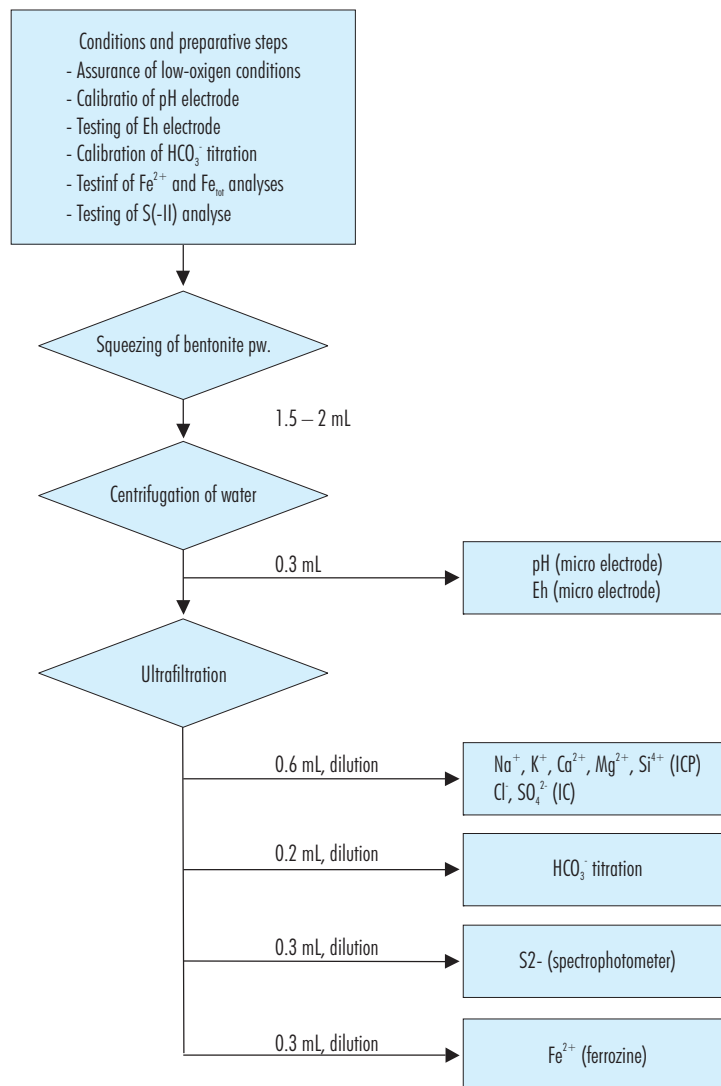


Figure 92: Methodology for the analysis of the squeezed pore waters.

4.4. Thermo-hydro-mechanical tests

The aim of the thermo-hydro-mechanical tests is twofold: (1) to characterise the actual state of the bentonite and (2) to determine the possible changes in its thermo-hydro-mechanical properties occurred during the experiment, due to the combined effect of temperature, water content, joints and solutes. The THM tests can be divided into six inter-related groups: tests to determine basic properties, tests for the study of microstructural changes, tests to under-

stand the water flow, tests to determine the changes in the mechanical properties of the clay, tests to determine the changes in the thermal properties of the clay and tests in joints.

The database acquired during FEBEX I and II on the properties of the untreated clay (ENRESA 1998a, 2000; CIEMAT 1999; UPC 1999; Villar 2000, 2002; Lloret *et al.* 2002, 2004; Villar *et al.* 2002b) has been used as reference, although some properties have been also determined in intact blocks that

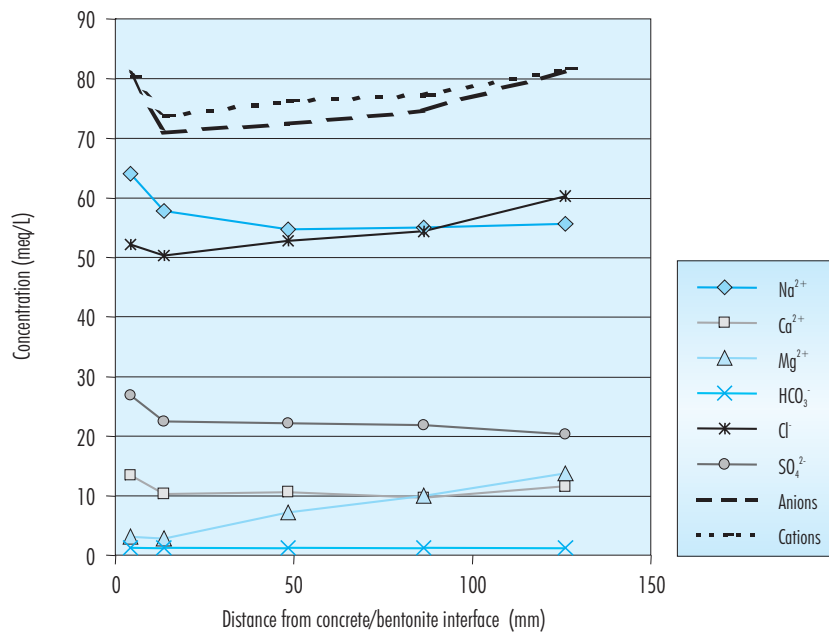


Figure 93: Concentrations in the squeezed pore water at different distances from the concrete/bentonite interface.

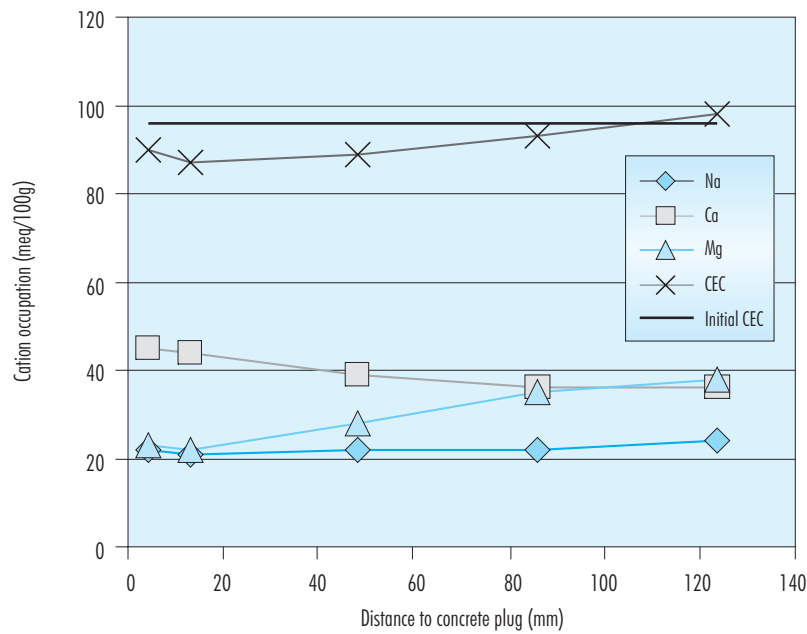


Figure 94: Occupation of exchangeable cations at different distances from the concrete/bentonite interface together with CEC before and after the experiment.

Table XXXV
Occupation of exchangeable cations in the bentonite samples of the *in situ* experiment and initial FEBEX bentonite (meq/100g).
Uncertainty of the measured values is $\pm 15\%$.

| Sample/slice | Na ⁺ | K ⁺ | Ca ²⁺ | Mg ²⁺ | CEC |
|----------------------------|-----------------|----------------|------------------|------------------|-----|
| 16/1 | 22 | < 2 | 45 | 23 | 90 |
| 16/2 | 21 | < 2 | 44 | 22 | 87 |
| 16/5 | 22 | < 2 | 39 | 28 | 89 |
| 16/8 | 22 | < 2 | 36 | 35 | 93 |
| 16/10 | 24 | < 2 | 36 | 38 | 98 |
| Initial FEBEX ¹ | 27 | 3 | 35 | 31 | 96 |

¹ Fernández et al. 2004, Table VI.

were not installed in order to have another reference (Work performed by CTU-CEG).

Thermo-hydro-mechanical tests have been performed in samples from sections S19, S23, S28 and S31 by CIEMAT, and in samples from section S7, S12, S19 and S28 by CTU. In each sampling section, 9 or 12 complete blocks belonging to 3 or 4 different radii have been taken and sent to the different laboratories. Tests on joints have been performed by Euro-Géomat on samples taken from sections S11 and S29 that were sent directly from the GTS to their laboratory. EIG EURIDICE performed hydraulic conductivity tests in samples from sections S12 and S19.

4.4.1. CIEMAT: Basic characterisation and THM properties

4.4.1.1. Sampling at the laboratory

The laboratory determinations were carried out at CIEMAT facilities from September 2002 to December 2003. Each block was unpacked only once in order to take the subsamples for the different determinations (THG, THM or tracers). The sampling was coordinated so that to be able to make the tests immediately after unpacking and sampling. The blocks have been half-sectioned along the radius, in order to obtain material for the THM and THG tests (Figure 95). In order to obtain a more detailed sampling, samples have been taken in different positions along the radius of the block. The subsamples obtained in this way have been referenced by adding a consecutive number to the initial reference of the block. The numbers have been given starting by the side of the block closer to the gallery wall.

All the THM tests have been performed on undisturbed samples, that have been obtained mostly by dry drilling and subsequent trimming to the appropriate dimensions (Figure 96). In those tests in which the sample must be saturated prior to the determination, deionised water has been used.

4.4.1.2. Retention curves

The retention curve has been determined for six samples from one of the sampled radii in two sections around the heater (S23 and S31), at the inner, outer and middle ring of the bentonite barrier. Two samples of each block have been trimmed with cylindrical cutters. The resulting height of the specimens was between 1.3 and 1.6 cm and their diameter was of 3.4 cm for samples from section S23 and between 3.3 and 5.1 cm for samples from section S31.

The specimens thus prepared were placed in desiccators with sulphuric acid, so that to apply a given suction to the samples by means of the control of the relative humidity. The samples are not confined during the determination and they can freely swell or shrink. The samples were initially submitted to a suction of 4 MPa, what meant for most of them an increase of water content and a decrease of dry density. Afterwards they were progressively dried by applying increasingly higher suctions: 14, 33, 75 and 120 MPa. The latter value corresponds approximately to the suction the blocks had prior to their installation in Grimsel (room temperature and relative humidity.) The samples were subjected to each suction for at least two months, a period of time to guarantee equilibrium. After each suction step the samples were weighed and measured to determine their water content and dry density. Once the reten-



Figure 95: Sectioning of a block for THM (left) and THG determinations (right).



Figure 96: Drilling of blocks to obtain samples for the THM determinations.

tion curve determination completed, the samples were measured and dried in the oven at 110 °C for 24 hours to check their final density and water content. The determinations were performed at 20 °C.

The results obtained for section S23 are shown in Figure 97 and Figure 98 and for section S31 in Figure 99 and Figure 100 (see Villar 2003 for further details). In these figures the initial conditions of the samples are indicated by a line. The samples closer to the gallery wall had initial higher water contents and lower dry densities. After being subjected to a suction of 4 MPa most of the samples experienced a density decrease and an increase of water content, except for the samples taken from the block closer to the gallery wall in section S23 whose water contents barely changed. In the following suction steps the water content of all the samples progressively decreased and the dry density increased. The evolution of all the samples is quite similar, despite their positions in the barrier. Moreover, the initial differences attenuate as the suction applied is higher. However, the initial differences in dry density among the different samples remain during the determination of the whole retention curve: the samples with higher initial dry density swelled more during the ini-

tial wetting and their density remains lower in the course of the entire determination.

The evolution of water content in wetting paths for untreated FEBEX clay obtained with Equation 4 for initial dry densities of 1.40 and 1.60 g/cm³ has been drawn in Figure 101 together with the results obtained for the samples from section S23. The results obtained for the samples from section S31 are plotted in Figure 102. Although the path followed by the samples from Grimsel has been of sudden wetting (from the initial suction to suction 4 MPa, not shown in the figures) and subsequent drying to suction 120 MPa, it is patent that the evolution of water content experienced by the samples from sections S23 and S31 is in the order of that expected for untreated FEBEX samples of similar initial dry density. The tendency towards a higher retention capacity observed in the samples from Grimsel can be accounted for by hysteresis, since the water content for a given suction is slightly higher in a drying after wetting path than in a wetting path (Villar 2002, Lloret *et al.* 2002, Villar *et al.* 2002b).

On the other hand, the relative humidity of some of the blocks from Grimsel has been measured with capacitive sensors in the laboratory. The plastic and

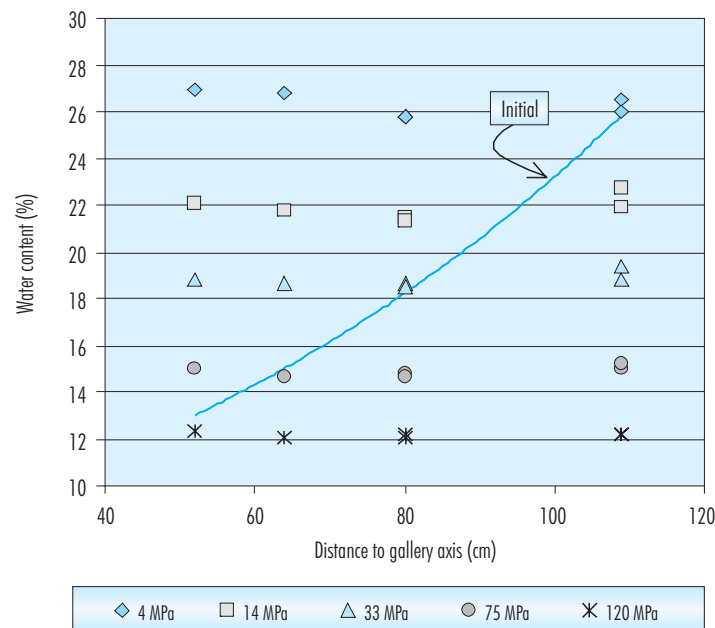


Figure 97: Water contents reached under different suctions for samples from section S23.

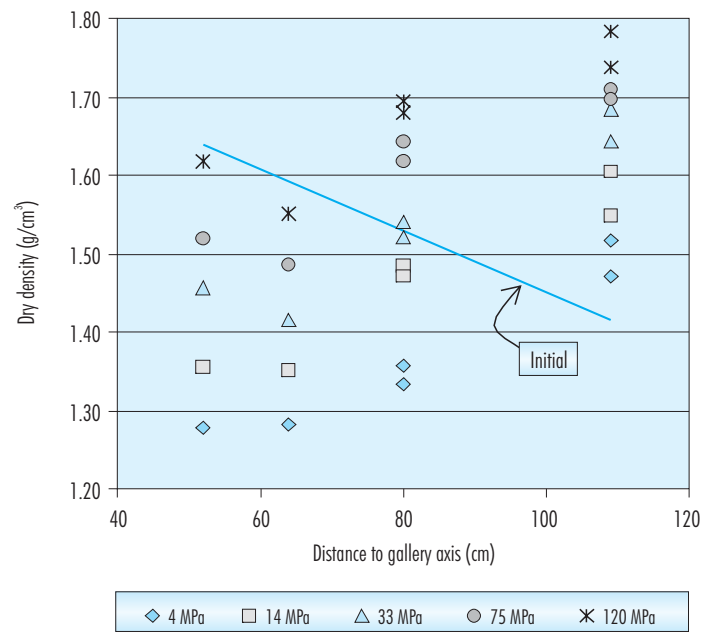


Figure 98: Dry densities reached under different suctions for samples from section S23.

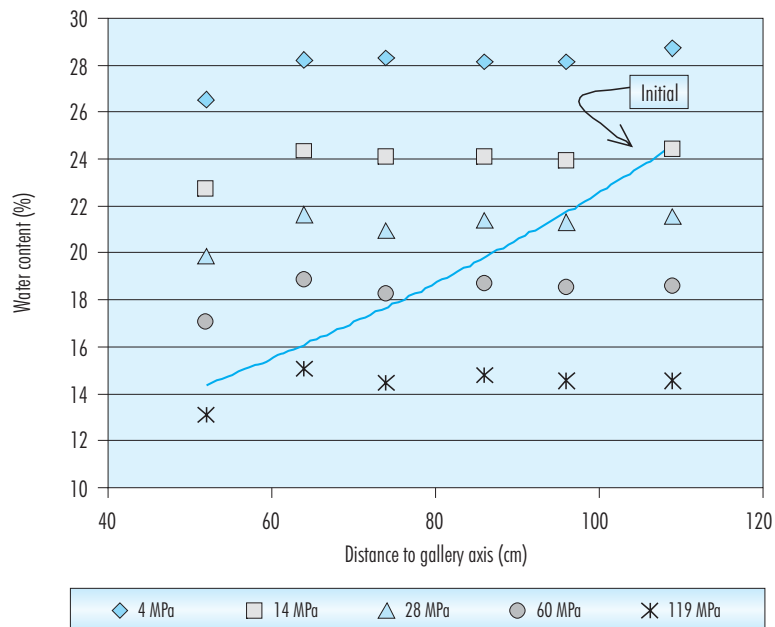


Figure 99: Water contents reached under different suctions for samples from section S31.

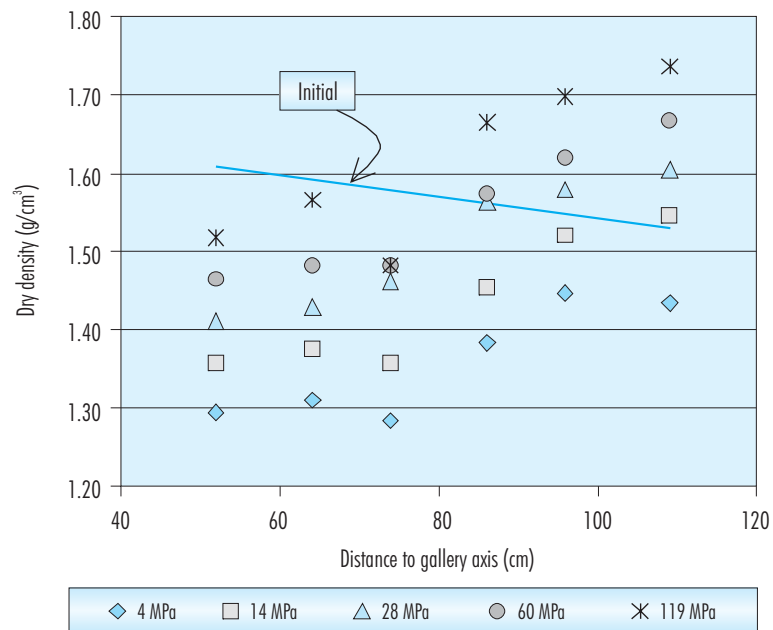


Figure 100: Dry densities reached under different suctions for samples from section S31.

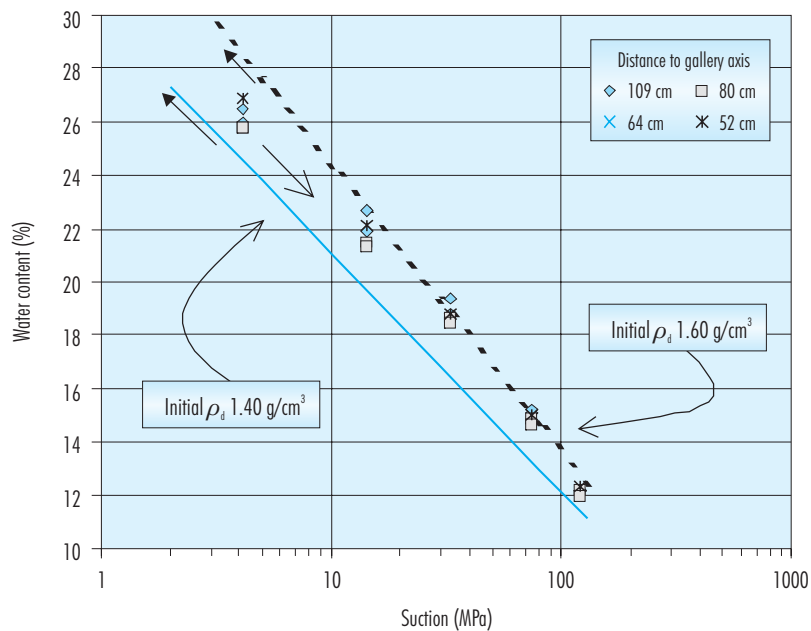


Figure 101: Evolution of water content in a drying path for samples from section S23. The lines correspond to untreated FEBEX bentonite in wetting paths (obtained with Equation 4).

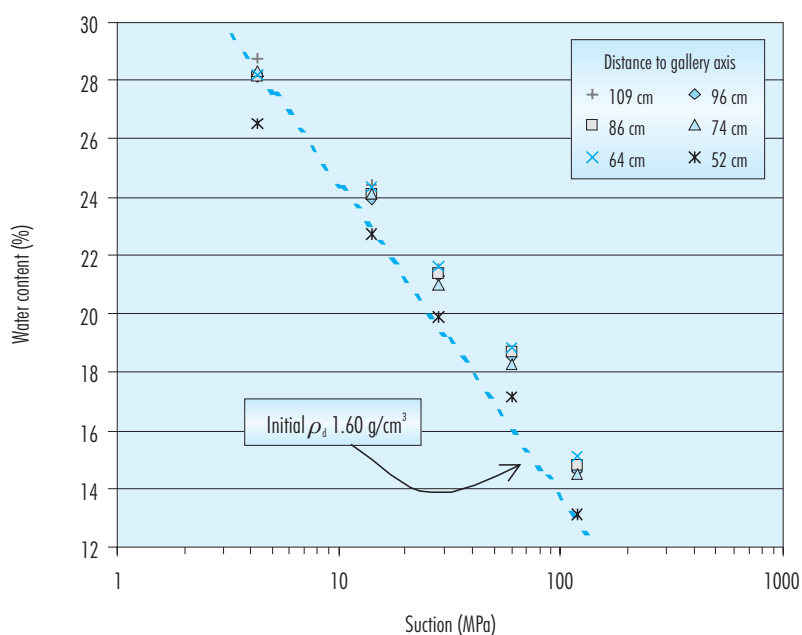


Figure 102: Evolution of water content in a drying path for samples from section S31. The line corresponds to untreated FEBEX bentonite in a wetting path (obtained with Equation 4).

aluminium foil bags were removed and, with the block wrapped in plastic foil, two holes were drilled in it to install the relative humidity sensors inside (Figure 103). When the integrity of the block allowed for it, the holes were drilled in external and internal positions with respect to the gallery axis. The clay block-sensors assembly is left for 3-4 hours to stabilise and afterwards the measures are taken. To convert the values of relative humidity to suction values the Kelvin's law has been used (Equation 7).

Most of the measurements were performed in August 2003, when the blocks had already been unwrapped and sampled once. This could have given place to modifications of their water contents with respect to the original ones. In fact it seems that there has been an homogenisation of the water content inside the blocks, since the suctions measured in different positions are frequently similar. The suction values measured are plotted in Figure 104 as a function of the position in the barrier, indicated as distance to the gallery axis. The values registered by the sensors placed in Grimsel in sections C, E1 and F1 just before the dismantling are also plotted in the figure. There is a good agreement between the measurements taken in the laboratory and

those taken *in situ* before dismantling, what corroborates the inertia of the blocks to change their water contents if they are well packed and the reliable performance of the *in situ* instrumentation.

The suction values measured in the laboratory have been related to the water contents determined in the same blocks and in the same positions (section 4.1.2) and are plotted in Figure 105 in the form of a retention curve. The curve determined for untreated FEBEX bentonite compacted at dry density 1.60 g/cm^3 in constant volume cells kept in desiccators with sulphuric acid solutions is also plotted in the figure (Figure 3, Lloret *et al.* 2004). This curve was obtained following a wetting path, which is the same process experienced by the samples from Grimsel. The samples with dry density lower than 1.60 g/cm^3 have higher water contents for the same suction than the untreated sample with density 1.60 g/cm^3 , while the contrary happens for samples of higher dry density, which is the expected trend. Overall, the points obtained in the blocks from Grimsel follow closely the curve for the untreated samples, and no appreciable change of the retention capacity of the FEBEX clay after five years under repository conditions has been detected.



Figure 103: Capacitive sensors installed in two different positions of a block from Grimsel.

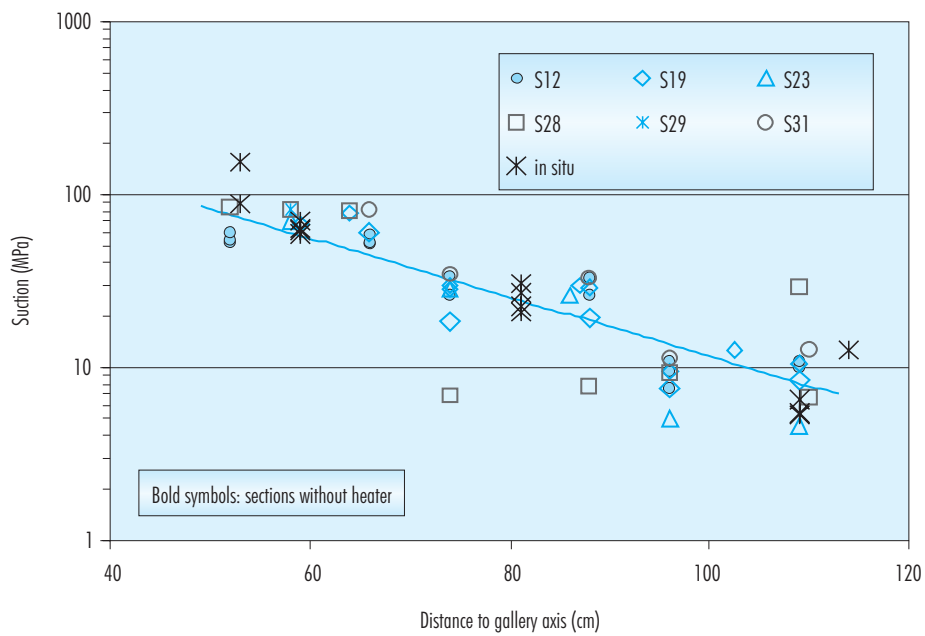


Figure 104: Suction values measured with capacitive sensors in situ before dismantling (instrumented sections C, E1 and F1) and in laboratory. The line is a fitting for all the laboratory measurements.

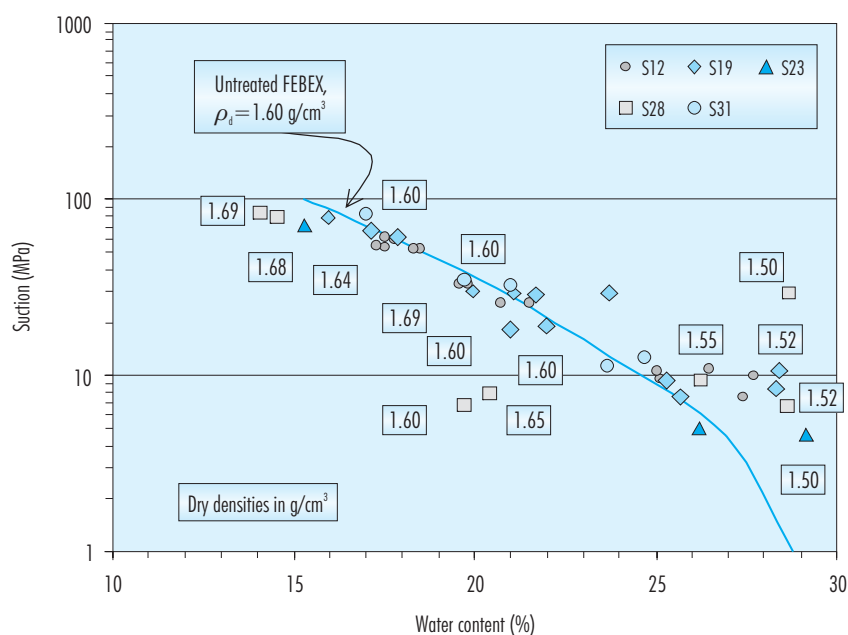


Figure 105: Retention curve as determined from sensor measurements at laboratory in blocks from different sections (points) and determined in untreated FEBEX samples by control of relative humidity at constant volume (line).

4.4.1.3. Porosimetry

Out of the context of the EC Contract, CIEMAT has performed analysis of pore size distribution by mercury intrusion porosimetry in 25 samples, taken along different radii from the sampling sections around the heater S19, S23, S28 and S31.

This technique allows the determination of the pore size distribution by injecting mercury into the sample at different pressures while controlling the volume intruded. The pressure applied can be related to the minimum pore diameter intruded, taking into account the characteristics of the fluid. The ratio of the volume of mercury intruded (pore volume) to applied pressure (which conditions the minimum pore diameter) allows distribution curves to be obtained establishing the percentage of pores of a size included within a given range.

For this work a Poresizer 9320 porosimeter by Micromeritics was used, with a mercury injection pressure range of 7 kPa to 210 MPa, this allowing pore diameters of between approximately 200 and 0.006 μm to be measured. Consequently, the mercury does not intrude the microporosity (pores of a size of less than

0.002 μm , according to the classification of Sing *et al.* 1985). The mercury intrusion method allows access to be gained only to the macroporosity and to part of the mesopores. Before the samples are inserted in the porosimeter, the water is removed from the pores by freeze-drying. The data obtained are given in accordance with the following key (Tuncer 1988):

- e_1 : void ratio calculated from the experimental measurement of specific gravity (with pycnometers: 2.70 g/cm^3) and dry density (by immersion in mercury, see section 4.1.2).
- e_2 : void ratio calculated by mercury intrusion in the porosimeter (or apparent void ratio).
- % total: total percent of pores intruded by mercury.
- ϕ avg. (μm): average pore diameter.
- % large, medium or small: percent of large pores volume (diameter greater than 6 μm), medium-sized pores (diameter between 6 and 0.12 μm) or small pores (diameter between 0.12 and 0.006 μm) with respect to the total volume of intruded pores. This size classifica-

tion was developed on the basis of porosimetry results obtained from all the clay samples from Grimsel analysed, and includes only macro and mesoporosity. The limits between families may vary slightly between different samples.

- Large, medium or small pore mode (μm).
- Unif.coef.: uniformity coefficient of pores ϕ_{40}/ϕ_{80} .

Figure 106 shows a typical porosimetric curve for a sample of untreated FEBEX bentonite compacted at dry density 1.70 g/cm^3 and for two samples taken from Grimsel. The three main families of pores (large, medium and small) may be appreciated in the three samples, the difference among them being the percentage of each family. A summary of the porosimetric data obtained is shown in Table XXXVI, in which the results have been grouped according to the position of the samples in the barrier: external, intermediate or inner ring. The results obtained for the untreated FEBEX bentonite compacted at dry density 1.68 g/cm^3 with hygroscopic water content –which are approximately the initial conditions of the blocks placed in Grimsel– are also included in the Table (Villar 2002). Figure 107 shows the distribution of pore sizes obtained for the external, inter-

mediate and internal rings of the barrier and the average distribution for specimens of untreated FEBEX bentonite. The analysis of these results reveals that after being subjected for five years to repository conditions, the bentonite seems to have experienced a redistribution of the size of pores, which is more homogeneous and with a higher average diameter, since the modes of all the pore families have increased. This causes higher uniformity coefficients. There is a relative increase of the percentage of large pores not related to the position of the samples in the barrier. However, the relative percentage of medium pores decreases with respect to the initial one towards the gallery wall while the percentage of small pores decreases with respect to the initial one towards the heater. There is also an overall increase of the percentage of the total porosity that is intruded by mercury in the samples from Grimsel, which maybe simply a consequence of the higher porosity of these samples (their dry density is lower) or may imply either a decrease of pores with a size of less than $0.006 \mu\text{m}$ (equipment access limit), or more probably, an increase of interconnected pores. In any case, the percent of the porosity intruded by the mercury is fairly low, this meaning that there

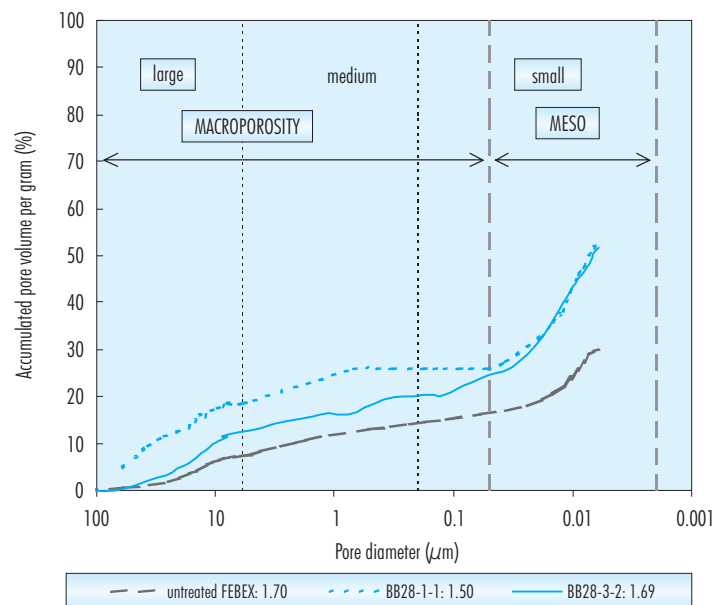


Figure 106: Accumulated porosimetric curve for untreated FEBEX bentonite and two samples from Grimsel, with indication of dry density in g/cm^3 (the percentages are recalculated according to the percentage of total porosity actually intruded by mercury).

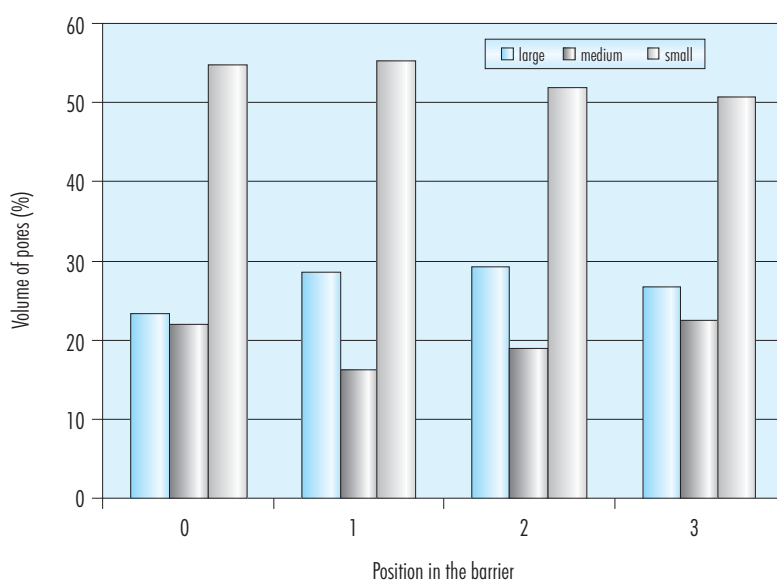


Figure 107: Distribution of large (> 6 μm diameter), medium (between 6 and 0.15 μm) and small (between 0.15 and 0.006 μm) pores obtained by mercury intrusion in the untreated bentonite compacted at 1.68 g/cm^3 with hygroscopic water content (0), and external (1), intermediate (2) and inner (3) rings of the clay barrier.

Table XXXVI

Data on porosimetry by mercury intrusion in the external, intermediate and inner rings of the bentonite barrier and for the untreated FEDEX bentonite

| | EXTERNAL | INTERM. | INNER | UNTREATED |
|-------------------------------------|-------------------|-------------------|-------------------|-------------------|
| No. of samples | 8 | 9 | 9 | 15 |
| Water content (%) | 26 \pm 2 | 20 \pm 1 | 16 \pm 1 | 14 \pm 1 |
| ρ_d (g/cm^3) | 1.55 \pm 0.04 | 1.62 \pm 0.02 | 1.65 \pm 0.03 | 1.68 \pm 0.19 |
| e_1 | 0.748 \pm 0.049 | 0.666 \pm 0.019 | 0.635 \pm 0.031 | 0.640 \pm 0.281 |
| e_2 | 0.400 \pm 0.099 | 0.364 \pm 0.032 | 0.359 \pm 0.090 | 0.193 \pm 0.088 |
| % total | 54 \pm 16 | 55 \pm 6 | 56 \pm 12 | 34 \pm 17 |
| Avg. diameter (μm) | 0.02 \pm 0.00 | 0.04 \pm 0.03 | 0.03 \pm 0.01 | 0.02 \pm 0.02 |
| % large | 28 \pm 6 | 29 \pm 4 | 27 \pm 7 | 23 \pm 5 |
| Mode large (μm) | 42 \pm 4 | 36 \pm 16 | 38 \pm 19 | 20 \pm 12 |
| % medium | 16 \pm 3 | 19 \pm 3 | 22 \pm 4 | 22 \pm 5 |
| Mode medium (μm) | 0.94 \pm 0.35 | 0.83 \pm 0.25 | 0.99 \pm 0.35 | 0.60 \pm 0.06 |
| % small | 55 \pm 7 | 52 \pm 5 | 51 \pm 10 | 55 \pm 6 |
| Mode small (μm) | 0.014 \pm 0.002 | 0.014 \pm 0.003 | 0.016 \pm 0.003 | 0.014 \pm 0.004 |
| Unif. coef. | 145 \pm 123 | 101 \pm 73 | 115 \pm 174 | 44 \pm 33 |

is still an important volume of pores with a size of less than $0.006\ \mu\text{m}$ or not interconnected.

The final interpretation of these results must be done taking into account the differences in the dry density and water content of the samples: the dry density of the samples from Grimsel is lower than that of the untreated sample considered, while the water contents are higher. The overall increase of volume experienced by the samples at the barrier (which implies a decrease of dry density from that of the compacted blocks $-1.70\ \text{g/cm}^3$ to the average dry density of the barrier $-1.58\ \text{g/cm}^3$, see section 4.1.2) is probably responsible of the increase of large pores.

4.4.1.4. Hydraulic conductivity

CIEMAT has determined the hydraulic conductivity of six samples taken from two sections (S19 and S28), at different distances from the heater along a sampling radius.

The theoretical principle on which the method used to determine the hydraulic conductivity is based is that of the fixed load permeameter. Basically, it consists in measuring against time the volume of water that passes through a specimen, confined in a rigid cell preventing it from deforming, to which is applied a constant hydraulic gradient between the upper and lower parts. For this purpose a hydraulic head, that is to say, a difference in potential, is applied between the upper and lower parts of the previously saturated sample. The complete saturation of the sample and associated swelling guarantee perfect contact with the walls of the cell, preventing the flow of water between these and the sample. At the same time, the flow of water passing through the specimen is measured versus time (Villar 2002).

The undisturbed samples have been adapted to the diameter of the cell ring by working them with a cylindrical cutter, attempting not to modify either their moisture or density. The nominal dimensions of the sample are $19.63\ \text{cm}^2$ in surface area and $2.50\ \text{cm}$ in length. The sample is saturated at $0.6\ \text{MPa}$ from both faces with deionised water for a time period usually established at a minimum of two weeks. Once the sample is saturated, the hydraulic gradient is applied by increasing the injection pressure at the lower part of the cell, while the downstream pressure is maintained at $0.6\ \text{MPa}$. The values of hydraulic head applied have ranged from $1.2\ \text{MPa}$ to $1.6\ \text{MPa}$, depending on the dry density of the specimen and its permeability. An automatic volume change apparatus is installed between the upper inlet of the

cell and the backpressure system. This device is connected to a data acquisition system and periodically records the volume of water passing through the sample. Once constant flow is achieved, permeability is calculated by applying Darcy's law. The determinations have been made at laboratory temperature. The final water content and dry density of the specimen is checked on completion of the test by drying the sample at $110\ ^\circ\text{C}$ during 24 hours.

The results obtained are plotted in Figure 108 as a function of the position of the samples in the barrier and detailed in Villar (2003). The hydraulic conductivity is clearly related to dry density and the latter in turn is related to the position of the block in the barrier. However, trimming has caused changes in the original dry density of the samples, for which reason dry densities lower than expected are found, particularly in samples from blocks BB19-2 and BB28-1. It must be pointed out that the values measured do not correspond to the permeability of the bentonite at the moment it was retrieved, since the samples have been saturated to perform the determination, and permeability depends greatly on the degree of saturation.

The empirical correlations between dry density and saturated permeability for untreated FEBEX bentonite (Equations 1 and 2) along with the average range of deviation of experimental values with respect to theoretical values (30 percent) are plotted in Figure 109, together with the hydraulic conductivities measured in samples from Grimsel. Although the values of hydraulic conductivity for the samples of lower density (more hydrated) are in the order of the theoretical ones, for the higher densities there is a large dispersion without any clear tendency.

4.4.1.5. Swelling deformation tests

The saturation (or swelling) under load test makes it possible to determine the strain capacity of the soil when it saturates under a previously established pressure. Twelve samples, from two different sections (S19 and S28), have been selected to perform this determination, six per section, taken at different distances from the heater along the sampling radii.

The tests have been performed in standard oedometers. Two samples from each block (external and internal position) have been trimmed to the appropriate dimensions (height $1.20\ \text{cm}$, diameter $3.81\ \text{cm}$). For this purpose cylindrical cutters were used, and the samples obtained were placed in the oedometer ring. Once in the oedometer, a vertical

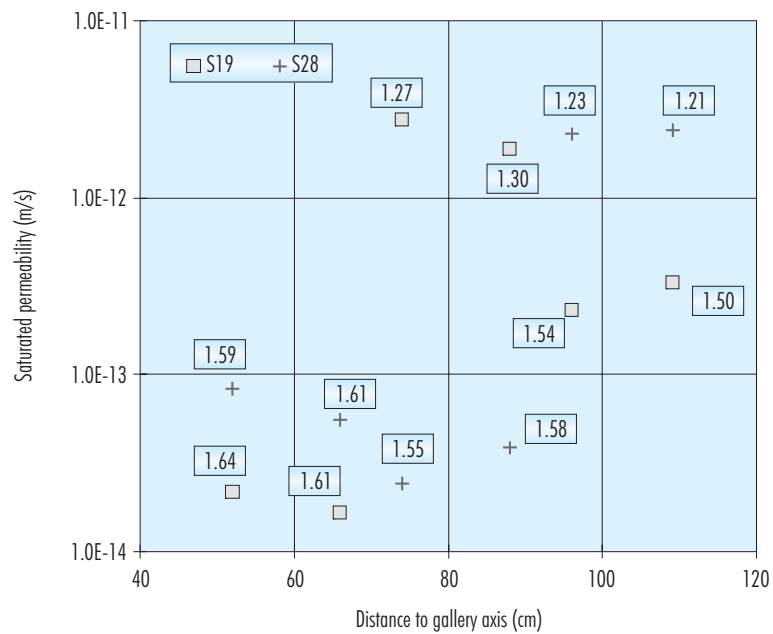


Figure 108: Hydraulic conductivity of samples from sections S19 and S28 (the dry density of the samples is indicated in g/cm^3).

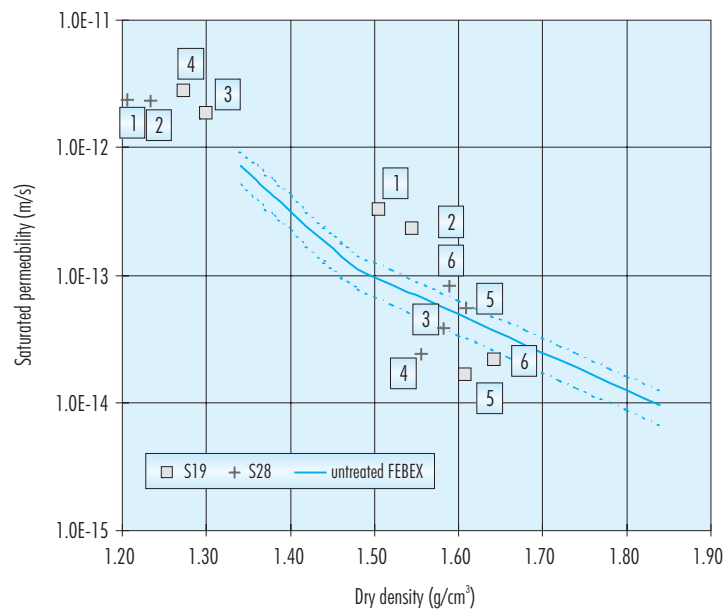


Figure 109: Hydraulic conductivity as a function of dry density for samples of sections S19 and S28. The lines correspond to the empirical fittings obtained with Equations 1 and 2 (the position of the samples is indicated with consecutive numbers from 1 –closest to gallery wall– to 6 –closest to heater–).

pressure of 0.5 MPa has been applied to the samples. Immediately afterwards, the samples are saturated with deionised water at atmospheric pressure from the bottom porous plate. The swelling strain experienced by the specimens upon saturation has been recorded as a function of time until stabilisation. The ratio between the final length increase undergone by the sample in equilibrium with the load applied and its initial length gives the strain value of the material on saturating, the negative values indicating swelling strains. The final result is, therefore, the percentage of strain of a sample of given initial dry density and water content on saturating under a fixed load. On completion of the test, the water content of the specimen was determined by oven drying at 110 °C for 24 hours. The tests have been performed at laboratory temperature.

The results obtained are detailed in Villar (2003). Figure 110 shows the evolution of strain versus time in tests performed with specimens of section S19. The figure illustrates how swelling develops more rapidly in the samples of higher initial dry density (and lower initial water content), which correspond to internal positions of the barrier. Their higher suction may be the explanation of this behaviour.

Indeed, the samples closer to the gallery wall had higher initial water content and lower initial dry density. The swelling capacity is related to both, increasing with initial dry density and decreasing with initial water content. For this reason the final strain of the samples closer to the heater is higher, as can be clearly seen in Figure 111. The duration of the tests was on average of 20 days. At the end of the tests all the specimens were verified to be completely saturated.

Similar tests were performed with samples of untreated FEBEX bentonite compacted at various dry densities with different water contents (Villar *et al.* 2002b). These tests were performed with the aim of having a database with which compare the results presented above. From the results obtained an empirical relation was found between swelling strain (ε , %), initial dry density (ρ_d , g/cm³), initial water content (w , %) and vertical pressure (σ , MPa), whose predicting capacity is rather good:

$$\varepsilon = [(-12.12 \ln \rho_d + 1.89) \ln \sigma + (36.81 \rho_d - 53.59)] \ln w + (38.27 \ln \rho_d - 1.25) \ln \sigma + (-149.05 \rho_d + 211.42) \quad [17]$$

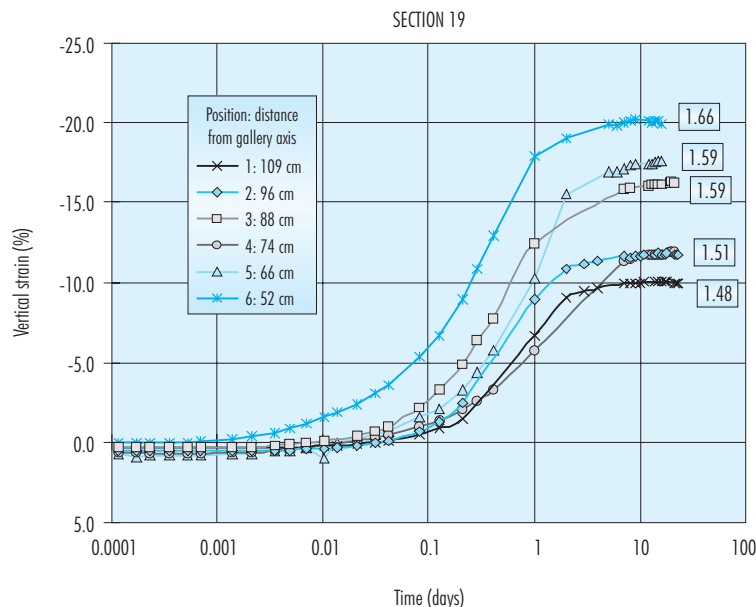


Figure 110: Evolution of vertical strain during saturation under vertical load 0.5 MPa for samples from section S19 (the initial dry density of the samples is indicated in g/cm³).

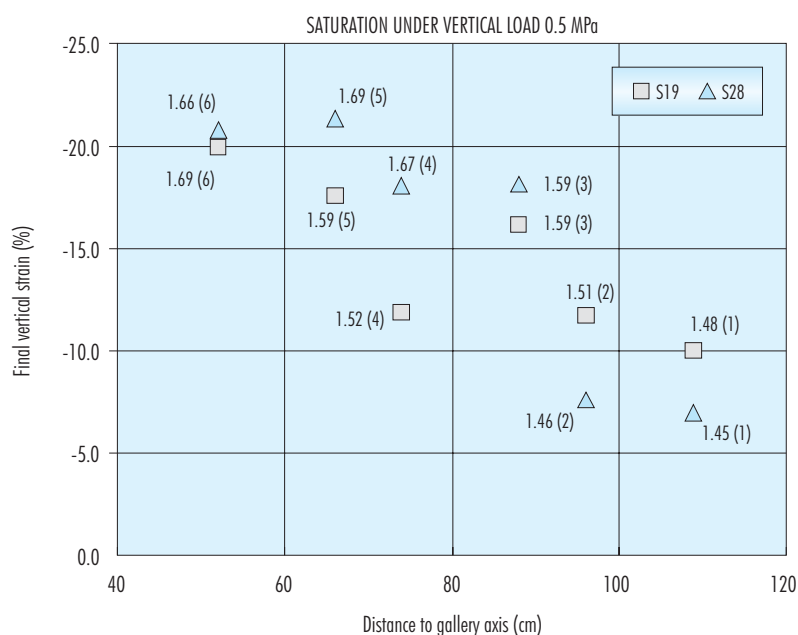


Figure 111: Vertical strain after saturation under 0.5 MPa of samples from sections S19 and S28 (the initial dry density of the samples is indicated in g/cm^3 and their position by consecutive numbers from 1 –close to the gallery wall– to 6 –close to the heater–).

The results obtained with the samples from sections S19 and S28 are plotted again in Figure 112 as a function of the initial water content of the samples. The figure shows also the theoretical lines obtained with Equation 17 for three different initial dry densities. It can be observed that the final swelling strains of the samples coming from Grimsel are in the order of those expected for the untreated FEBEX bentonite compacted at the same initial dry density with the same water content. This can be clearly seen in Figure 113, in which the values actually measured and the theoretical values obtained with Equation 17 are compared. Consequently, it can be claimed that the swelling capacity of the FEBEX bentonite has not irreversibly changed after five years of being subjected to repository conditions.

4.4.1.6. Determination of preconsolidation pressure

The blocks installed in the FEBEX *in situ* test at Grimsel were manufactured by applying uniaxial vertical pressures of between 40 and 45 MPa (ENRESA 2000), which would correspond approximately to the preconsolidation stress of the clay. However, the mo-

dification of the structure of the sample –for example as a result of hydration under low load, with which more open structures with higher levels of porosity are obtained– may cause the value of preconsolidation to decrease. This may be analysed through determination of the preconsolidation pressure (σ_p') in graphs showing the evolution of void ratio due to increasing load under constant suction. For this reason the preconsolidation pressure of samples from Grimsel has been determined under oedometric conditions and control of suction.

Twelve samples from 2 different sections (S19 and S28) have been tested, 6 per section, taken at different distances from the heater along one sampling radius. The sampled radii chosen are different to those sampled for the strain at saturation tests. The water content and dry density of the adjacent clay is checked, and the samples are tested under the suction corresponding to that water content according to the water retention curves (Figure 3, Lloret *et al.* 2004). Suction is set by means of sulphuric acid solutions. The sample equilibrates at the target suction under a low vertical load. Afterwards, the sample is loaded progressively up to 2, 4, 6, 12 and 20 MPa.

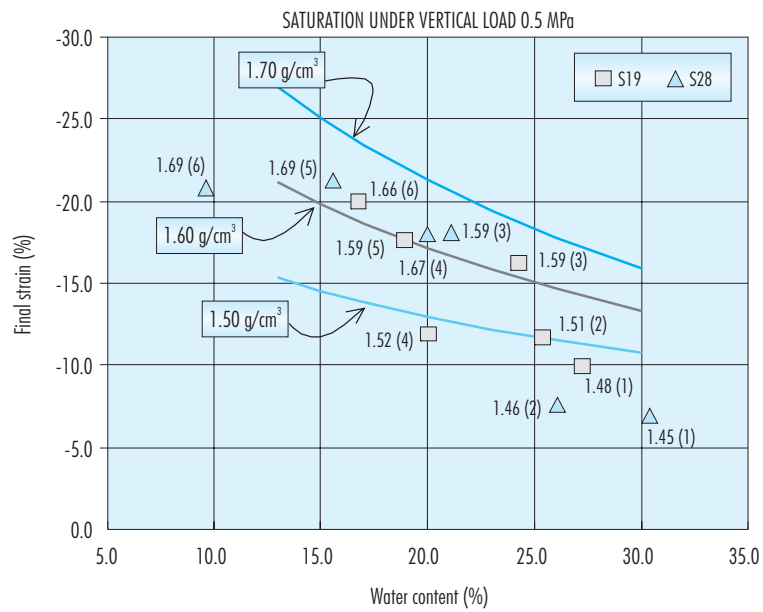


Figure 112: Final strain reached in soaking tests under a vertical pressure of 0.5 MPa for samples of sections S19 and S28. The lines correspond to the empirical fittings obtained with Equation 17 (the initial dry density of the samples is indicated in g/cm^3 and their positions with consecutive numbers from 1—closest to gallery wall—to 6—closest to heater—).

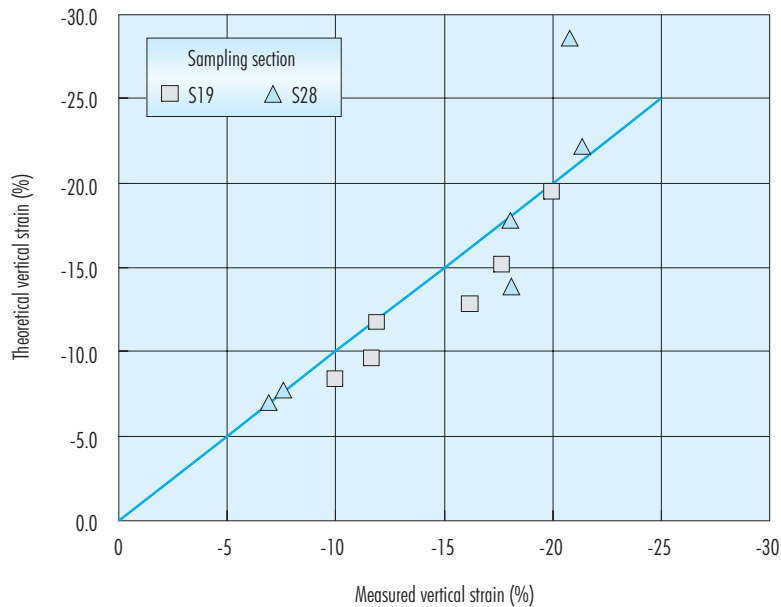


Figure 113: Final strain reached in soaking tests under a vertical pressure of 0.5 MPa compared to the theoretical value obtained with Equation 17.

The duration of each loading step is fixed to 7 days. The tests are performed at laboratory temperature.

To perform these tests the oedometric cells of Figure 114 have been adapted to withstand the high pressure supplied by an oedometric frame equipped with a load cell (Figure 115). Cylindrical samples of height 1.2 cm and diameter 3.8 cm are drilled in the bentonite blocks, trimmed if necessary and placed in the oedometer ring. The vertical deformation of the specimen during the test is measured by two LVDTs.

The initial dry density (ρ_d) and water content (w) of each sample and the suction applied during the tests are shown in Table XXXVII for section S19 and in Table XXXVIII for section S28 (see Villar (2003) for further details of each test). Examples of the consolidation curves obtained are shown in Figure 116 and Figure 117, and the oedometric curves are shown in Figure 118 for samples of section S19 and in Figure 119 for samples of section S28. In these figures it can be observed that the preconsolidation pressure is for all the samples lower than 10 MPa, and consequently has decreased with respect to the initial one, the volume increase experienced by the bentonite during hydration accounting for that. Furthermore, the preconsolidation stresses found are

lower the lower the suction applied during the test, i.e. the higher the water content reached during the *in situ* experiment. These values are plotted as a function of suction in Figure 120, in which the apparent preconsolidation stresses found for samples of untreated FEBEX bentonite compacted initially to similar dry densities and subjected to different suctions are also shown (Villar 2002, Lloret *et al.* 2003). The latter values correspond to consolidation of samples initially hydrated under low vertical stresses, and since they have swollen during the wetting more than the Grimsel samples (which are “confined”), their preconsolidation pressures are even lower.

4.4.1.7. Thermal conductivity

The superficial thermal conductivity has been measured in the sampled blocks before any other determination. The thermal conductivity has been measured over the surface of the block that faced the gallery entrance in two positions transversal to the radius, in order to have six measurements evenly distributed along the sampling radii (Figure 121). The results obtained are plotted in Figure 122, in which it can be seen that the values range within the

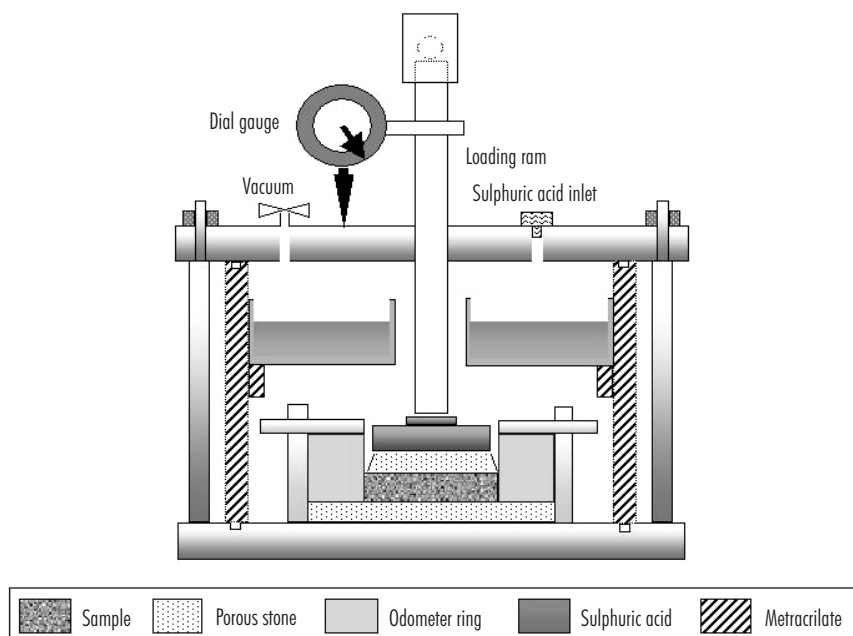


Figure 114: Schematic cross section of an oedometric cell with deposit for solutions.

Table XXXVII
Initial conditions of the samples from section S19 used in the consolidation tests.

| Sample | Position ¹ (cm) | Initial ρ_d (g/cm ³) | Initial w (%) | Suction (MPa) |
|------------|----------------------------|---------------------------------------|-----------------|---------------|
| BB19-10A-1 | 109 | 1.52 | 28.4 | 3 |
| BB19-10A-2 | 96 | 1.57 | 25.3 | 9 |
| BB19-11A-1 | 88 | 1.59 | 23.7 | 7 |
| BB19-11A-2 | 74 | | 21.7 | 35 |
| BB19-12A-1 | 66 | 1.64 | 17.8 | 67 |
| BB19-12A-2 | 52 | 1.65 | 16.5 | 84 |

¹ Distance to gallery axis.

Table XXXVIII
Initial conditions of the samples from section S28 used in the consolidation tests.

| Sample | Position ¹ (cm) | Initial ρ_d (g/cm ³) | Initial w (%) | Suction (MPa) |
|-----------|----------------------------|---------------------------------------|-----------------|---------------|
| BB28-7A-1 | 109 | 1.54 | 27.9 | 2 |
| BB28-7A-2 | 96 | 1.54 | 25.8 | 7 |
| BB28-8A-1 | 88 | 1.63 | 21.0 | 27 |
| BB28-8A-2 | 74 | 1.57 | 20.0 | 30 |
| BB28-9A-1 | 66 | 1.69 | 14.4 | 104 |
| BB28-9A-2 | 52 | 1.74 | 15.6 | 132 |

¹ Distance to gallery axis.

interval 0.8-1.3 W/m·K. Higher thermal conductivities have been measured in the external blocks of the barrier, due to their higher water content.

The theoretical thermal conductivity for the blocks from Grimsel has been calculated with Equation 5, obtained from measurements in untreated FEBEX specimens, taking into account their dry density and water content. The values thus calculated have been compared to those actually measured. It has been observed that, in general, the “theoretical” values calculated with Equation 5 are a 6 percent higher than those measured. Figure 123 shows the values measured in blocks from Grimsel belonging to sections with heater as a function of their water content. The dry density of some of the blocks is indicated. Three lines obtained with Equation 5 corresponding

to the theoretical thermal conductivity for three different dry densities are also drawn in the figure. It can be seen that the conductivities measured are in most cases below the expected values for blocks of the same dry density and water content. This can be clearly seen in Figure 124, in which the values actually measured and the theoretical values obtained with Equation 5 are directly compared. However, this is not the case for section S12, in which the heater was not present. In fact, if the deviations with respect to the theoretical value are calculated for the different rings of the barrier (external, intermediate, internal) it is observed that the higher deviations are obtained in the blocks of the internal and intermediate rings, which present clearly lower conductivities than expected (10 and 8 percent lower, respectively.) To a lesser extent this is also observed in



Figure 115: Suction controlled oedometer cells installed in the frames to perform high pressure consolidation tests.

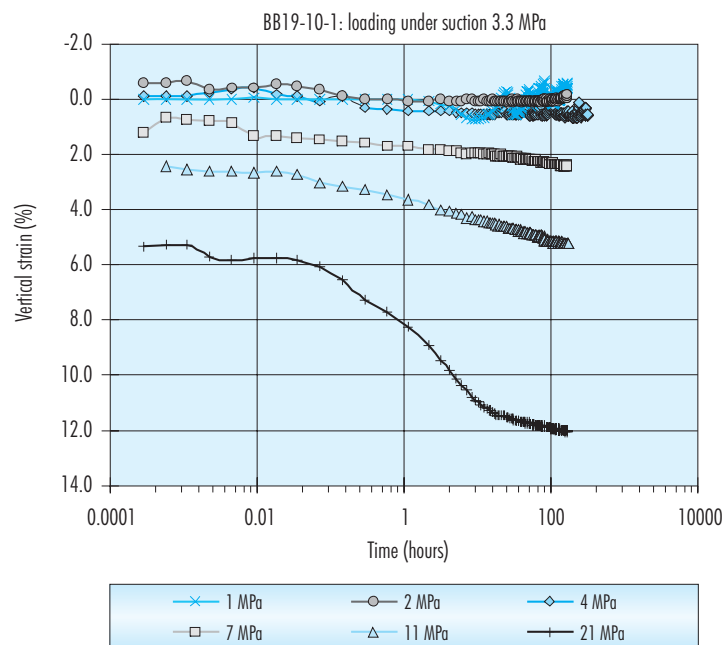


Figure 116: Evolution of strain during the different steps of the process of loading under suction 3 MPa for sample BB19-10A-1 (located at 109 cm from the gallery axis).

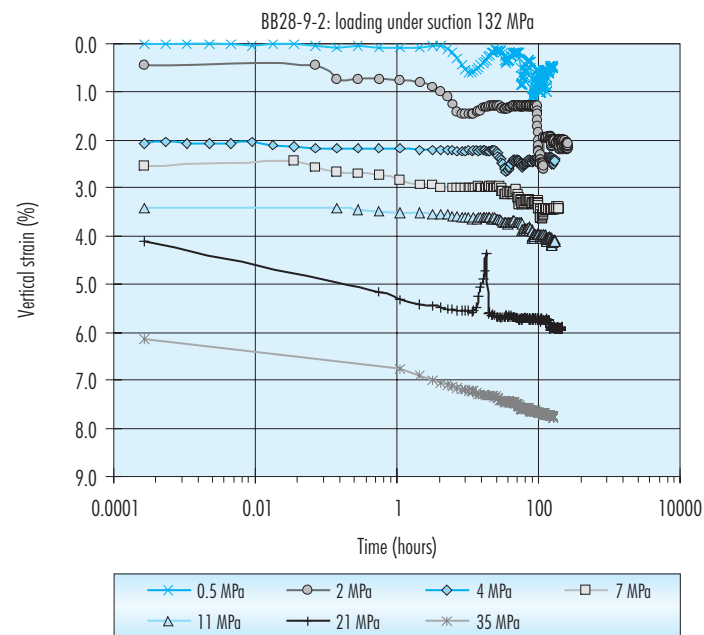


Figure 117: Evolution of strain during the different steps of the process of loading under suction 132 MPa for sample BB28-9A-2 located at 52 cm from the gallery axis).

section S12 (Villar 2003). All these observations suggest that the decrease in thermal conductivity could be related to heating.

4.4.2. CTU: Basic characterisation and THM properties

4.4.2.1. Basic properties

CTU has determined bulk density (ρ), dry density (ρ_d), density of solid particles (ρ_s), porosity (n), water content (w), volumetric water content (w_v), liquid limit (w_L), plasticity limit (w_p), shrinkage limit (w_s), plasticity index (I_p), consistency index (I_c), colloidal activity of clay (I_A) and grain size distribution on samples taken from sections S7, S12, S19, S28 at the inner, middle and outer ring (36 samples). The determinations have been performed following the Czech standards (CTU-CET 2003) in crushed material obtained from the blocks. As the CTU laboratory was not used to work with the FEBEX bentonite, preliminary tests to check the raw material and the equipment were performed before the dismantling. The tests were performed in a block sent by AITEMIN that had not

been installed at Grimsel and that is considered as the reference block.

The results obtained are summarised in Table XXXIX, in which also data for the reference block are given for comparison. An example of the grain size curves obtained is shown in Figure 125.

Tested materials were classified according to Czech standard ČSN 73 1001 “Foundations of structures – Subsoil under shallow foundations” as loams with extremely high plasticity (with exception of BB19-7). Liquid limits of these materials are in the interval 107–138 percent, plasticity index in the interval 53–85 percent. The latter is highly related to the water content of the samples and thus to their position in the barrier, the plasticity index clearly increasing with water content (Figure 126). The lowest values of liquid limit and plasticity index were obtained for blocks that underwent the highest temperature (BB19-9 temperature 77 °C and BB28-12 temperature 74 °C.) Block BB19-7 is classified as clay with extremely high plasticity and has the highest value of liquid limit (152 %) and plasticity index (99 %). This block underwent an average temperature of 40 °C.

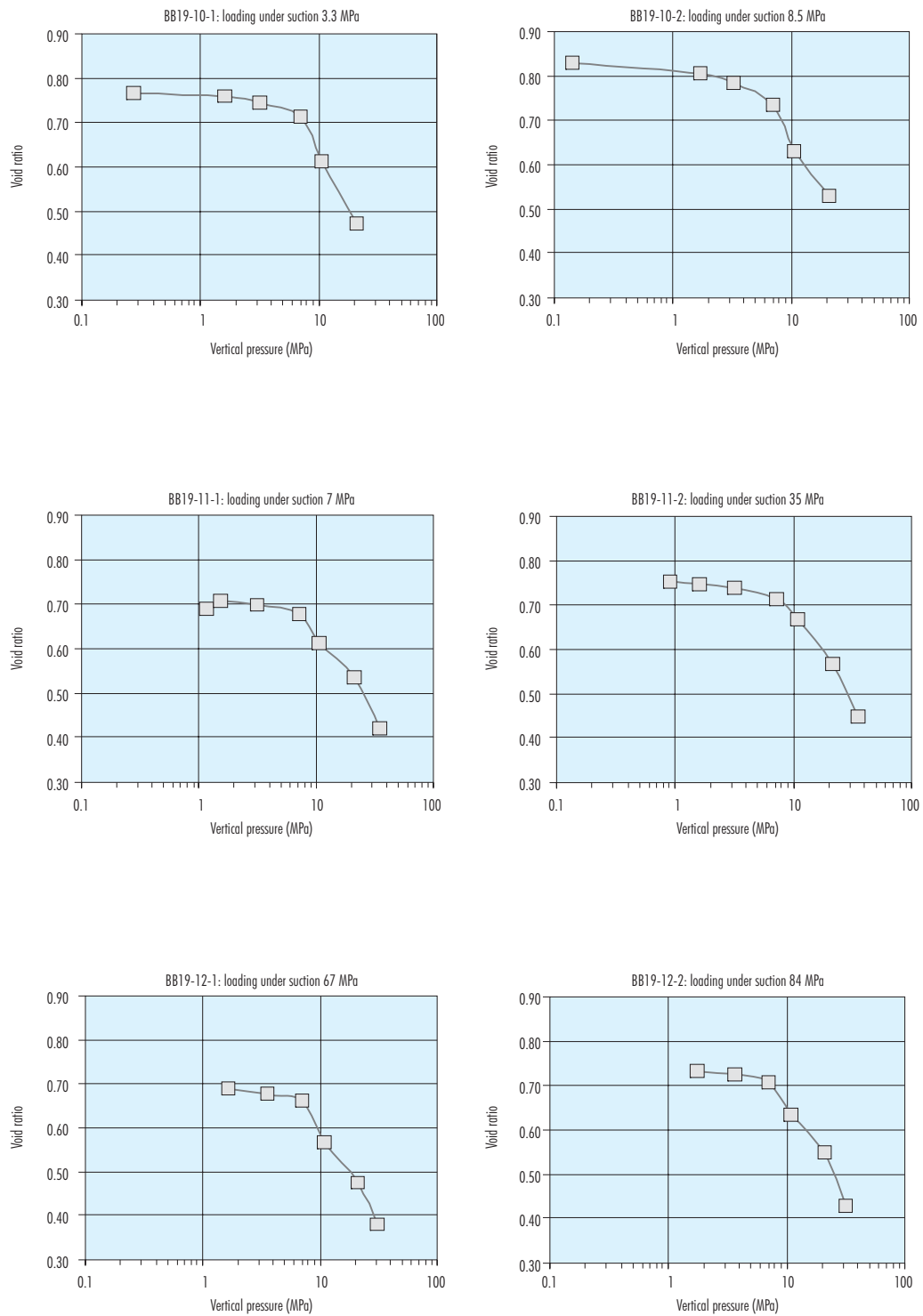


Figure 118: Oedometric curves of the tests performed in samples from section S19.

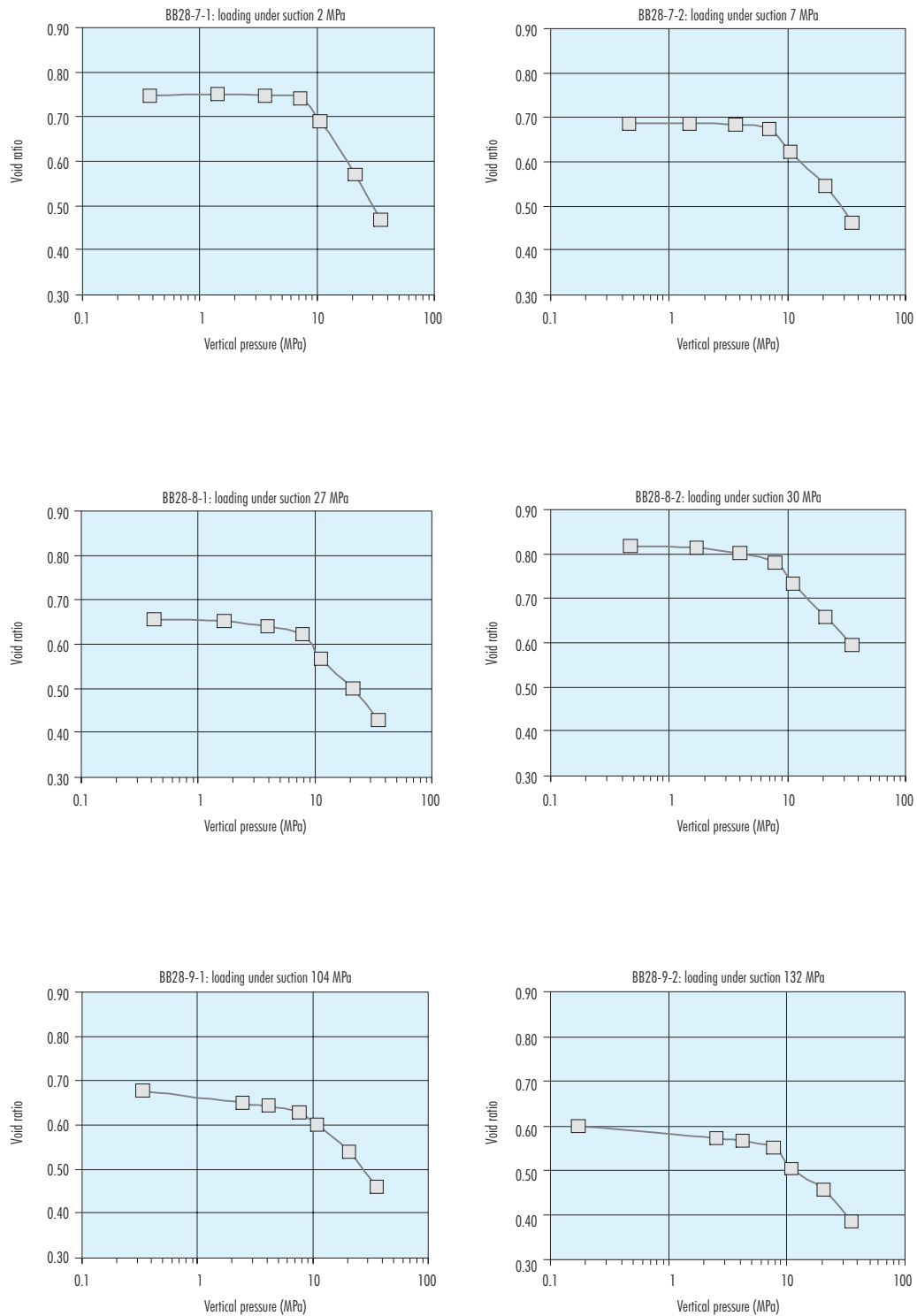


Figure 119: Oedometric curves of the tests performed in samples from section S28.

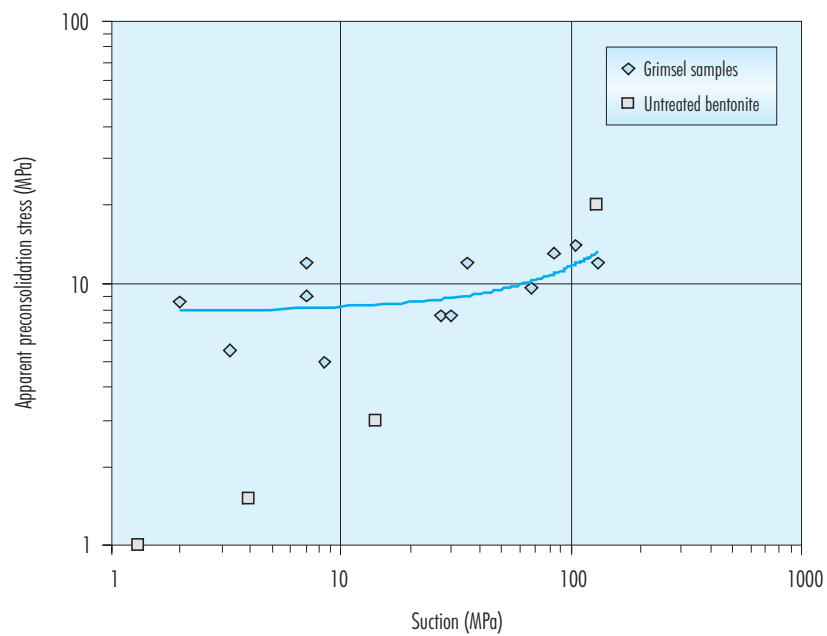


Figure 120: Apparent preconsolidation stress of samples from Grimsel and of untreated bentonite determined under constant suction corresponding to the water content of the clay.



Figure 121: Measurement of superficial thermal conductivity (the plastic foil under the conductivity probe is removed for the determination).

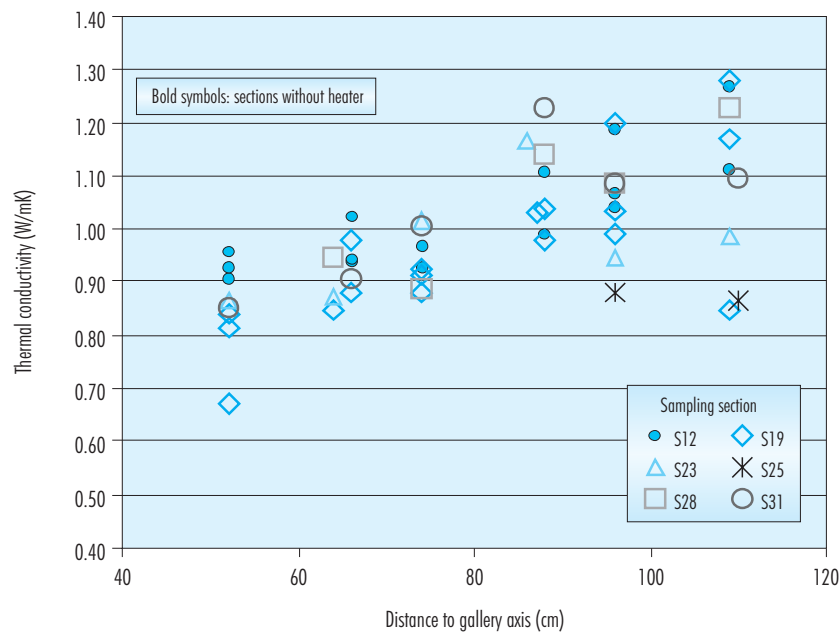


Figure 122: Thermal conductivity along radius of different sections.

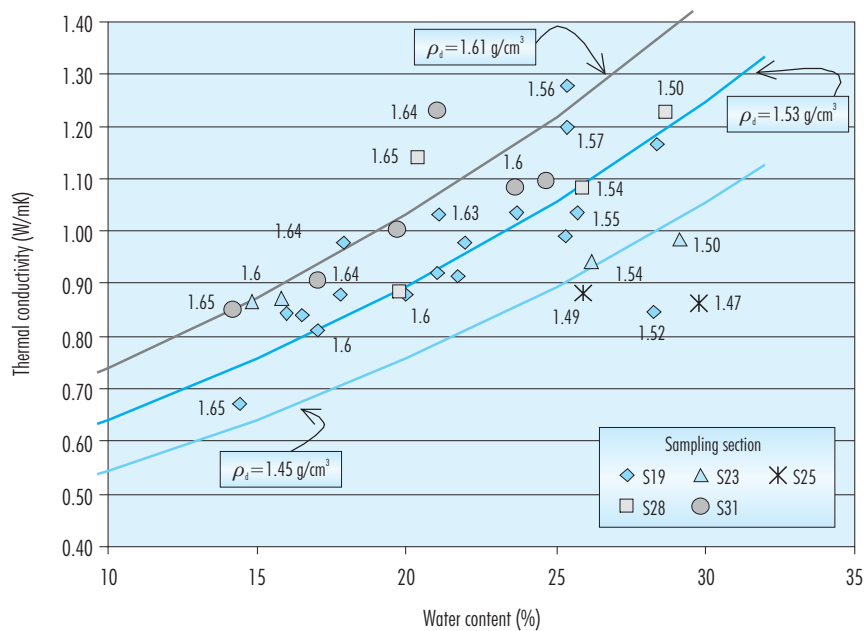


Figure 123: Thermal conductivity values measured in blocks from Grimsel (dry density indicated in g/cm³) and theoretical fittings obtained with Equation 5.

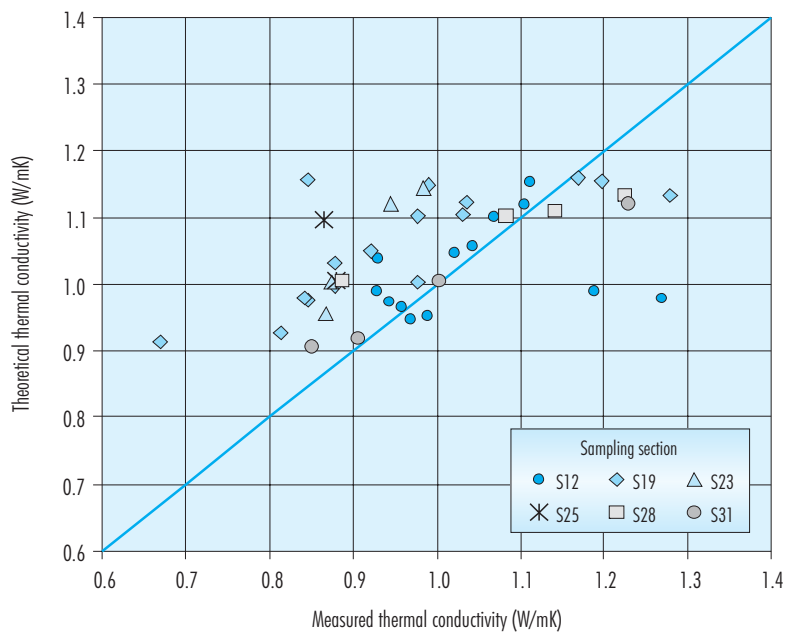


Figure 124: Thermal conductivity values measured compared to the theoretical values obtained with Equation 5.

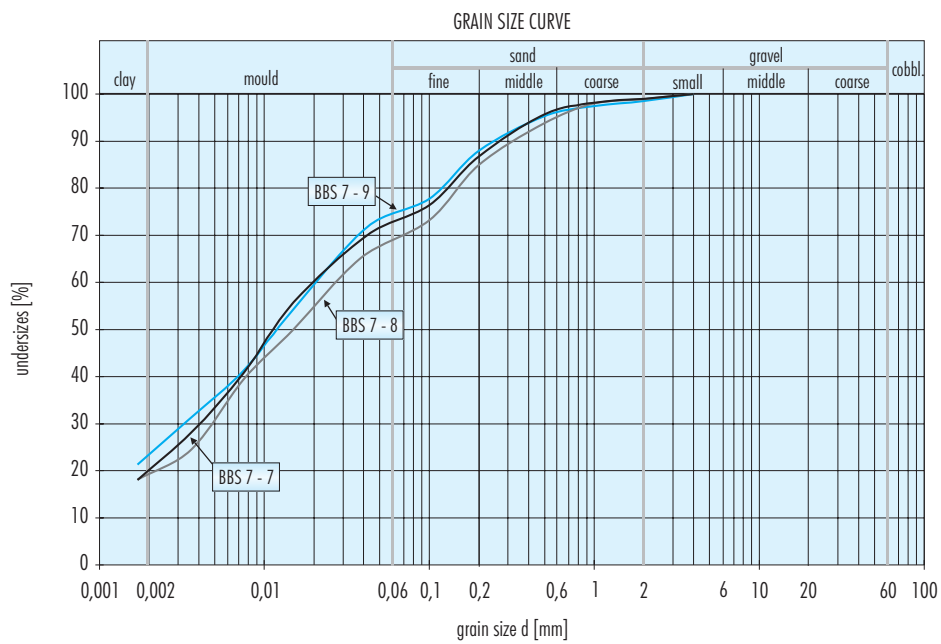


Figure 125: Grain size curves of samples from blocks from section S7.

Table XXXIX
Basic properties of the bentonite determined by CTU.

| Sample | Temp. ¹ (°C) | ρ (g/cm ³) | ρ_d (g/cm ³) | ρ_s (g/cm ³) | n (%) | w (%) | w_L (%) | w_P (%) | I_P (%) | I_c | I_A |
|-----------|----------------------------|--------------------------------|----------------------------------|----------------------------------|------------|------------|--------------|--------------|--------------|-------|-------|
| Reference | - | 1.86 | 1.65 | 2.70 | 39 | 10-13 | 115 | 51 | 64 | 1.6 | 3.8 |
| BBS7-7 | 18 | 2.00 | 1.62 | 2.65 | 39 | 23.6 | 117 | 57 | 60 | 1.6 | 3 |
| BBS7-8 | 18 | 1.99 | 1.54 | 2.53 | 39 | 29.3 | 125 | 51 | 74 | 1.3 | 3.7 |
| BBS7-9 | 18 | 1.89 | 1.54 | 2.68 | 42 | 22.2 | 133 | 54 | 79 | 1.4 | 3.6 |
| BB12-7 | 23 | 2.01 | 1.60 | 2.74 | 42 | 25.5 | 138 | 53 | 85 | 1.3 | 3.4 |
| BB12-8 | 23 | 1.98 | 1.68 | 2.68 | 37 | 18.2 | 122 | 52 | 70 | 1.5 | 3.5 |
| BB12-9 | 23 | 1.96 | 1.66 | 2.67 | 38 | 18.5 | 131 | 48 | 83 | 1.4 | 3.8 |
| BB19-7 | 40 | 2.01 | 1.59 | 2.68 | 41 | 26.4 | 152 | 53 | 99 | 1.3 | 4.5 |
| BB19-8 | 59 | 2.07 | 1.71 | 2.63 | 35 | 21.2 | 112 | 50 | 62 | 1.5 | 3.3 |
| BB19-9 | 77 | 1.88 | 1.64 | 2.57 | 36 | 14.9 | 107 | 54 | 53 | 1.7 | 4.1 |
| BB28-10 | 49 | 2.04 | 1.60 | 2.70 | 41 | 28.1 | 131 | 56 | 75 | 1.4 | 3.4 |
| BB28-11 | 62 | 2.01 | 1.67 | 2.75 | 39 | 20.4 | 117 | 55 | 62 | 1.6 | 3.4 |
| BB28-12 | 74 | 1.89 | 1.65 | 2.75 | 40 | 14.7 | 112 | 54 | 58 | 1.7 | 3.9 |

¹Temperature of the block during the operation phase of the test at Grimsel.

The measurements given above indicate that the thermal loading of blocks has not had significant negative influence on their plasticity.

4.4.2.2. Swelling properties

To determine the swelling pressure a new equipment has been fine-tuned. It is based on the use of oedometric frames equipped with a load ring. In the special stand designed, the volume of the sample is kept almost constant in the steel frame, and the pressure exerted by the sample as it is flooded is measured by means of the load ring (Figure 127). In this way the evolution of swelling pressure with time can be known. The small deformation of the sample is measured by means of strain dial gauges.

The specimens were prepared by uniaxial compaction of crushed material from the blocks. Before compaction the clay was dried to water contents between 11 and 13 percent. The height of the specimens was 15 mm, their diameter 120 mm and they were compacted at a bulk density analogous to that

of the reference block (about 1.90 g/cm³). Once compacted the sample was extracted and placed in the oedometer ring.

As an example, the evolution of volume change during the swelling test for sample BB28-12 is shown in Figure 128, and the evaluation of swelling pressure at zero deformation for the same sample is shown on Figure 129.

On the other hand, the swell index has been determined according to standard ASTM D 5890-02. The swell index test is used to determine the general swelling characteristics of the bentonite. The tests were carried out on part of the blocks previously ground and dried at 110 °C for 24 h.

The results of the swelling pressure (P_s) and swell index (SI) tests are shown in Table XL. No significant difference was found between the swelling pressure values obtained for the reference material and for the blocks coming from Grimsel. Therefore, and due to the long duration of the tests, swelling pres-

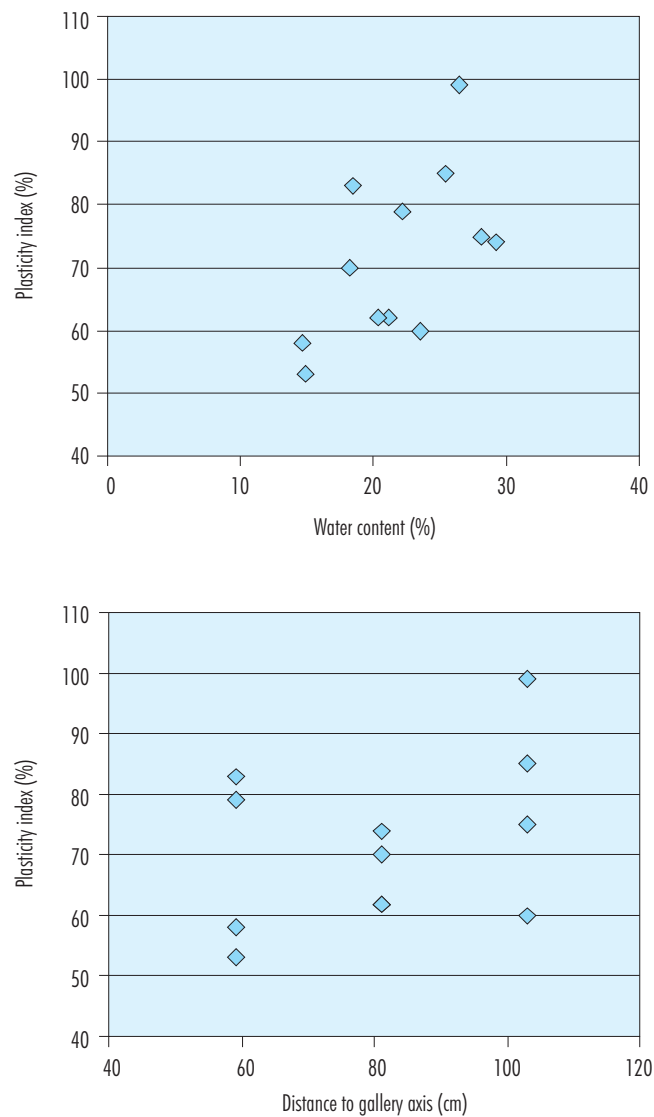


Figure 126: Plasticity index of the samples from Grimsel as a function of their water content and position along the radius.

sure was determined only for two blocks from each sampling section.

Summarising, the specimens obtained from blocks from Grimsel (by crushing, drying to water contents between 10 and 13 percent and compaction at bulk density of about 1.90 g/cm^3) have swelling pressures between 5.3 and 8.7 MPa. The value obtained for the reference material is 6.8 MPa. As both the values of swelling pressure and swell index for the samples from Grimsel are comparable to the

values obtained for the reference untreated block, it can be concluded that there is not any significant change of these properties after the five years of *in situ* experiment.

4.4.2.3. Uniaxial strength

Uniaxial strength is one of the strength characteristics of soils. Exceeding of strength can cause cracks and damage of soil. The European standard EN 1926 "Natural stone test methods – Determination

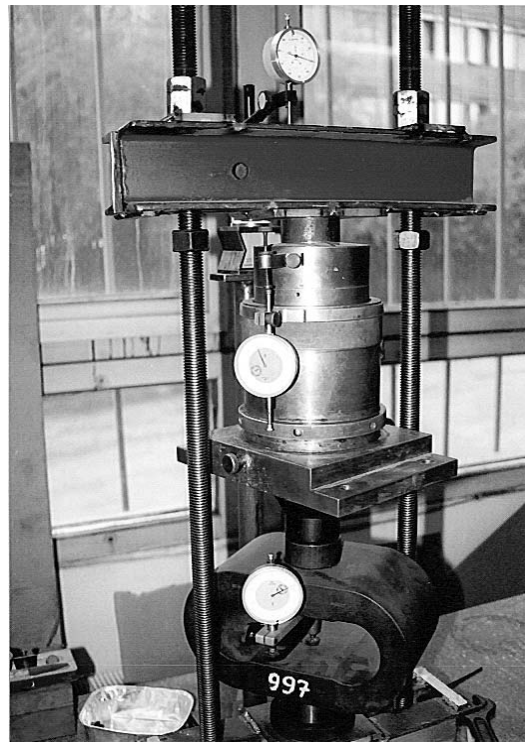


Figure 127: Stand for measuring swelling pressure with dynamometers.

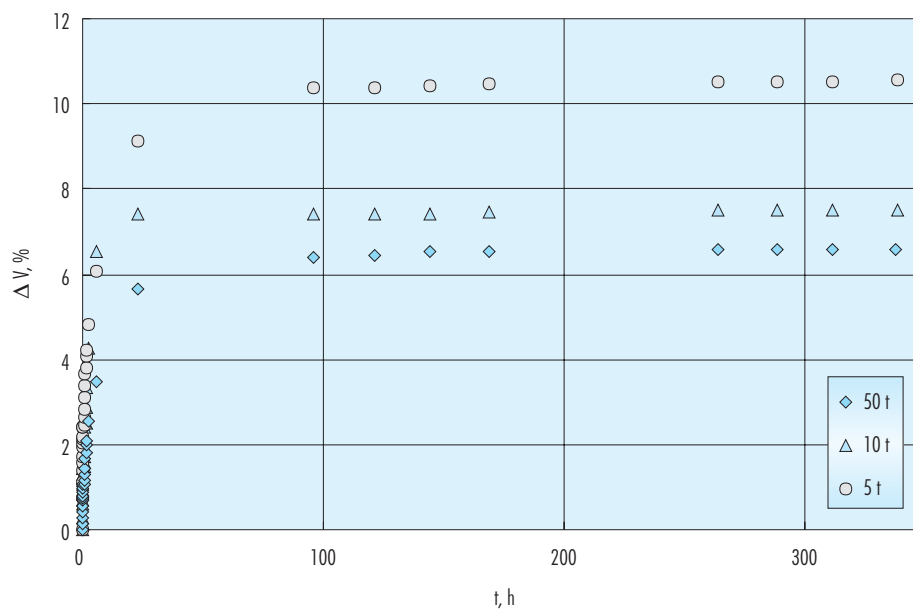


Figure 128: Determination of volume change on time for FEBEX block BB28-12.

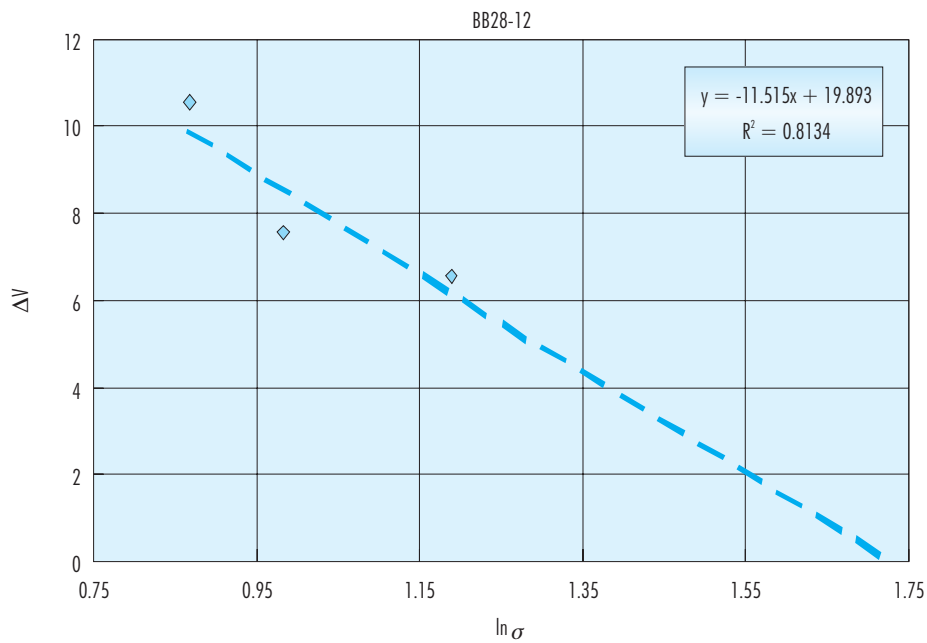


Figure 129: Determination of swelling pressure at zero deformation for block BB28-12

Table XL
Swelling pressure (P_s) and swell index (S) tests results.

| Sample | T^1 (°C) | Initial w (%) | S^2 (mL of gel/ 2 g) | w^3 (%) | ρ (g/cm ³) | P_s^4 (MPa) |
|-----------|---------------|--------------------|---------------------------|--------------|--------------------------------|------------------|
| Reference | - | 10–13 | 5.0 | 13 | 1.86 | 6.8 |
| BBS7-7 | 18 | 23.6 | 5.0 | 12 | 1.84 | 5.3 |
| BBS7-8 | 18 | 29.3 | 5.8 | 10 | 1.85 | 6.1 |
| BBS7-9 | 18 | 22.2 | 6.1 | 12 | 1.82 | 6.4 |
| BB12-7 | 23 | 25.5 | 6.0 | 11 | 1.81 | 6.7 |
| BB12-8 | 23 | 18.2 | 5.0 | 13 | 1.84 | 6.7 |
| BB12-9 | 23 | 18.5 | 4.6 | 12 | 1.86 | 6.2 |
| BB19-7 | 40 | 26.4 | 5.2 | 12 | 1.83 | 6.1 |
| BB19-8 | 59 | 21.1 | 6.2 | 11 | 1.82 | 5.5 |
| BB19-9 | 77 | 14.9 | 4.5 | | | |
| BB28-10 | 49 | 28.1 | 5.4 | | | |
| BB28-11 | 62 | 20.4 | 6.0 | 13 | 1.92 | 8.7 |
| BB28-12 | 74 | 14.7 | 5.3 | 13 | 1.88 | 5.6 |

¹Temperature during the experiment at Grimsel; ²Swell index measured for samples with $w=0\%$; ³Water content after air-drying; ⁴Swelling pressure measured for samples previously air-dried

of compressive strength" has been followed to determine this property.

Cube samples with edge dimensions 50 ± 5 mm were cut from the bentonite blocks. The standard requires at least a set of six samples. This condition was fulfilled for almost all blocks. Only two samples were prepared from block BBS7-8 and four samples from block BB19-9, as they were both very damaged. Two sets of tests were carried out: one with samples loaded in the same direction in which the block was compacted, and the other one with samples loaded perpendicularly to the compaction direction.

The cubes prepared were dried before testing at a temperature of 70°C for 24 hours. Afterwards they were weighed and their dimensions measured. The density of the sample is calculated from these values.

A combination of press and PC (with WINTRH 2.0 software) was used for the uniaxial strength testing. The sample is placed axially into the press and is loaded continuously up to its breaking (Figure 130). The maximum force is registered. The loading velocity was 5 or 10 kN/min. At the end of the test one part of the block is taken for determination of dry density and water content. Uniaxial strength (R , MPa) is calculated as $R = F/A$, where F is the maximum force (N) and A the sample area (mm^2).

Since the samples were tested after drying, their water content was 3 to 5 percent. The results are plotted in Figure 131. The results are strongly dependent on water content and therefore it is difficult to compare them. The uniaxial strength is higher in the direction of compaction almost for all the blocks. With increasing temperature during the *in situ* test a decrease in strength can be observed. The lowest values were measured for BB19-9 (temperature was 77°C , strength 4.8 and 2.8 MPa) and for BB28-12 (temperature was 74°C and strength 5.0 and 3.2 MPa).

4.4.2.4. Thermal properties

The main parameters that determine the thermal behaviour of a material are the coefficient of thermal conductivity (λ , $\text{W/m}\cdot\text{K}$), the heat capacity (c , $\text{J/kg}\cdot\text{K}$) and the thermal diffusivity (α , m^2/s). They are related by the following equation, in which ρ is the bulk density of the material (kg/m^3):

$$\alpha = \lambda / (\rho \cdot c) \quad [18]$$

Thermal conductivity (λ) depends on water content, temperature and density of the sample. It is considered that the dependence of λ on temperature is the

least important, while water content and bulk density have an important influence. Dependence of λ on water content is minimal for low bulk density but it increases as bulk density increases. The dependence of λ on temperature is not influenced by bulk density.

The measurements have been carried out with ISOMET and THT-tester, which use surface probes and are based on the impulse of thermal flow into the analysed material. A surface probe is used for blocks. Deviations of measured values are for thermal conductivity $\pm(10\% + 0.005\text{W/m}\cdot\text{K})$ and for heat capacity $\pm(15\% + 3 \cdot 10^3 \text{ J/m}^3\text{K})$.

The blocks from Grimsel were first tested with their natural water content. Afterwards, they were crushed and dried to water contents around 12 percent, compacted to the same nominal dry density, and their thermal properties measured again. Finally, these samples were fully dried for testing at water content of 0 percent.

The values for the intact blocks with their natural water content are given in Table XLI and plotted in Figure 132. Water content varies from 12 to 29 % and dry density from 1.54 to 1.71 g/cm^3 . Thermal conductivity increases with water content from 0.69 up to $1.12 \text{ W/m}\cdot\text{K}$ and thermal diffusivity from 0.46 to $0.64 \text{ m}^2/\text{s}$, while the specific heat decreases with water content from 944 to $819 \text{ J/kg}\cdot\text{K}$. Obviously the water content is inversely related to the temperature experienced by the blocks during the operation phase.

For the remoulded and partly dried samples (with water content between 8-12 %, mean dry density of 1.66 g/cm^3), thermal conductivity ranges from 0.62 to $0.82 \text{ W/m}\cdot\text{K}$ and specific heat from 863 to $993 \text{ J/kg}\cdot\text{K}$. For the dried samples, thermal conductivity ranges from 0.48 to $0.57 \text{ W/m}\cdot\text{K}$ and specific heat from 851 to $986 \text{ J/kg}\cdot\text{K}$. After these treatments, neither differences in λ and c have been observed with respect to the reference block nor related to the position of the blocks in the barrier, *i.e.* of the temperature underwent by the blocks during the five years of the *in situ* experiment (CTU-CEG 2003). Therefore, it could be said that heating up to 77°C during five years has not had an irreversible influence on the thermal properties of the FEBEX bentonite.

4.4.3. EIG-EURIDICE: Hydraulic conductivity

Parts from the blocks BB12-2 (close to the gallery wall in S12, without heater), BB19-13, BB19-14



Figure 130: Appearance of a cubic sample after uniaxial strength test.

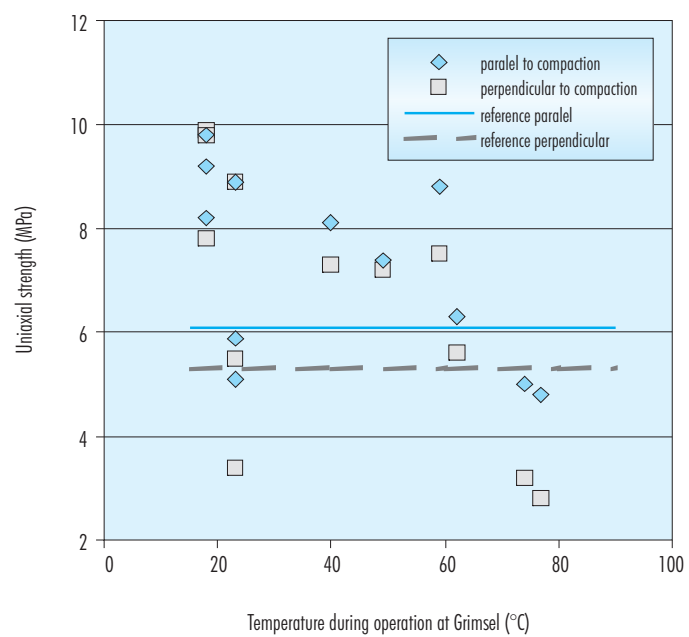


Figure 131: Results of the uniaxial strength tests in samples from blocks from Grimsel dried at 70°C for 24 hours.

Table XLI
Thermal properties of blocks from Grimsel.

| Sample | T^1 (°C) | ρ (g/cm ³) | ρ_d (g/cm ³) | w (%) | λ (W/m·K) | α (m ² /s) | c (J/kg·K) |
|-----------|---------------|--------------------------------|----------------------------------|------------|----------------------|---------------------------------|-----------------|
| Reference | | 1.86 | 1.65 | 12.7 | 0.69 | 0.418 | 886 |
| BBS7-7 | 18 | 1.20 | 1.62 | 23.6 | 1.12 | 0.644 | 869 |
| BBS7-8 | 18 | 1.99 | 1.54 | 29.3 | 1.01 | 0.584 | 868 |
| BBS7-9 | 18 | 1.89 | 1.54 | 22.2 | 0.92 | 0.558 | 874 |
| BB12-7 | 23 | 2.01 | 1.60 | 25.5 | 1.04 | 0.584 | 885 |
| BB12-8 | 23 | 1.98 | 1.68 | 18.2 | 0.92 | 0.567 | 819 |
| BB12-9 | 23 | 1.96 | 1.66 | 18.5 | 0.82 | 0.486 | 854 |
| BB19-7 | 40 | 2.01 | 1.59 | 26.4 | 1.05 | 0.591 | 884 |
| BB19-8 | 59 | 2.07 | 1.71 | 21.2 | 0.99 | 0.538 | 892 |
| BB19-9 | 77 | 1.88 | 1.64 | 14.9 | 0.79 | 0.456 | 922 |
| BB28-10 | 49 | 2.04 | 1.60 | 28.1 | 1.02 | 0.554 | 898 |
| BB28-11 | 62 | 2.01 | 1.67 | 20.4 | 0.97 | 0.521 | 924 |
| BB28-12 | 74 | 1.89 | 1.65 | 14.7 | 0.82 | 0.460 | 944 |

¹Temperature during the in situ experiment.

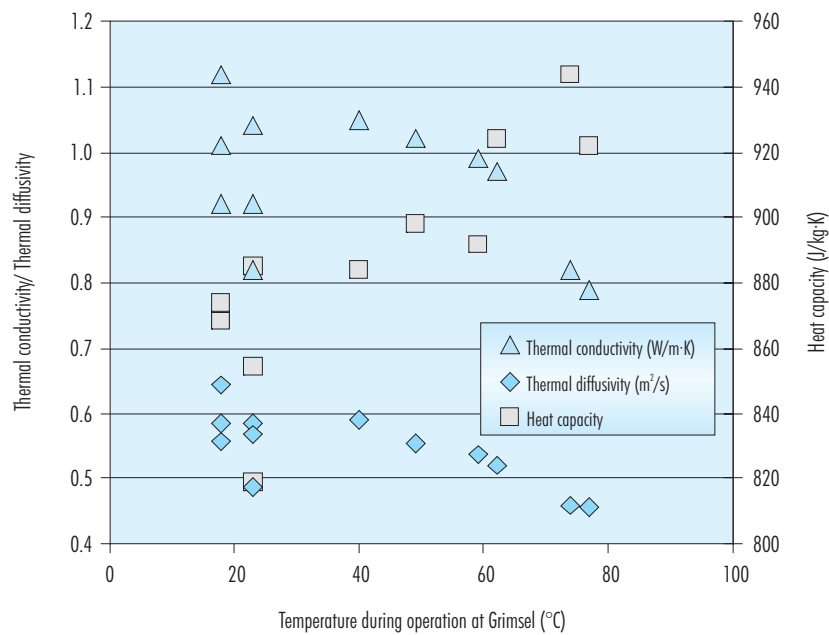


Figure 132: Thermal properties of blocks from Grimsel.

and BB19-15 (external, middle and inner block along a radius of section S19) were sent by CIEMAT to EIG EURIDICE. From these parts, samples of 50-mm length and 38-mm diameter were obtained by core drilling and trimming. All samples were taken according to the axial direction, except for block BB12-2 (one radially oriented sample).

The samples were introduced in the measuring cell (permeameter) and closed by two end covers. Each cover contains a sintered stainless steel porous filter ($10\ \mu$). First all the voids in the permeameter cell (tolerance less than 1 mm) are filled with deionised water to remove all the remaining air in the system and to fill these voids by the swelling clay. After a short period (typically a few hours), the pressure is applied in a continuous way. The lower filter is subjected to a pressure of 0.55 to 0.60 MPa, delivered by an injection cylinder. The outflowing water (upper filter) is collected in a hermetic flask placed on a precision balance. Inflow and outflow volumes and pressures are recorded as function of time and their stability is checked at regular intervals. To obtain the highest accuracy, the flow measurement is based on the inflow; the outflow (in the bottle) is rather considered as a check. The inflow is measured through a displacement transducer, connected to the piston.

Figure 133 shows a schematic of the measurement setup. The hydraulic conductivity is determined by applying Darcy's law once stable flow is reached. The determinations have been made at laboratory temperature (19-26 °C). The final water content of the specimens is checked on completion of the tests by drying the sample a 105 °C until no weight loss is observed.

A summary of the results obtained is given in Table XLII and they are detailed in Verstricht (2004). All cores gave similar permeability values, in the order of 10^{-13} m/s, which would correspond to the hydraulic conductivity of untreated FEDEX samples of dry density around $1.5\ \text{g/cm}^3$ (Equation 2). Sample BB19-14A-2 gave a higher value of permeability, what must be due to the fact that its dry density was lower than the other's. The same comments stated in section concerning the representativity of the saturated permeability values obtained apply for the determinations of SCK-CEN.

4.4.4. Euro-Géomat: Tests in joints

Engineered barriers made of blocks contain a lot of joints that can create preferential ways for the solute

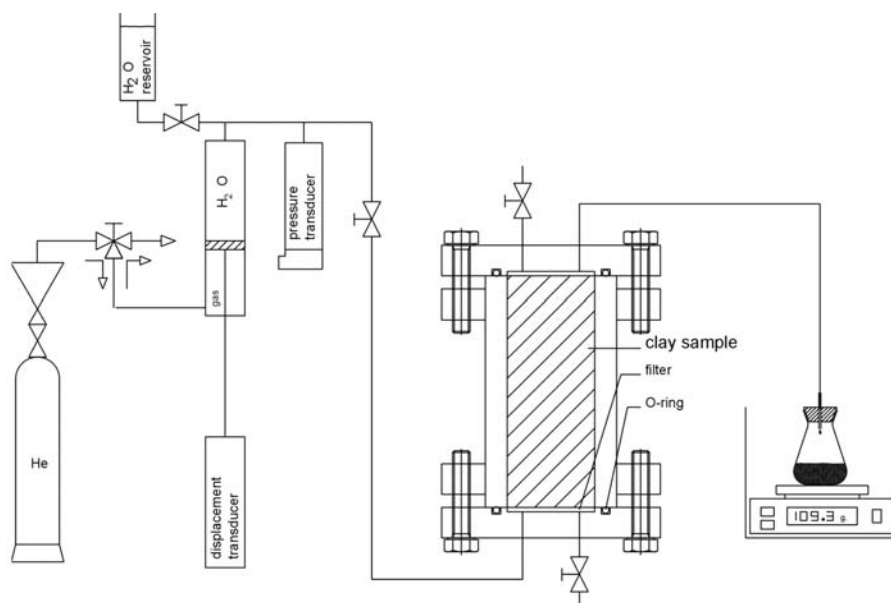


Figure 133: Schematic view of the permeameter cell used at SCK-CEN for the measurement of low hydraulic conductivities.

Table XLII
Results of the permeability tests performed by ESV EURIDICE GIE.

| Sample ID | Position ¹ (cm) | ρ_d (g/cm ³) | Initial w (%) | Final w (%) | k_w (m/s) | Test duration (days) |
|--------------|----------------------------|-------------------------------|-----------------|---------------|----------------------|----------------------|
| BB12-2Radial | 102.5 | 1.63 | | 23.2 | $1.3 \cdot 10^{-13}$ | 23 |
| BB12-2Axial | 102.5 | 1.65 | | 22.5 | $1.0 \cdot 10^{-13}$ | 74 |
| BB19-13-1 | 109 | 1.57 | 22.9 | 25.9 | $1.3 \cdot 10^{-13}$ | 50 |
| BB19-14-1 | 88 | 1.63 | 20.1 | 24.3 | $1.4 \cdot 10^{-13}$ | 63 |
| BB19-14-2 | 74 | 1.35 | 19.2 | 36.1 | $1.1 \cdot 10^{-12}$ | 31 |
| BB19-15-1 | 66 | 1.63 | | 23.5 | $1.1 \cdot 10^{-13}$ | 57 |

¹Distance to gallery axis.

transfer. This introduces an important macroporosity that must be taken into account to evaluate the thermo-hydro-mechanical behaviour of the engineered barriers. Figure 134 schematises the behaviour of a clay block and shot-clay structure during its hydration, obtained by modelling with a discrete model that takes into account the distinct behaviour of blocks and joints (Chandler *et al.* 2001):

1. Flow along block-to-block interfaces occurred first and rapidly. This flow would then stop and the water would be absorbed by the dry clay blocks.
2. Saturated flow through the shot-clay path became more slowly over time.

For a comprehensive understanding of these joints and their influence upon the hydraulic conductivity, kinetics of saturation and swelling pressure development, laboratory experimental investigations can be very helpful, especially to confirm the saturation time, the self-sealing capacity of the bentonite barrier and to establish relationships between initial density, hydraulic conductivity and swelling pressure.

Three kinds of joints in the bentonite barrier had been selected by Euro-Géomat Consulting (EGC) to make this study: radial direction (r), tangential (orthoradial) direction (π) and the intersection of the two previous joints (T) as it can be seen on Figure 135.

The work of EGC was to study the effect of joints between bentonite blocks on the hydrodynamic and hydro-mechanical properties of the dismantled samples containing the joints. The experiments carried out are focused on three macroscopic parameters:

capillary capacity, intrinsic permeability and swelling pressure.

4.4.4.1. Preparation of samples

Eight samples from section S29 (with heater) and six samples from section S11 (without heater) were received from AITEMIN. Their nominal diameter was 6 cm, and the length between 20 and 33 cm, with a weight between 1.1 and 1.6 kg.

The samples received from Grimsel had a geometry too irregular and damaged to carry out laboratory tests directly, so an experimental strategy for manufacturing bentonite samples with joints was developed. Two diameters of samples were used, 65 mm and 40 mm, for the tests of percolation and infiltration. In order to obtain cylinders of 65 mm or 40 mm diameter the following stages were followed:

- Transformation of samples coming from dismantling into powder.
- Stabilisation of the powder at relative humidity of 66 percent (imposed by NaNO_2) to obtain a clay water content of 11 percent.
- Compaction of the stabilised powder at a dry density of 1.7 g/cm^3 to obtain samples of diameter 40 mm or 65 mm.
- Creation of joints (one, two or three) by sawing with a carbide disc.

The powder with 11 percent water content is compacted in the oedometer and then it is unloaded to obtain a 20-mm high sample of dry density 1.7 g/cm^3 . During the compaction stage, axial strain,

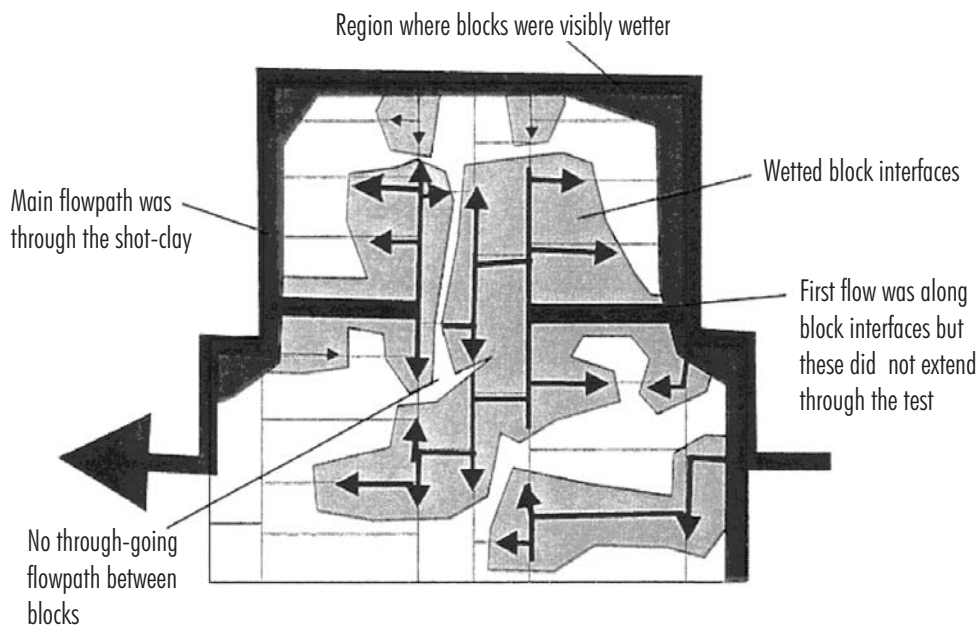


Figure 134: Flow paths in the physical model (Tunnel sealing experiment, Chandler et al. 2001).

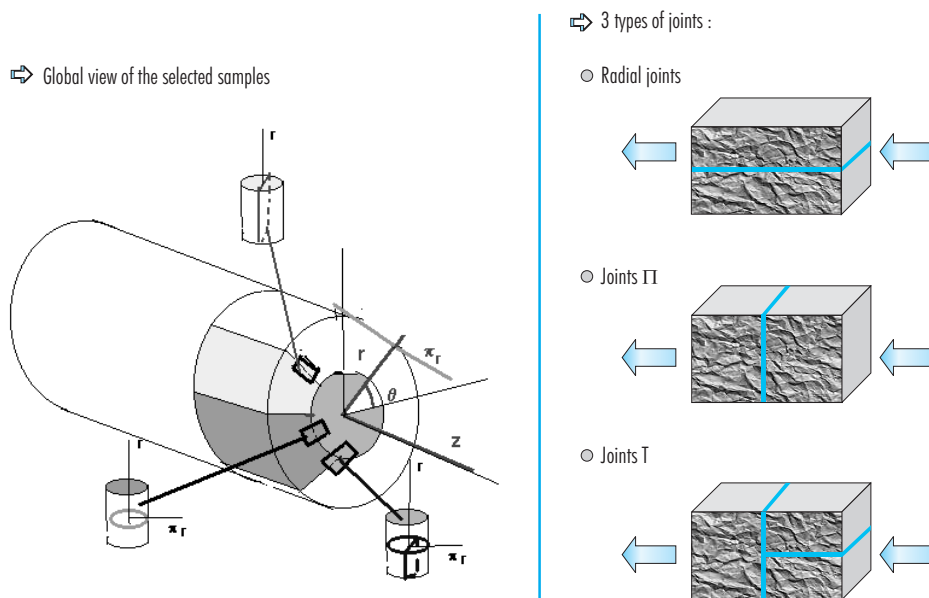


Figure 135: Types of interfaces of the bentonite barrier relevant for the study of the textures and of the hydraulic properties.

radial and axial stresses are measured. These measurements enable to establish the curves in the $e\text{-}\log(\sigma_v)$ plan (void ratio in function of the logarithmic vertical stress) and in the $(\sigma_h\text{-}\sigma_v)$ plan (horizontal stress in function of the vertical stress). Figure 136 shows the results obtained for the dry density of 1.7 g/cm^3 .

The samples obtained are referenced according to the following key: after an R , the dismantling reference of the block is given, including the sampling section; the type of joint is indicated by JV (vertical) or JH (horizontal) followed by a figure that indicates the number of joints; finally, and after a d , the final dry density of the specimen is indicated.

4.4.4.2. Experimental methodology

The experimental study of the coupling between hydration processes and macroscopic physical properties requires a perfect experimental control of the quantity of percolated fluids and of the volume of the confined samples. Besides, working with joints implies the specific experimental difficulty of the large contrast of permeability between the compacted bentonite blocks and the joints, particularly the measurement of high permeabilities at the begin-

ning (values about 10^{-10} m/s) and very low permeabilities after sealing (values lower than 10^{-13} m/s), associated to high swelling stresses (several MPa). This made necessary to use a specific oedometric apparatus and infiltration column associated to a special apparatus of percolation. The use of an oedometric device allows to put a device of percolation and to determine simultaneously the macroscopic hydraulic conductivity and the swelling pressure.

Three type of apparatus were developed by Euro-Géomat for this study: an oedometer cell for the measurement of permeability and swelling pressure, an odometric cell with control of the suction gradient, and columns to perform infiltration tests so that to obtain the retention curve by back-analysis.

Oedometric cell with control of the hydraulic gradient

The oedometer cell consists of a bronze jacket where a piston slides (Figure 137). A radial sensor, installed in the jacket, enables to follow the evolution of the radial stress as a function of the axial one. A displacement gauge is placed on the piston and gives the axial strains. A piston linked to a GILSON hydraulic pump, which can reach 60 MPa,

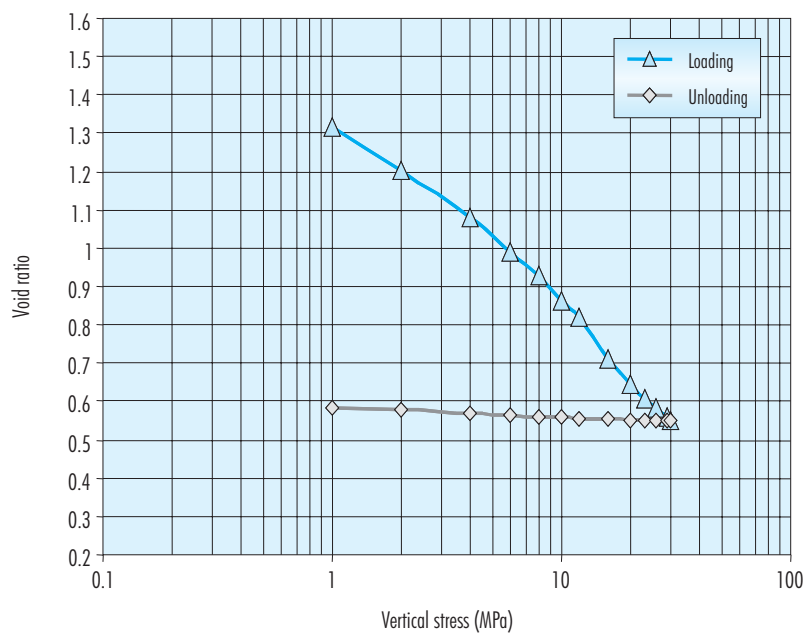


Figure 136: Evolution of void ratio during compaction and unloading to obtain samples of dry density 1.7 g/cm^3 .

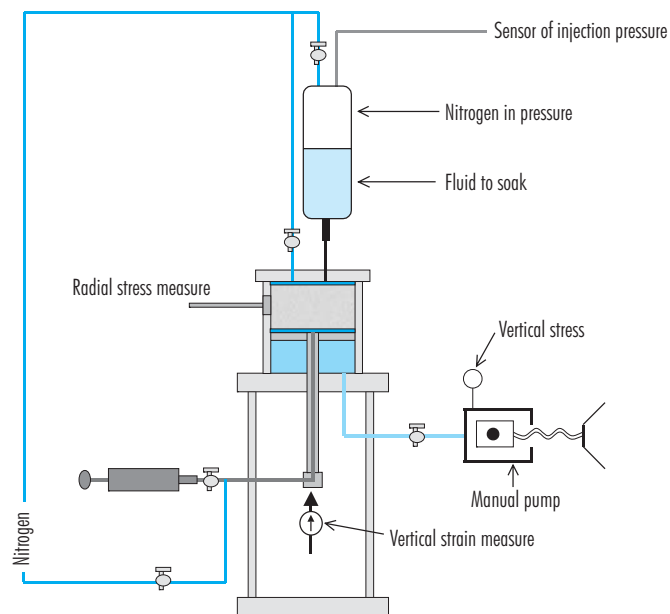


Figure 137: Schematic representation of the oedometric apparatus with control of the hydraulic gradient.

provides the compaction of the sample. The experiments have been performed at constant volume. This is insured by the manual pump that provides a counter pressure on the piston, balancing the swelling pressure of the sample.

Euro-Géomat has developed an injection pump to inject the fluid. It is a cylindrical tank in stainless steel. In the upper part of this tank, two stitchings enable to apply a nitrogen pressure on the fluid inside the tank and to measure continuously this pressure. In the lower part of the injection pump there is an exit linked to the top of the oedometer, which enables the injection of the fluid inside the sample. Two valves enable to isolate the injection pump from the percolation apparatus in order to monitor the weight of the sample, which increases until the sample is saturated.

The measurement of the radial stress in tests of percolation under hydraulic gradient is essential in order to maintain a total radial stress higher than the fluid injection pressure; so that the fluid percolation takes place through the sample and not between the sample and the stainless steel jacket of the oedometer.

Oedometric cell with control of the suction gradient

The oedometer equipment consists of a bronze jacket where a piston slides. The assembly is closed with a cover. A radial sensor, installed in the jacket, enables to follow the evolution of the radial stress as a function of the axial one. A displacement gauge is placed on the piston and gives the axial strains. A piston linked to a GILSON hydraulic pump, which can reach 60 MPa, provides the axial stress to the sample.

Two circuits of air consisting of two ventilators, two deposits containing the salt solutions and drains make it possible to impose a relative humidity on each face of the sample (Figure 138).

Various salts were used in the upper and lower deposits to impose on the surfaces of the sample different relative humidities (Robinet 2003). In this way it is possible to apply suction gradients and determine permeability.

Column of infiltration

The experimental infiltration device was made with a classical oedometer, which was adapted to support a

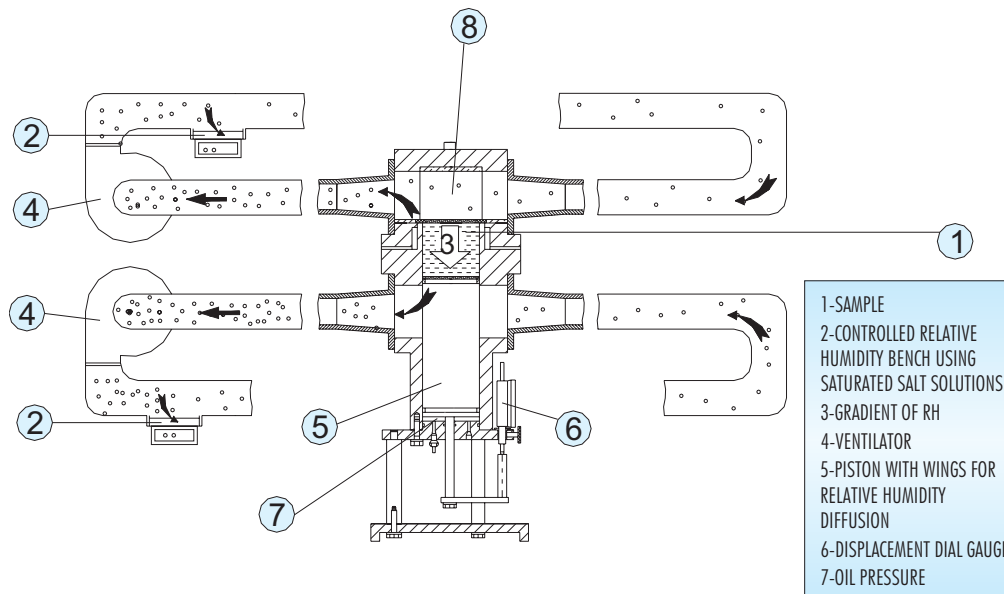


Figure 138: Schematic representation of the oedometer apparatus with control of the suction gradient.

cell made by piling rings of 65-mm diameter and 20-mm height (Figure 139). Each ring has got three ties, used to centre them together. Circular seals were installed on one face of each ring to assure the tightness of the assembly. A piston linked to a GILSON hydraulic pump, which allows applying an external pressure of 60 MPa, operates the loading of the sample.

The water injection is carried out from the lower part of the apparatus. The profile of water content is obtained by dismantling the column at the end of the experiment. At the top of the column a piston is installed, linked to the vacuum pump and to the nitrogen tank. The piston is also linked to a manual pump that allows, by modification of the stress, to perform the tests at constant volume. The injection pressure and the axial strain are recorded all along the infiltration test.

4.4.4.3. Microstructure

The evolution of textures under the effect of the joints has been studied by mercury porosimetry. Figure 140 shows the incremental pore volume as a function of entrance pore diameter for samples with joints and

without joints of the same dry density. In all configurations with and without joint a three modal pore size distribution is observed. Thus, there is not creation of macropores by the presence of the joints.

Figure 141 shows the results of desiccation tests performed on samples with vertical joints. The samples were submitted to a relative humidity of 66 percent imposed by NaNO_2 . It can be seen that the shrinkage cracks originated are all located apart from the initial joints.

This experimental study highlighted that after saturation, the sealing of the joints is complete. The material can be regarded as homogeneous and characterized by its dry density.

4.4.4.4. Permeability and swelling pressure

All the samples with joints and jointless present at the saturated state a permeability that depends on the dry density. Figure 142 shows the variation of saturated permeability (k_w , m/s) of the FEBEX clay with the dry density (ρ_d , g/cm^3), which is given by the following relation:

$$k_w = 4 \cdot 10^{-9} \exp(-6.3526 \rho_d) \quad [19]$$

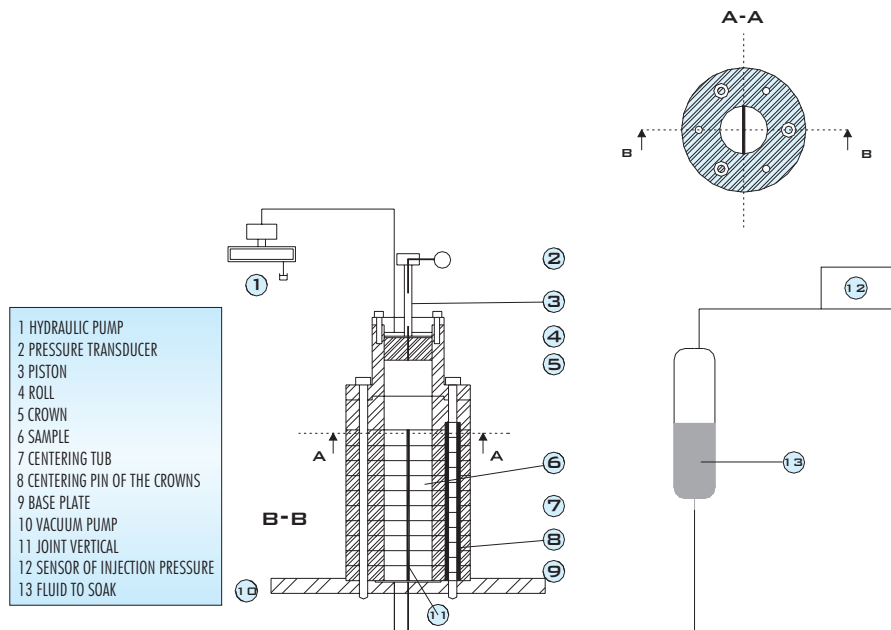


Figure 139: Schematic representation of the cell to perform infiltration tests.

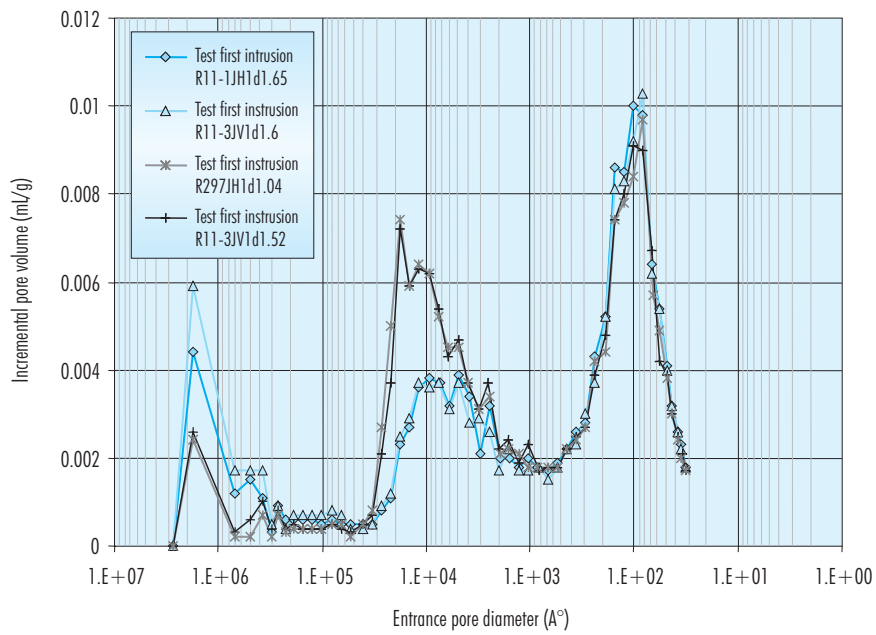


Figure 140: Pore size distribution for samples with joints (JV: vertical joint, JH: horizontal joint).

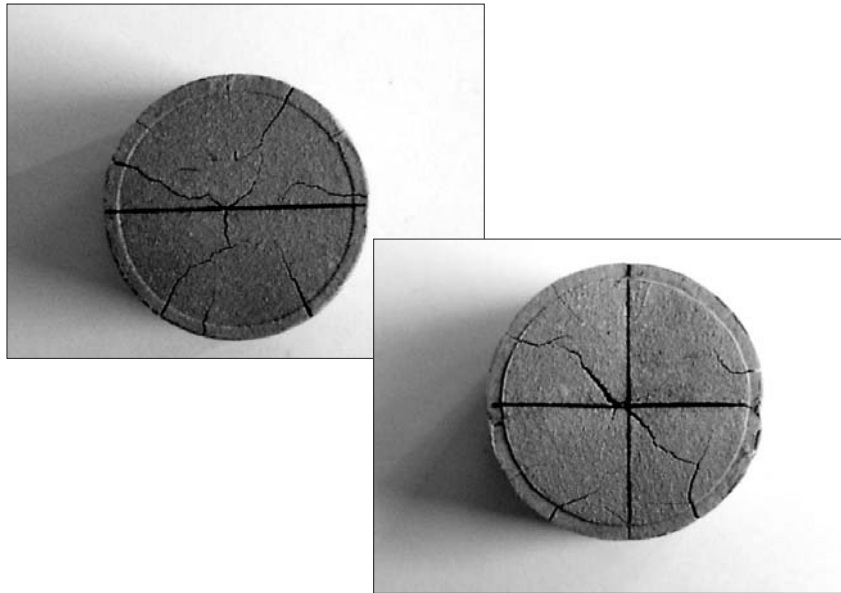


Figure 141: Photographs of the samples R11-3JV1d1.58 and R297JV2d1.56 after desiccation: the black line represents the initial joint.

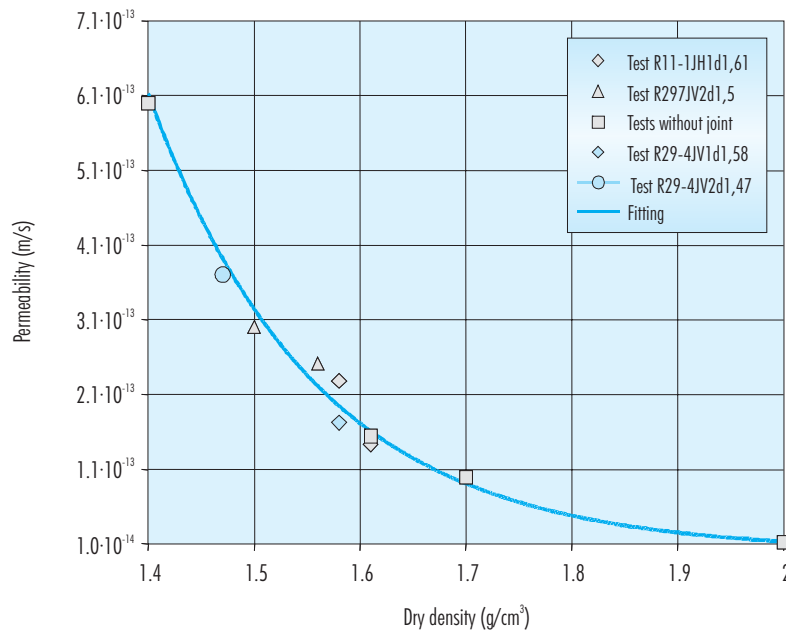


Figure 142: Saturated permeability as a function of the dry density of the samples.

The swelling pressure (P_s , MPa) at the saturated state is also independent of the presence of joints (Figure 143). It depends on the dry density (ρ_d , g/cm³) and can be written in the form:

$$P_s = 5 \cdot 10^{-4} \exp(6 \rho_d) \quad [20]$$

4.4.4.5. Moisture diffusion coefficient

The diffusion of moisture in a porous solid is due to a gradient of concentration. The moisture diffusion coefficient (D_{v0} , m²/s) at 20 °C can be expressed by:

$$f_v = -0.0173 D_{v0} \text{grad}(RH) \quad [21]$$

where f_v is the rate of moisture transfer per unit area (kg/m²s) and RH is the relative humidity.

The evolution of the diffusion coefficient from the unsaturated to the saturated state has been determined in the oedometers with control of the gradients of suction. The values obtained for samples of dry density 1.4, 1.7 and 2.0 g/cm³ are plotted in Figure 144, and are detailed in Robinet (2003).

4.4.4.6. Infiltration tests in columns

The evaluation of the permeability as a function of the degree of saturation is impossible to determine by

direct measurement in expansive materials. Consequently, to obtain the hydrodynamic parameters (intrinsic permeability and retention curves) of the samples with joints, the methodology suggested consists on the back-analysis of infiltration tests on column. So the tests of infiltration allow us:

- to back-analyse and adjust the value of the permeability
- to evaluate the retention curves in relation to the types of joints

In the infiltration tests, a block is compacted in an airtight cell and saturated through the bottom, while the water intake is measured as a function of time. After a prefixed time, the cell is disassembled and the water content of the bentonite is determined at different distances from the hydration front. A summary of the tests performed is shown in Table XLIII. In all the tests performed the clay was initially compacted at a dry density of 1.7 g/cm³. The tests were performed at 20 °C.

The clay blocks were placed with the joints parallel to the infiltration flow. The sealing of these joints produced diminutions of the dry density of 5, 10 and 12 percent. Figure 145 shows the evolution of

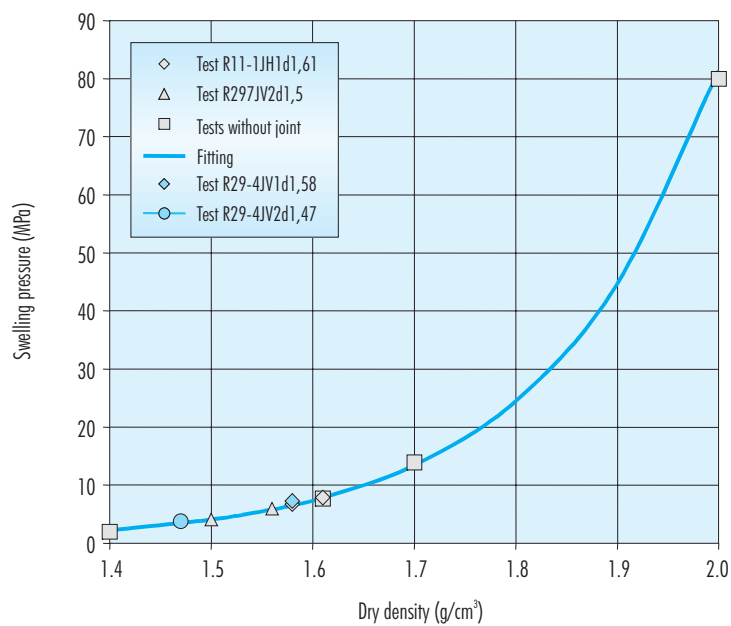


Figure 143: Swelling pressure as a function of the dry density of the sample.

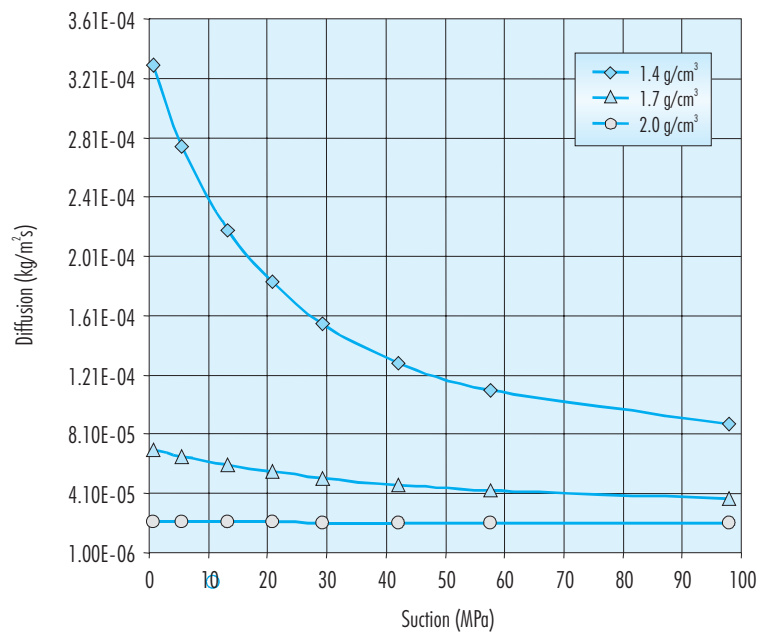


Figure 144: Evolution of diffusion coefficient with suction for samples compacted at three different dry densities.

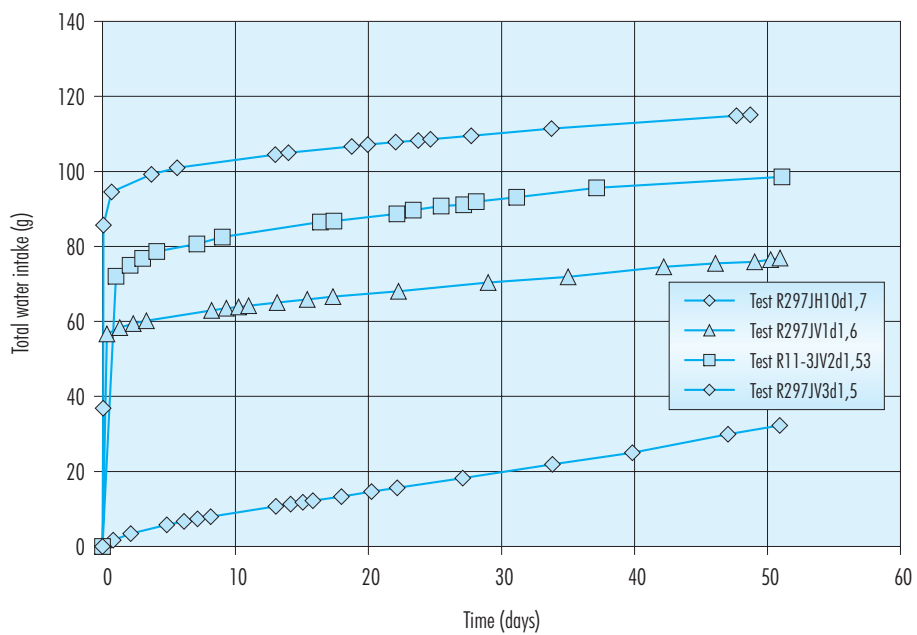


Figure 145: Water intake in the infiltration tests.

Table XLIII
Summary of infiltration tests performed.

| Reference FEBEX | Reference EGC | Type and number of joints | Initial ρ_d (g/cm ³) | Final ρ_d (g/cm ³) |
|-----------------|---------------|---------------------------|---------------------------------------|-------------------------------------|
| BS29-7 | R297JH10d1.7 | 1 - Horizontal | 1.7 | 1.70 |
| BS11-1 | R11-1JV1d1.6 | 1 - Vertical | 1.7 | 1.60 |
| BS11-3 | R11-3JV2d1.53 | 2 - Vertical | 1.7 | 1.53 |
| BS29-7 | R29-7JV3d1.5 | 3 - Vertical | 1.7 | 1.50 |

water intake in these tests and Figure 146 shows the profiles of water content at the end of the tests.

The infiltration tests highlight a very strong variation of the permeability during the first days of the percolation (Figure 147).

The numerical fitting of the infiltration tests needs a conceptual model to describe the profile of water content and evaluate the hydrodynamic properties. Some considerations and hypothesis have been sug-

gested for building the conceptual model schematised in Figure 134 (Robinet 2003):

- The joints and gaps between the blocks of bentonite are replaced by an equivalent continuous medium corresponding to the final dry density after saturation
- The hydrodynamic properties of the equivalent medium are assumed to obey to the laws of continuous medium without joints.

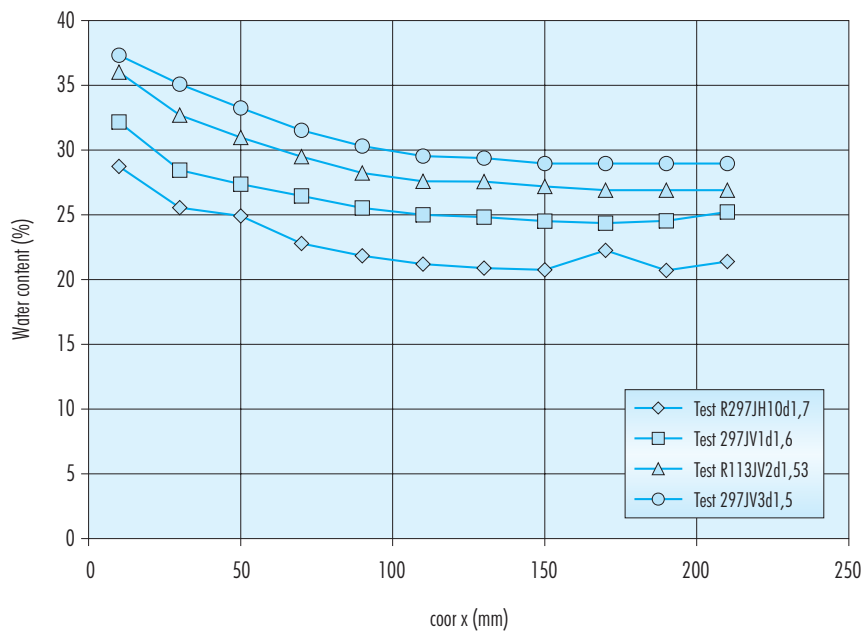


Figure 146: Final water content as a function of the distance to the hydration surface for four infiltration tests.

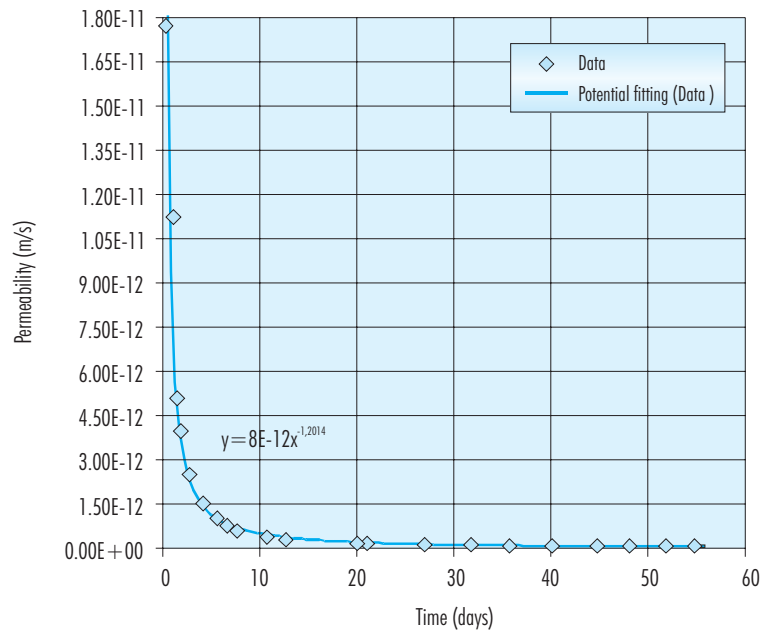


Figure 147: Evolution of the permeability with the time for a sample with a joint parallel to the infiltration flow.

- Fully coupled hydraulic and mechanical evolutions of the bentonite column with joints are considered with code CLEO.
- Stress distribution of the bentonite is assumed to obey to the effective stress principle. The effective stresses are the contribution of the total stresses and the homogeneous pore pressure.
- The water retention properties of the bentonite are not affected by the joints and can be described by the following relation (in which A and B are two coefficients defined by back-analysis):

$$S_{rw} = \frac{A}{\left(A + \frac{P_c}{\rho_w \cdot g} \right)} \quad [22]$$

- The relative permeability is not affected by the joints. The law used for the relative permeability is $k_{rl} = S_r^3$.

- The dynamic viscosity of the liquid is considered constant and equal to $1 \cdot 10^{-3}$ (Pa·s)

The detailed analysis of each of the tests performed and the parameters obtained can be found in Robinet (2003). The back-analysis of all the tests with joints parallel to the infiltration flow shows that the equivalent intrinsic permeability remained constant and equal to $3.8 \cdot 10^{-20}$ m². On the other hand, there is a variation of the retention curve as a function of the reduction of the dry density caused by the sealing of the joints (Figure 148). The coefficients A and B of the retention curve (Equation 22) depend on the percentage reduction of dry density according to the following expressions (for the homogeneous sample, $\Delta\rho_d = 0$):

$$A = -0.0002 (\Delta\rho_d)^2 + 0.0047 \Delta\rho_d + 0.0321 \quad [23]$$

$$B = 0.0011 (\Delta\rho_d)^2 + 0.0174 \Delta\rho_d + 0.6802 [24]$$

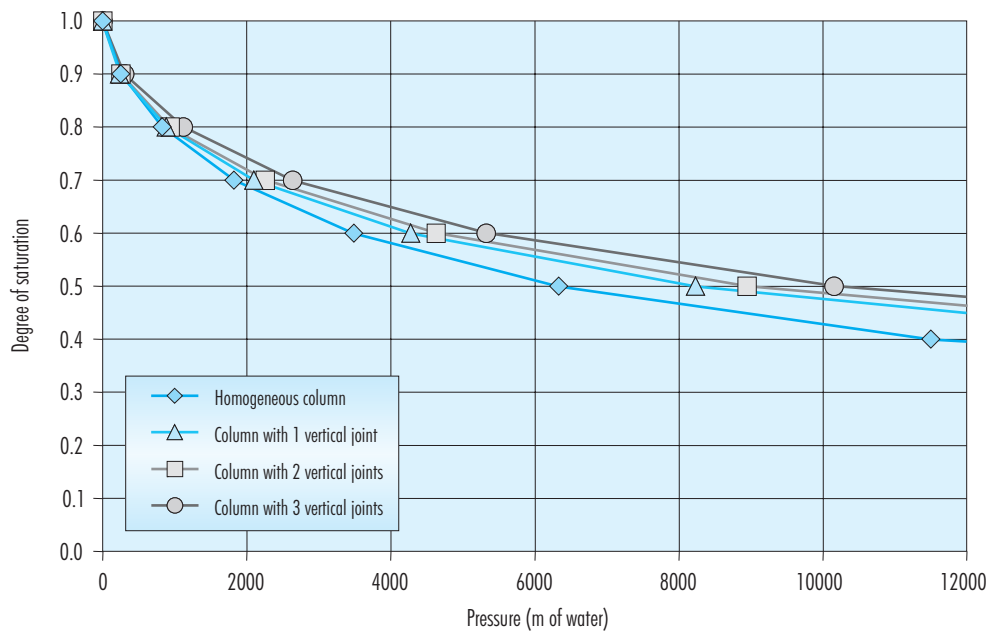


Figure 148: Retention curves of the columns with joints parallel to the infiltration flow.

5. Discussion

5. Discussion

In this section some of the results presented above are further discussed, stressing the comparisons among the outcomes obtained by the different organisations.

5.1. Physical state of the barrier

During the five-year experiment the granite has supplied water enough for the barrier to reach a high overall degree of saturation (85 percent). The bentonite seems to have controlled the hydration process, since no differences have been found in the average water content among different sections, despite the fact that the hydrogeological characteristics of the gallery were not homogeneous, due to the presence of a lamprophyre dike. The water content increase, which follows a radial pattern both in the sections around the heater and in those out of it, has provoked an overall swelling of the barrier, the filling of all the construction gaps and the decrease of the bentonite dry density. The dry density decrease—that follows also a radial pattern—is more accentuated near the gallery wall, and almost appreciable near the heater.

The water contents obtained by different groups *in situ* and in the laboratory for nearby sections have been compared in [Figure 149](#) and [Figure 150](#). The agreement between both kind of measurements—*in situ* and in laboratory—is very good, as well as the agreement among different laboratories. This suggests that the packing and transport conditions have been the appropriate to keep the *in situ* conditions of the blocks even several months after their retrieval. The higher water contents found by NAGRA near the rock in section S29 may be explained because these samples were taken from the proximity to the cable bundles. Although NAGRA dried the samples for five days instead of one day, this last being the case for the rest of participants, the water contents obtained agree well with those found by others.

The dry densities measured by different groups *in situ* and in the laboratory for nearby sections have been compared in [Figure 151](#) and [Figure 152](#). As in the case of water contents, the agreement between both kind of measurements—*in situ* and in laboratory—and among different laboratories is very good, despite the fact that the techniques employed by the various laboratories are different (mercury immersion for CIEMAT and NAGRA, coating with paraffin and weighing the sample first in air and then again while immersed in distilled water for

CIMNE, weighing first in air and then again while immersed in paraffin oil for Clay Technology). The densities determined by Clay Technology are higher than those determined by the other laboratories, especially for the two external blocks of the barrier. The reason for these densities being so high is that the water contents corresponding to these samples are lower than those determined by other laboratories—and even by Clay Technology, see [Figure 26](#)—for equivalent samples (the dry density is computed from bulk density and water content.)

Section S7—the one in contact with the concrete plug—presents a physical state distinct from the other sections. The average water content is higher and the dry density lower, and none of these parameters presents the clear radial pattern of the other sections; on the contrary, they are quite homogeneous throughout the section, as can be seen in [Figure 153](#), where the results obtained by CIEMAT and CTU are plotted together. It must be taken into account that to build the plug the concrete was pumped and compacted by vibration, its water content being very high. This probably caused a sudden increase of the water content of the clay and its heaving before the concrete hardening, with a subsequent decrease of the dry density of the clay. Besides, the concrete/bentonite interface has probably been a preferential water passageway during the operational phase of the experiment, what has allowed further intense hydration.

As described above, it has been observed that, after being subjected for five years to repository conditions, the bentonite at the barrier has experienced an overall increase of volume, which implies an increase of porosity (section 4.1), explained by the swelling and filling of all the construction gaps. The distribution of pore sizes in the bentonite samples has been studied by mercury intrusion (CIEMAT, section 4.4.1.3) and nitrogen adsorption (INPL, section 4.3.3.7, and CIEMAT, section 4.3.1.7). The main difference between these techniques is the different range of accessible pore sizes, which is between 0.006 and 100 μm diameter for mercury, and between 0.001 and 0.8 μm diameter for nitrogen adsorption. Other differences relate to the diverse preliminary preparation of the samples and to the possible effect of the intrusion of the fluid on the clay structure. Despite these differences, all the studies have shown that the treated samples have experienced a decrease in the percentage of the smaller pores. Furthermore, the mercury intrusion showed an overall homogenisation of the pore sizes and an increase of the average pore size. There is a relative

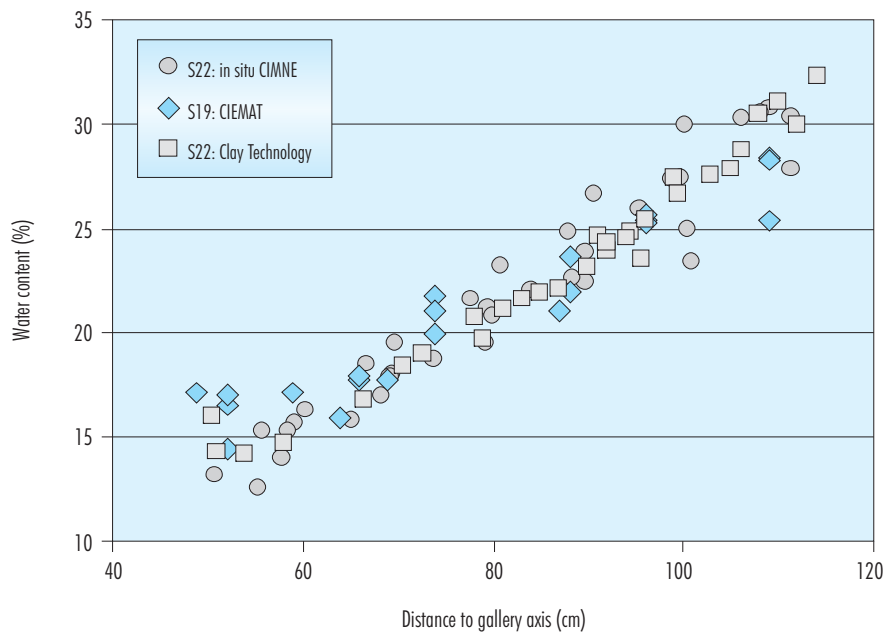


Figure 149: Comparison of water contents measured in situ (CIMNE) and in laboratory (CIEMAT and Clay Technology) for nearby sections.

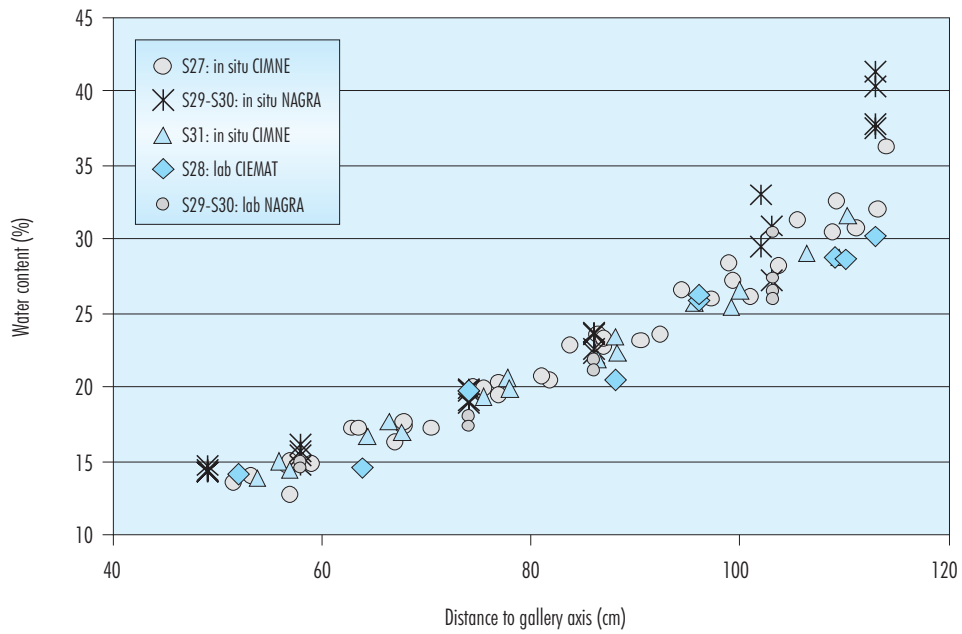


Figure 150: Comparison of water contents measured in situ and in laboratory by different organisations in nearby sections.

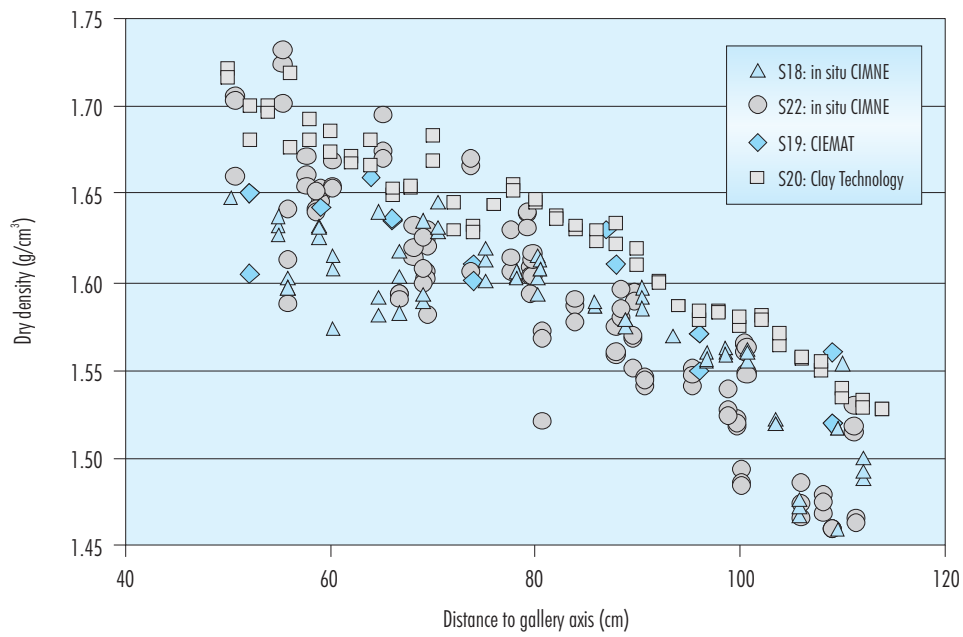


Figure 151: Comparison of dry densities measured in situ (CIMNE) and in laboratory (CIEMAT and Clay Technology) in two adjacent sections.

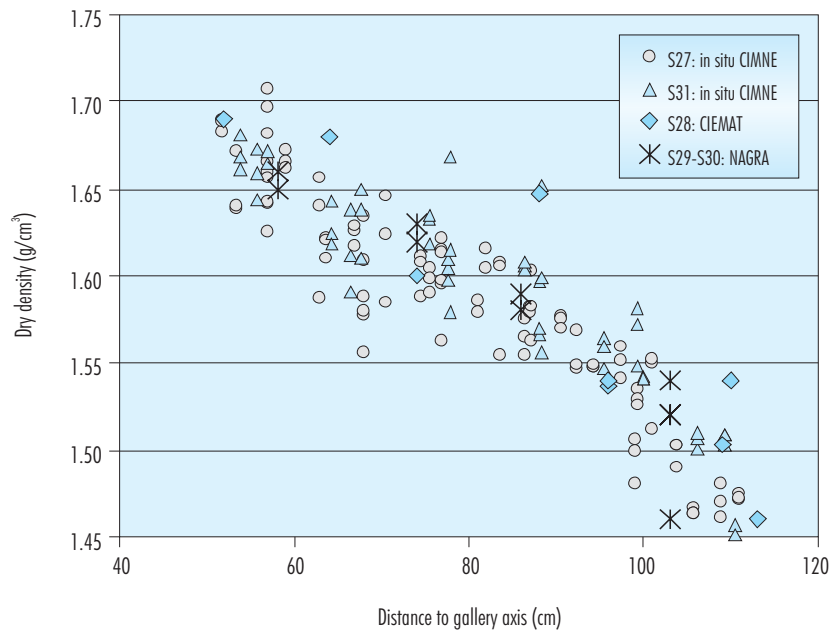


Figure 152: Comparison of dry densities measured in situ (CIMNE) and in laboratory (CIEMAT and NAGRA) in nearby sections.

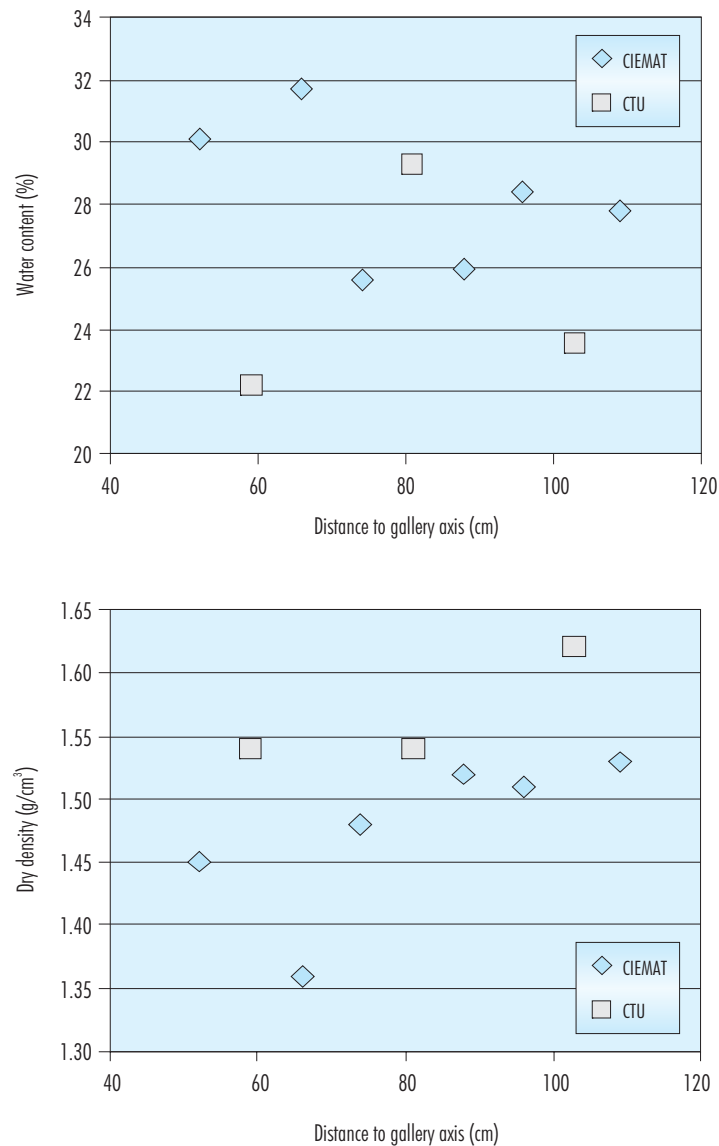


Figure 153: Water content and dry density measured in section S7 by CIEMAT and CTU.

decrease of microporosity with respect to the untreated sample, since the large pores proportion has increased. These variations, that do not seem to be related to the position of the samples in the barrier, have given place to a higher uniformity in the pore size distribution of the samples after five years of treatment. On the other hand, nitrogen adsorption has revealed that the external surface area of the compacted samples from Grimsel has decreased with respect to the initial one, especially near the heater.

The interpretation of these results must be done taking into account that, overall, the dry density of the samples from Grimsel is lower than the initial dry density of the blocks, while the water content is higher. The saturation experienced by the samples at the barrier and the associated swelling and global increase of volume (which implies a decrease of dry density from that of the compacted blocks -1.70 g/cm^3 to the average dry density of the barrier -1.58 g/cm^3 , see section 4.1.2) is probably

responsible of the pore size redistribution (Tessier 1984).

5.2. THG properties

The mineralogical and geochemical properties of the bentonite have been examined by CIEMAT in samples taken from different radii of sections with and without heater. INPL has carried out a detailed analysis of samples from one radius of a section around the heater. The results obtained are highlighted below.

The mineralogical composition of the samples from Grimsel, as determined by X-ray diffraction both by CIEMAT and INPL, is quite similar to that of the untreated FEBEX and does not show variations related to the position of the sample in the barrier: it is a mainly calcic smectite with minor quantities of quartz, plagioclase, K-feldspars, calcite and opal-CT. On the other hand, the basal spacing line in the oriented aggregates of the less than 2 μm fraction of all the samples, treated and untreated, is centred around 14.4 Å.

With respect to the chemical composition, no major differences have been observed between the reference sample and the samples from Grimsel, or among the latter. Moreover, the slight variations appreciated by one laboratory have not been corroborated by the results of the other. Thus, CIEMAT observed a general decrease of the percentage of divalent cations in the treated samples, while in the analyses by INPL, the content of Ca in the treated samples has increased with respect to the original one. Accordingly, these changes may be attributed to the natural heterogeneity of the material or to variations in the experimental methodology employed in the determinations, and it is considered that the bentonite has not suffered any important modification of its chemical composition after the five-year treatment.

Regarding the cationic exchange complex, the five-year treatment seems to have induced an increase of the sum of exchangeable cations in most of the samples analysed. This has been registered by CIEMAT as well as by INPL, although the values obtained by both laboratories are not directly comparable, since the determination techniques employed are different. CIEMAT has recorded an increase from 96 meq/100g in the original sample to values systematically higher than 100 meq/100g, frequently around 105 meq/100g; and INPL from 99 meq/100g for the reference sample to values higher than 103 meq/100g in all the treated sam-

ples. There is an important increment of potassium in exchange positions with respect to the initial value, more stressed in the external and internal blocks. An increase in sodium content is observed in the samples closer to the gallery wall, both in sections with thermal gradient and isothermal (Figure 154). CIEMAT has observed the same distribution pattern also for magnesium, whereas INPL has found an increase of this ion occupation towards the heater. In the case of calcium, there is an increase in its content at the heater contact and at the bentonite-granite contact. Therefore, different processes –linked to hydration and to high temperature– could be responsible of these variations. In thermo-hydraulic experiments performed in laboratory-scale cells with bentonite from the same deposit than the FEBEX bentonite (the S-2 bentonite) a decrease of sodium in the exchange complex towards the hotter areas was observed, as well as an increase of magnesium (Cuevas *et al.* 1997, Villar *et al.* 1997).

The analysis of the aqueous extracts of the bentonite and of the pore water obtained by squeezing performed by CIEMAT has shown that sulphates and chlorides are dissolved and leached from the external block of the barrier and that these ions concentrate in internal parts of the barrier. Both ions move further in the sections under thermal gradient, being chloride –which is counteracted by sodium– the faster ion. Thus, in the isothermal sections chlorides concentrate at 80-90 cm from the gallery axis and sulphates at 100 cm, while in the sections with heater the maximum chloride content is found at 60-70 cm from the gallery axis and the maximum sulphate at 90 cm (section 4.3.1.4). Magnesium and calcium move in a rather linked way, as both are leached from the external block and concentrate at a distance of between 60 and 80 cm from the gallery axis, depending on the existence of a thermal gradient, which favours the movement of these cations, as well as that of sodium and potassium. On the other hand, the bicarbonate content is higher in the outer blocks of the barrier, probably due to the dissolution of calcite and dolomite. The salinity of the pore water squeezed from the outer blocks of the barrier is similar to that of the water samples taken from the gas pipes located near the gallery wall (section 4.3.2).

On the other hand, both CIEMAT and VTT have performed studies in section S7, the one in contact with the concrete plug. The study by VTT has been more detailed and concentrated in the variations observed in the bentonite as a function of the distance to the concrete surface; while the study of

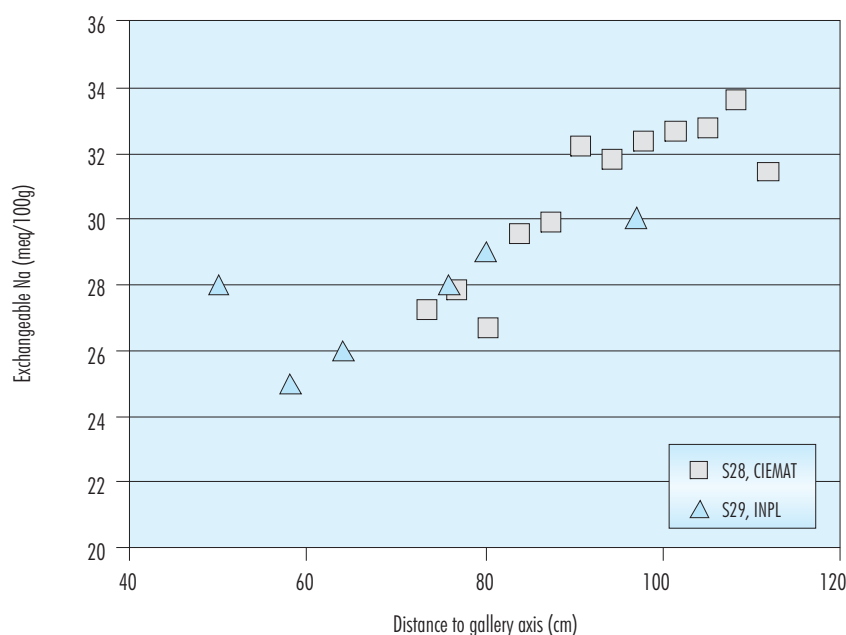


Figure 154: Distribution of exchangeable sodium along the barrier determined by CIEMAT and INPL

CIEMAT has been more extensive and has tried to establish the differences with those sections of bentonite not under the influence of the concrete.

The fact of being in contact with the concrete may have altered the mineralogical and chemical characteristics of the bentonite in this section, but also has provided a distinct hydraulic context, since the contact surface was intensely hydrated during the construction of the concrete plug and it has probably behaved as a preferential water passageway, as we have seen above.

According to the results of CIEMAT, the bentonite from section S7 has shown several differences with respect to the other sections analysed and to the reference bentonite. Although its mineralogical composition is similar to the one of the untreated FEBEX bentonite, an increase of calcite and gypsum, not observed in other sections, has been detected in one sample. On the other hand, the chemical composition of the bentonite from section S7 is similar to that of the other sections, except for a clear increase of Al. There is also a noticeable increase of Ca, Na and K in exchange positions in all the samples analysed by CIEMAT. The increase is particu-

larly important towards the central part of the barrier, where it is accompanied by a significant decrease in Mg occupation. The increase in Ca occupation has been also observed by VTT, especially in those samples taken closely to the concrete. These tendencies have been observed by other authors in experiments of hydrothermal alteration of bentonite by alkaline solutions (Leguey *et al.* 2002).

However, the main difference observed in section S7 with respect to the other sections is that the salinity of the pore water obtained by squeezing is much higher, especially concerning Cl, Ca, Mg and Na (Table XX). Nevertheless, it is remarkable that this high salinity has not been measured in the aqueous extracts (Figure 54). VTT has found a considerable increase of Na^+ , Ca^{2+} and SO_4^{2-} in the pore water of the bentonite directly in contact with the concrete, while the content of Mg^{2+} considerably decreases (Table XXXIV). The pH measured by VTT in the water from the 14 cm closer to the concrete has ranged between 8.25 and 8.32, while the waters obtained by CIEMAT had pHs of 7.8-7.9. This difference is probably due to the special care taken by VTT to perform the sampling, water extraction and analysis under anoxic conditions.

The studies performed in the context of ECOCLAY I and II projects on the alteration of bentonite by alkaline solutions have shown that intense mineralogical and geochemical modifications of the clay occur when it is in contact with concrete solutions at high temperature; for example, there is an important increase of Mg in octahedral positions that has not been detected in the bentonite from Grimsel (Table XIX). The fact that no such important changes have been observed in section S7 may be explained by the low temperatures experienced by the bentonite in this position (around 18 °C), since the reactivity of bentonite is clearly dependent on temperature, highly increasing above 75 °C. On the other hand, it seems that these alterations are greatly localised in the very contact with the bentonite, and since, in the case of CIEMAT, the bentonite coming from every block of the section has been analysed as a whole, local alterations may have been obliterated.

5.3. THM properties

The variation of the thermo-hydro-mechanical properties of the bentonite from Grimsel has been analysed by CIEMAT, CTU, EIG EURIDICE and Euro-Géomat, the latter having focused their studies on the influence of joints on remoulded samples, while CIEMAT has worked only on intact samples and CTU in both intact and remoulded samples.

The plasticity of the treated samples has not changed with respect to the original values (Table XXXIX), except for a tendency to increase in the samples that reached a higher hydration during the experiment (those of the external ring), maybe due to the increase in exchangeable sodium that took place near the gallery wall. On the other hand, the original water retention capacity of the clay seems to have remained unchanged during the operational phase of the experiment.

The saturated permeability of samples from Grimsel remoulded and compacted to different dry densities has been measured by Euro-Géomat in samples with and without joints, as well as by CIEMAT and EIG EURIDICE in intact samples. The values obtained do not correspond to the permeability of the bentonite at the moment it was retrieved; in the case of remoulded samples for obvious reasons, and in the case of intact samples, because they have been saturated to perform the determination, and permeability depends greatly on the degree of saturation. The usefulness of this kind of measurements is related to the discovering of irreversible modifications.

Euro-Géomat has found that the permeability of the remoulded samples from Grimsel (both with and without joints) is related to dry density according to Equation 19. The results obtained by Euro-Géomat, EIG EURIDICE and CIEMAT are plotted in Figure 155, together with the fittings found for the untreated bentonite during FEBEX I (Equations 1 and 2). The permeability values measured are low and strongly dependent on dry density. Both the values measured by Euro-Géomat in remoulded samples from Grimsel and the values measured by EIG EURIDICE in intact samples from Grimsel are higher than those for untreated samples of similar dry density, especially for the higher densities. However, for not remoulded samples from Grimsel, CIEMAT has found that the permeability has not clearly changed in any sense after the five years of treatment. On the other hand, measurements of hydraulic conductivity performed in specimens of FEBEX bentonite that had been subjected to thermo-hydraulic treatment in cells for periods of time between 6 and 24 months revealed a slight increase of saturated permeability with respect to the untreated sample (Villar *et al.* 2005). Consequently, it is considered that the increase of saturated permeability with respect to the permeability of the untreated FEBEX bentonite found by Euro-Géomat in remoulded samples from Grimsel and by EIG EURIDICE in intact samples, may be a consequence of the different methodology employed for its determination and of the process of remoulding.

The swelling properties have been checked by swelling under load tests performed with intact samples (CIEMAT, section 4.4.1.5) and by determination of the swell index and the swelling pressure of remoulded samples (CTU, section 4.4.2.2; Euro-Géomat, section 4.4.4.4). All these determinations may indicate if there have been irreversible changes in the swelling capacity of the clay, but the values obtained do not correspond to those of the samples when they were placed at the barrier, especially those that have been obtained in remoulded samples.

The results obtained with intact samples show that the swelling capacity of the samples from Grimsel has not changed with respect to the capacity of untreated samples of the same dry density and water content (Figure 112). The results obtained with remoulded samples point to the same direction. Swelling pressure has been determined for samples from Grimsel remoulded and compacted to different dry densities by CTU and Euro-Géomat (Equation 20). The results obtained are plotted in Figure 156 to-

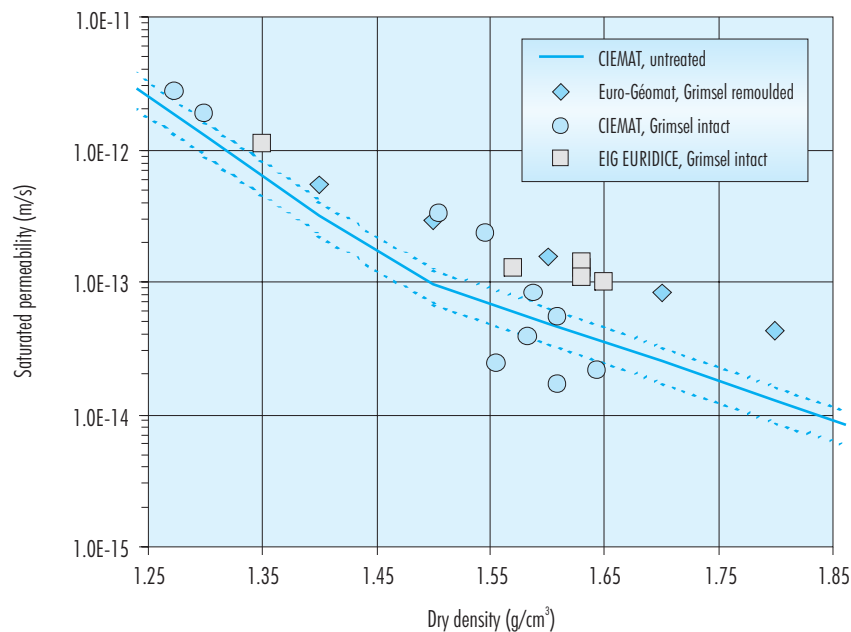


Figure 155: Permeability values of samples from Grimsel (intact and remoulded) and of untreated FEBEX bentonite.

gether with the correlation determined by CIEMAT during FEBEX I for untreated FEBEX samples (Equation 3). In all the cases the initial water content of the bentonite was the hygroscopic. Despite the fact that the methods employed by the different laboratories are quite different, the swelling pressure values obtained in samples from Grimsel are in the expected range of variation of this property for the untreated FEBEX bentonite. The results obtained by Euro-Géomat refer also to samples with joint, since they have not found differences in the swelling pressure development in samples with and without joint.

Other mechanical properties examined in the treated bentonite have been the uniaxial strength and the preconsolidation pressure. The uniaxial strength –determined by CTU in samples slightly dried (section 4.4.2.3)– is higher in the direction of compaction of the blocks than in the perpendicular, and tends to be lower for the samples that were subjected to higher temperature. Regarding the preconsolidation pressure, it has clearly decreased in all the samples tested with respect to the pressure applied to manufacture the blocks, due to the hydration and heaving of the clay (CIEMAT, section 4.4.1.6). This decrease

is higher the higher the water content reached during the operational phase of the *in situ* experiment.

On the other hand, the thermal conductivity of intact samples from different sections has been measured by CIEMAT and CTU. The results obtained are plotted in Figure 157, where it can be checked the good accordance between the results of both laboratories: the thermal conductivity is higher in the samples with higher water content, *i.e.* those that were placed near to the gallery wall. Once remoulded and dried, all the samples from Grimsel showed overall the same thermal conductivity, without any tendency related to the position the samples had in the barrier (section 4.4.2.4). However, the comparison of the values obtained in intact samples with those expected for untreated samples of the same dry density and water content, revealed a certain decrease of the original thermal conductivity related to heating.

Finally, the evaluation of the effect of joints on the thermo-hydro-mechanical properties of the samples from Grimsel has been carried out only on remoulded samples. The experiments performed in samples with joints parallel and perpendicular to the percolation flow show that, upon saturation, the me-

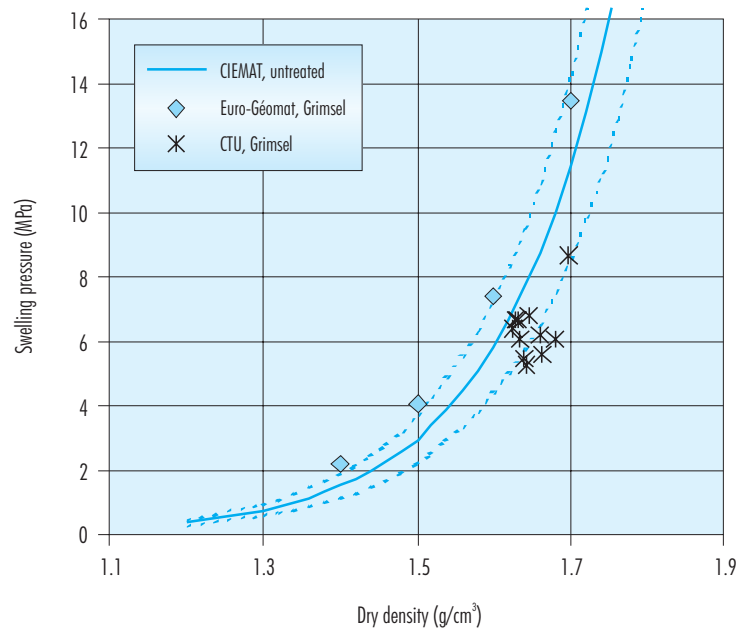


Figure 156: Swelling pressure values of remoulded samples.

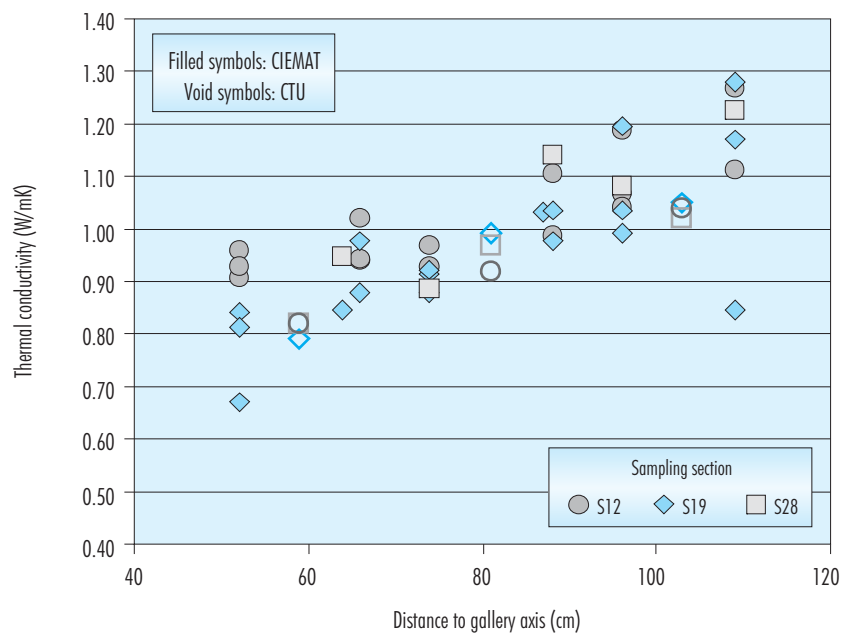


Figure 157: Thermal conductivity measured in samples from Grimsel by CIEMAT and CTU.

dium becomes homogeneous and the joints completely sealed, the hydro-mechanical properties of the material depending only on its dry density.

However, on unsaturated samples, the hydrodynamic properties of the clay are modified by the existence of joints parallel to the infiltration flow.



6. Summary and conclusions



6. Summary and conclusions

After five years of operation, heater 1 of the FEBEX experiment at the Grimsel Test Site (GTS) was switched off in February 2002. Following cooling of the system during four months, the bentonite barrier was dismantled and the heater extracted. During dismantling many bentonite samples –in the form of cores or of complete blocks– were taken. Several determinations have been carried out in these samples with the aim of: (1) characterise the actual state of the bentonite and (2) determine the possible changes in its thermo-hydro-mechanical and geochemical properties occurred during the experiment, due to the combined effect of temperature, water content, joints and solutes. The results of the characterisation performed by different laboratories have been reported and analysed.

It must be taken into account that the state of the barrier has been analysed after four months of cooling, during which temperature and relative humidity were modified with respect to the values previous to the switching off (Figure 4 to Figure 6). To evaluate the actual physical state of the barrier after dismantling, the water content and dry density of numerous samples were determined, as well as their suctions. Besides the pore size distribution of some samples has been determined by mercury intrusion porosimetry. The following conclusions can be drawn:

- The distribution of water content and dry density in vertical sections presents an axial symmetry. The average values of water content and dry density in different vertical sections along the studied zone are similar. There are no major variations in overall water content between the sections around the heater and those out of it, except that a sharper gradient of water content is found in the sections with heater than in the sections without heater. The average degree of saturation computed in all the retrieved bentonite is about 85 percent.
- Despite the fact that the geological characteristics of the gallery, especially with respect to water conductivity, were not homogeneous around the first heater, due to the presence of a lamprophyre dike, there are no differences in average water content among the different sections around the heater. Even in vertical sections that are partially crossed by fissures or dikes, the water content distribution shows a perfect radial symmetry that does not reflect the location of the conductive feature.
- The facts described above –the radial distribution of water content measured in vertical sections and the similarity among different sections– are a consequence of the predominant control of the bentonite upon the hydration kinetics, as a result of the big difference between the bentonite and granite permeabilities.
- There is a good agreement between the results obtained at the GTS immediately after retrieval of the blocks and the results obtained at the laboratory even several months afterwards. This proves that the packing and transport procedures of the blocks have been the appropriate to keep their conditions even several months after retrieval.
- After being subjected for five years to repository conditions, the samples at the barrier have experienced an overall increase of volume, which implies a decrease of dry density from that of the compacted blocks, 1.70 g/cm^3 , to an average density of the barrier of 1.58 g/cm^3 . This is explained by the filling of all the construction gaps. However, the average value of dry density found is slightly lower than that given by AITEMIN upon construction of the barrier, 1.60 g/cm^3 (ENRESA 2000, p. 210). This could be a consequence of the slight decompression suffered by the barrier on dismantling and sampling.
- The overall drop in dry density is linked to a redistribution of pore sizes and an increase of the average pore size, which are not related to the position of the samples in the barrier. There is an increment of the percentage of large pores and a relative decrease of the percentage of smaller pores. However, the higher percentage of porosity –as in the case of the untreated blocks– corresponds to the size of less than $0.006 \mu\text{m}$. On the other hand, the external specific surface of the bentonite has decreased with respect to the initial value, especially near the heater.
- The agreement between the gravimetric water contents measured (by oven drying) and the measurements of relative humidity recorded by the instrumentation installed in the bentonite blocks at Grimsel is good. On the other hand, the relative humidity of the blocks extracted has been measured in the laboratory with capacitive sensors. The comparison of the suctions thus measured agrees well with those recorded by sensors in Grimsel immediately before dismantling, what corroborates the inertia of the blocks to change their overall water content if

they are well packed and the correct performance of the *in situ* sensors.

On the other hand, the mineralogical and geochemical characterisation of Grimsel samples suggests that no great modifications occurred in the bentonite during the experiment:

- The global chemistry appears rather constant, except for a slight decrease in magnesium content with respect to the untreated sample. CIE-MAT observed also diminutions in Ca^{2+} , FeO and SO_2 contents.
- At a macroscopic scale, no mineralogical change could be evidenced. XRD analysis on the fine fraction revealed the conservation of the microscopic swelling capacity. The charge location has not changed for the postmortem samples. However, at a microscopic level, several signs of dissolution and re-precipitation of potassic feldspars could be evidenced on the samples closest to the central heater. Supplementary analyses should be carried out to insure that no dissolution marks do exist in the reference bentonite. Since potassic feldspars represent a very low part of the material, the observed phenomena are very restricted. Therefore, temperature appears as the main potential factor inducing mineralogical changes.
- The cationic exchange capacity has increased with respect to the initial one, due mainly to the overall increase of exchangeable potassium and calcium. An increase of exchangeable sodium (and probably of magnesium) has been observed towards the granite, both in sections with thermal gradient and isothermal. In the case of calcium, there is an increase in its content at the heater contact and at the bentonite-granite contact.
- Hydration of bentonite at the external blocks in contact with the granite produces the dissolution and dilution of the more soluble trace minerals in the bentonite (sulphates, carbonates and chlorides), that are transported towards the inner part of the barrier. As a result, saline fronts are generated due to the different mobility of the dissolved ions: the tendency of Na, Ca and Mg concentrations is similar to that of chloride, while sulphate mobilisation is significantly retarded with respect to chloride. Temperature seems to have great influence in salt movement: the salt movement is faster in the heater section than in the zone without temperature effect. As a result, the chloride content considerably increases towards the hot zones.

- The bentonite in contact with the concrete plug (section S7) has been analysed, searching for possible mineralogical and chemical changes induced by the lixiviation of the concrete. The particularity of this section is that the bentonite was hydrated during the construction of the plug and that the concrete/bentonite interface could have behaved as a preferential water passage-way during the experiment. On the other hand, it was the coldest bentonite section, remaining around 18 °C throughout the experiment. Both facts have probably hinder a high reactivity. In fact, the chemical and mineralogical composition of the bentonite from section S7 is rather similar to that of the untreated bentonite, except for an increase in the aluminium content and for the local occurrence of higher quantities of calcite and gypsum. There is also an increase of Ca, Na and K in the exchange positions and an increase of the salinity of the pore water.

In addition, to determine the possible changes in the THM behaviour of the bentonite occurred during the experiment, several thermal, hydraulic and mechanical properties of the retrieved bentonite were determined at the laboratory at room temperature. To evaluate the variation of hydro-mechanical properties of the bentonite after five years of TH treatment, the values obtained have been compared to those for the untreated FEBEX bentonite. Since the samples from Grimsel had different densities and water contents, it was necessary to have a complete database on the influence of these factors on the properties that are going to be tested. The results obtained can be summarised as follows:

- The water retention capacity observed in the samples from Grimsel is similar to that of samples of untreated FEBEX clay compacted to the same dry density and subjected to similar suctions. This has been confirmed by measuring the suction of the blocks from Grimsel, what suggests that the retention capacity of the FEBEX clay has not appreciably changed after five years under repository conditions.
- The hydraulic conductivity of the samples from Grimsel is clearly related to dry density and the latter in turn is related to the position of the block in the barrier. The values of hydraulic conductivity measured for the samples of lower density (more hydrated) are in the order of the theoretical ones, but for samples of higher densities there is a large dispersion in the values obtained without any clear tendency. This

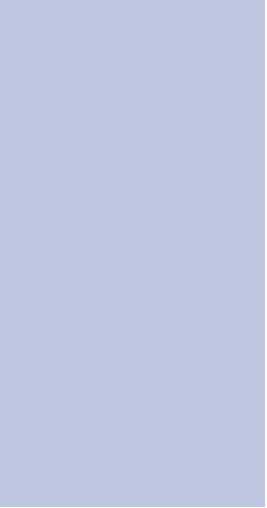
is probably due to the complexity of the experimental techniques applied, which increases for the higher densities, giving place to less accurate values.

- The swelling capacity of the FEBEX bentonite –determined as deformation upon saturation, swelling index and swelling pressure– has not changed irreversibly after five years of being subjected to repository conditions.
- Preconsolidation pressures lower than 10 MPa have been measured for all the Grimsel samples, being lower in the samples from the external ring of the barrier. It means an important decrease with respect to the initial preconsolidation pressure (around 40 MPa), the micro-structural changes associated to the volume increase experienced during hydration accounting for that.
- The uniaxial strength of the bentonite is higher in the direction of compaction of the blocks than in the perpendicular, and tends to be lower for the samples that were subjected to higher temperature.
- Thermal conductivity has been measured on the surface of around 42 blocks. Indeed, it increases with the water content of the clay and conse-

quently it is higher for the blocks of the external ring. However, the blocks of the internal and intermediate rings present lower conductivities than expected according to the theoretical values. This could suggest a certain decrease in thermal conductivity related to heating.

- The experiments performed in remoulded samples with joints parallel and perpendicular to the percolation flow show that, upon saturation, the medium becomes homogeneous and the joints completely sealed, the hydro-mechanical properties of the material depending only on its dry density. However, on unsaturated samples, the hydrodynamic properties of the clay are modified by the existence of joints parallel to the infiltration flow.

Finally, it could be said that the slight modifications observed in the chemical and mineralogical composition of the bentonite cannot be clearly correlated with any important variation on the macroscopic thermo-hydro-mechanical properties, except maybe for an increase in plasticity of the samples from the outer ring that could be linked to the increase in exchangeable sodium that took place near the gallery wall, which would be also responsible of the tendency of these samples to form colloids (4.3.1.4).



7. References



7. References

- AITEMIN (2000): Test Plan FEBEX II Project. v1. *FEBEX report 70-ST-H-0-4*. Madrid.
- AITEMIN (2002): Sampling plan for dismantling of section 1 of in situ test (Sampling Book). *FEBEX Procedure 70-AIT-G-6-27 v.2*. 114 pp. Madrid.
- Albert, W.; Weber, H.P.; Meier, E. & Dubois, D. (2003): Grimsel Test Site: FEBEX II. Excavation of TDR probes, section M1; Laboratory analyses of bentonite samples; New calibration + calculation of water content from TDR data. *Interneter Bericht 03-03*. NAGRA, 61 pp. Wettingen.
- Bárcena, I.; Fuentes-Cantillana, J.L. & García-Siñeriz, J.L. (2003): Dismantling of the heater 1 at the FEBEX "in situ" test. Description of operations. *Publicación Técnica ENRESA 09/2003*. 134 pp. Madrid.
- Barrett, E.P.; Joyner, L.G. & Halenda, P.P. (1951): The determination of pore volumes and area distribution in porous substances: I. Computation from nitrogen isotherms. *J. Am. Chem. Soc.* 73: 373-380.
- Brunauer, S.; Emmett, P.H. & Teller, E. (1938): Adsorption of gases in multimolecular layers. *J. Am. Chem. Soc.* 60: 309.
- Chandler, N.A.; Martino, J.B. & Dixon, D.A. (2001): The tunnel sealing experiment five year report *Whiteshell Laboratories ROE1LO*. 322 pp. Pinawa.
- CIEMAT (1999): Ensayos THM para el proyecto FEBEX. Internal report CIEMAT/DIAE/54111/9/99. *FEBEX report 70-IMA-M-L-66*. 115 pp. Madrid. (In Spanish).
- CTU-CEG (2003): FEBEX Project II. Report from September 1, 2002 to August 31, 2003. 42 pp. Prague.
- Cuevas, J.; Villar, M.V.; Fernández, A.M.; Gómez, P. & Martín, P.L. (1997): Pore waters extracted from compacted bentonite subjected to simultaneous heating and hydration. *Applied Geochemistry* 12: 473-481.
- Daucausse, D. & Lloret, A. (2003): Results of "in situ" measurements of water content and dry density. *FEBEX report 70-UPC-L-5-012*. 85 pp. Barcelona.
- de Boer J. H.; Linsen B. G. & Osinga Th. J. (1965): Studies on pore systems in catalysts. VI. The universal t-curve. *J. Catalysis* 4: 643.
- ENRESA (1995): Almacenamiento geológico profundo de residuos radiactivos de alta actividad (AGP). Diseños conceptuales genéricos. *Publicación Técnica ENRESA 11/95*. 105 pp. Madrid. (In Spanish).
- ENRESA (1998a): FEBEX. Bentonite: origin, properties and fabrication of blocks. *Publicación Técnica ENRESA 4/98*. 146 pp. Madrid.
- ENRESA (1998b): Final design and installation of the in situ test at Grimsel. *Publicación Técnica ENRESA 12/98*. 184 pp. Madrid.
- ENRESA (2000): FEBEX Project. Full-scale engineered barriers experiment for a deep geological repository for high level radioactive waste in crystalline host rock. Final Report. *Publicación Técnica ENRESA 1/2000*. 354 pp. Madrid.
- Entwisle, D.C. & Reeder S. (1993): New apparatus for pore fluid extraction from mudrocks for geochemical analysis. In: Manning D.A.C.; Hall P. L. & Hughes C.R. (eds): *Geochemistry of Clay-Pore Fluid Interactions*. Chapter 15: 365-388. *Chapman & Hall*. London.
- Fernández A.M. (2003): Caracterización y modelización del agua intersticial en materiales arcillosos. Estudio de la bentonita de Cortijo de Archidona. *Ph. D. Thesis*. Universidad Autónoma de Madrid, 505 pp. (In Spanish).
- Fernández, A.M. & Rivas, P. (2004): Task 141: Postmortem bentonite analyses. Geochemical behaviour. *FEBEX report 70-IMA-L-0-109*. 71 pp. Madrid.
- Fernández, A.M.; Cuevas, J. & Rivas, P. (2001): Pore water chemistry of the FEBEX bentonite. *Mat. Res. Soc. Symp. Proc.* 663: 573-588.
- Fernández, A.M.; Bath, A.; Waber, H.N. & Oyama, T. (2003): Annex 2: Water sampling by squeezing drillcores. In: Pearson et al. (Eds.): *Mont Terri Project – Geochemistry of Water in the Opalinus Clay Formation at the Mont Terri Rock Laboratory*. *Reports of the FOWG, Geology Series 5*: 171-199. Bern.
- Fernández, A.M.; Baeyens, B.; Bradbury, M. & Rivas, P. (2004): Analysis of the pore water chemical composition of a Spanish compacted bentonite used in an engineered barrier. *Physics and Chemistry of the Earth* 29(1): 105-118.
- Greene-Kelly R. (1952): A test for montmorillonite. *Nature* 170: 1130-1131.
- Gregg, S.J. & Sing K.S.W. (1982): Adsorption, Surface area and Porosity. Academic Press. London.
- GRS (1996): Project FEBEX. Installation Report of Pressure Pipes and Filter Pipes for Gas sampling and Permeability Measurements. Braunschweig.
- Harkins W.D. & Jura G. (1944): Vapor adsorption method for determining the area of solid without assumption of a molecular area. *J. Am. Chem. Soc.* 66: 1366.
- Harvey C.O. (1943) Some notes on the calculation of molecular formulae for glauconite. *Am. Min.* 28: 541-543.
- Hower J. & Mowatt T.C. (1966): The mineralogy of illites and mixed layer illite-montmorillonites. *Am. Miner.* 51: 825-857.
- Jockwer N. & Wiczorek K. (1999): FEBEX Summary Report 1996-1999: GRS Contribution. Investigation of Gas Generation, Release and Migration. *FEBEX report*.
- Keusen, H.R.; Ganguin, J.; Schuler, P. & Bulletti, M. (1989): Grimsel Test Site, Geology. *NAGRA Technical Report 87-14E*. Baden.
- Leguey, S.; Cuevas, J.; Ramírez, S.; Vigil, R. & Martín, M. (2002): Alteración alcalina hidrotermal de la barrera de bentonita por aguas intersticiales de cementos. *Publicación Técnica ENRESA 03/02*. 172 pp. Madrid. (In Spanish).

- Lim C.H. & Jackson M.L. (1986): Expandable phyllosilicate reactions with lithium on heating. *Clays and Clay Minerals* 34 (3): 346-352.
- Lloret, A.; Villar, M.V. & Pintado, X. (2002): Ensayos THM: Informe de síntesis. Internal report CIEMAT/DIAE/54111/9/99. FEBEX report 70-UPC-M-0-04. 97 pp. Barcelona.
- Lloret, A.; Villar, M.V.; Sánchez, M.; Gens, A.; Pintado, X. & Alonso, E.E. (2003). Mechanical behaviour of heavily compacted bentonite under high suction changes. *Géotechnique* 53(1): 27-40.
- Lloret, A.; Villar, M.V. & Romero, E. (2004): FEBEX II Project. Final report on thermo-hydro-mechanical laboratory tests. Publicación Técnica ENRESA 10/04, 180 pp. Madrid.
- Montarges-Pelletier, E.; Devineau, K.; Villieras, F.; Bouquet, E.; Pelletier, M.; Razafitianamaharavo, A.; Barres, O.; Lambert, P.; Charpentier, D.; Mosser-Ruck, R. & Cathelineau, M. (2003): Postmortem FEBEX bentonite samples. Mineralogical and textural analysis. Final report LEM. 34 pp. Vandoeuvre-lès-Nancy.
- Montenegro, L.; Samper, J.; Zheng, L. ; Fernández, A.M. & Rivas, P. (2004): Sampling, laboratory analyses and numerical modelling of deuterium in the in situ FEBEX experiment. FEBEX report 70-ULC-L-6-03. La Coruña.
- Müller-Vonmoos, M. & Kahr, G. (1983): Mineralogische Untersuchungen von Wyoming Bentonite mx-80 and Montigel. *NAGRA Technischer Bericht* 83-12, 15 pp. + app. 13 pp. Baden.
- Muurinen, A. (2001): Development and testing of analysis methods for bentonite pore water. *Posiva OY, Working Report* 2001-07, 33 pp. + app. 4 pp. Helsinki.
- Muurinen, A. (2003): Analysis of the samples from the cement-bentonite interface of the FEBEX in situ experiment. VTT processes. FEBEX Study 70-VTT-I-6-02. 14 pp. Helsinki.
- Pearson, F.J.; Arcos, D.; Bath, A.; Boisson, J.-Y.; Fernández, A.M.; Gäbler, H.-E.; Gaucher, E.; Gautschi, A.; Griffault, L.; Hernán, P. & Waber, H.N. (2003): Mont Terri Project – Geochemistry of Water in the Opalinus Clay Formation at the Mont Terri Rock Laboratory. *Reports of the FOWG, Geology Series* 5. 319 pp. Bern.
- Peters, C. A.; Yang, Y. C.; Higgins, J. D. & Burger, P. A. (1992): A preliminary study of the chemistry of pore water extracted from tuff by one-dimensional compression. In: Kharaka & Maest (eds): *Water-Rock Interaction*, pp. 741-745.
- Poirier J. E.; François M. & Cases J. M. (1987): Study of water adsorption on Na-Montmorillonite/ New data owing the use of a continuous procedure. In: Liapis, A.T. (Ed.): *Fundamentals of adsorption. A. I. Ch. E.* New York. pp 473-482.
- Robinet, J.C. (2003) : Study of the effects of the joints on the hydraulic and hydro-mechanical properties of the FEBEX in situ test. Internal Report Euro-Géomat Consulting. FEBEX report. 43 pp. Orléans.
- Rouiller J.; Burtin G. & Souchier B. (1972): La dispersion des sols dans l'analyse granulométrique. Méthode utilisant les résines échangeuses d'ions. *Bulletin de l'Ecole Nationale Supérieure d'Agronomie et des Industries Alimentaires*. Tome XIV, fascicule II. pp 193-205. (In French).
- Russel J.D. & Fraser A.R. (1992): Infrared methods. In: Wilson, M.J. (ed.): *Clay Mineralogy: Spectroscopic and chemical determinative methods*. Chapter 2, pp. 11-67. *Chapman & Hall*, London.
- Sawhney, B. L. (1970): Potassium and cesium ion selectivity in relation to clay mineral microstructure. *Clays & Clay Minerals* 18: 47-52.
- Schultz, L.G. (1964): Quantitative interpretation of mineralogical composition from X-Ray and chemical data for the Pierre Shale. *Geological Survey of U.S.A. Professional Paper* 591-C: C1-C31.
- Sing, K.S.W.; Everett, D.H.; Haul, R.A.W.; Moscou, L.; Pierotti, R.A.; Rouquérol, J. & Siemieniewska, T. (1985): Reporting physisorption data for gas/solid systems with special reference to the determination of surface area and porosity. *Pure & Appl. Chem.* 57(4): 603-619. IUPAC.
- Tessier, D. (1984): Etude expérimentale de l'organisation des matériaux argileux. Hydratation, gonflement et structuration au cours de la dessiccation et de la réhumectation. *Ph.D. Thesis*. Université de Paris VII. 361 pp. Paris. (In French).
- Tuncer, E.R. (1988): Pore size distribution characteristics of tropical soils in relation to engineering properties. *Proc. 2nd Int. Conf. on Geomechanics in Tropical Soils* 1: 63-70. Singapore.
- UPC (1999): Ensayos THM para el proyecto FEBEX realizados por la UPC-DIT. Internal report UPC. FEBEX report 70-UPC-M-0-03. 157 pp. Barcelona. (In Spanish).
- Verstricht, J. (2004): Work Package 1. Task 1.4 Post-mortem analysis. Bentonite. Technical Report 70-EIG-L-6-02. ESV EURIDICE GIE. 24 pp. Mol.
- Villar, M.V. (2000): Caracterización termo-hidro-mecánica de una bentonita de Cabo de Gata. *Ph.D. Thesis*. Universidad Complutense de Madrid. 396 pp. Madrid. (In Spanish).
- Villar, M.V. (2002): Thermo-hydro-mechanical characterisation of a bentonite from Cabo de Gata. A study applied to the use of bentonite as sealing material in high level radioactive waste repositories. *Publicación Técnica ENRESA* 01/2002. 258 pp. Madrid.
- Villar, M.V. (2003): Task 141: Postmortem bentonite analysis. Contribution of CIEMAT (THM) to Deliverable D11. Internal report CIEMAT/DIAE/54520/12 /03. FEBEX report 70-IMA-L-6-107v0. 45 pp. Madrid.

- Villar, M.V. & Lloret, A. (2004): Influence of temperature on the hydro-mechanical behaviour of a compacted bentonite. *Applied Clay Science* 26: 337-350.
- Villar, M.V.; Fernández, A.M. & Cuevas, J. (1997): Caracterización geoquímica de bentonita compactada: Efectos producidos por flujo termohidráulico. Versión 1. Internal report CIEMAT/IMA/54A15/ 6/97. *FEBEX report* 70-IMA-M-0-2. Madrid. (In Spanish).
- Villar M.V.; Fernández A.M.; Hernández A.I.; Muurinen A.; Pacovský J.; Montenegro L.; Gourry J.C.; Lloret A.; Verstricht J.; Villieras F. & Robinet J.C. (2002a): Work proposal for task 141: Postmortem bentonite analysis. *FEBEX report* 70-IMA-H-6-16 v1. 35 pp. Madrid.
- Villar, M.V.; Martín, P.L.; Lloret, A. & Romero, E. (2002b): 2nd Report on Thermo-hydro-mechanical laboratory tests. Deliverable D-17/2. September 00-March 02. May 2002. CIEMAT/DIAE/54520/6/02. *FEBEX report* 70-IMA-L-0-97. 53 pp. Madrid.
- Villar, M.V.; Martín, P.L. & Barcala, J.M. (2005): Modification of physical, mechanical and hydraulic properties of bentonite by thermo-hydraulic gradients. *Eng. Geol.*

PUBLICACIONES TÉCNICAS

1991

- 01 REVISIÓN SOBRE LOS MODELOS NUMÉRICOS RELACIONADOS CON EL ALMACENAMIENTO DE RESIDUOS RADIACTIVOS.
- 02 REVISIÓN SOBRE LOS MODELOS NUMÉRICOS RELACIONADO CON EL ALMACENAMIENTO DE RESIDUOS RADIACTIVOS. ANEXO 1. Guía de códigos aplicables.
- 03 PRELIMINARY SOLUBILITY STUDIES OF URANIUM DIOXIDE UNDER THE CONDITIONS EXPECTED IN A SALINE REPOSITORY.
- 04 GEOSTADÍSTICA PARA EL ANÁLISIS DE RIESGOS. Una introducción a la Geostatística no paramétrica.
- 05 SITUACIONES SINÓPTICAS Y CAMPOS DE VIENTOS ASOCIADOS EN "EL CABRIL".
- 06 PARAMETERS, METHODOLOGIES AND PRIORITIES OF SITE SELECTION FOR RADIOACTIVE WASTE DISPOSAL IN ROCK SALT FORMATIONS.

1992

- 01 STATE OF THE ART REPORT: DISPOSAL OF RADIOACTIVE WASTE IN DEEP ARGILLACEOUS FORMATIONS.
- 02 ESTUDIO DE LA INFILTRACIÓN A TRAVÉS DE LA COBERTERA DE LA FUA.
- 03 SPANISH PARTICIPATION IN THE INTERNATIONAL INTRAVAL PROJECT.
- 04 CARACTERIZACIÓN DE ESMECTITAS MAGNÉSICAS DE LA CUENCA DE MADRID COMO MATERIALES DE SELLADO. Ensayos de alteración hidrotermal.
- 05 SOLUBILITY STUDIES OF URANIUM DIOXIDE UNDER THE CONDITIONS EXPECTED IN A SALINE REPOSITORY. Phase II
- 06 REVISIÓN DE MÉTODOS GEOFÍSICOS APLICABLES AL ESTUDIO Y CARACTERIZACIÓN DE EMPLAZAMIENTOS PARA ALMACENAMIENTO DE RESIDUOS RADIACTIVOS DE ALTA ACTIVIDAD EN GRANITOS, SALES Y ARCILLAS.
- 07 COEFICIENTES DE DISTRIBUCIÓN ENTRE RADIONUCLEIDOS.
- 08 CONTRIBUTION BY CTN-JPM TO THE PSACON LEVEL-5 EXERCISE.
- 09 DESARROLLO DE UN MODELO DE RESUSPENSIÓN DE SUELOS CONTAMINADOS. APLICACIÓN AL ÁREA DE PALOMARES.
- 10 ESTUDIO DEL CÓDIGO FFSM PARA CAMPO LEJANO. IMPLANTACIÓN EN VAX.
- 11 LA EVALUACIÓN DE LA SEGURIDAD DE LOS SISTEMAS DE ALMACENAMIENTO DE RESIDUOS RADIACTIVOS. UTILIZACIÓN DE MÉTODOS PROBABILISTAS.
- 12 METODOLOGÍA CANADIENSE DE EVALUACIÓN DE LA SEGURIDAD DE LOS ALMACENAMIENTOS DE RESIDUOS RADIACTIVOS.
- 13 DESCRIPCIÓN DE LA BASE DE DATOS WALKER.

Publicaciones no periódicas

PONENCIAS E INFORMES, 1988-1991.
SEGUNDO PLAN DE I+D, 1991-1995. TOMOS I, II Y III.
SECOND RESEARCH AND DEVELOPMENT PLAN, 1991-1995, VOLUME I.

1993

- 01 INVESTIGACIÓN DE BENTONITAS COMO MATERIALES DE SELLADO PARA ALMACENAMIENTO DE RESIDUOS RADIACTIVOS DE ALTA ACTIVIDAD. ZONA DE CABO DE GATA, ALMERÍA.
- 02 TEMPERATURA DISTRIBUTION IN A HYPOTHETICAL SPENT NUCLEAR FUEL REPOSITORY IN A SALT DOME.
- 03 ANÁLISIS DEL CONTENIDO EN AGUA EN FORMACIONES SALINAS. Su aplicación al almacenamiento de residuos radiactivos
- 04 SPANISH PARTICIPATION IN THE HAW PROJECT. Laboratory Investigations on Gamma Irradiation Effects in Rock Salt.
- 05 CARACTERIZACIÓN Y VALIDACIÓN INDUSTRIAL DE MATERIALES ARCILLOSOS COMO BARRERA DE INGENIERÍA.
- 06 CHEMISTRY OF URANIUM IN BRINES RELATED TO THE SPENT FUEL DISPOSAL IN A SALT REPOSITORY (I).
- 07 SIMULACIÓN TÉRMICA DEL ALMACENAMIENTO EN GALERÍA-TSS.
- 08 PROGRAMAS COMPLEMENTARIOS PARA EL ANÁLISIS ESTOCÁSTICO DEL TRANSPORTE DE RADIONUCLEIDOS.
- 09 PROGRAMAS PARA EL CÁLCULO DE PERMEABILIDADES DE BLOQUE.
- 10 METHODS AND RESULTS OF THE INVESTIGATION OF THE THERMOMECHANICAL BEHAVIOUR OF ROCK SALT WITH REGARD TO THE FINAL DISPOSAL OF HIGH-LEVEL RADIOACTIVE WASTES.

Publicaciones no periódicas

SEGUNDO PLAN DE I+D. INFORME ANUAL 1992.
PRIMERAS JORNADAS DE I+D EN LA GESTIÓN DE RESIDUOS RADIACTIVOS. TOMOS I Y II.

1994

- 01 MODELO CONCEPTUAL DE FUNCIONAMIENTO DE LOS ECOSISTEMAS EN EL ENTORNO DE LA FÁBRICA DE URANIO DE ANDÚJAR.
- 02 CORROSION OF CANDIDATE MATERIALS FOR CANISTER APPLICATIONS IN ROCK SALT FORMATIONS.
- 03 STOCHASTIC MODELING OF GROUNDWATER TRAVEL TIMES
- 04 THE DISPOSAL OF HIGH LEVEL RADIOACTIVE WASTE IN ARGILLACEOUS HOST ROCKS. Identification of parameters, constraints and geological assessment priorities.
- 05 EL OESTE DE EUROPA Y LA PENÍNSULA IBÉRICA DESDE HACE -120.000 AÑOS HASTA EL PRESENTE. Isostasia glacial, paleogeografías paleotemperaturas.
- 06 ECOLOGÍA EN LOS SISTEMAS ACUÁTICOS EN EL ENTORNO DE EL CABRIL.
- 07 ALMACENAMIENTO GEOLÓGICO PROFUNDO DE RESIDUOS RADIACTIVOS DE ALTA ACTIVIDAD (AGP). Conceptos preliminares de referencia.
- 08 UNIDADES MÓVILES PARA CARACTERIZACIÓN HIDROGEOQUÍMICA
- 09 EXPERIENCIAS PRELIMINARES DE MIGRACIÓN DE RADIONUCLEIDOS CON MATERIALES GRANÍTICOS. EL BERROCAL, ESPAÑA.
- 10 ESTUDIOS DE DESEQUILIBRIOS ISOTÓPICOS DE SERIES RADIACTIVAS NATURALES EN UN AMBIENTE GRANÍTICO: PLUTÓN DE EL BERROCAL (TOLEDO).
- 11 RELACIÓN ENTRE PARÁMETROS GEOFÍSICOS E HIDROGEOLÓGICOS. Una revisión de literatura.
- 12 DISEÑO Y CONSTRUCCIÓN DE LA COBERTURA MULTICAPA DEL DIQUE DE ESTÉRILES DE LA FÁBRICA DE URANIO DE ANDÚJAR.

Publicaciones no periódicas

SEGUNDO PLAN I+D 1991-1995. INFORME ANUAL 1993.

1995

- 01 DETERMINACIÓN DEL MÓDULO DE ELASTICIDAD DE FORMACIONES ARCILLOSAS PROFUNDAS.
- 02 UO LEACHING AND RADIONUCLIDE RELEASE MODELLING UNDER HIGH AND LOW IONIC STRENGTH SOLUTION AND OXIDATION CONDITIONS.
- 03 THERMO-HYDRO-MECHANICAL CHARACTERIZATION OF THE SPANISH REFERENCE CLAY MATERIAL FOR ENGINEERED BARRIER FOR GRANITE AND CLAY HLW REPOSITORY: LABORATORY AND SMALL MOCK UP TESTING.
- 04 DOCUMENTO DE SÍNTESIS DE LA ASISTENCIA GEOTÉCNICA AL DISEÑO AGP-ARCILLA. Concepto de referencia.
- 05 DETERMINACIÓN DE LA ENERGÍA ACUMULADA EN LAS ROCAS SALINAS FUERTEMENTE IRRADIADAS MEDIANTE TÉCNICAS DE TERMOLUMINISCENCIA. Aplicación al análisis de repositorios de residuos radiactivos de alta actividad.
- 06 PREDICCIÓN DE FENÓMENOS DE TRANSPORTE EN CAMPO PRÓXIMO Y LEJANO. Interacción en fases sólidas.
- 07 ASPECTOS RELACIONADOS CON LA PROTECCIÓN RADIOLÓGICA DURANTE EL DESMANTELAMIENTO Y CLAUSURA DE LA FÁBRICA DE ANDÚJAR.
- 08 ANALYSIS OF GAS GENERATION MECHANISMS IN UNDERGROUND RADIOACTIVE WASTE REPOSITORIES. (Pegase Project).
- 09 ENSAYOS DE LIXIVIACIÓN DE EMISORES BETA PUROS DE LARGA VIDA.
- 10 2º PLAN DE I+D. DESARROLLOS METODOLÓGICOS, TECNOLÓGICOS, INSTRUMENTALES Y NUMÉRICOS EN LA GESTIÓN DE RESIDUOS RADIACTIVOS.
- 11 PROYECTO AGP-ALMACENAMIENTO GEOLÓGICO PROFUNDO. FASE 2.
- 12 IN SITU INVESTIGATION OF THE LONG-TERM SEALING SYSTEM AS COMPONENT OF DAM CONSTRUCTION (DAM PROJECT). Numerical simulator: Code-Bright.

Publicaciones no periódicas

TERCER PLAN DE I+D 1995-1999.
SEGUNDAS JORNADAS DE I+D. EN LA GESTIÓN DE RESIDUOS RADIACTIVOS. TOMOS I Y II.

1996

- 01 DESARROLLO DE UN PROGRAMA INFORMÁTICO PARA EL ASESORAMIENTO DE LA OPERACIÓN DE FOCOS EMISORES DE CONTAMINANTES GASEOSOS.
- 02 FINAL REPORT OF PHYSICAL TEST PROGRAM CONCERNING SPANISH CLAYS (SAPONITES AND BENTONITES).
- 03 APORTACIONES AL CONOCIMIENTO DE LA EVOLUCIÓN PALEOCLIMÁTICA Y PALEOAMBIENTAL EN LA PENÍNSULA IBÉRICA DURANTE LOS DOS ÚLTIMOS MILLONES DE AÑOS A PARTIR DEL ESTUDIO DE TRAVERTINOS Y ESPELEOTEMAS.
- 04 MÉTODOS GEOESTADÍSTICOS PARA LA INTEGRACIÓN DE INFORMACIÓN.
- 05 ESTUDIO DE LONGEVIDAD EN BENTONITAS: ESTABILIDAD HIDROTÉRMICA DE SAPONITAS.
- 06 ALTERACIÓN HIDROTÉRMICA DE LAS BENTONITAS DE ALMERÍA.

- 07 MAYDAY. UN CÓDIGO PARA REALIZAR ANÁLISIS DE INCERTIDUMBRE Y SENSIBILIDAD. Manuales.

Publicaciones no periódicas

EL BERROCAL PROJECT. VOLUME I. GEOLOGICAL STUDIES.
EL BERROCAL PROJECT. VOLUME II. HYDROGEOCHEMISTRY.
EL BERROCAL PROJECT. VOLUME III. LABORATORY MIGRATION TESTS AND IN SITU TRACER TEST.
EL BERROCAL PROJECT. VOLUME IV. HYDROGEOLOGICAL MODELLING AND CODE DEVELOPMENT.

1997

- 01 CONSIDERACIÓN DEL CAMBIO MEDIOAMBIENTAL EN LA EVALUACIÓN DE LA SEGURIDAD. ESCENARIOS CLIMÁTICOS A LARGO PLAZO EN LA PENÍNSULA IBÉRICA.
- 02 METODOLOGÍA DE EVALUACIÓN DE RIESGO SÍSMICO EN SEGMENTOS DE FALLA.
- 03 DETERMINACIÓN DE RADIONUCLEIDOS PRESENTES EN EL INVENTARIO DE REFERENCIA DEL CENTRO DE ALMACENAMIENTO DE EL CABRIL.
- 04 ALMACENAMIENTO DEFINITIVO DE RESIDUOS DE RADIOACTIVIDAD ALTA. Caracterización y comportamiento a largo plazo de los combustibles nucleares irradiados (I).
- 05 METODOLOGÍA DE ANÁLISIS DE LA BIOSFERA EN LA EVALUACIÓN DE ALMACENAMIENTOS GEOLÓGICOS PROFUNDOS DE RESIDUOS RADIACTIVOS DE ALTA ACTIVIDAD ESPECÍFICA.
- 06 EVALUACIÓN DEL COMPORTAMIENTO Y DE LA SEGURIDAD DE UN ALMACENAMIENTO GEOLÓGICO PROFUNDO EN GRANITO. Marzo 1997
- 07 SÍNTESIS TECTOESTRATIGRÁFICA DEL MACIZO HESPÉRICO. VOLUMEN I.
- 08 III JORNADAS DE I+D Y TECNOLOGÍAS DE GESTIÓN DE RESIDUOS RADIACTIVOS. Pósters descriptivos de los proyectos de I+D y evaluación de la seguridad a largo plazo.
- 09 FEBEX. ETAPA PREOPERACIONAL. INFORME DE SÍNTESIS.
- 10 METODOLOGÍA DE GENERACIÓN DE ESCENARIOS PARA LA EVALUACIÓN DEL COMPORTAMIENTO DE LOS ALMACENAMIENTOS DE RESIDUOS RADIACTIVOS.
- 11 MANUAL DE CESARR V.2. Código para la evaluación de seguridad de un almacenamiento superficial de residuos radiactivos de baja y media actividad.

1998

- 01 FEBEX. PRE-OPERATIONAL STAGE. SUMMARY REPORT.
- 02 PERFORMANCE ASSESSMENT OF A DEEP GEOLOGICAL REPOSITORY IN GRANITE. March 1997.
- 03 FEBEX. DISEÑO FINAL Y MONTAJE DEL ENSAYO "IN SITU" EN GRIMSEL.
- 04 FEBEX. BENTONITA: ORIGEN, PROPIEDADES Y FABRICACIÓN DE BLOQUES.
- 05 FEBEX. BENTONITE: ORIGIN, PROPERTIES AND FABRICATION OF BLOCKS.
- 06 TERCERAS JORNADAS DE I+D Y TECNOLOGÍAS DE GESTIÓN DE RESIDUOS RADIACTIVOS. 24-29 Noviembre, 1997. Volumen I
- 07 TERCERAS JORNADAS DE I+D Y TECNOLOGÍAS DE GESTIÓN DE RESIDUOS RADIACTIVOS. 24-29 Noviembre, 1997. Volumen II
- 08 MODELIZACIÓN Y SIMULACIÓN DE BARRERAS CAPILARES.
- 09 FEBEX. PREOPERATIONAL THERMO-HYDRO-MECHANICAL (THM) MODELLING OF THE "IN SITU" TEST.
- 10 FEBEX. PREOPERATIONAL THERMO-HYDRO-MECHANICAL (THM) MODELLING OF THE "MOCK UP" TEST.
- 11 DISOLUCIÓN DEL UO (S) EN CONDICIONES REDUCTORAS Y OXIDANTES.
- 12 FEBEX. FINAL DESIGN AND INSTALLATION OF THE "IN SITU" TEST AT GRIMSEL.

1999

- 01 MATERIALES ALTERNATIVOS DE LA CÁPSULA DE ALMACENAMIENTO DE RESIDUOS RADIACTIVOS DE ALTA ACTIVIDAD.
- 02 INTRAVAL PROJECT PHASE 2: STOCHASTIC ANALYSIS OF RADIONUCLIDES TRAVEL TIMES AT THE WASTE ISOLATION PILOT PLANT (WIPP), IN NEW MEXICO (U.S.A.).
- 03 EVALUACIÓN DEL COMPORTAMIENTO Y DE LA SEGURIDAD DE UN ALMACENAMIENTO PROFUNDO EN ARCILLA. Febrero 1999.
- 04 ESTUDIOS DE CORROSIÓN DE MATERIALES METÁLICOS PARA CÁPSULAS DE ALMACENAMIENTO DE RESIDUOS DE ALTA ACTIVIDAD.
- 05 MANUAL DEL USUARIO DEL PROGRAMA VISUAL BALAN V. 1.0. CÓDIGO INTERACTIVO PARA LA REALIZACIÓN DE BALANCES HIDROLÓGICOS Y LA ESTIMACIÓN DE LA RECARGA.
- 06 COMPORTAMIENTO FÍSICO DE LAS CÁPSULAS DE ALMACENAMIENTO.
- 07 PARTICIPACIÓN DEL CIEMAT EN ESTUDIOS DE RADIOECOLOGÍA EN ECOSISTEMAS MARINOS EUROPEOS.

- 08 PLAN DE INVESTIGACIÓN Y DESARROLLO TECNOLÓGICO PARA LA GESTIÓN DE RESIDUOS RADIACTIVOS 1999-2003. OCTUBRE 1999.
- 09 ESTRATIGRAFÍA BIOMOLECULAR. LA RACEMIZACIÓN/EPIMERIZACIÓN DE AMINOÁCIDOS COMO HERRAMIENTA GEOCRONOLÓGICA Y PALEOTERMOMÉTRICA.
- 10 CATSIUS CLAY PROJECT. Calculation and testing of behaviour of unsaturated clay as barrier in radioactive waste repositories. STAGE 1: VERIFICATION EXERCISES.
- 11 CATSIUS CLAY PROJECT. Calculation and testing of behaviour of unsaturated clay as barrier in radioactive waste repositories. STAGE 2: VALIDATION EXERCISES AT LABORATORY SCALE.
- 12 CATSIUS CLAY PROJECT. Calculation and testing of behaviour of unsaturated clay as barrier in radioactive waste repositories. STAGE 3: VALIDATION EXERCISES AT LARGE "IN SITU" SCALE.

2000

- 01 FEBEX PROJECT. FULL-SCALE ENGINEERED BARRIERS EXPERIMENT FOR A DEEP GEOLOGICAL REPOSITORY FOR HIGH LEVEL RADIOACTIVE WASTE IN CRYSTALLINE HOST ROCK. FINAL REPORT.
- 02 CÁLCULO DE LA GENERACIÓN DE PRODUCTOS RADIOLÍTICOS EN AGUA POR RADIACIÓN *et.*. DETERMINACIÓN DE LA VELOCIDAD DE ALTERACIÓN DE LA MATRIZ DEL COMBUSTIBLE NUCLEAR GASTADO.
- 03 LIBERACIÓN DE RADIONUCLEÍDOS E ISÓTOPOS ESTABLES CONTENIDOS EN LA MATRIZ DEL COMBUSTIBLE. MODELO CONCEPTUAL Y MODELO MATEMÁTICO DEL COMPORTAMIENTO DEL RESIDUO.
- 04 DESARROLLO DE UN MODELO GEOQUÍMICO DE CAMPO PRÓXIMO.
- 05 ESTUDIOS DE DISOLUCIÓN DE ANÁLOGOS NATURALES DE COMBUSTIBLE NUCLEAR IRRADIADO Y DE FASES DE (U)VI-SILICIO REPRESENTATIVAS DE UN PROCESO DE ALTERACIÓN OXIDATIVA.
- 06 CORE2D. A CODE FOR NON-ISOTHERMAL WATER FLOW AND REACTIVE SOLUTE TRANSPORT. USERS MANUAL VERSION 2.
- 07 ANÁLOGOS ARQUEOLÓGICOS E INDUSTRIALES PARA ALMACENAMIENTOS PROFUNDOS: ESTUDIO DE PIEZAS ARQUEOLÓGICAS METÁLICAS.
- 08 PLAN DE INVESTIGACIÓN Y DESARROLLO TECNOLÓGICO PARA LA GESTIÓN DE RESIDUOS RADIACTIVOS 1999-2003. REVISIÓN 2000.
- 09 IV JORNADAS DE INVESTIGACIÓN Y DESARROLLO TECNOLÓGICO EN GESTIÓN DE RESIDUOS RADIACTIVOS. POSTERS TÉCNICOS.
- 10 IV JORNADAS DE INVESTIGACIÓN Y DESARROLLO TECNOLÓGICO EN GESTIÓN DE RESIDUOS RADIACTIVOS. POSTERS TÉCNICOS.
- 11 PROGRAMA DE INVESTIGACIÓN PARA ESTUDIAR LOS EFECTOS DE LA RADIACIÓN GAMMA EN BENTONITAS CÁLCICAS ESPAÑOLAS.
- 12 CARACTERIZACIÓN Y LIXIVIACIÓN DE COMBUSTIBLES NUCLEARES IRRADIADOS Y DE SUS ANÁLOGOS QUÍMICOS.

2001

- 01 MODELOS DE FLUJO MULTIFÁSICO NO ISOTERMO Y DE TRANSPORTE REACTIVO MULTICOMPONENTE EN MEDIOS POROSOS.
- 02 IV JORNADAS DE INVESTIGACIÓN Y DESARROLLO TECNOLÓGICO EN GESTIÓN DE RESIDUOS RADIACTIVOS. RESÚMENES Y ABSTRACTS.
- 03 ALMACENAMIENTO DEFINITIVO DE RESIDUOS DE RADIACTIVIDAD ALTA. CARACTERIZACIÓN Y COMPORTAMIENTO A LARGO PLAZO DE LOS COMBUSTIBLES NUCLEARES IRRADIADOS (II).
- 04 CONSIDERATIONS ON POSSIBLE SPENT FUEL AND HIGH LEVEL WASTE MANAGEMENT OPTIONS.
- 05 LA PECHBLENDA DE LA MINA FE (CIUDAD RODRIGO, SALAMANCA), COMO ANÁLOGO NATURAL DEL COMPORTAMIENTO DEL COMBUSTIBLE GASTADO. Proyecto Matrix I.

- 06 TESTING AND VALIDATION OF NUMERICAL MODELS OF GROUNDWATER FLOW, SOLUTE TRANSPORT AND CHEMICAL REACTIONS IN FRACTURED GRANITES: A QUANTITATIVE STUDY OF THE HYDROGEOLOGICAL AND HYDROCHEMICAL IMPACT PRODUCED.
- 07 IV JORNADAS DE INVESTIGACIÓN Y DESARROLLO TECNOLÓGICO EN GESTIÓN DE RESIDUOS RADIACTIVOS. Volumen I.
- 08 IV JORNADAS DE INVESTIGACIÓN Y DESARROLLO TECNOLÓGICO EN GESTIÓN DE RESIDUOS RADIACTIVOS. Volumen II.
- 09 IV JORNADAS DE INVESTIGACIÓN Y DESARROLLO TECNOLÓGICO EN GESTIÓN DE RESIDUOS RADIACTIVOS. Volumen III.
- 10 IV JORNADAS DE INVESTIGACIÓN Y DESARROLLO TECNOLÓGICO EN GESTIÓN DE RESIDUOS RADIACTIVOS. Volumen IV.

2002

- 01 FABRICACIÓN DE BLANCOS PARA LA TRANSMUTACIÓN DE AMERICIO: SÍNTESIS DE MATRICES INERTES POR EL MÉTODO SOL-GEL. ESTUDIO DEL PROCEDIMIENTO DE INFILTRACIÓN DE DISOLUCIONES RADIACTIVAS.
- 02 ESTUDIO GEOQUÍMICO DE LOS PROCESOS DE INTERACCIÓN AGUA-ROCA SOBRE SISTEMAS GEOTERMALES DE AGUAS ALCALINAS GRANITOÍDES.
- 03 ALTERACIÓN ALCALINA HIDROTÉRMICA DE LA BARRERA DE BENTONITA POR AGUAS INTERSTICIALES DE CEMENTOS.
- 04 THERMO-HYDRO-MECHANICAL CHARACTERISATION OF A BENTONITE FROM CABO DE GATA. A study applied to the use of bentonite as sealing material in high level radioactive waste repositories.
- 05 ESTUDIOS GEOLÓGICO-ESTRUCTURALES Y GEOFÍSICOS EN MINA RATONES (PLUTÓN DE ALBALÁ).
- 06 IMPACTO DE LA MINA RATONES (ALBALÁ, CÁCERES) SOBRE LAS AGUAS SUPERFICIALES Y SUBTERRÁNEAS: MODELIZACIÓN HIDROGEOQUÍMICA.
- 07 CARACTERIZACIÓN PETROLÓGICA, MINERALÓGICA, GEOQUÍMICA Y EVALUACIÓN DEL COMPORTAMIENTO GEOQUÍMICO DE LAS REE EN LA FASE SÓLIDA (GRANITOÍDES Y RELLENOS FISURALES) DEL SISTEMA DE INTERACCIÓN AGUA-ROCA DEL ENTORNO DE LA MINA RATONES.
- 08 MODELLING SPENT FUEL AND HLW BEHAVIOUR IN REPOSITORY CONDITIONS. A review of the state of the art.
- 09 UN MODELO NUMÉRICO PARA LA SIMULACIÓN DE TRANSPORTE DE CALOR Y LIBERACIÓN DE MATERIA EN UN ALMACENAMIENTO PROFUNDO DE RESIDUOS RADIACTIVOS.
- 10 PROCESOS GEOQUÍMICOS Y MODIFICACIONES TEXTURALES EN BENTONITA FEBEX COMPACTADA SOMETIDA A UN GRADIENTE TERMOHIDRÁULICO.

2003

- 01 CONTRIBUCIÓN EXPERIMENTAL Y MODELIZACIÓN DE PROCESOS BÁSICOS PARA EL DESARROLLO DEL MODELO DE ALTERACIÓN DE LA MATRIZ DEL COMBUSTIBLE IRRADIADO.
- 02 URANIUM(VI) SORPTION ON GOETHITE AND MAGNETITE: EXPERIMENTAL STUDY AND SURFACE COMPLEXATION MODELLING.
- 03 ANÁLOGOS ARQUEOLÓGICOS E INDUSTRIALES PARA ALMACENAMIENTO DE RESIDUOS RADIACTIVOS: ESTUDIO DE PIEZAS ARQUEOLÓGICAS METÁLICAS (ARCHEO-II).
- 04 EVOLUCIÓN PALEOAMBIENTAL DE LA MITAD SUR DE LA PENÍNSULA IBÉRICA. APLICACIÓN A LA EVALUACIÓN DEL COMPORTAMIENTO DE LOS REPOSITORIOS DE RESIDUOS RADIACTIVOS.
- 05 THE ROLE OF COLLOIDS IN THE RADIONUCLIDE TRANSPORT IN A DEEP GEOLOGICAL REPOSITORY. Participation of CIEMAT in the CRP project.
- 06 V JORNADAS DE INVESTIGACIÓN Y DESARROLLO TECNOLÓGICO EN GESTIÓN DE RESIDUOS RADIACTIVOS. Resúmenes de ponencias.

- 07 V JORNADAS DE INVESTIGACIÓN Y DESARROLLO TECNOLÓGICO EN GESTIÓN DE RESIDUOS RADIACTIVOS. Sinopsis de pósters.
- 08 V JORNADAS DE INVESTIGACIÓN, DESARROLLO TECNOLÓGICO Y DEMOSTRACIÓN EN GESTIÓN DE RESIDUOS RADIACTIVOS. Pósters técnicos.
- 09 DISMANTLING OF THE HEATER 1 AT THE FEBEX "IN SITU" TEST. Descriptions of operations
- 10 GEOQUÍMICA DE FORMACIONES ARCILLOSAS: ESTUDIO DE LA ARCILLA ESPAÑOLA DE REFERENCIA.
- 11 PETROPHYSICS AT THE ROCK MATRIX SCALE: HYDRAULIC PROPERTIES AND PETROGRAPHIC INTERPRETATION.

2004

- 01 PLAN DE INVESTIGACIÓN, DESARROLLO TECNOLÓGICO Y DEMOSTRACIÓN PARA LA GESTIÓN DE RESIDUOS RADIACTIVOS 2004-2008.
- 02 ESTUDIO DE LOS PRODUCTOS DE CORROSIÓN DE LA CÁPSULA Y SU INTERACCIÓN CON LA BARRERA ARCILLOSA DE BENTONITA "CORROBEN".
- 03 EFECTO DE LA MAGNETITA EN LA RETENCIÓN DE LOS RADIONUCLEÍDOS EN EL CAMPO PRÓXIMO: CESIO, ESTRONCIO, MOLIBDENO Y SELENIO.
- 04 Vª JORNADAS DE INVESTIGACIÓN Y DESARROLLO TECNOLÓGICO EN GESTIÓN DE RESIDUOS RADIACTIVOS. Volumen I.
- 05 Vª JORNADAS DE INVESTIGACIÓN Y DESARROLLO TECNOLÓGICO EN GESTIÓN DE RESIDUOS RADIACTIVOS. Volumen II.
- 06 Vª JORNADAS DE INVESTIGACIÓN Y DESARROLLO TECNOLÓGICO EN GESTIÓN DE RESIDUOS RADIACTIVOS. Volumen III.
- 07 Vª JORNADAS DE INVESTIGACIÓN Y DESARROLLO TECNOLÓGICO EN GESTIÓN DE RESIDUOS RADIACTIVOS. Volumen IV.
- 08 FEBEX PROJECT. POST-MORTEM ANALYSIS: CORROSION STUDY.
- 09 FEBEX II PROJECT. THE LABORATORY EXPERIMENTS.
- 10 FEBEX II PROJECT. FINAL REPORT ON THERMO-HYDRO-MECHANICAL LABORATORY TEST.
- 11 FEBEX II PROJECT. POST-MORTEM ANALYSIS EDZ ASSESSMENT.

2005

- 01 DEVELOPMENT OF A MATRIX ALTERATION MODEL (MAM).
- 02 ENGINEERED BARRIER EMPLACEMENT EXPERIMENT IN OPALINUS CLAY FOR THE DISPOSAL OF RADIOACTIVE WASTE IN UNDERGROUND REPOSITORIES.
- 03 USE OF PALAEOHYDROGEOLOGY IN RADIOACTIVE WASTE MANAGEMENT.
- 04 METODOLOGÍAS DE CARACTERIZACIÓN RADIOLÓGICA DE BULTOS DE RESIDUOS RADIACTIVOS DESARROLLADAS POR ENRESA
- 05 ANÁLOGOS NATURALES DE LA LIBERACIÓN Y MIGRACIÓN DEL UO Y ELEMENTOS METÁLICOS ASOCIADOS
- 06 FLUJO RADIAL EN MEDIOS HETEROGÉNEOS
- 07 VENTILATION EXPERIMENT IN OPALINUS CLAY FOR THE MANAGEMENT OF RADIOACTIVE WASTE
- 08 INFORME FINAL. IMPACTO ECONÓMICO DEL DESMANTELAMIENTO DE LA CENTRAL NUCLEAR VANDELLÓS I
- 09 FEBEX PROJECT. FINAL REPORT. FINAL PROJECT ON THERMO-HYDRO-MECHANICAL MODELLING

FEBEX Project
Final report

Post-mortem bentonite analysis

PUBLICACIÓN TÉCNICA 05-1/2006

Para más información, dirigirse a:



Departamento de Soportes de Información
C/ Emilio Vargas, 7
28043 MADRID

<http://www.enresa.es>

Diciembre 2006